Development, Characterization and Processing of a novel Family of Bulk Metallic Glasses: Sulfur-containing Bulk Metallic Glasses

Dissertation

zur Erlangung des Grades des

Doktors der Ingenieurwissenschaften (Dr.-Ing.)

der

Naturwissenschaftlich-Technischen Fakultät

der

Universität des Saarlandes

vorgelegt von

Alexander Kuball

Saarbrücken

September 2019

Tag des Kolloquiums: 16.03.2020

Dekan: Prof. Dr. rer. nat. Guido Kickelbick
Berichterstatter: Prof. Dr. rer. nat. Ralf Busch
Prof. Dr. mont. Christian Motz
Prof. Dr. rer. nat. Andreas Meyer
Vorsitz: Prof. Dr.-Ing. Frank Mücklich
Akad. Mitarbeiter: Dr.-Ing. Daniela Foetz

Abstract

In this work, a new family of bulk metallic glasses (BMGs), containing sulfur as major constituent, has been discovered. Before, sulfur has not been considered for the development of metallic glass forming compositions, but this work reveals that sulfur-containing BMGs can be produced in a vast compositional space. The question arises, why sulfur stabilizes the metastable undercooled liquid, allowing the formation of bulk glassy samples in these systems. Therefore, the role of sulfur for the process of glass formation is elucidated, which is governed by thermodynamic and kinetic contributions.

Besides their scientific interest, in particular, new Ti-based alloys are interesting candidates for industrial use. The high Ti-contents result in favorable mechanical and electrochemical properties and the glassy structure enables an unique process-ability. For an industrial-scale processing, a novel die-casting machine is designed, which is customized for the processing of BMGs.

High energy synchrotron X-ray diffraction experiments on the new alloys were performed and lead to a deeper insight in the relationship between the thermo-physical properties, mechanical behavior and the atomic structure. Indications for structural similarities between the glass and the corresponding crystalline mixture have been found and new structure-property-relations are proposed. All in all, these results will lead to a comprehensive understanding of the process of glass formation in these systems.

Zusammenfassung

Im Rahmen dieser Arbeit wurde eine neue Familie von metallischen Massivgläsern (MMG) entdeckt, die Schwefel als elementaren Legierungsbestandteil aufweisen. Bis heute wurde Schwefel nicht als Komponente in metallischen Gläsern in Erwägung gezogen, aber in dieser Arbeit wird gezeigt, dass die Bildung von MMGs in einem breiten Legierungsspektrum möglich ist. Es stellt sich die Frage, auf welche Weise Schwefel die metastabile unterkühlte Schmelze stabilisiert und so die Bildung von MMGs ermöglicht wird. Daher wird untersucht, welche Rolle der Schwefel bei dem Prozess der Glasbildung einnimmt, welcher von thermodynamischen und kinetischen Beiträgen bestimmt wird.

Insbesondere die neuen Ti-Legierungen sind neben ihrem wissenschaftlichen, auch von großem technischen Interesse. Die hohen Ti-Gehalte resultieren in herausragende mechanischen und elektrochemischen Eigenschaften und der Strukturzustand des Glases ermöglicht eine einzigartige Verarbeitbarkeit. Für die Verarbeitung im industriellen Maßstab wurde ein maßgeschneidertes Druckgussverfahren für das Urformen von metallischen Massivgläsern entwickelt.

Experimente mit hochenergetischer Röntgenstrahlung werden genutzt, um Beziehungen zwischen den thermo-physikalischen Eigenschaften, dem mechanischen Verhalten und der atomaren Struktur zu untersuchen. Es wurden Hinweise für einen Zusammenhang zwischen der Struktur des Glases und der dazugehörigen kristallinen Phasen entdeckt und neue Struktur-Eigenschafts-Beziehungen angeführt. Diese Ergebnisse ermöglichen einen tiefen Einblick in den Prozess der Glasbildung in diesen Systemen.

Danksagung

Als erstes möchte ich an dieser Stelle meinem Betreuer Prof. Dr. Ralf Busch für die Betreuung meiner Doktorarbeit am Lehrstuhl für Metallische Werkstoffe in den vergangenen vier Jahren herzlich danken. Er hat mit den konstruktiven Gesprächen die Arbeit wesentlich voran gebracht und mir gleichzeitig die Freiheiten eingeräumt, die erforderlich waren, um neue Ideen umzusetzen.

Außerdem gilt meinem Freund und Kollegen Moritz Stolpe ein ganz besonderer Dank, da er mich überhaupt erst ermutigt hat Werkstofftechnik zu studieren und meine Arbeiten am Lehrstuhl für Metallische Werkstoffe durchzuführen. Dann möchte ich mich insbesondere bei meinen Freunden und "Mitdoktoranden" Dr. Simon Hechler, der mein langjähriger Büronachbar war, sowie Dr. Oliver Gross, Beneditk Bochtler, Maximilian Frey und Nico Neuber für die gute Zusammenarbeit und Zeit am Lehrstuhl bedanken. Wir konnten uns immer gegenseitig motivieren und haben das ein oder andere im Labor erlebt, auf das ich gerne zurückschaue. Ohne die gegenseitige Unterstützung hätte so manches mit Sicherheit nicht so reibungslos funktioniert. Mein Dank gilt auch den anderen Mitarbeitern des Lehrstuhls, wobei ich hierbei insbesondere Hermann Altmeyer und Jörg Eiden hervorheben möchte, die mich von der technischen Seite unterstützt haben und ohne die das ein oder andere Projekt wesentlich länger gedauert hätte bzw. gar nicht erst möglich gewesen wäre. Dr. Frank Aubertin und Dr. Isabella Gallino standen jederzeit mit einem Rat zur Seite und haben mir mit zahlreichen Diskussionen weitergeholfen.

Ein ganz besonderen Dank möchte ich dann natürlich meinen Freunden und meiner Familie für die Unterstützung während meines gesamten Studiums aussprechen. Besonders meine Eltern, Silke und Rainer, haben mich stets auf meinem Weg unterstützt, was mir sehr viel bedeutet. Ein besonderer Dank für die Unterstützung gilt auch meiner Großmutter Anneliese. Ich danke meiner Schwester Sabrina und ihrem Ehemann Lars für die schönen Tage und Abende, die wir gemeinsam verbracht haben und die mir Energie für diese Arbeit gegeben haben. Auch meine Freunde haben für eine ausreichende Ablenkung in dieser Zeit gesorgt, um meine Arbeit immer wieder mit neuem Elan fortzuführen. Dabei möchte ich vorallem meinen langjährigen Freund Steffen hervorheben, der trotz der großen Entfernung immer ein offenes Ohr hatte.

Schließlich möchte ich an dieser Stelle ganz besonders meiner Freundin Lisa für alles Danken, was Sie in den letzten Jahren für mich gemacht hat und wie sie mich während der Zeit meines Promotionsstudiums unterstützt hat. Wir haben in dieser Zeit schöne Momente zusammen erlebt und ich freue mich auf unsere gemeinsame Zukunft.

Publications and Contributions

In the frame of this work the author contributed to the following articles:

Peer-reviewed articles as first author:

- A. Kuball, O. Gross, B. Bochtler, B. Adam, L. Ruschel, M. Zamanzade and R. Busch, Development and Characterization of Titanium-based Bulk Metallic Glasses, Journal of Alloys and Compounds 790, 337-346 (2019)
- A. Kuball, B. Bochtler, O. Gross, V. Pacheco, M. Stolpe, S. Hechler and R. Busch, On the Bulk Glass Formation in the Ternary Pd-Ni-S System, Acta Materialia 158, 13-22 (2018)
- A. Kuball, O. Gross, B. Bochtler and R. Busch, Sulfur-bearing metallic glasses: A new family of bulk glass-forming alloys, Scripta Materialia 146, 73-76 (2018)

Peer-reviewed publications as Co-author:

- O. Gross, N. Neuber, A. Kuball, B. Bochtler, S. Hechler, M. Frey and R. Busch, Signatures of structural differences in Pt-P- and Pd-P-based bulk glass-forming liquids, Communications Physics 2, 83 (2019)
- O. Gross, S.S. Riegler, M. Stolpe, B. Bochtler, A. Kuball, S. Hechler, R. Busch and I. Gallino, On the high glass-forming ability of Pt-Cu-Ni/Co-P-based liquids, Acta Materialia 141, 109-119 (2017)

Articles without peer-review process:

- A. Kuball, O. Gross, B. Bochtler and R. Busch, Konstruktionswerkstoff für hochfeste Kleinteile, Konstruktion - Zeitschrift für Produktentwicklung und Ingenieur-Werkstoffe, VDI Fachmedien GmbH & Co. KG (2018), https://www.konstruktion-online.de/ 2018/ Ausgabe-04/ Fachteil-Ingenieur-Werkstoffe/ Konstruktionswerkstoff-fuer-hochfeste-Kleinteile (accessed: 29.01.2019)
- O. Gross, A. Kuball, B. Bochtler and R.Busch, Amorphe Metalle aus Titan und Schwefel, GIT Laborportal, Wiley-VCH Verlag GmbH & Co. KGaA (2018), https://www.git-labor.de/forschung/ chemie-physik/ amorphe-metalle-aus-titan-und-schwefel (accessed: 29.01.2019)

The results of this work have been presented as contibutions to the below listed conferences:

- 2019. 17th International Conference on Liquid and Amorphous Metals (LAM-17) Lyon, France. Oral presentation: Thermo-physical characterization of sulfur-bearing bulk metallic glasses.
- 2018. DPG (Deutsche Physikalische Gesellschaft) Frühjahrstagung Berlin, GERMANY. Oral presentation: Development and Characterization of Sulfur-bearing Bulk Metallic Glasses.
- 2017. The 16th International Conference on Rapidly Quenched and Metastable Materials (RQ16) Leoben, AUSTRIA. Oral presentation: Development of a novel family of Bulk Metallic Glasses.

Filed Patents:

- WO2019038415A1. Inventor: A. Kuball, O. Gross, B. Bochtler, R. Busch. "Alloy forming metallic glasses containing sulphur "
- 2018062914194200DE. Inventor: A. Kuball, O. Gross, B. Bochtler, S. Hechler, R. Busch. "Vorrichtung und Verfahren zur Herstellung eines aus einem amorphen oder teilamorphen Metall gebildeten Gussteils sowie Gussteil"

Successfull Founding and Education

Successfull proposals:

- Anschubfinanzierung für Forschungsprojekte der Universität des Saarlandes, "Untersuchung der Kühlratenabhängigkeit der makroskopischen und mikrospkopischen mechanischen Eigenschaften metallischer Gläser". Authors: A. Kuball, M. Zamanzade, R. Busch, C. Motz, 2019.
- DFG BU 2276/10-1. "Neue schwefelhaltige Metallische Massivgläser". Authors: A. Kuball, O. Gross, B. Bochtler and R. Busch, 2019.
- Research cooperation. Heraeus Deutschland GmbH. Authors: A. Kuball, B. Bochtler, R. Busch, 2019.
- ZIM 16KN021269. "NorLin - Druckgussanlage / Schmelz- und Gießprozess". Authors: A. Kuball, J. Hilsmann, R. Busch, 2017.
- EXIST-Forschungstransfer. "Industrielle Herstellung und Verarbeitung amorpher Metalle" Authors: A. Kuball, O. Gross, B. Bochtler, S. Hechler, P. Linek, 2019.
- TEMPUS (Tiegelfreies Elektromagnetisches Prozessieren unter Schwerelosigkeit)
  - 5 Parabolas, A. Kuball, B. Bochtler, O. Gross, R. Busch, "Viskosität und Oberflächenspannung der Schmelze der massivglasbildenden Legierung $Zr_{56.5}$-$Ti_{13.3}Ni_{13.6}Cu_{9.6}S_7$", 2019.
  - 5 Parabolas, A. Kuball, B. Bochtler, O. Gross, R. Busch, "Viskosität und Oberflächenspannung der Schmelze der neuartigen, massivglasbildenden Titanlegierung $Ti_{65}Zr_{10}Cu_{15}Ni_2S_8$", 2018.
- Scheduled beamtime at DESY (Deutsches Elektronen Synchrotron)
  - I-20180284, 48 h in 2018, A. Kuball, O. Gross, R. Busch, "Investigation of the cooling rate dependent structural changes of the relaxation mechanisms in bulk metallic glass forming alloys", 2018.
  - I-20170938, 48 h in 2018, O. Gross, B. Bochtler, A. Kuballl, R. Busch, "Investigation of the compositional dependence of structural changes of Pt/Pd-Cu-Ni-P bulk glass forming liquids and their connection to kinetic fragility", 2017.
  - I-20180946, 94 h in 2018, O. Gross, I. Gallino, B. Ruta, A. Kuball, B. Bochtler, N. Neuber, R. Busch, "Dynamics on the medium range order length scale in a metallic glass-former", 2018.

Supervised theses:

- Master Thesis: A. Thiery, "Evaluation of the alloying process of bulk glass forming alloys and development of Ti-based bulk metallic glasses", Saarland University, 2019.
- Master Thesis: B. Adam , "Characterization and development of the $Ti_{40}Zr_{35}$-$Cu_{17}S_8$ bulk glass forming alloy", Saarland University, 2019.
- Master Thesis: M. Kipper, "Herstellung und Charakterisierung hochharter metallischer Massivgläser", Saarland University, 2019.
- Master Thesis: M. Babin, "Development of novel Ti-based bulk glass forming alloys in the Ti-Cu-Ni-Sn system", Saarland University, 2017.
- Master Thesis : V. Pacheco, "Optimization and characterization of a novel Pd -Ni based bulk metallic glass forming alloy", Saarland University, 2016.

- Bachelor Thesis: C. Köhler, "Influence of industrial grade material on the glass forming ability and mechanical behavior of bulk metallic glasses", Saarland University, 2019.
- Bachelor Thesis: B. Adam, "Entwicklung und Herstellung titanreicher Metallischer Massivgläser im System Ti-Ni-S", Saarland University, 2018.
- Bachelor Thesis: T. Saravanapavan, "Einfluss der Reinheitsgrade des metallischen Massivglases AMZ4 ($Zr_{59.3}Cu_{28.8}Al_{10.4}Nb_{1.5}$ auf die mechanischen Eigenschaften", Saarland University, 2019.
- Bachelor Thesis: M. Schmidt, "Thermische Untersuchungen an den gesputterten ternären Legierungssystemen Zr-Cu-Al und Zr-Cu-Ag", Saarland University, 2018.
- Bachelor Thesis: Y. Min, "Development of Novel Ti-based Bulk Glass Forming Alloys in the Ti-Cu-Ni System", Saarland University, 2017.
- Bachelor Thesis: M. Kipper, "Einfluss der induktiven Legierungssynthese auf die Glasbildungsfähigkeit ausgewählter Metallischer Massivgläser", Saarland University, 2017.

Contents

Abbreviations

3PBB	**3** **P**oint **B**eam **B**ending
bcc	**b**ody **c**entered **c**ubice
BSE	**B**ack **S**cattered **E**lectrons
BMG	**B**ulk **M**etallic **G**lass
CCR	**C**ritical **C**ooling **R**ate
CCT	**C**ritical **C**asting **T**hickness
DSC	**D**ifferential **S**canning **C**alorimetry
DTA	**D**ifferential **T**hermal **A**nalysis
EDX	**E**lectron **D**ispersive **X**-Ray spectroscopy
EML	**E**lectro **M**agnetic **L**evitation
ESL	**E**lectro **S**tatic **L**evitation
fcc	**f**ace **c**entered **c**ubic
FSDP	**F**irst **S**harp **D**iffraction **P**eak
GFA	**G**lass **F**orming **A**bility
GFR	**G**lass **F**orming **R**ange
hcp	**h**exagonal **c**losed **p**acked
JMAK equation	**J**ohnson-**M**ehl-**A**vrami-**K**olmogorov equation
KWW equation	**K**ohlrausch-**W**illiam-**W**atts equation
MG	**M**etallic **G**lass
SCE	**S**ample **C**oupling **E**lectronics
SCL	**S**uper **C**ooled **L**iquid
SCLR	**S**uper **C**ooled **L**iquid **R**egion
SE	**S**condary **E**lectrons
SEM	**S**canning **E**lectron **M**icroscopy
SE relation	**S**tokes-**E**instein relation

SSDP	**S**econd **S**harp **D**iffraction **P**eak
TEMPUS	**T**iegelfreies **E**ectro**m**agnetisches **P**rozessieren **U**nter **S**chwerelosigkeit
TMA	**T**hermo **M**echanical **A**nalysis
TTT	**T**ime-**T**emperature-**T**ransformation
VFT equation	**V**ogel-**F**ulcher-**T**ammann equation
XRD	**X**-**R**ay **D**iffraction

Frequently used Symbols

t_{rg}	reduced glass transition temperature	
T_g	glass transition temperature[1]	K
T_x	crystallization temperature	K
T_m	melting temperature	K
T_l	liquidus temperature	K
T_K	Kauzmann temperature	K
$\Delta H^l(T)$	enthalpy of the liquid phase	J g-atom^{-1}
$\Delta S^l(T)$	entropy of the liquid phase	J g-atom^{-1} K^{-1}
$\Delta c_p^l(T)$	molar heat capcity of the liquid phase	J g-atom^{-1} K^{-1}
$\Delta H^x(T)$	enthalpy of the crystalline phase	J g-atom^{-1}
$\Delta S^x(T)$	entropy of the crystalline phase	J g-atom^{-1} K^{-1}
$\Delta c_p^x(T)$	molar heat capcity of the crystalline phase	J g-atom^{-1} K^{-1}
$\Delta G^l(T)$	Gibbs free energy of the liquid phase	J g-atom^{-1}
$\Delta G^x(T)$	Gibbs free energy of the crystalline phase	J g-atom^{-1}
$\Delta H^{l-x}(T)$	excess enthalpy	J g-atom^{-1}
$\Delta S^{l-x}(T)$	excess entropy	J g-atom^{-1} K^{-1}
$\Delta c_p^{l-x}(T)$	excess molar heat capacity	J g-atom^{-1} K^{-1}
$\Delta G^{l-x}(T)$	driving force for crystallization	J g-atom^{-1}
ΔH_f	enthalpy of fusion	J g-atom^{-1}
ΔS_f	enthalpy of fusion	J g-atom^{-1} K^{-1}
γ^{x-l}	interfacial energy between the crystal and the liquid	J m^{-2}
γ_{glass}^{X-ray}	volume expension coefficient from XRD measurements	K^{-1}
q	heating rate	K/s
Q	wave vector	Å^{-1}

---

[1] For a more detailed discription the reader is referred to section 2.2.2.4.

r	distance	Å
$S(Q)$	total structure factor	
$I(Q)$	corrected intensitiy	counts
$G(r)$	reduced pair distribution function	Å^{-2}
σ	surface tension	Jm^{-1}
E	Youngs modulus	GPa
$\sigma_{yield}^{0.2\%}$	0.2 % offset yield strength	MPa
σ_{total}	total flexural strength	MPa
ϵ_{el}	elastic strain	%
ϵ_{frac}	fracture strain	%
ϵ_{total}	total strain to failure	%
ν	Poisson ratio	
G_{∞}	high frequency shear modulus	GPa
E_{corr}	corrosion potential	V
E_{pit}	pitting potential	V
E_{break}	breakdown potential	V
E_{pp}	repassivation potential	V
i_{pass}	passive current density	A cm^{-2}
D^{*}	fragility parameter	
m or m_{kin}	kinetic fragility index	
m_{str}	structural fragility index	
T_0	VFT temperature	K
η_0	viscosity limit at infinite temperature	Pa s
$\eta(T)$	dynamic viscosity	Pa s
τ_0	relaxation time limit at infinite temperature	s
$\tau_{\alpha}(T)$	structural relaxation	s
ρ	volumetric mass density	$g\ cm^{-3}$
d_c	critical casting thickness	mm
R_c	critical cooling rate	K/s
$t_{iso}^{x\%}$	isothermal crystallization time of x % of crystals	s

I dedicate this work to my parents Silke and Rainer Kuball.

Chapter 1

Introduction

The process of casting pure metals at temperatures above their melting point is known for thousands of years. The mixing of metals in the liquid state, known as alloying, led to an incredible progress in human history. In these early days, only the pathway of crystalline solidification was known for metallic alloys processed from their equilibrium liquid. Therefore, one major goal in metallurgy was the development and design of new crystalline metals with a higher performance and reasonable material costs. For instance, new crystalline Ni-superalloys enable the further development of turbines or new Ti-Ni shape memory alloys lead to advances in medical engineering.

A relatively young class of metals has been discovered in the early 1960s by Duwez and co-workers, when working on the supersaturation of a solid solution [1]. These accidentally discovered amorphous metals or metallic glasses are frozen-in liquids, exhibiting an disordered atomic structure. This structural state is achieved by high cooling rates, which are high enough to bypass the crystalline solidification. Visually, these metals do not differ from conventional metals, but the obtained unique atomic structure for a metallic solid results in extraordinary properties like inter alia an extraordinarily high strength and elasticity, which outshine the mechanical properties of crystalline metals [2–5]. Besides their unique properties the process-ability of these new class of metals attracted the intention of the industry [6].

Because of their ability to achieve high undercoolings at moderate cooling rates and their high thermal stability, bulk glass forming liquids (BMGs) allow the investigation of the thermo-physical properties of deeply undercooled metallic melts. The results allow conclusions about the process of glass formation, which is especially in case of metallic glasses not fully understood. Therefore, the temperature dependence of different thermodynamic and kinetic functions of the amorphous phase (glass or liquid) are of certain interest in order to understand the nature of the glass. Finally, the interplay between processing conditions, physical properties and the connection to the structural evolution is of great interest.

From both, the scientific and technical point of view, the development of new bulk glass forming alloys is of great interest. Most bulk glass forming alloys with promising properties for application consist to a large extent of expensive or toxic elements such as zirconium or beryllium, strongly limiting their application and new compositions are interesting for in-depth investigations of the above mentioned structure-property-relations.

In this work, a completely new family of glass forming alloys has been discovered: Sulfur-bearing metallic glasses [7–9]. So far, sulfur was not considered as a potential constituent in metallic glasses, opening new possibilities for the development of new alloys [7, 10, 11]. Sulfur is well known in different industry sectors like for example as alloying element for free machining steels or as decisive ingredient for the vulcanization of natural rubber. Hence, the handling and processing of sulfur is not critical on an industrial scale.

In total, more than 500 different new, sulfur-containing glass forming compositions have been discovered. Moreover, a customized die-casting process has been developed, enabling the economic processing of BMGs on an industrial scale. Among these novel alloys, in particular, the Pd- and Ti-/Zr-based alloys are of interest due to their unique properties in comparison to well known, sulfur-free BMGs. Therefore, the novel alloys are characterized comprehensively regarding their properties.

The content of this thesis is structured as follows:

In chapter 2 the reader is introduced to the topic and the historical background about the development of BMGs and the state of the art about BMGs is reviewed, so that the reader is able to asses the outcome of this work. Subsequently, the experimental procedures and methods are explained briefly in chapter 3. The results of the alloy development of sulfur-bearing bulk metallic glasses are presented in chapter 4, distinguishing between alloys in the Pd-Ni-S and the Ti-Zr-Ni-Cu-S system. Additionally, a new processing technology that has been designed is introduced in this chapter. Chapter 5 deals with the results of the thermo-physical, mechanical, electrochemical and structural characterization of the representatives for each alloying system $Pd_{31}Ni_{42}S_{27}$, $Ti_{60}Zr_{15}Cu_{17}S_8$ and $Zr_{56.5}Ti_{13.3}Ni_{13.6}Cu_{9.6}S_7$. The findings are discussed for each alloying system in context to literature data and common features of sulfur-containing bulk metallic glasses are analyzed in chapter 6. Finally, the outcome of this work is summarized in chapter 7 and an outlook for future works is given to the reader.

Chapter 2

State of the Art

In this chapter a literature review will introduce the topic to the reader and reflect the state of the art in the field of bulk metallic glasses, highlighting the potentials for the use of bulk metallic glasses in different technological fields of applications and showing the motivations for the work on bulk metallic glasses. On the one hand, the focus lies on a brief summary of the historical background along with the properties achieved by this relatively new class of alloys. On the other hand, the process of glass formation regarding thermodynamics and kinetics is discussed, in order to provide a theoretical basis for the experiments carried out in the frame of this thesis.

2.1 Historical Background

Since the discovery of metallic glasses (MGs) in the early 1960's [1], intensive work on new alloy compositions lead to the development of so-called bulk metallic glasses (BMGs) [12]. Until then, MGs were produced by rapid solidification techniques like melt spinning or splat quenching, which realize cooling rates above 10^6 K/s, being sufficient to avoid crystallization. In contrast, in BMG forming systems a monolithic amorphous structure can be produced by permanent mold casting with dimensions of more than 1 mm, corresponding to a significantly lower critical cooling rate. The critical casting thickness is related to the critical cooling rate, since the heat transfer takes place over the crosssection of the sample. If typical values of the thermal conductivity and heat capacity of a metallic alloy are assumed and if a constant heat transfer at the interface between the mold and the metallic melt is present, both quantities can be related by [13]

$$R = \frac{10}{(d_c)^2} \tag{2.1}$$

where R corresponds to the critical cooling rate in Ks^{-1} and d_c to the critical casting thickness in cm.

After recognizing that the critical diameter of BMGs can be tuned up to 1 mm, further intensive research lead to the discovery of several systems with a casting thickness of even far above 1 cm. The achievable diameters or rather sample geometries allowed a proper analysis of their bulk properties, revealing an enormous potential for manifold applications. The amorphous structure results in yield strength values close to the theoretical strength in combination with an elasticity, which was so far only observed for polymers [4]. Moreover, the defect-free, monolithic atomic structure leads to an excellent corrosion behavior [4]. This combination of unique properties drives on the development of the new class of metals. However, excluding alloys in the Zr-Ti-Cu-Ni-Be [14] and the Pd-Cu-Ni-P system [15], most of the technically relevant alloying systems, such as Fe-, Ni- or Ti-based alloys, show casting thicknesses of only up to roughly 1 cm [16–18]. It is for this reason that the discovery of new bulk glass forming alloys is still one major aim in metallic glass community.

To this date, roughly 32 elements are used for the development of new, applicable bulk metallic glasses (marked in blue in Fig. 2.1), excluding rare and toxic elements such as rare earth metals (except yttrium) or harmful elements like uranium [11, 19], resulting in a number of about 3 billion possible bulk glass forming alloys. So far, only about 1 000 BMGs have been discovered [10]. Thus, the compositional space for the development of completely new BMGs is still enormous. It has to be stressed that in the study of Li et al., sulfur is not considered as constituent in applicable BMGs (highlighted in red in Fig. 2.1) and not because it is not practical, but because sulfur was not considered in any bulk glass forming composition yet. In the frame of this work, sulfur-bearing BMGs were discovered for the first time. In the following section, different empirical and theoretical guidelines for the development and design of new glass forming compositions in metallic systems are explained.

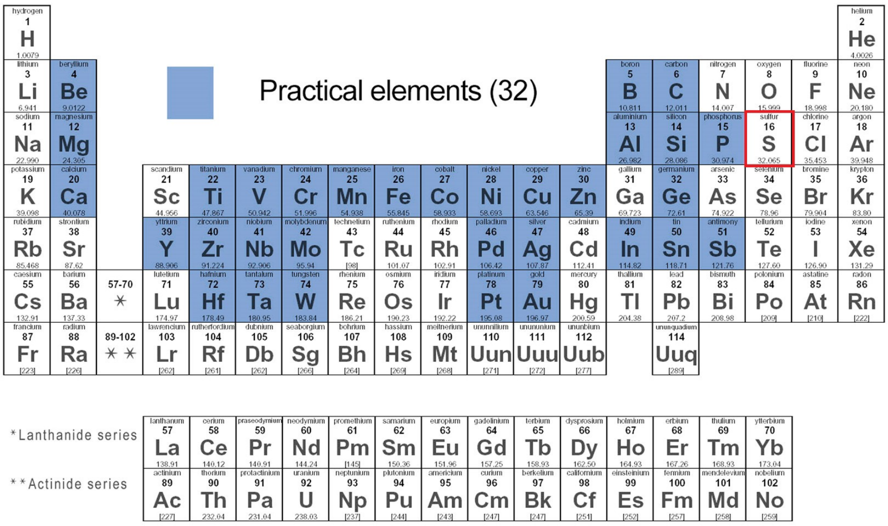

FIGURE 2.1: Illustration of the periodic table. Elements, which are used for the synthesis of bulk metallic glasses and are practical for an industrial scale processing are highlighted in blue. Sulfur (highlighted in red) is not considered in the work of Li et al. [10] as practical element for the synthesis of bulk metallic glasses. Adapted from Ref. [10].

2.2 Glass Forming Range and Glass Forming Ability

The glass forming range (GFR) describes the size of the compositional space in an alloying system within glass formation can be observed. This is shown schematically in Fig. 2.2 for a ternary system with the components A, B and C. The size of the experimental GFR depends on the respective cooling rate during the experiment. In general, higher cooling rates (or smaller critical diameters d_c) lead to a wider compositional space than lower ones. For instance, in Fig. 2.2 the GFR for the formation of glassy ribbons ($d_c \sim 0.02$ mm) is wider than for BMGs with a 1 mm $< d_c \leq 5$ mm or BMGs with a $d_c > 5$ mm.

One method for the estimation of the GFR is the so-called T_0 concept [20, 21]. Originally this method was used to determine the thermodynamic boundary for the supersaturation of solid solutions. Therefore, it is assumed that only polymorphic transformations and no phase separation take place during crystallization. In other words, the composition of the liquid phase and the corresponding crystal are identical and no diffusion is necessary. These assumptions are made because of the fast cooling rates used in experiments for the supersaturation. The same considerations can be assigned to the process of glass formation: If the cooling rates are sufficiently high to avoid phase separation in compositional regions were the Gibbs free energy of the crystalline solid is lower than that of the liquid phase (at a given temperature below the melting point[1]),

---

[1] In this context, it is assumed that the melting point = solidus temperature = liquidus temperature.

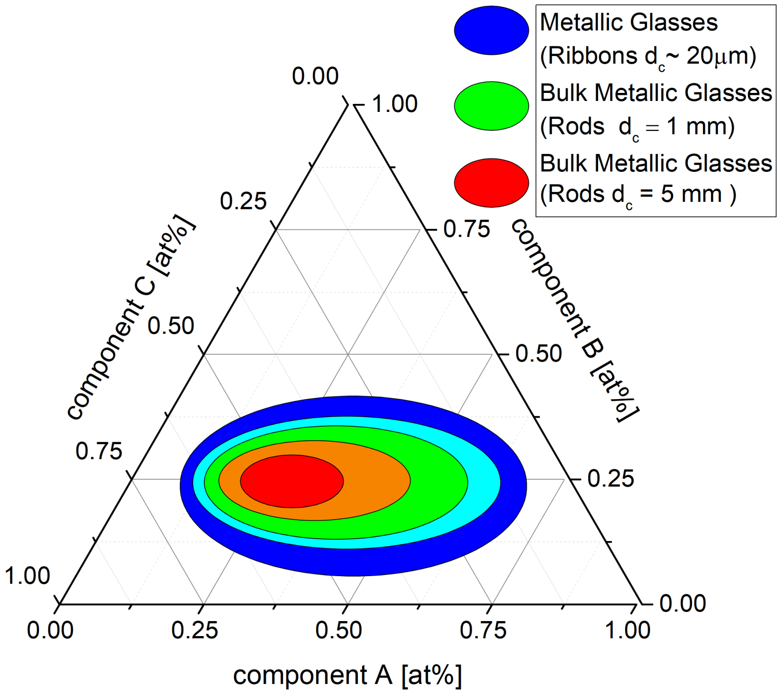

Figure 2.2: Glass forming range (GFR) as a function of the critical diameter d_c for glassy ribbons (blue), BMGs with a $d_c = 1$ mm (green) and BMGs with a $d_c = 5$ mm (red). The area decreases with an increasing d_c.

a polymorphic transition into a crystalline structure can not take place and a glass can be formed. However, this method is not able to describe the kinetic contributions for glass formation and hence, gives no information about the required cooling rate.

The cooling rate being necessary to avoid crystallization is called critical cooling rate and is a measure of the glass forming ability (GFA). Since the critical cooling rate is inversely proportional to the critical diameter of an as-cast sample (equation 2.1), the GFA is experimentally often determined by casting samples with different diameters. Thus, the experimental effort for the evaluation of the GFA in a compositional space (within the GFR) is rather high. It is for this reason that in the last decades one major aim in the metallic glass community was to find theoretical approaches for the prediction and description of the GFA in an alloying system.

2.2.1 Emperical Rules for Glass Formation

Already in 1960, Duwez et al. proposed that a larger number of elements is beneficial for glass formation due to "confusion"of the liquid [1, 22, 23] an associated inhibited crystallization. Thus, bulk glass formation is most likely expected to take place in multi-component systems.

Another good indicator for glass formation in a metallic system is the presence of deep eutectics in these multi-component systems. Here, the metallic melt is stabilized down to lower temperatures in comparison to the surrounding crystalline phases. This was picked up by Turnbull in 1969, introducing the concept of the reduced glass transition temperature $t_{rg} = T_g/T_m$ [24], where T_g and T_m correspond to the glass transition temperature and the melting temperature[2], respectively. For higher values of t_{rg} a higher GFA is expected, since the temperature range in which the metastable undercooled liquid exists and which has to be passed is smaller. In contrast to T_m, T_g is not sensitive to compositional changes within the GFR and hence, t_{rg} reaches the highest value in vicinity of an eutectic point. In 2000, Lu et al. revised the concept of t_{rg} in several metallic glass forming systems, revealing that the GFA correlates in general well with t_{rg}, but since the liquidus temperature T_l and not inevitable the solidus temperature T_m increases for off-eutectic compositions, T_l should be used for the determination of t_{rg} instead of T_m [25].

Inoue proposed a summary of the interaction of different parameters influencing the GFA of an alloying system [26], leading to three empirical rules for choosing a multi-component system to discovery new bulk glass forming compositions:

- the composition should consist of more than three kinds of elements
- the constituents should exhibit a size mismatch of at least 12 % between their atomic radii
- the constituents should show a highly negative heat of mixing

By following these rules, the liquid phase is stabilized by the formation of a densely packed atomic structure, a decreasing atomic mobility and an increasing interfacial energy. This makes the formation of the thermodynamically stable crystal more difficult. From this, it is evident, that the process of glass formation is driven by different thermodynamic and kinetic contributions.

2.2.2 Thermodynamics and Kinetics of Glass Formation

In order to identify the contributions, which are decisive for the process of glass formation, and to give an exact description of the GFA of an alloy, the competing process of crystallization has to be considered. Crystallization occurs via a first order phase transition and hence, by nucleation and growth. The fundamentals of this transition are reviewed briefly in the following section.

---

[2] Here, T_m corresponds to the solidus temperature.

2.2.2.1 The Driving Force for Crystallization

Conventionally, when cooling a metallic liquid below its liquidus temperature, the most stable thermodynamic state is reached by crystallization, since the system can decrease its Gibbs free energy G. The Gibbs free energy of the liquid (G^l) and the crystalline (G^x) phase at constant pressure can be described as

$$G^l = H^l - TS^l \tag{2.2}$$

$$G^x = H^x - TS^x \tag{2.3}$$

where $H^{l/x}$ and $S^{l/x}$ correspond to the enthalpy and entropy of the respective phase.

In Fig. 2.3a the Gibbs free energy of the liquid and the crystalline state are shown schematically as a function of temperature. The arrow indicates the drop in the Gibbs free energy $\Delta G^{l-x}(T)$ at a certain undercooling ($\Delta T = T_l - T$) below the melting point T_l.

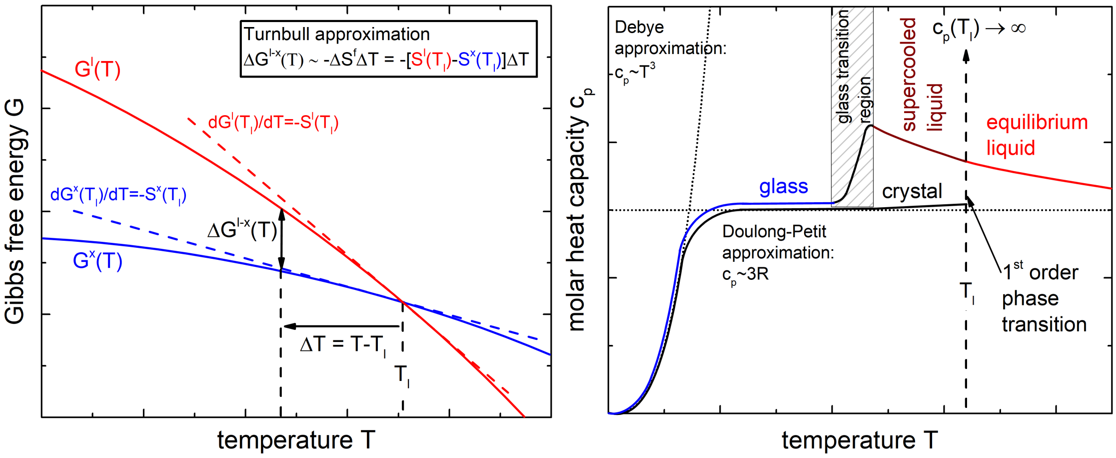

(a) (b)

FIGURE 2.3: a) The course of the Gibbs free energy of the liquid phase ($\Delta G^l(T)$) and the crystalline phase ($\Delta G^x(T)$) are shown as solid lines. According to Turnbull's approximation, the Gibbs free energy difference $\Delta G^{l-x}(T)$ at a certain undercooling $\Delta T = T_l - T$ can be estimated from the difference in the slopes at T_l. This difference corresponds to the entropy of fusion ΔS_f. b) Illustration of the molar heat capacity c_p as a function of temperature. Commonly, upon cooling from the equilibrium liquid the crystalline state is achieved by a 1st order phase transition, resulting in a drop of c_p. In the case of vitrification, the liquid phase is undercooled and freezes-in by passing the glass transition region. The course of c_p in the solid state can be described by Debye's approximation and Doulong-Petit's law.

This gain in Gibbs free energy ΔG^{l-x}, due to the formation of the crystalline phase, is termed as driving force for crystallization, being the first contribution for the formation of the crystalline phase. This Gibbs free energy difference can be expressed as

$$\begin{aligned}
\Delta G^{l-x}(T) &= \Delta H^{l-x}(T) - T\Delta S^{l-x}(T) \\
&= \Delta H_f - \left[\int_T^{T_l} c_p^l(T')dT' - \int_T^{T_l} c_p^x(T')dT'\right] \\
&- T\left[\Delta S_f - \left\{\int_T^{T_l} \frac{c_p^l(T')}{T'}dT' - \int_T^{T_l} \frac{c_p^x(T)'}{T'}dT'\right\}\right] \\
&= \Delta H_f - \int_T^{T_l} \Delta c_p^{l-x}(T')dT' - T\left[\Delta S_f - \int_T^{T_l} \frac{\Delta c_p^{l-x}(T')}{T'}dT'\right]
\end{aligned} \tag{2.4}$$

where ΔH_f and ΔS_f are the enthalpy and entropy of fusion. ΔH_f corresponds to the released or absorbed heat during the transition from liquid to crystal or vice versa. Both can be determined in melting experiments with a differential thermal analyzer (DTA) or by differential scanning calorimetry (DSC) (see section 3.2.1.1). Additionally, the difference of the molar heat capacity between the liquid and the crystalline phase $\Delta {c_p}^{l-x}$ has to be measured in order to determine $\Delta G^{l-x}(T)$. The appropriate experimental procedure is discussed in section 3.2.1.2. As already pointed out, bulk glass forming alloys are complex alloys and thus, the crystalline solid might consist of several, different crystalline phases. It is for this reason that for the determination of the molar heat capacity difference $\Delta {c_p}^{l-x}$ the heat capacity of the crystalline mixture is considered.

At this point, a closer look is taken at the driving force for crystallization in multicomponent systems [27]. The illustration of $\Delta G^{l-x}(T)$ in Fig. 2.3 does only correspond to the driving force for crystallization in case of a single component system, where the crystalline phase is formed polymorphous without separation of the liquid phase in different crystalline phases. In multicomponent alloys, however, $\Delta G^{l-x}(T)$ only represents the difference in Gibbs free energy between the liquid and the crystalline mixture, which is not necessarily equivalent to the driving force for crystallization. This results from the fact that, in case of bulk glass forming alloys, the primary precipitating phase (e.g. α), which is most likely only one phase of the crystalline mixture, is not formed polymorphous. Hence, the composition of the liquid is not equal to the composition of the primary phase. The Gibbs free energy difference between the primary phase and the liquid, $\Delta G^{l-\alpha}(T)$, which corresponds to the true driving force for crystallization, results from the difference in the chemical potential $\Delta\mu^{l-\alpha}(T)$ ($\Delta G^{l-\alpha}$=$\Delta\mu^{l-\alpha}(T)$). For the determination of the true driving force $\Delta\mu^{l-\alpha}(T)$, the parallel tangent method can be used, giving the composition with the maximum driving force in a multicomponent system, corresponding to the composition of the primary precipitating phase. However, the construction of the parallel tangents is hardly possible in multicomponent systems, since the Gibbs free energy of the individual crystalline phases in the compositional landscape is commonly not available. Therefore, $\Delta G^{l-x}(T)$ is the most straight forward approximation of the driving force for crystallization, since it represents at least the lower limit of $\Delta G^{l-\alpha}{=}\Delta\mu^{l-\alpha}(T)$.

In Fig. 2.3b the molar heat capacity is shown schematically as a function of temperature of the different phases (liquid, crystal, glass). If crystallization can be avoided, the liquid is undercooled, finally passing the glass transition region and reaching the glassy state. Considering the course of c_p of the undercooled liquid phase upon cooling, an increase is observed, which is unexpected from Debye's model [28]. However, it is commonly observed in glass forming liquids and can be attributed to the formation of SRO and a decreasing free volume and configurational entropy [28, 29]. The meaning of the course of the heat capacity with temperature and the link to the kinetic fragility will be picked up in section 6.4. The drastic drop of c_p of the undercooled liquid to the value of the glass is attributed to the transition from the ergodic nature of the liquid phase to the non-ergodic nature of the glass [30], which is connected to a structural arrest and the freezing of the enthalpy and entropy. In the solid state (glassy and crystalline), the temperature dependence of heat capacity at low temperatures ($<< 273K$) can be described by Debyes model, reaching, according to Dulong-Petit's law, a value close to $3R = 24.94$ J g-$atom^{-1}$ K^{-1} at ambient temperature. From equation 2.4 it is evident, that ΔS_f corresponds to the negative slope of ΔG^{l-x} at T_l. The strongly rising driving force is compensated by the increasing heat capacity of the undercooled liquid. Nevertheless, for small undercoolings up to 100 K [29], where $\Delta {c_p}^{l-x} \approx 0$ according to Turnbull [31], the driving force for crystallization can be approximated via

$$\begin{aligned}\Delta G^{l-x}(T) &\approx \Delta H^{l-x} - T\frac{\Delta H^{l-x}}{T_l} \\ &\approx \Delta H_f - T\frac{\Delta H^{l-x}}{T_l} \approx T_l\Delta S_f - T\Delta S_f \\ &\approx -\Delta S_f \Delta T \approx -\frac{\Delta H_f \Delta T}{T_l}\end{aligned} \tag{2.5}$$

Equation 2.5 enables an initial estimation of the driving force of an alloy without determining $\Delta {c_p}^{l-x}$ (Fig. 2.3).

2.2.2.2 Dynamics of the (Undercooled) Liquid

Besides the driving force for crystallization, the mobility of the atoms plays an important role for nucleation as well as growth. The temperature dependent mobility of the atoms in a metallic liquid can be described primarily by three different quantities:

1. the diffusion coefficient $D(T)$[3]
2. the dynamic viscosity $\eta(T)$
3. the structural (α-) relaxation time $\tau_\alpha(T)$

The first two quantities, are linked via the Stokes-Einstein relation (SE relation) [27] by

$$D = \frac{kT}{6\pi\eta r} \tag{2.6}$$

where k is Boltzmann's constant and r the radius of the particle, corresponding to the atomic radius of the respective element in the metallic liquid. The validity of the SE relation for high undercoolings will be discussed in detail in section 2.2.2.4, but, because of a decoupling of the diffusivities of the different constituents, some liquids show a breakdown of the SE-relation [33–35].

η and τ_α are connected by the Maxwell relation [36] by

$$\eta = G_\infty \tau_\alpha \tag{2.7}$$

where G_∞ corresponds to the high frequency shear modulus. Since this work focuses on the measurement of structural relaxation times τ_α and shear viscosities η, the following explanations will be concentrated on these two quantities.

The temperature dependence of both, τ_α and η, can be described by a modification of the Vogel-Fulcher-Tammann equation (VFT equation) [30]

$$\eta = \eta_0 exp\left[\frac{D^* T_0}{T - T_0}\right] \tag{2.8}$$

or

---

[3] For an alloy D corresponds to the diffusion coefficient of the slowest constituent, if the SE relation holds [32].

$$\tau_\alpha = \tau_0 exp\left[\frac{D^* T_0}{T - T_0}\right] \tag{2.9}$$

where τ_0 and η_0 correspond to the relaxation time and viscosity limit at infinite temperature. η_0 can be calculated from the relation

$$\eta_0 = \frac{N_a \hbar}{V_m} \tag{2.10}$$

where N_a is Avogardo's constant, $\hbar$ is Planck's constant and V_m the molar volume [37]. The fragility parameter D^* describes the deviation of the VFT equation from a pure Arrhenius behavior with a temperature independent activation energy. T_0 is the temperature at which the relaxation quantity (τ_α or η) diverges. In Angell's classification of liquids, two different extreme types of liquids are distinguishable, regarding the temperature dependence of the dynamics/ kinetics. Strong liquids, like SiO_2 or GeO_2, exhibit a low temperature sensitivity of τ_α and η around T_g and hence, show a high fragility parameter of $D^* \approx 150$. Their temperature dependency of the dynamics follows an Arrhenius behavior with a constant activation energy. In contrast, fragile liquids, like o-terphenyl, deviate strongly from a pure Arrhenius behavior, being highly sensitive to temperature changes around T_g, and show small values of $D^* \approx 2$. This difference in the kinetics represented by the viscosity is shown in Fig. 2.4 for a strong network glass former GeO_2 [38] and a fragile metallic glass former $Pt_{60}Cu_{16}Co_2P_{22}$ [39].

Another measure for the kinetic fragility is the fragility index m, describing the slope of the VFT fit at the glass transition temperature T_g^* [30], which is defined as the temperature at which the viscosity is equal to 10^{12} Pas (Fig. 2.4). The corresponding relaxation time at T_g^* can be calculated from equation 2.7.

The fragility index m and the fragility parameter D^* are connected via [41, 42]

$$D^* = \frac{590}{m - 17}. \tag{2.11}$$

As can be seen from Fig. 2.4a, a more fragile glass former exhibits a lower viscosity in the high temperature regime. A lower viscosity means a higher atomic mobility, favoring crystallization and, in turn, tending towards a lower GFA [43].

Already in 1965, Adam and Gibbs considered that the relaxation processes in an undercooled liquid depend on cooperative rearrangements of groups of atoms [44]. Therefore, the more atoms are involved in such a cooperative rearrangement, the higher is the relaxation time at a certain temperature, which is connected to a lower configurational

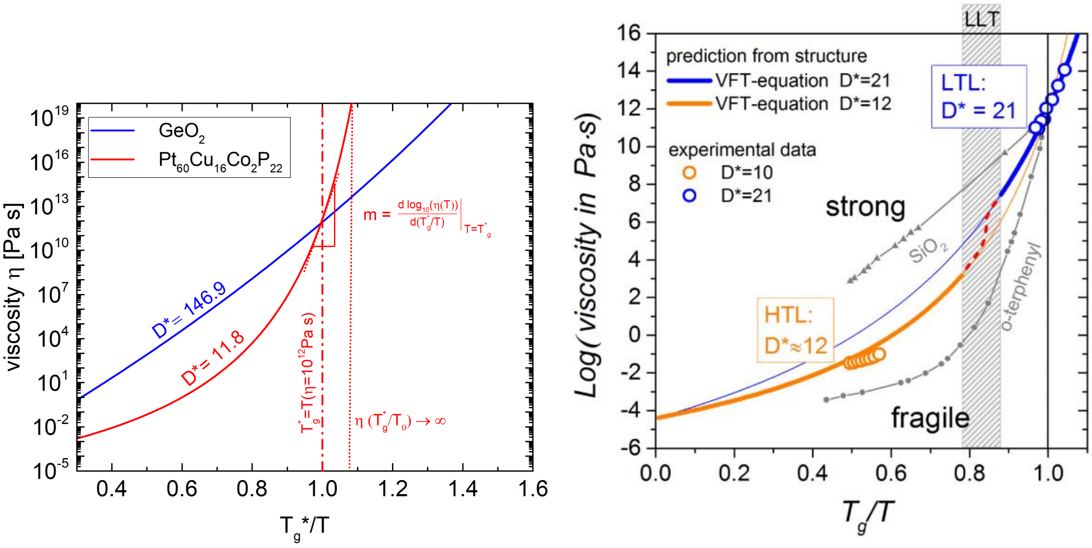

(a)

(b)

FIGURE 2.4: a) Schematic $log(\eta)$ versus T_g/T plot (Angell plot) of a strong oxide glass former GeO_2 [38] and a fragile metallic glass former $Pt_{60}Cu_{16}Co_2P_{22}$ [39]. The fragile glass former shows a deviation from a pure Arrhenius behavior. The fragility index m (slope of $\eta(T)$ at $T_g^* = T(\eta = 10^{12} Pas)$ or the fragility parameter D^* ("curvature" of $\eta(T)$) are commonly used as a measure of the kinetic fragility. b) Angell plot of the Zr-based bulk glass forming composition $Zr_{58.5}Cu_{15.6}Ni_{12.8}Al_{10.3}Nb_{2.8}$ (Vitreloy 106a). Structural signatures and experimental data from low and high temperature viscosity measurements indicate a fragile-to-strong crossover (liquid-liquid transition). Taken from Ref. [40].

entropy. It is for this reason, that the slowdown of the kinetics is connected to the loss of the configurational entropy [38, 45]: Alloys with a more fragile kinetic behavior show a higher configurational entropy difference in the high temperature equilibrium liquid, which decreases more rapidly upon undercooling in comparison to stronger liquids. This loss in configurational entropy is assumed to be connected to structural ordering, which is connected to a growth of the cooperatively rearranging regions in the theory of Gibbs and Adam [44]. This increasing structural order is also reflected by the ascending excess heat capacity shown in Fig. 2.3 [39, 46–48].

In summary, fragile liquids are, with respect to the corresponding crystal, less ordered than strong liquids around their liquidus temperature, but the ordering upon undercooling down to the glass transition occurs more rapidly for fragile liquids. Thus, the temperature dependence of thermodynamics, kinetics and structure are linked to each other. This connection will be picked up in detail in section 6.4.

Regardless of the model for the description of the dynamics upon undercooling, a fragile-to-strong crossover is observed in different bulk metallic glass forming compositions

[40, 49–52] and an evidence of such a transition is suggested in other bulk glass forming systems [53–57]. Here, the fragile high temperature liquid (HTL) transforms into a strong low temperature liquid (LTL) (Fig. 2.4b). Such a transition is related to structural changes, which can be detected inter alia in high energy synchrotron X-ray experiments [40, 50–52]. These structural signatures will be discussed in section 2.3. Similar transitions have already been observed in other liquids like triphenyl phosphite [58], water [59], Al_2O_3-Y_2O_3 [59, 60] or silicon[61]. However, considering bulk metallic glass forming alloys, such a liquid-liquid phase transition has an considerable impact on the glass forming ability and the resulting properties of the glassy phase.

2.2.2.3 Nucleation and Growth

As already pointed out, the process of crystallization is controlled by both, nucleation and growth. Nucleation of a precursor of a crystal (nucleus) can take place homogeneously or heterogeneously and is a statistical process, which is caused by energetic fluctuations in the liquid phase. For nucleation two different contributions have to be taken into account. On the one hand, the formation of a nucleus below the melting point results in a Gibbs free energy reduction by ΔG^{l-x} (driving force - see section 2.2.2.1). On the other hand, an interface between the existing liquid phase and the crystalline nucleus has to be formed, resulting in a Gibbs free energy increase by the interfacial energy γ^{x-l}. Therefore, the energy change in case of homogeneous nucleation can be expressed as

$$\Delta G_{hom} = -V\Delta G_v^{l-x} + A^{x-l}\gamma^{x-l} \tag{2.12}$$

where V corresponds to the volume of a nucleus and A^{x-l} to the surface area of the interface. If the shape of the nuclei is assumed to be spherical and that they are isotropic, equation 2.12 changes to:

$$\Delta G_{hom} = -\frac{4\pi r^3}{3}\Delta G_v^{l-x} + 4\pi r^2\gamma^{x-l}. \tag{2.13}$$

From equation 2.13, the critical radius r^* and the energy barrier ΔG^* for the formation of a critical (stable) nucleus can be derived:

$$\Delta G^*(T) = -\frac{16\pi(\gamma^{x-l})^3}{3(\Delta G_v^{l-x})^2} \tag{2.14}$$

$$\Delta r^*(T) = \frac{2\gamma^{x-l}}{\Delta G_v^{l-x}} \tag{2.15}$$

Undercritical nuclei with smaller radii than r^* are dissolved, whereas overcritical nucleii ($r > r^*$) are stable. ΔG^* is the reason for an inevitable undercooling below T_l until crystallization can occur, depending on both the driving force for crystallization ΔG^{l-x} and the interfacial energy γ^{x-l}. Thus, γ^{x-l} is beneficial for glass formation, since it contributes to an energy barrier for crystallization. In case of heterogeneous nucleation, the value of ΔG^* is smaller, since the energy barrier is decreased due to a smaller interfacial energy between the solid and the liquid phase. Heterogeneous nucleation can be caused inter alia by mold walls or impurities, which both can only be hardly avoided during the alloying and casting of alloys.

However, regardless of heterogeneous or homogeneous nucleation, the nucleation rate $I(T)$ is given by

$$I(T) = AD(T)exp\left(-\frac{\Delta G^*}{k_BT}\right) \tag{2.16}$$

where A is a fitting parameter and k_B Boltzmann's constant.

After the formation of stable nuclei, the Gibbs free energy of the system can further be lowered by growth of the crystallites along with the reduction of energetically unfavored interfaces. The growth rate $u(T)$ of the crystals can be expressed as

$$u(T) = \frac{f}{a_0}D(T)\left[1 - exp\left(-\frac{\Delta G^{l-x}}{RT}\right)\right] \tag{2.17}$$

where f is a constant, a_0 corresponds to the average atomic diameter and D(T) to the diffusion coefficient.

Both, $I(T)$ and $u(T)$, are strong functions of temperature. In the high temperature regime the growth rate is dominant due to a small driving force but a high atomic mobility (nucleation controlled), whereas in the low temperature the strongly limited atomic mobility limits growth but the high driving force triggers nucleation (growth controlled).

Equation 2.17 and 2.16 are combined in the Johnson-Mehl-Avrami-Kumogorov equation (JMAK equation), describing the time for crystallization t_x of a crystalline fraction x at a given temperature:

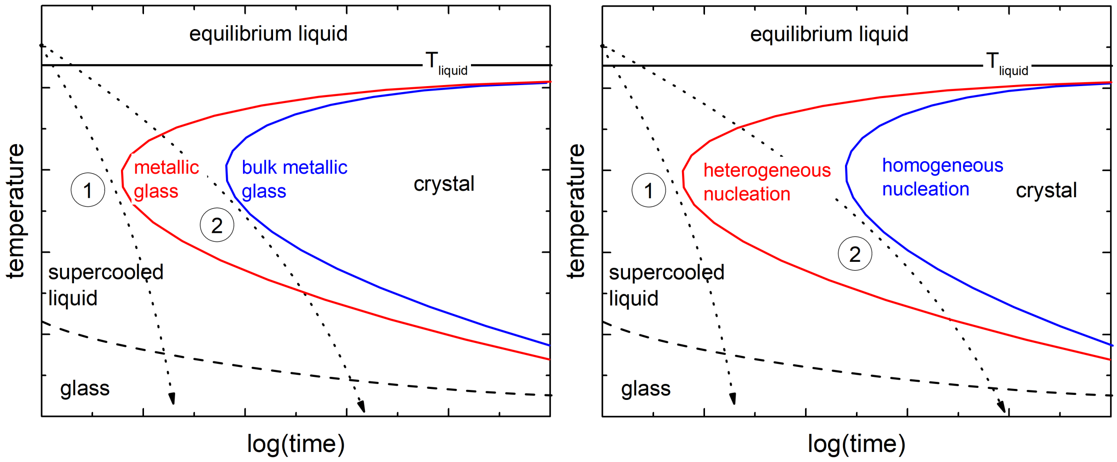

(a) (b)

FIGURE 2.5: Time-temperature-transformation (TTT) diagram for a) A metallic glass (poor GFA - shorter times) and a BMG (high GFA - longer times) and for b) The difference between homogeneous and heterogeneous nucleation. The black dotted lines reflect the corresponding critical cooling rates to bypass crystallization (1>2). In both, the glass transition temperature is shown as a function of temperature according to equation 2.10 (dotted line).

$$t_x = \left(\frac{-3ln(1-x)}{\pi I_v(T)[u(T)]^3}\right)^{\frac{1}{4}} \tag{2.18}$$

t_x can be illustrated in a time-temperature-transformation (TTT) diagram as a function of temperature as depicted in Fig. 2.5a. The red solid line represents the crystallization times for a metallic glass (poor GFA - shorter times) and the blue solid line the crystallization times of a BMG (high GFA - longer times). Here, the crystallization time has a typical "nose shape"[4] because of the different temperature dependence of the growth and the nucleation rate. The black dotted lines reflect the corresponding critical cooling rates to bypass crystallization for a metallic glass former (1) and a bulk metallic glass former (2). The glass transition temperature is shown as a function of temperature according to equation 2.9. Fig. 2.5b highlights the difference between homogeneous and heterogeneous nucleation. The latter one drastically decreases the crystallization times and hence, increases the necessary cooling rate to avoid crystallization ($1 > 2$).

The minimum in t_x defines the cooling rate necessary to avoid the crystallization, but the rate can not be calculated directly, since the JMAK equation considers the crystallization times at a constant temperature (isothermal TTT diagram). However, using equation 2.18 for the fitting of isothermal crystallization times (see section 3.2.1.4) the interfacial

---

[4] If only one crystalline phase is considered. Complex systems often exhibit several noses due to the formation of a complex microstructure, consisting of different crystalline phases.

energy γ^{x-l}, the second thermodynamic contribution, can be calculated, which is experimentally hard to determine. Fig. 2.6a shows experimentally determined isothermal crystallization times at different crystalline fractions (1%, 50%, 99%) of the bulk glass forming composition $Pt_{42.5}Cu_{27}Ni_{9.5}P_{21}$ measured upon cooling from the equilibrium liquid and heating from the glassy state. The data points have been described using equation 2.18. Additionally, the viscosity ranges of the supercooled liquid are depicted as grey bars for different temperature ranges. The transition times, which indicate the transition from the glassy state to the liquid state, are determined using the T_g-shift method (see section 3.2.1.3) and isothermal thermomechanical experiments (see section 3.2.2). Although the minimum in t_x yields no direct information about the critical casting thickness or rather the critical cooling rate for glass formation, both quantities correlate with each other. Recently, Johnson et al. proposed a model, which allows the calculation of the nose time τ_x of an alloy from the reduced glass transition temperature t_{rg} (see section 2.2.1) and the fragility index m (see section 2.2.2.2) [62]. In their work, the nose time τ_x is correlated with the critical diameter d_c, allowing the prediction of the GFA in an alloying system.

However, the most straight forward approach for the determination of the critical cooling rate are continuous crystallization experiments (see section 3.2.1.4). Here, the crystallization times are recorded upon continuous cooling from the equilibrium liquid and hence, the conditions are comparable to these in the casting process. However, one major issue are the high critical cooling rates of the most metallic glass forming compositions. In current experimental setups like conventional calorimetry (see section 3.2.1.1) or levitation experiments (see section 3.3.2, 3.2.3), the achieveable cooling rate is below 10 K/s. Only a limited number of alloys can be cooled to the glassy state with cooling rates of less than 5 K/s [5]. In Fig. 2.6b the results of continuous crystallization experiments measured by power-compensated differential scanning calorimetry (DSC) of $Pt_{42.5}Cu_{27}Ni_{9.5}P_{21}$ are shown. Here, the maximum cooling rate (3 K/s) is not sufficient to cool the sample from the equilibrium liquid into the glassy state, and hence, the exact critical cooling rate cannot be determined, although the alloy exhibits a critical casting thickness of 20 mm [64]. Nevertheless, already the ability to achieve a certain undercooling at a given cooling rate provides an insight in the GFA of an alloy.

All in all, three different contributions influence the GFA of an alloy:

1. the driving force for crystallization $\Delta G^{l-x}(T)$
2. the interfacial energy γ^{x-l}
3. the kinetic fragility D^*

---

[5] corresponding to a critical diameter of larger than 14 mm, using the relation in equation 2.1.

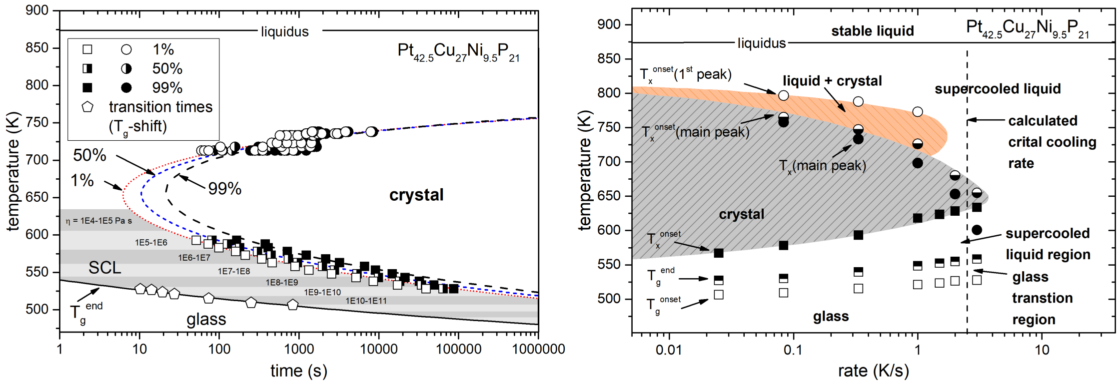

(a)

(b)

FIGURE 2.6: a) Time temperature transformation diagram of $Pt_{42.5}Cu_{27}Ni_{9.5}P_{21}$. The open, half-filled and filled circles and squares represent the times at which 1, 50 and 99% of the crystallization is completed. The open pentagons correspond to relaxation times obtained from T_g-shift measurements [39]. The solid line reflects the equilibrium line at which the glass is isothermally relaxed into the supercooled liquid state calculated form the VFT parameter determined in Ref. [39]. The brighter and darker shaded areas represent different orders of magnitude in the equilibrium viscosity (in Pa s) of the supercooled liquid. The dotted line represents the fit to the open, the short-dashed line to the half-filled and the dashed to the filled symbols using equation 2.18. b) Continuous heating and cooling transformation diagram of $Pt_{42.5}Cu_{27}Ni_{9.5}P_{21}$. The open circles represent the onset of the primary crystallization. The half-filled and filled circles correspond to the onset and the peak-minimum of the main crystallization peak. In the low temperature regime T_g^{onset}, T_g^{end} and T_x^{onset} are illustrated as open, half-filled and filled squares. Prior to heating, samples were cooled from the supercooled liquid state with the same rate as used upon heating. The shaded areas represent the region where the liquid partially or fully crystallizes. The dashed line corresponds to the critical cooling rate, calculated from the critical casting thickness (equation 2.1) [13]. Both, figures and figure descriptions are taken from Ref. [63].

2.2.2.4 The Glassy State

In this section the transition from the undercooled liquid to the glassy state and its definition are discussed, if crystallization is avoided. Considering the course of the enthalpy (or volume, entropy) of the liquid upon cooling (Fig. 2.7), one can see that at a given temperature the rate of change (specific heat capacity c or thermal expansion coefficient α) changes and the volumetric or enthalpic state of the undercooled liquid is frozen-in. Here, the metastable undercooled liquid "falls out of equilibrium" and the liquid's structure is preserved due to a kinetic frustration [30]. At this temperature, the glass transition temperature T_g, the internal relaxation processes (internal timescale) can not keep up with the experimental timescale (the system is not able to equilibrate). In thermal experiments, it can be observed that this inflection point in the enthalpy and volume shows a strong cooling rate dependence, proving the kinetic nature of the transition to the glassy state. Higher cooling rates lead to an earlier bifurcation of these timescales manifested by a higher glass transition temperature. This is shown schematically in Fig. 2.7, where the cooling rate of "glass 1" is higher than the cooling rate of "glass 2" and hence, $T_g^{fictive}(1)$ is higher than $T_g^{fictive}(2)$.

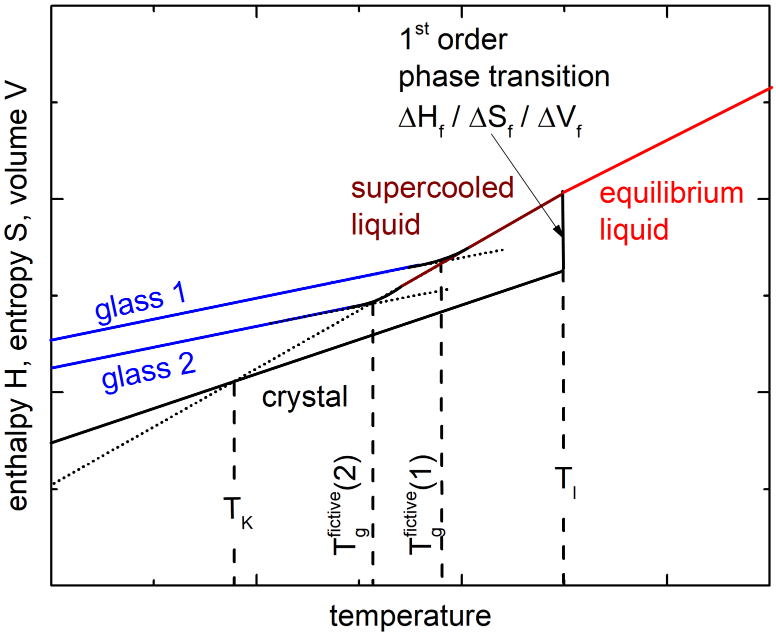

FIGURE 2.7: Schematic illustration of the enthalpy H, the volume V and the entropy S as a function of temperature. During solidification a metallic liquid forms the crystalline structure via a 1^{st} order phase transition, which is connected to a jump in the extensive quantities H, S and V. If crystallization is avoided the liquid is undercooled until the transition to the glass occurs, the liquid structure is vitrified and a glass is formed, resulting in a change of slope. Higher cooling rates result in higher values of $T_g^{fictive}$, because of a crossing of the experimental and internal timescales. The extrapolation of the entropy of the liquid leads to an intersection with the entropy of the crystal at Kauzmann's temperature T_K (entropy crisis).

However, if the evolution of the excess entropy with temperature ($\frac{dS^{l-x}}{dT} = \frac{c_p^{l-x}(T)}{T}$) is considered, it comes to a surprise [65]. At a given temperature (Kauzmann's temperature T_K) the extrapolation of the entropy intersects the entropy of the crystal. Thus, further cooling would lead to the fact that, the entropy of the disordered undercooled liquid would be lower than that of the ordered crystal (dotted line in Fig. 2.7). To this date, this so-called entropy crisis is controversially discussed. One explanation for the avoidance of this phenomenon would be an inevitable thermodynamic transition [65]. Since the changes of the specific heat capacity c or the linear thermal expansion coefficient α are not abrupt, a 1^{st} order phase transition can be excluded, tending to a higher order phase transition [65]. In 1933, Ehrenfest postulated a scheme for the classification of phase transitions on the basis of thermodynamic quantities [66]. According to this, the following equations can be derived

$$\Delta\kappa \frac{dp}{dT} = \Delta\alpha \tag{2.19}$$

$$\frac{\Delta C_p}{TV} = \Delta\alpha \frac{dp}{dT} \tag{2.20}$$

where κ corresponds to the coefficient of compressibility. For a second order phase transition, both, equation 2.19 and 2.20 have to be valid and hence, they can be combined to the Prigogine-Defay ratio R:

$$R = \frac{VT\Delta\alpha^2}{\Delta\kappa\Delta C_p} \tag{2.21}$$

In case of a 2^{nd} order phase transition, equation 2.21 is equal to unity. At the glass transition, R is determined to be higher than unity, implying that the glass transition is not a 2^{nd} order phase transition. However, as already pointed out, until now different resolutions of Kauzmann's paradox have been postulated and the exact one is still debated.

In Fig. 2.8a three possible scenarios to avoid the entropy crisis are shown [67]. The first scenario (Fig. 2.8 (top)) considers an inevitable 2^{nd} order phase transition as origin of the glass transition, which occurs before reaching T_K [68]. In contrast, Fig. 2.8 (middle) describes a scenario in which the excess entropy between the glass and the crystal smoothly approaches zero [69]. The third resolution of Kauzmann's paradox might be an inevitable onset of crystallization before T_K is reached, since the undercooled liquid gets less stable when approaching T_K (Fig. 2.8 (bottom)) [65, 67].

Based on the experimental findings of Masuhr et al. on $Zr_{41.2}Ti_{13.8}Cu_{12.5}Ni_{10.0}Be_{22.5}$ (Vitreloy 1) [70], Tanaka suggested a decoupling of the translational and rotational diffusivity, leading, in turn, to a decoupling of the structural relaxation time τ_α and the relaxation time for material transport τ_D. τ_D is dominant in the process of crystallization (Fig. 2.8b), showing an Arrhenius-like behavior with temperature-independent activation energy and not a VFT-type behavior like τ_α [70] (Fig. 2.8b bottom). This decoupling of the two relaxation times occurs at a bifurcation temperature T_B, being below the melting temperature, but above the VFT-temperature T_0, leading to a branching of the nose in the low temperature regime. Hence, at a so-called lower metastable limit T_{LML} the structural relaxation time crosses the crystallization time ($\tau_\alpha = t_x$), preventing the existence of an "equilibrium" supercooled liquid below T_{LML} ($T_g \geq T_x$). Finally, crystallization is caused before T_K is reached. Note, that in case of complex alloys Kauzmann's temperature does not necessarily correspond to the zero of the entropy difference between the liquid and the crystal (equation 2.4), since for the excess entropy $\Delta S^{l-x}(T)$ the entropy of the crystalline mixture is considered, which can differ from that of the single crystalline phases. It was already shown that the crystalline

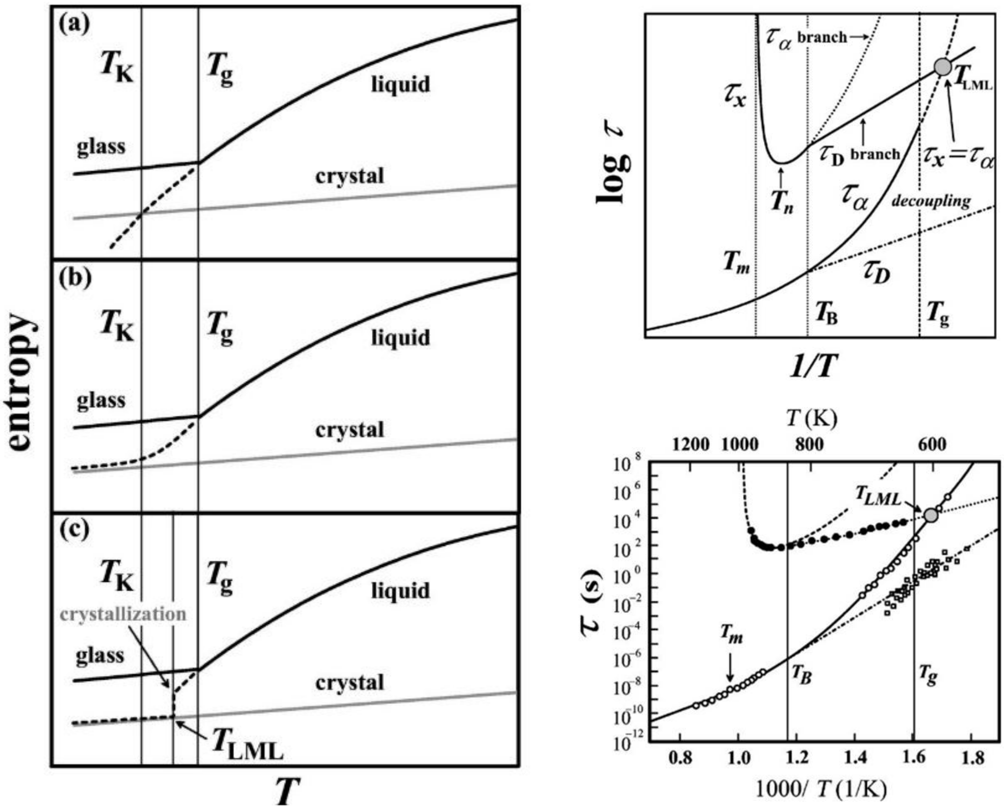

(a)

(b)

FIGURE 2.8: a) Possible resolutions of Kauzmann's paradox: a 2^{nd} order phase transition to an ideal glass (top); the excess entropy smoothly decreases to zero (center); crystallization occurs before the entropy crisis can take place (bottom). Taken from [67]. b) Top: Schematic illustration of Tanaka's theory of an inevitable crystallization process. At the lower metastable limit T_{LML} the structural relaxation time τ_α intersects the crystallization time t_x, because of a decoupling of the relaxation time for material transport τ_D and the structural relaxation time τ_α at a bifurcation temperature T_B. Taken from Ref. [67]. Bottom: Illustration of Tanaka's theory based on the experimental findings about Vitreloy 1. The open circles correspond to the measured structural relaxation time, the open squares to the relaxation time for material transport and the closed circles to the crystallization times.

mixture can have a considerably higher value of the excess entropy because of a higher configurational entropy, which is caused by a high entropy of mixing [45, 71, 72]. All in all, in multicomponent systems the zero of $\Delta S^{l-x}(T)$ can be seen as an isotropic temperature, which seems to have no physical meaning [45].

However, regardless of the underlying phenomenon of the glass transition, different definitions of T_g have been proposed, which are used in different contexts in this work:

1. $T_g^{onset}(q)$: the onset of the glass transition upon heating with a given rate q by thermal analysis [30]
2. $T_g^{end}(q)$: the end of the glass transition upon heating with a given rate by thermal analysis
3. $T_g^{fictive}(q)$: the fictive glass transition temperature being defined as the inflection point of the enthalpy [36, 73]
4. $T_g^{*}(\eta)$: the temperature at which the viscosity η reaches $10^{12} Pas$ [30]
5. $T_g^{*}(\tau)$: the temperature at which the structural relaxation time τ reaches $10^{2} s$ [30]

2.3 Structure of Bulk Metallic Glasses and Metallic Glass Forming Liquids

In general, the atomic structure of a material provides information about its properties. Thus, revealing such structure-property-relations is one major objective in materials science. In case of BMGs, the structural evolution with temperature plays a key role for the process of glass formation and the resulting properties of the glass. In this section, the current state of the art is briefly discussed.

Diffraction experiments revealed that metallic glasses and liquids lack long-range order (LRO), only showing short and medium range ordering (SRO and MRO) in their respective structure [74]. This difference to a crystalline metal is manifested by the absence of sharp Bragg diffraction peaks and the existence of "amorphous halos" on different length scales, originating from statistical fluctuation of the atomic positions in the disordered atomic structure. In Fig. 2.9a the total structure factor $S(Q)$ with the peak positions Q_1, Q_2 and the reduced pair distribution function $G(r)$ with the peak positions $r_1 - r_4$ of the bulk glass forming alloy $Pd_{31}Ni_{42}S_{27}$, which are obtained by high energy synchrotron X-ray scattering experiments, are shown. Here, Q corresponds to the wave vector in reciprocal space and r to the distance in real space. $G(r)$ is determined from $S(Q)$, using Fourier transformation. For a more detailed description of these functions the reader is referred to section 3.3.2.

Based on different experimental X-ray diffraction investigations and the work of Prins [75], first geometrical approaches for the description of the atomic structure in simple molecular liquids were proposed by Bernal in 1936 [76] and 1959 [77]. In his model, he considered the atoms or molecules as equal hard spheres, which are dense randomly packed in irregular polyhedral arrangements, representing the short range order (SRO) [78, 79]. Already in 1952 Frank postulated that the ability to undercool pure metals originates from a high interfacial energy between the liquid and crystalline phase, which is, in turn, caused by the formation of a pronounced icosahedral SRO in the metallic liquid [80]. Several years later, after the discovery of metallic glasses, Gaskell developed a new structural model for the description of the SRO in transition metal (TM) - metalloid[6] glasses [81, 82], which is based on the works of Finney and Cargill [83, 84].

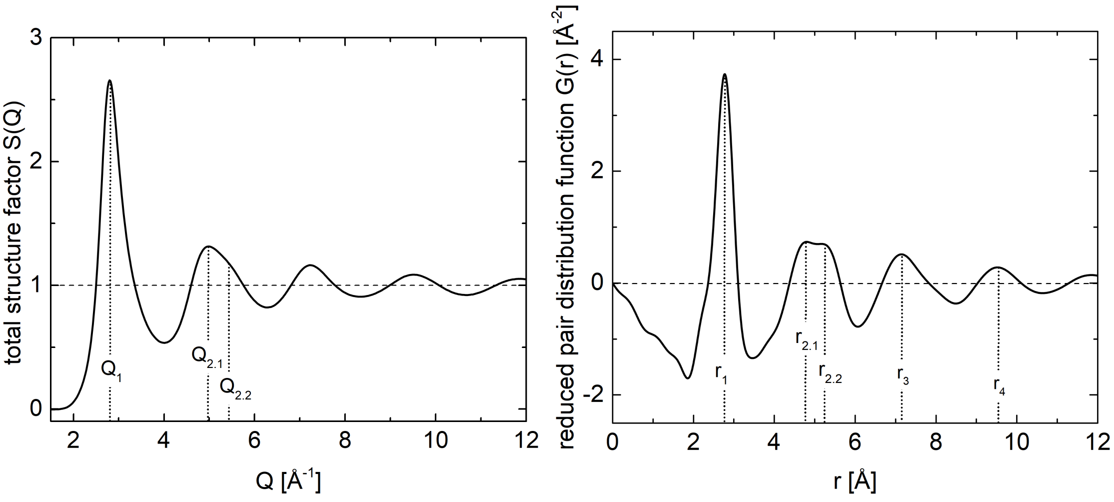

(a) (b)

FIGURE 2.9: a) Total structure factor $S(Q)$ of the bulk glass forming alloy $Pd_{31}Ni_{42}S_{27}$. The peak positions of the first sharp diffraction peak (FSDP) and the second sharp diffraction peak (SSDP) are marked with dotted lines. At the right flank of the SSDP a shoulder is observed. b) Reduced pair distribution function $G(r)$ of the bulk glass forming alloy $Pd_{31}Ni_{42}S_{27}$. The peak positions up to the fourth atomic shell ($r_1 - r_4$) are indicated with dotted lines. The SSDP in G(r) also shows a splitting of the peak maximum.

In 2013 Ångstrom-beam electron diffraction (ABED) allowed for the first time the two-dimensional visualization of the SRO in a metallic glass and the confirmation of the formation of icosahedral ordering [85]. In Fig. 2.10 the corresponding ABED images of an icosahedral structure are shown. The experimental results are in good agreement with the results obtained from simulated icosahedral clusters with a five-fold geometry.

However, the question arises how the local structural elements, representing the SRO, are connected with each other in the three-dimensional space. This packing scheme of the local units is termed as medium range order (MRO). A comprehensive computational and experimental study of E. Ma and Co-workers revealed that the atomic clusters

---

[6] In this work all elements of the D-block in the periodic table are considered as TM and the term metalloids comprise the elements B, C, Si, P, Ge.

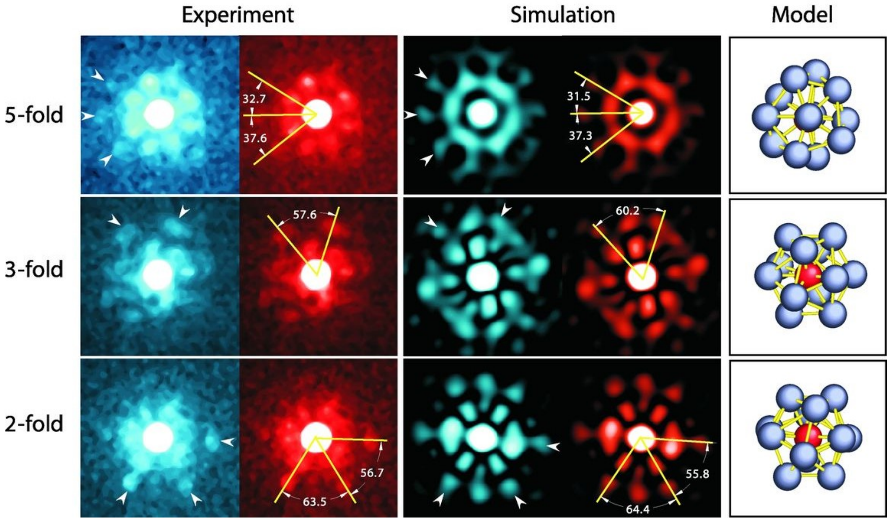

FIGURE 2.10: Experimental and simulated angstrom beam electron diffraction (ABED) pattern of the binary glass forming alloy $Zr_{80}Pt_{20}$ at room temperature. The results of the simulation agree well with the experimentally determined pattern. The corresponding 3D model of each cluster type is shown on the righthand side. Taken from Ref. [85].

of the SRO, which are influenced by the chemical affinity and the atomic radii of the constituents, are likewise ordered in different arrangements representing the MRO, which strongly depend on the proportion of the different atomic species [74]. As an example, the simulated atomic structure of $Zr_{84}Pt_{16}$ is shown in Fig. 2.11a.

Based on the currently available database, different authors developed geometrical models for the description of both, the SRO and the MRO in metallic glasses, which provide information about the glass forming ability by considering dense random packing and a frustration of the kinetics in the liquid. Egami proposed that the radius ratios of the constituent elements in metallic systems (considering hard spheres) are crucial for the glass forming ability or rather the glass forming range [87, 88]. Therefore, a minimum concentration of the solute atomic specie, which is inversely proportional to the atomic size mismatch, is necessary for the destabilization of the solid solution. Later, Miracle reported on the so-called efficient cluster packing (ECP) model [89, 90]. This model allows the calculation and visualization of the atomic structure of a given metallic glass forming composition under geometrical considerations. In this respect, on the basis of the above mentioned models, Miracle expects the representation of the SRO by atomic clusters, being topologically efficiently packed [91]. These efficiently packed clusters (or coordination polyhedra) are arranged in a crystalline lattice such as bcc, fcc or hcp, representing the medium range order [89, 90] (Fig. 2.11b). These clusters can share atoms with each other in order to reduce internal stresses, preventing the formation of an "ideal" periodic ordering of the atoms. E. Ma and co-workers reviewed Miracles ECP

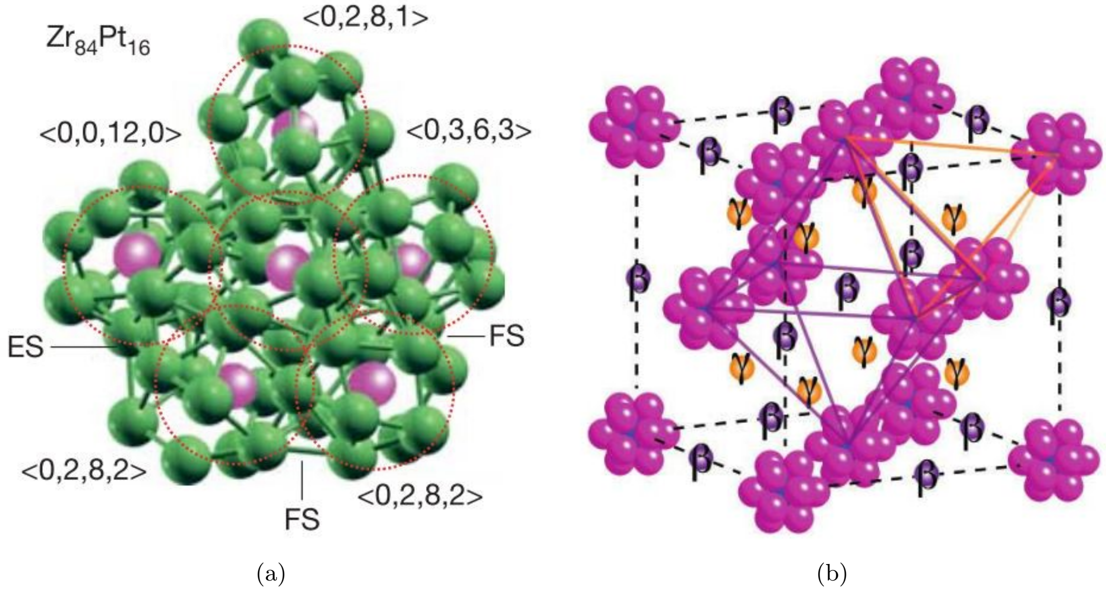

(a) (b)

FIGURE 2.11: a) 3D illustration of the atomic structure in the binary $Zr_{84}Pt_{16}$ metallic glass. The solute (Pt) centered clusters represent the short range order (SRO). The numbers in the triangular brackets correspond to the Voronoi index of each cluster-type and ES and FS mark the positions where the clusters share edges or faces. The arrangement of the clusters represents the medium range order (MRO). Taken from Ref. [74]. b) Illustration of the 3D atomic structure of a metallic glass according to the efficient cluster packing model (ECP). The densely packed clusters (SRO) are arranged in a fcc lattice, representing the MRO. The greek letters β and γ mark the octahedral and tetrahedral voids in a fcc arrangement, which have to be occupied by a constituent to achieve an ECP structure. Taken from Ref. [86].

model based on their findings in Ref. [74] and extended it by considering the chemical affinity in the SRO so that the system can lower its energy. In 2015 Miracle and Laws reported, based on the initial ECP model, on an extended structural model for the prediction of the GFR [92]. In their work, they modified the initial model of Miracle in order to calculate compositional lines at which all atoms are packed in dense clusters around each other. At these compositional lines they predict bulk glass formation because of a higher frustration of the metallic liquid.

However, all of these topological models have in common that MRO is formed by the connection of (polyhedral) atomic clusters, which represent the SRO. This short-to-medium range order can be observed in different structural metrics in S(Q) and G(r). Since the MRO is found at higher length scales than the SRO, its signature is located at lower values of Q in S(Q) or at higher values of r in G(r), whereas characteristics for pronounced SRO are located at high values of Q and low values of r, respectively. Note, that S(Q) and G(r) of complex alloys are the superposition of the partial scattering functions and the partial distribution functions. Hence, different characteristics, which are strongly pronounced in the binary contributions are erased by the superposition, since the binaries are differently weighted because of their different proportions, atomic form factors and weighting factors.

On the basis of the Ginzburg-Landau theory, Sachdev et al. showed that in case of an ideal icosahedral ordering, representing the SRO, the second sharp diffraction peak (SSDP) shows a shoulder at higher values of Q (Fig. 2.9). The ratios of the peak positions are then $Q_{2.1}/Q_1 = 1.71$ and $Q_{2.2}/Q_1 = 2.04$ [93].

As already pointed out, indications of the MRO are located at higher atomic distances, hence, at low Q values, resulting in the formation of a pre-peak or a shoulder at the left flank of the first sharp diffraction peak (FSDP) [94, 95]. In some alloys, this indication for MRO is present in the glassy state and the deeply undercooled liquid, but not in the high temperature equilibrium liquid, implying that it is formed during undercooling [39, 51]. Such an increase in order is also reflected in thermodynamic quantities like the molar heat capacity c_p of the liquid phase, where an increase can be observed upon undercooling below the liquidus temperature down to the glass transition temperature [28, 29].

Another indication for the ordering of the atomic coordination polyhedra was identified by Voloshin et al. in 1997, when investigating the degeneration of the second sharp diffraction peak in G(r) of amorphous solids [96]: A splitting into two distinct maxima $r_{2.1}$ and $r_{2.2}$ can be observed (Fig. 2.9b). The same feature is evident in some metallic glass forming alloys and is attributed to the sharing of edges, faces and vertices of the quasi-equivalent atomic clusters (Fig. 2.12), contributing to the MRO [74]. Depending on different types and distribution, the connections influence the most probable position of the second nearest neighbor of an atom (Fig. 2.12). On the basis of geometrical considerations, these positions can be calculated from the average bond length as $2r_1$ (1-atom connection), $\sqrt{3}r_1$ (2-atom connection), $\sqrt{8/3}r_1$ (3-atom connection) and $\sqrt{2}r_1$ (4-atom connection) [97–101]. Additionally, molecular dynamic simulations imply, that the atomic packing at the MRO length scale of a glass might be influenced by the crystalline structure, which are hidden in the total structure factor [102], being in good agreement with the considerations of Miracle [89, 90].

However, this work will focus on the temperature dependence of the structure in the glassy and the (undercooled) liquid state, which is investigated by in-situ high energy synchrotron X-ray experiments (see section 3.3.2). The results will be connected to the results from the thermo-physical characterization.

Yavari et al. revealed a connection between the thermal expansion of the excess volume in the glassy state and the total structure factor S(Q) [103]. The peak position Q_1 of the FSDP in S(Q) (see Fig. 2.9a) contains information about the mean atomic

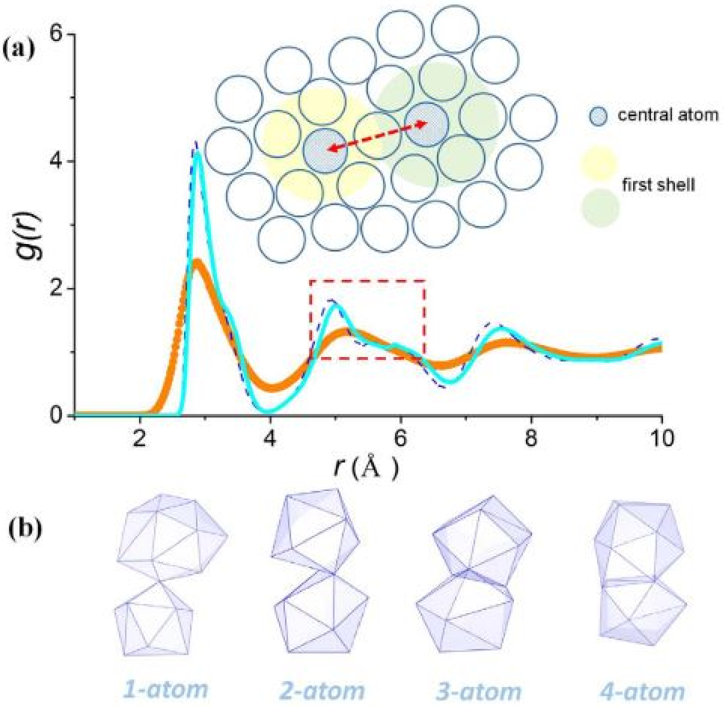

FIGURE 2.12: a) Simulated radial distribution function of amorphous Ta at different temperatures and states. The orange pattern corresponds the liquids structure at 3300 K, the cyan line to the inherent liquid structure at 3300 K and the dashed line to the glassy structure at 300 K. The term inherent corresponds to a state with a minimum in energy. Therefore, thermally induced vibrational contributions are removed by a conjugate-gradient energy minimization method. A detailed description can be found in Ref. [101]. Both, the inherent liquid structure and the glassy structure show a splitting of the second sharp diffraction peak, which is attributed to the formation of different connections between the atomic clusters. b) Schematic illustration of 1-atom, 2-atom, 3-atom and 4-atom connections. Taken from Ref. [101].

spacing in reciprocal space. Hence, the third power of Q_1^{-1} correlates with the linear expansion coefficient of the glassy structure [103]. In order to compare the results of this work to available literature data about the excess volume expansion coefficient, a $3 \cdot Q_1^{-3} \propto \gamma_{glass}^{X-ray}$ relation is taken into account.

Recently, temperature-induced changes on the length scale of the MRO have been analyzed and linked quantitatively to the kinetic fragility [104]. Therefore, the volume change of the atomic shells with the radius r_3 and r_4 is considered (Fig. 2.9a). This volume change can be expressed as

$$V_{4-3}(T) = V_4 - V_3 = \frac{4}{3}\pi(r_4^3 - r_3^3) \tag{2.22}$$

where r_3 and r_4 are determined from the reduced pair distribution function G(r) as shown in Fig. 2.9. The thermal induced changes can then be calculated according to

$$\Delta V_{4-3}(T) = V_{4-3}(T) - V_{4-3}(T'_g) \tag{2.23}$$

where T'_g is defined as the onset temperature of the supercooled liquid region obtained in DSC scans with an equal heating rate [104]. In order to compare alloys with different values of T'_g, the thermally induced changes are normalized by the absolute value at T'_g. Like in case of relaxation quantities (η, τ_α - see section 2.2.2.2), more fragile liquids show a higher temperature sensitivity of $-\Delta V_{4-3}(T)/V_{4-3}(T'_g)$. Finally, the kinetic fragility index m_{kin} (equation 2.4) can be related to the structural fragility index $m_{str}^{(V4-3)}$ (Fig. 2.13b)

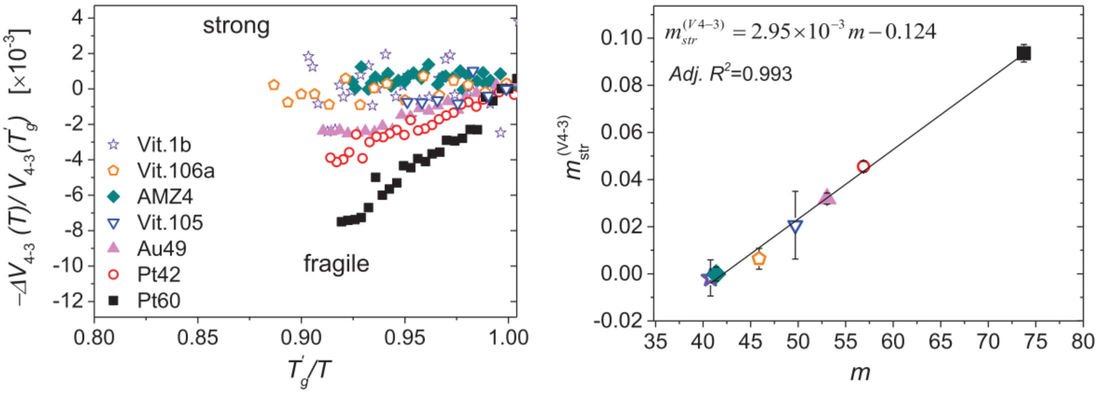

(a) (b)

FIGURE 2.13: a) $-\Delta V_{4-3}(T)/V_{4-3}(T'_g)$ versus T'_g scaled temperature. The slope (structural fragility), representing the sensitivity to temperature changes, can be related to the kinetic fragility. b) Correlation between the structural fragility index $m_{str}^{(V4-3)}$ and the kinetic fragility index m_{kin}. Both taken from Ref. [104].

Kelton et al. studied the temperature dependence of the peak maximum of the FSDP ($S(Q_1)$) and observed a correlation with the kinetic fragility parameter D^* [105]. For this, the change of $S(Q_1)$ with temperature in the high temperature liquid is fitted linearly and extrapolated to T_g. The offset between the extrapolated value and the experimental value of $S(Q_1)$ is then correlated with the fragility parameter D*. However, the relation of Kelton et al. is not valid if a liquid-liquid transition from a fragile high temperature liquid to a strong low temperature liquid occurs, as shown in Fig. 2.4. Structural signatures of such a transition were observed experimentally at different length scales and metrics in different bulk metallic glass forming alloys [40, 50, 56], which have recently been confirmed in simulation studies [106]. In Fig. 2.14a the cubic value of the inverse peak position of the FSDP of S(Q) of the $Zr_{41.2}Ti_{13.8}Cu_{12.5}Ni_{10}Be_{22.5}$ bulk glass forming alloy (Vitreloy 1) is shown. Here, a discontinuity at roughly 800 K is observed. On the basis of macroscopic measurements of the specific heat capacity and the dynamic viscosity [49, 53] this discontinuity is allocated to a change of the atomic structure during a liquid-liquid transition from a fragile high temperature to a strong low temperature liquid [50]. Similar observation of the temperature dependence of Q_1 were made in Ref. [40] for the $Zr_{58.8}Cu_{15.6}Ni_{12.8}Al_{10.3}Nb_{2.8}$ BMG forming alloy (Vitreloy 106a). Here, also discontinuities were observed in the temperature dependence of the peak positions r_1 - r_5 and the corresponding peak maxima of G(r) (Fig. 2.14b).

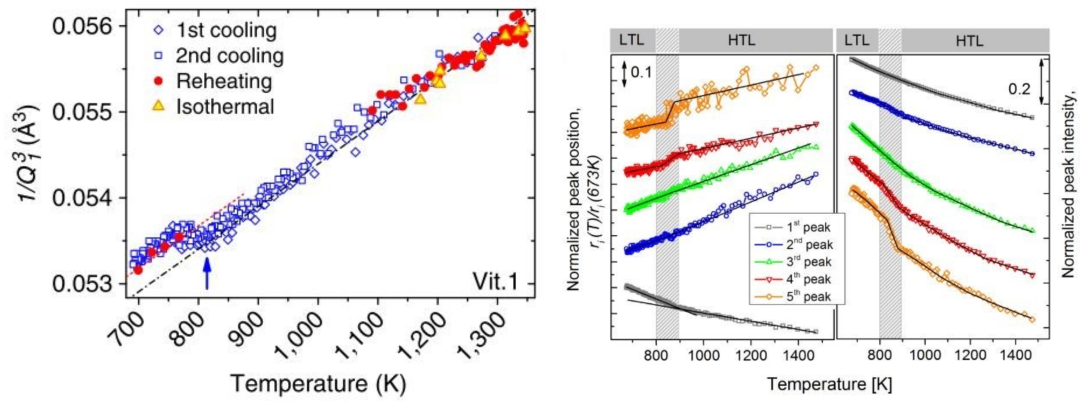

(a) (b)

FIGURE 2.14: a) Q_1^{-3} versus temperature plot of the Zr-based bulk glass forming alloy $Zr_{41.2}Ti_{13.8}Cu_{12.5}Ni_{10}Be_{22.5}$ upon heating and cooling. At about 800 K a discontinuity is observed, which is attributed to change of the dynamic viscosity as shown in Fig. 2.4b. At this point the high temperature fragile liquid changes to a low temperature strong liquid (liquid-liquid transition). Taken from Ref. [50]. b) Position and intensity of the first four peaks in G(r) of $Zr_{58.8}Cu_{15.6}Ni_{12.8}Al_{10.3}Nb_{2.8}$. At different length scales a discontinuity can be observed, pointing towards a liquid-liquid transition of the high temperature liquid (HTL) and the low temperature liquid (LTL). Taken from Ref. [40].

2.4 Mechanical Behavior of Bulk Metallic Glasses

The mechanical performance under certain loading conditions often determines the field of application of a material. As pointed out in section 2.3, the atomic structure of BMGs lacks any long range order and periodicity, drastically changing the deformation mechanisms and mechanical properties in comparison to crystalline metals and alloys. Like observed for other disordered systems, the plastic deformation takes place by the formation of shear bands [107].

The elastic behavior of amorphous metals features a relatively low Young's modulus with respect to the pure metals, a yield strength that is very close to the theoretical strength and an extraordinary elasticity [3, 4, 108]. Thus, BMGs can reach strength values higher than steel in combination with an elasticity of about 2% comparable to polymers (Fig. 2.15).

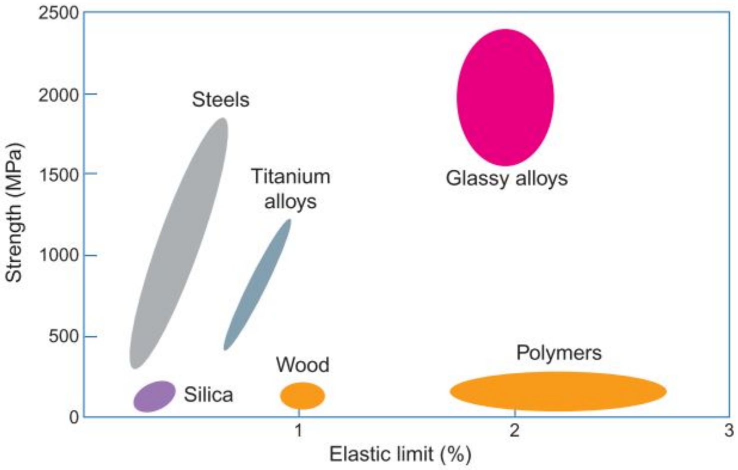

FIGURE 2.15: Yield strength versus elastic limit plot of different materials. It is evident that amorphous metals comprise the high elasticity of polymers with a yield strength higher than steel. This is an unique combination of mechanical properties for BMGs. Taken from Ref. [3].

This work will focus on the quasi-static properties such as the elastic modulus, yield strength, fracture strength, hardness and Poisson's ratio. As already mentioned, plastic deformation in metallic glasses takes place by the formation of shear bands to relive the stress that the sample is exposed to. Hereby, the processes in the shear bands or rather the mechanism of the shear band formation is of great interest. For both, the excess volume Δv^{g-x} and the free volume v_f are decisive. Δv^{g-x} is defined as the volume difference between the present structural state of the glass with respect to the "ideal glass". The "ideal glass" corresponds to the glass with the lowest energetic state, close to that of the corresponding crystal. The free volume v_f is the part of Δv^{g-x} that can be redistributed without a change of the energy of the entire system [109].

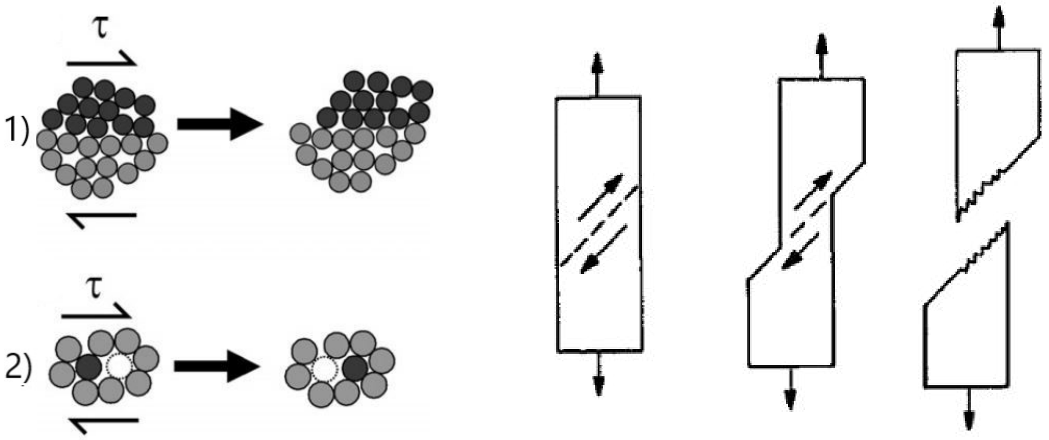

(a) (b)

FIGURE 2.16: a) In the top (1) a schematic illustration of the atomic motion in a "shear transformation zone" (STZ) as proposed by Argon is shown [111]. In the lower panel (2), the model of Spaepen, which assumes atomic jumps as deformation mechanism in metallic glasses is shown schematically [112]. Taken from Ref. [113]. b) Schematic illustration of the failure behavior of metallic glasses under tensile load. Taken from Ref. [107, 114].

According to Turnbull the free volume contributes to the overall entropy of the system and is randomly distributed [109]. However, two general models for the description of the process of shear band formation have been proposed:

1. Based on the model for "plastic flow in a disordered bubble raft" , Argon postulated a model for the deformation of metallic glasses [110, 111]. Herein, the deformation occurs at first in local "shear transformation zones" (STZ), where a cooperative shear motion of up to roughly 100 atoms takes place (Fig. 2.16a top).
2. On the basis of the considerations of Turnbull, Spaepen proposed a model for the atomic movement during deformation in metallic glasses [112]. In this model, the deformation takes place by a series of atomic jumps favored in regions with higher free volume (Fig. 2.16a bottom).

Both models take a thermally activated process as basis to enable the opposing atomic motion. The evasive movement of the atoms causes a "dilatation" of the precipitating atomic region [113], resulting in a local softening effect, since free volume is increased by a local plastic deformation in the respective region. The formation or rather percolation of several regions by nucleation along a plane is one possible scenario for the formation of a shear band at which the inhomogeneous shear flow takes place. However, independent from the exact mechanism, several models indicate a local temperature increase to lead to a liquid-like behavior in the shear band [107]. This is supported by experimental observations by Lewandowski and Greer [115].

The difference in the deformation mechanism of BMGs in comparison to crystalline metals strongly influences the macroscopic deformation and fracture behavior. Tension and compression experiments revealed that, metallic glasses show an about 20 % higher strength in compression compared to tension [113] and also the angle of fracture differs under different loading conditions. In case of compression a fracture angel of about 44° can be observed, whereas it is most likely between 48° and 60° in case of tension [113]. Such an asymmetry is also reflected in the plasticity. In compression tests BMGs can show a true strain of more than 150 %, but in tension they exhibit no plasticity [116]. Thus, the strength as well as the fracture behavior in metallic glasses shows a sensitivity to nominal stresses, leading to this "tension-compression asymmetry" [113]. This asymmetry results inter alia from the different length scale at which the deformation takes place. In BMGs the deformation occurs by the formation of a few or even a single shear band, causing the failure of the sample. Hence, the plastic deformation is strongly localized to the thickness of a shear band (several nm) [113]. In contrast, in crystalline metals the stress is relived by plastic deformation in a larger volume, as observed for example in the form of sample-necking in tension tests, leading to a higher macroscopic plasticity.

As already mentioned, the excess volume and the free volume have great impact on the deformation behavior. Hence, the mechanical performance depends on the structural state that is frozen-in, which is in turn a function of the cooling rate. A higher cooling rate results in a higher excess volume reflected by a higher fictive temperature $T_g^{fictive}$ (see section 2.2.2.4). This was picked up by Kumar et al. and linked to the plasticity of a metallic glass [117]. Their work proposed the critical fictive temperature T_{fc}, a threshold temperature, below which the value of Δv^{g-x} is lowered due to structural relaxation processes, occurring upon cooling, leading to an embrittlement. In contrast, if $T_g^{fictive} > T_{fc}$ an alloy appears to be ductile. Thus, the mechanical behavior or rather the ductility of a BMG is a function of the sample size, since $T_g^{fictive}$ is influenced by the sample thickness. The structural state of a sample can also be influenced by low temperature structural relaxation (below T_g) or by structural rejuvenation. The former one is caused by annealing process and the later one by different processes introducing excess free volume to the sample by mechanical deformation on different length scales, such as cold rolling [118, 119], shot peening [120] or cryogenic rejuvenation [121].

In summary, metallic glasses are not intrinsically brittle, rather even locally highly ductile. The macroscopic ductility depends on the one hand on the case of loading and on the other hand on the structural state of the sample.

2.5 Corrosion Behavior of Bulk Metallic Glasses

Besides the mechanical properties, the corrosion resistance is of great importance for many fields of application. In comparison to their crystalline counterparts[7], BMGs show a better corrosion resistance due to their amorphous structure. An amorphous single phase shows no defect like grain boundaries or second phases, which act as preferential sites for a corrosive attack [122]. Furthermore, the microscopical homogeneous structure facilitates the formation of amorphous passivation layers, which, in turn, also lack defects and hence, are assumed to be more stable. However, like technical, crystalline alloys such as Ti6Al4V ($Ti_{86.2}Al_{10.2}V_{3.6}$ in at%) or X5CrNi 18-10 stainless steel ($Fe_{67.7}Cr_{18.9}Ni_{9.3}Mn_{2.0}Si_{1.9}C_{0.2}$ in at%) [123, 124], bulk glass forming compositions tend to pitting corrosion, especially in saline solutions [122, 125]. Many ETM (early transition metal)-LTM (late transition metal)[8] systems like for example Ti-(Cu,Ni), Zr-(Cu,Ni), and Ni-Nb show on the one hand deep eutectics, favoring glass formation, but also show a large electrochemical potential difference between the noble LTM and the less noble ETM [125]. This causes, in particular in chloride-containing solutions, a dissolution of the ETM in some weak regions and the noble LTM remains at the surface [125]. Nevertheless, for example amorphous Fe-based alloys like $Fe_{80-x}Cr_xP_{13}C_7$ show a superior corrosion resistance in comparison to stainless steel in acidic as well as alkaline solutions [122, 126]. Thus, amorphous metals are able to outperform conventional metals and alloys regarding their corrosion resistance. Amorphous alloys in the Ti-Zr-Nb-Si system surpass the electrochemical properties of cp-Ti in Ringer's solution as well [127], but exhibit a rather poor glass forming ability and can only be cast in the form of thin sheets (roughly 20 μm), strongly limiting their application. Ti-based bulk glass forming alloys, such as $Ti_{40}Zr_{10}Cu_{36}Pd_{14}$, often show high amounts of Cu or Ni, facilitating pitting corrosion and resulting in a reduced corrosion resistance in comparison to pure titanium or Ti6Al4V [128]. However, especially for the use as biomaterial, in different body solutions, the corrosion behavior or rather the passivation behavior plays an important role. For example an implant material should not evolve corrosion products to the human body, since these products can be harmful to the human body. In particular, high releases of Ni or Cu have to be avoided. Currently, crystalline Ti-alloys are used because of their extraordinary passivation behavior and corrosion resistance.

---

[7] In this context crystalline counterpart is referred to an alloy with a crystalline microstructure but an equal or at least similar composition.

[8] In this work all elements of the D-block in the periodic table are considered as TM. ETM are elements from group 3 to group 7 and LTM are elements from group 8 to group 11.

2.6 Synthesis and Shaping of Bulk Metallic Glasses

The glassy state and the SCL state enables an unique shaping of amorphous metals. In general, three different techniques can be distinguished, which reveal the advantages of bulk metallic glasses over crystalline metals:

1) Casting - Injection Molding

Major advantages of casting amorphous metal parts are on the one hand the molding accuracy and on the other hand the fact that the mechanical properties are present directly after the casting process. Thus, subsequent heat treatments are not necessary. The high molding accuracy originates from the smooth transition from the (undercooled) liquid to the glassy state. The volume shrinkage, which occurs usually during the liquid-to-crystal transition, does not take place and the liquid is shapeable down to the glass transition temperature (Fig. 2.7). To date, modified polymer injection molding machines can be used for the processing of BMGs on an industrial scale (Fig. 2.17a). Fig. 2.17b shows a commercially available watch case produced from a Zr-based bulk glass forming alloy in a high pressure injection-molding process. For the processing by casting, the GFA of the alloy determines the process-ability and the maximum size of the part [129, 130].

(a)

(b)

FIGURE 2.17: a) Commercially available injection molding machine for the processing of BMGs. Taken from Ref. [131]. b) Watchcase produced from a Zr-based bulk metallic glass by injection molding. Taken from Ref. [132].

2) Thermoplastic Forming (TPF)

The term thermoplastic forming refers to the hot working of a bulk metallic glass in its superplastic state above the glass transition (below its melting point) [133]. For this purpose an already amorphous feedstock material is heated from room temperature above the glass transition temperature, into the deeply undercooled liquid. The process sequence is shown in Fig. 2.18a. This kind of shaping process is unique for amorphous metals and comparable to blow molding of oxide glasses or hot extrusion of polymers. The process is capable to replicate surface structures on the nanometer-scale [134] (Fig. 2.18b). The requirement of the alloy for TPF is a high thermal stability upon heating from the glassy state, which is commonly described by the length of the supercooled liquid region ($\Delta T_x = T_x^{onset} - T_g^{onset}$). ΔT_x can be determined using calorimetry. Since the thermal stability of an alloy will not necessarily correlate with its GFA [135], the alloys have to be designed for this processing route.

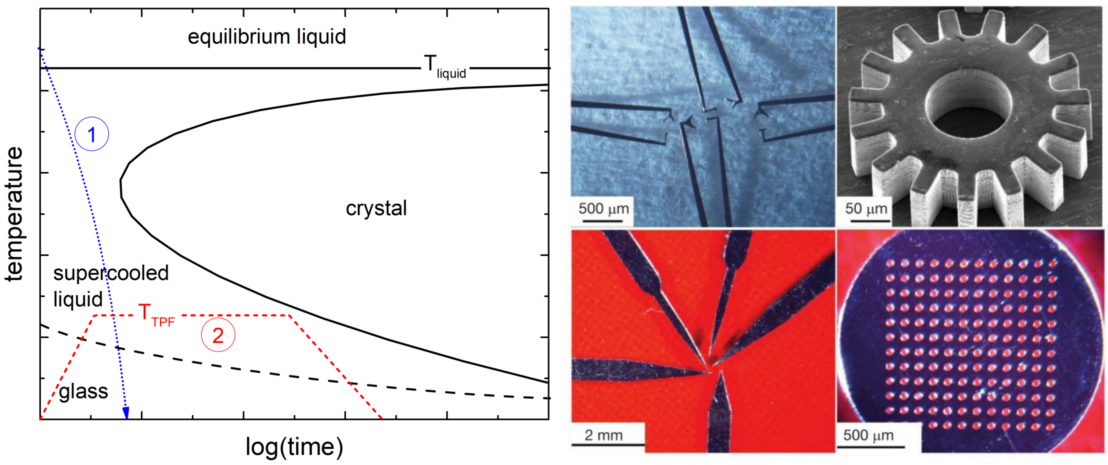

(a) (b)

FIGURE 2.18: a) Schematic time-temperature-transformation (TTT) diagram of a bulk glass forming alloy. For thermoplastic Forming (TPF) an initially amorphous sample (1) is heated to a certain temperature T_{TPF} above the glass transition temperature (T_g) but below the onset temperature for crystallization T_x. At T_{TPF} the sample or part can then be deformed mechanically in the superplastic state of the deeply undercooled liquid (2). b) Parts produced by TPF of different bulk metallic glass forming alloys. Taken from Ref. [136].

3) Selective Laser Melting (SLM)

Selective laser melting (SLM), often termed 3D-printing, is an additive manufacturing technique for the fusing of metal powder or foils to complex parts (Fig. 2.19), using different energy sources such as a laser or an electron beam. The geometry is developed layer-by-layer. For the production of amorphous parts the powder or foil, does not necessarily need to be amorphous, since it is remelted in the process. The accessible cooling rates are in the range of 10^3 to 10^4 K/s [137] and hence, are high enough for a wide range of (bulk) glass forming compositions [137–140]. Using this method, the size limitation of a part, which depends on the GFA of the respective alloy, can be evaded. The requirements to the alloy are on the one hand the GFA, so that the cooling rates are sufficiently high for vitrification. On the other hand, the layer-by-layer construction and the accompanied heat-affacted zone places high demands on the thermal stability against crystallization of the alloys. However, so far the main drawback of this technique are the rather high cycle times and the worse mechanical plasticity in comparison to as-cast parts [140, 141].

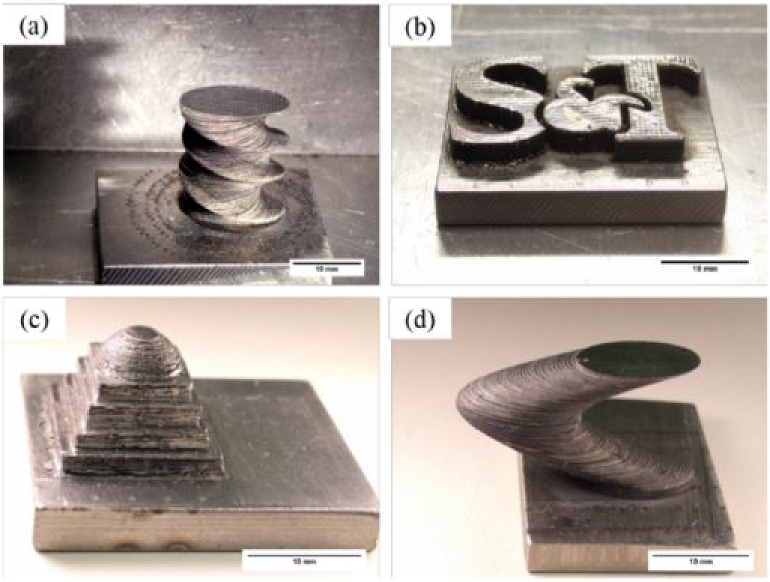

Figure 2.19: BMG parts produced by laser foil printing (LFP) of a Zr-based BMG. Taken from Ref. [138].

Chapter 3

Experimental Procedures

In this chapter the experimental setups and characterization techniques, which have been used to obtain the data of this work, are discussed briefly. Furthermore, the procedures of data acquisition and analysis are explained and a comprehensive overview of literature is introduced to the reader, in which in-depth information is provided.

3.1 Sample Preparation

Since sulfur is used as constituent in metallic glass forming alloys in this work for the first time, the focus of this section lies on the particularities in the processing of sulfur. The preparation process of the master-alloys depends on the sulfur-content of each type of alloy. Alloys with a high content of sulfur (>11 *at*%), which are found in the ternary Pd-Ni-S system, are produced by melting the high-purity raw elements (99.999 wt% Pd, 99.95 wt% Ni, 99.9995 wt% S) in a high-purity argon atmosphere in a silica tube. The arrangement of the elements in the silica tube is shown schematically in Fig. 3.1a. Fast inductive heating of the metals lead to melting and evaporation of sulfur. Subsequently, the gaseous sulfur condensates at the cool silica tube and is running down to the glowing metals followed by a reaction of both. The stable liquid phase of sulfur features one major advantage over phosphorous, since the process is much more stable regarding the compositional accuracy. However, alloying of the raw elements in a conventional furnace or an arc furnace is still not possible due to evaporation of sulfur. After the alloying procedure, the alloys are treated in dehydrated B_2O_3 for at least 4 hours at 1473 K to remove impurities such as oxides, which might work as heterogeneous nucleation sites (see section 2.2.2.3).

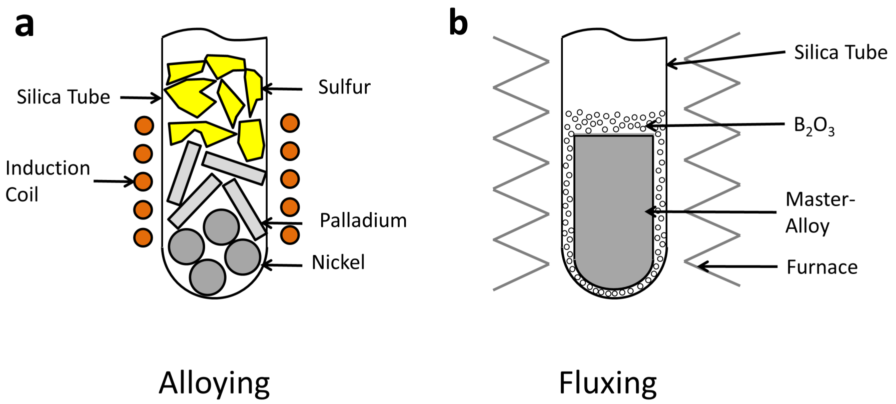

FIGURE 3.1: a) Arrangement of the raw elements for the alloying process in a silica tube. The metals (e.g. Pd, Ni) are melted by eddy currents, which are introduced by an induction coil. b) In the second step, the master-alloy is treated in liquid B_2O_3 in order to remove impurities like oxides (fluxing process). Figure taken from Ref. [8].

Alloys with lower sulfur-contents (≤11 *at*%) are produced using high-purity sulfur-bearing pre-alloys (Fig. 3.1). These pre-alloys (for instance $Cu_{65}S_{35}$, $Ni_{55}S_{45}$) are produced by inductively melting the pure elements (99.999 wt% Cu, 99.95 wt% Ni, 99.9995 wt% S) in a silica tube under a high purity argon atmosphere and are then treated in dehydrated B_2O_3 like in the above described procedure. As soon as sulfur is not present in its pure form, but as a metallic compound, the processing in arc furnaces is possible. Hence, the master-alloys are prepared by arc melting mixtures of the remaining high-purity raw elements (99.999 wt% Ti, 99.99 wt% Zr, 99.99 wt% Al, 99.99 wt% Nb, 99.999 wt% Cu, 99.95 wt% Ni) and the high-purity pre-alloy in a Ti-gettered argon atmosphere. The ingots were flipped and remelted at least 5 times in order to guarantee homogeneous master-alloys. In case of industrial grade alloys, lower grade Ti and Zr are used together with a commercially available Cu-S (Cu80S20) pre-alloy in order to evaluate the influence of high contents of oxygen or other accompanying elements on the GFA and the properties of the glass. The compositions of different master-alloy batches were checked by measuring the weight of the ingots after each alloying step and by comparing it to the mass of the raw elements to detect a possible deviation from the nominal composition.

Subsequent to the alloy synthesis, amorphous samples are produced by casting the master-alloys in a custom built suction casting device. Here, the ingots were melted under high-purity argon with an electric arc and cast into water-cooled copper molds by applying a vacuum force to the molten droplet. The sample size depends on the glass forming ability of each individual alloy. For the alloy development molds, with plate- and rod-like geometries ranging from 0.25 mm to 5 mm, were used to evaluate the critical casting thickness and the glass forming range of the different alloying systems.

EDX analysis were carried out at various as-cast samples to identify a possible loss of sulfur and to validate the sample preparation procedure.

3.2 Thermo-physical Characterization

3.2.1 Calorimetry

In calorimetry the measurement signal is proportional to the heat release or heat absorption of a sample. Therefore, the sample is subjected to a defined temperature-time protocol and the heat flow $\dot{Q}$, caused by physical or chemical processes, is recorded. In case of a differential thermal analyzer (DTA) the measurement signal is the temperature difference between two thermocouples ΔT, which are adjacent to the sample-crucible and a reference-crucible. Power-compensated differential scanning calorimetry (DSC) measures the electric power ΔP being necessary to heat or cool two separated furnaces (sample and reference), which are identical in construction. A detailed description of the setup, the technical designs and the underlying principles can be found elsewhere [142]. In this work, a power-compensated Perkin Elmer DSC 8500 and a Perkin Elmer Diamond DSC are used for high precision measurements in the temperature range of 173 K - 973 K. Melting detection measurements above 973 K are carried out with a NETSCH STA 449 Jupiter DTA with a temperature limit of 1873 K. Prior to the measurements, the devices have been calibrated for each specific heating rate (0.025, 0.083, 0.33, 1, 1.5, 2, 3 K/s)[1] and crucible material (Al, Cu, Graphite, Al_2O_3). Therefore, different calibration substances (In, Zn, Al, Ag, Au[2]) with different melting temperatures are used. During all measurements the sample environment was flushed with a flow of high purity Ar (99.9999 wt%) to reduce reactions between the sample and the surrounding environment. Nevertheless, at high temperatures above the melting point, the reactivity especially of Ti- and Zr- BMGs is very high, which could cause measurement artifacts during the melting detection experiments. In order to reduce the influence of reactions, graphite crucibles are coated with Y_2O_3 spray.

3.2.1.1 Transformation Temperatures and Enthalpies

By applying a constant heating rate to an (partially) amorphous sample, different thermal properties can be determined. In the low temperature regime, between the

---

[1] In case of the DTA measurements with a NETSCH STA 449 Jupiter DTA only lower heating rates are accessible.

[2] Al, Ag, Au were only used in case of Graphite and Al_2O_3 crucibles.

glass transition and the initial temperature, different relaxation processes (structural α-relaxation, β-relaxation) can take place (Fig. 3.2). At a certain temperature the atomic mobility in the sample is sufficiently high to reach the metastable supercooled liquid state. This transition is the glass transition, which is connected to a rise in the molar heat capacity to the value of the supercooled liquid and hence, appears to be endothermic. As pointed out in section 2.2.2.4, different temperatures can be assigned to this transition. In continuous heating experiments the onset temperature T_g^{onset} and the end temperature T_g^{end} of the glass transition can be detected (Fig. 3.2), which depend on the specific rate (see section 3.2.1.3). Above T_g^{end} the sample reaches the supercooled liquid state, being a metastable equilibrium. Further heating results in the formation of the thermodynamic more stable crystalline state, which starts at the onset temperature for crystallization T_x^{onset}. The temperature range between T_g^{onset} and T_x^{onset} is commonly defined as the extend of the supercooled liquid region ($\Delta T_x = T_x^{onset} - T_g^{onset}$), providing information about the thermal stability of an alloy. The released heat during the exothermic process of crystallization can be determined by integration. In order to compare different samples and compositions, the baseline for the integration is chosen to be a straight line as shown in Fig. 3.2. After the completion of all crystallization events (formation of different phases or solid state reactions) the "stable" crystalline state is reached [3]. For an accurate determination of the characteristic temperatures and enthalpies below T_m, a second temperature scan was carried out with the crystalline sample for all DSC measurements. In this manner, the heat capacity of the crystalline state can be subtracted. If the temperature is increased further, melting of sample occurs at the solidus temperature T_m (right panel in Fig. 3.2). Due to dynamic effects in the heat transfer during the measurement, the solid-liquid transition is smeared out ($T_m < T_l$), even if it is expected, at least for a congruent melting processes as in case of a eutectic reaction, to be a singularity ($T_m = T_l$) . However, by integration of the melting peak between T_m and T_l the enthalpy of fusion ΔH_f calculated (Fig. 3.2). Using equation 2.5, the entropy of fusion ΔS_f can be calculated, yielding a first estimation of the driving force for crystallization ΔG^{l-x} for small undercoolings below T_l.

3.2.1.2 High-precision Heat Capacity Measurements

For the determination of the thermodynamic functions (ΔH^{l-x}, ΔS^{l-x}, ΔG^{l-x}), high accuracy measurements of the specific heat capacities in the low and high temperature regime are necessary. Therefore, a "step-scan method" is used in a Perkin Elmer DSC.

---

[3] In this context, the term stable is referred to a state in which no further exothermic events take place before melting begins.

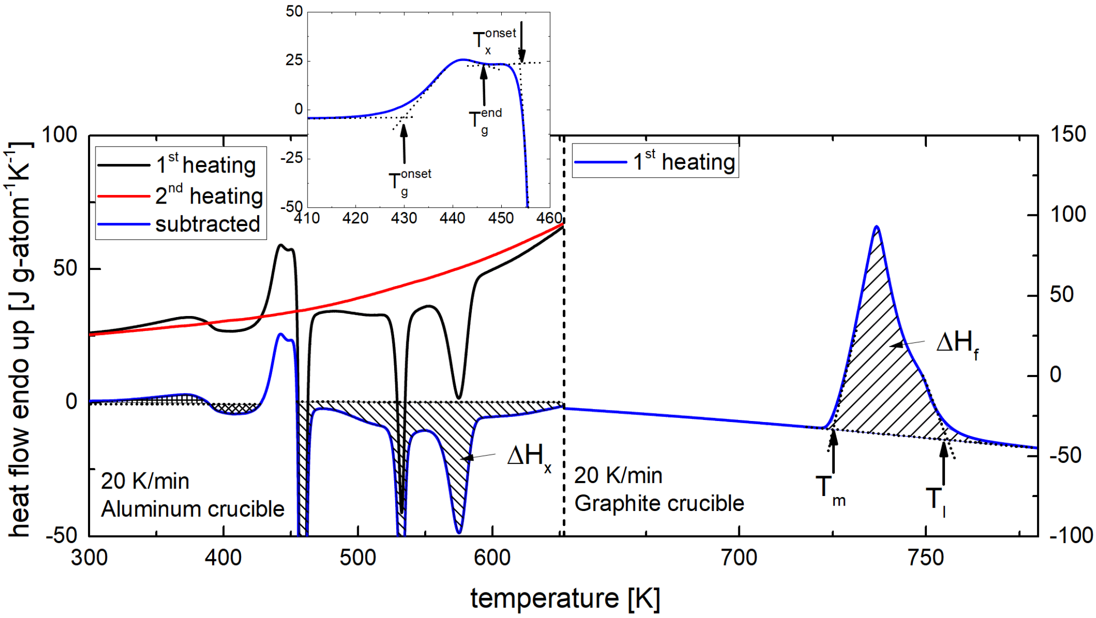

FIGURE 3.2: Differential scanning calorimetry (DSC) trace of a Pd-based bulk glass forming alloy at a heating rate of 0.33 K/s in different crucibles (Al, C). In the low temperature regime (left diagram), different endothermic or exothermic events can be observed. Below the onset of the glass transition temperature T_g^{onset} (inset) relaxation processes take place. At T_g^{onset} the heat capacity of the sample increases due to the transition to the supercooled liquid. The caloric glass transition ends at T_g^{end} followed by the onset of crystallization T_x^{onset} (inset). During the crystallization process heat is released from the sample, which is determined by integration of the heat flow signal (ΔH_x). In the low temperature range, the heat flow is corrected by subtracting the baseline of a crystalline sample. In the high temperature range, for the detection of the melting behavior, the heat flow of the sample is not corrected. The melting process starts at the melting or solidus temperature T_m and ends at the liquids temperature T_l. The heat, that is absorbed during the melting process, is termed enthalpy of fusion ΔH_f and is determined by integration of the heat flow signal.

The specific heat capacity of the sample $c_p(T)_{sample}$ is measured in reference to a standard material with a well-known temperature dependence of the specific heat capacity. In this work, sapphire ($c_p(T)_{sapphire}$) is taken as reference material. According to Ref. [71] the molar heat capacity $c_p(T)_{sample}$ can be calculated by

$$c_p(T)_{sample} = \frac{\dot{Q}_{sample} - \dot{Q}_0}{\dot{Q}_{sapphire} - \dot{Q}_0} \frac{m_{sample} M_{sample}}{m_{sapphire} M_{sapphire}} c_p(T)_{sapphire} \tag{3.1}$$

where $\dot{Q}_{sample}$ and $\dot{Q}_{sapphire}$ correspond to the heat flow necessary to heat or cool the sample and the sapphire standard, respectively. $\dot{Q}_0$ is the heat flow, which is necessary to heat the empty crucible. m and M refer to the mass and the molar mass of the respective material in the crucible. To determine the unknown quantities $\dot{Q}_0$, $\dot{Q}_{sapphire}$ and $\dot{Q}_{sample}$, one measurement with a "step-program" has to be conducted for each quantity. Therefore, the temperature protocol comprises consecutive isothermal temperature steps

ΔT. Each step with a step size of $\Delta T = 10\ K$ consists of a heating ramp with a rate of 0.33 K/s to the desired temperature T and a isothermal holding time Δt. The temperature increase results, in turn, in a step in the heat flow ($\dot{Q}_{\dot{T}\neq 0}$), which is necessary to heat the sample, followed by a drop in the heat flow $\dot{Q}$ to the level necessary to hold the temperature isothermally ($\dot{Q}_{\dot{T}=0}$). The holding time is chosen to be 120 s, which is sufficiently high for the equilibration of the signal ($\dot{Q}_{\dot{T}=0} \approx const.$). The amount of the drop of $\dot{Q}$ corresponds to the value of the respective heat flow $\dot{Q}_{sample}$, $\dot{Q}_{sapphire}$ or $\dot{Q}_0$.

For measurements in the solid state aluminum pans are chosen. In order to avoid contamination of the samples, the measurements are carried out under a flow of high-purity argon. Accurate measurements of the heat capcaity of the liquid state are only conducted for alloys in the Pd-Ni-S system, since these alloys do not show any reactions with graphite or alumina crucibles in the liquid phase and the melting point was far below 973 K, enabling the use of the Perkin Elmer DSC 8500.

The data of the different phases (crystalline, glassy, liquid) in the different temperature regimes are fitted by

$$c_p^{liquid}(T) = 3R + aT + bT^{-2} \tag{3.2}$$

for the liquid phase [143],

$$c_p^{x-tal}(T) = 3R + cT + dT^2 \tag{3.3}$$

for the crystalline phase in the high temperature regime [143], and

$$c_p^{glass/x-tal}(T) = 3R/M[1 - exp[-1.5(T/T_D)] \tag{3.4}$$

for the glassy and the crystalline phase in the low temperature regime [144].

3.2.1.3 Determination of the Fragility of the Liquid

As already mentioned in section 2.2.2.4, the fictive glass transition temperature $T_g^{fictive}$ shows a cooling rate dependence, due to the temperature sensitivity of the dynamics. This can be used to determine the kinetic fragility by applying different heating rates in DSC [36]. Angell et al. proposed that the onset of the glass transition T_g^{onset} measured in DSC coincidences with the fictive glass transition temperature $T_g^{fictive}$, if the heating rate is identical to the cooling rate at which the glassy structure is frozen-in [36].

Hence, for the determination of the fictive temperature, samples are heated to their supercooled liquid state ($T \geq T_g^{end}$) and are cooled afterwards with a defined rate (0.083, 0.33, 0.66, 1 K/s, 1.5 K/s, 2 K/s, 3 K/s) down to room temperature (pre-treatment). A second temperature scan with the same rate as in the pre-treatment allows the graphical determination of $T_g^{fictive}$ using the tangent method [36, 145]. This is shown in Fig. 3.3 for the $Pd_{31}Ni_{42}S_{27}$ alloy with a heating rate of 0.33 K/s.

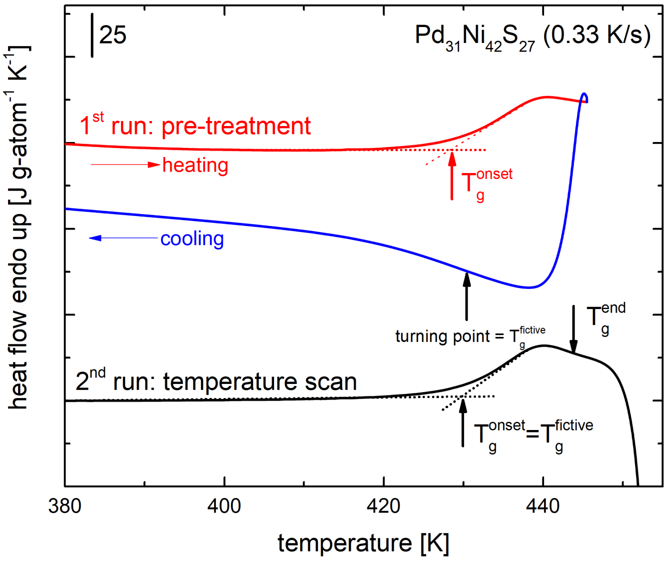

FIGURE 3.3: Illustration of the experimental procedure for the determination of liquid's fragility using the "T_g-shift method". In the first DSC run, the sample is heated with a certain heating rate above T_g^{end} into the supercooled liquid region and is then cooled with the same rate down to room temperature. A second up-scan, again with the same heating rate, is carried out until crystallization occurs. This standard treatment results in the coincidence of T_g^{onset} and $T_g^{fictive}$. Adapted from Ref. [8].

Afterwards, different methods can be used for the calculation of liquid's fragility:

According to Busch et al. [145, 146], the width of the glass transition ($\Delta T(q) = T_g^{end}(q) - T_g^{onset}(q)$ with $T_g^{onset}(q) = T_g^{fictive}(q)$) can be assigned to a given rate q, allowing the calculation of a transition time τ via

$$\tau(T_g^{onset}(q)) = \frac{\Delta T(q)}{q} \tag{3.5}$$

The resulting transition time is a function of $T_g^{onset}(q)$ and can be fitted using equation 2.9.

Another method for the evaluation of the rate dependence of the glass transition temperature was proposed by Angell et al. [36]. Here, the logarithm of the heating rate normalized by the standard heating rate q_s (= 0.33 K/s) is plotted over the fictive temperature normalized by the fictive temperature at 0.33 K/s ($T_g^{standard} = T_g^{onset}(q = 0.33\ K/s)$). The fragility index m is given by

$$log\left(\frac{q}{q_s}\right) = m - m\left(\frac{T_g^{standard}}{T_g^{onset}(q)}\right) \tag{3.6}$$

Alternative approaches for the estimation of the kinetic fragility of liquids are proposed by Wang et al. [47] and Wei et al. [41]. Wang's estimation refers to the difference of the molar heat capacity of the liquid and the glassy phase at the glass transition temperature with respect to the absolute value of the crystalline mixture ($\Delta c_p^{l,g-x}(T_g)$). To some extend it was shown experimentally for different glass forming liquids, that the height of the c_p-jump at T_g correlates with the kinetic fragility of the undercooled liquid [36, 43, 147, 148]. According to Wang et al., the fragility index m (Fig. 2.4) can be estimated by

$$m = 40\frac{\Delta c_p^{l,g-x}(T_g)}{\Delta S_f}. \tag{3.7}$$

$\Delta c_p^{l,g-x}(T_g)$ can be read in a DSC scan and ΔS_f can be determined in melting detection experiments (Fig. 3.2).

The study of Wei et al. revealed an empirical correlation between the slope of the heat flow at $T_g^{onset}(q = 1\ K/s)$ and the fragility parameter D^* in a $T_g^{onset}(q = 1\ K/s)$-scaled DSC scan:

$$\left.\frac{d\Delta c_p^{l,g-x}(T)}{d(T/T_g)}\right|_{max} = \frac{k}{D^*} \tag{3.8}$$

Here, k is a fitting constant, which is calculated to be $k = 7803 \pm 290$ J g-atom$^{-1}K^{-1}$.

3.2.1.4 Experimental Determination of Time- Temperature- Transformation (TTT) Diagrams

In the low temperature regime, isothermal time-temperature-transformation (TTT) diagrams are measured by heating amorphous samples in Al crucibles at a heating rate of 2 K/s to an appropriate temperature T_{iso}, at which the sample is isothermally hold until the end of crystallization. During the measurement, the heat flow is recorded with time. The crystallization peaks are integrated in order to determine the overall crystallization enthalpy. This allows the determination of the transformation times at which 1 %[4], 50 % and 99 % of the crystallization process are completed. These transformation times ($t_x^{1\%}, t_x^{50\%}, t_x^{99\%}$) are plotted as a function of the temperature, leading to the isothermal TTT diagram. In case of the $Pd_{31}Ni_{42}S_{27}$ alloy, it is also possible to measure the isothermal TTT diagram upon cooling from the equilibrium liquid, since the liquidus temperature is low enough for melting by DSC (< 973 K). Furthermore, no reactions with the crucible material (graphite) are detected. During the high temperature measurements, the sample is covered with B_2O_3 in order to prevent contamination's by the atmosphere, reducing the effect of heterogeneous nucleation. After heating the samples above the liquidus temperature to 973 K and a holding time of 120 s for equilibration, the samples are cooled with 2 K/s to a certain temperature and then hold isothermally until crystallization occurs. The determination of the crystallization times is done in the same manner as for the low temperature measurements, yielding $t_x^{1\%}$, $t_x^{50\%}$ and $t_x^{99\%}$. After the experimental determination of the TTT diagram of $Pd_{31}Ni_{42}S_{27}$, the crystallization "nose" is fitted using equation 2.18 (Fig. 2.6a), enabling the calculation of the interfacial energy and the critical cooling rate.

Continuous TTT diagrams are obtained in the high temperature regime by continuous cooling experiments from the equilibrium liquid. For this, the samples are heated above the liquidus temperature to 973 K and hold for 120 s for equilibration. Subsequently, at a certain rate the undercooling until crystallization occurs is detected. In the low temperature region, the onset of crystallization and the glass transition temperatures of glassy samples are measured upon heating with different rates. The onsets of the crystallization events as well as the glass transition were graphically determined using the tangent method. Finally, the onsets of the glass transition and the onsets of crystallization upon heating and cooling are combined in a temperature versus rate diagram (Fig. 2.6b).

3.2.2 Low-temperature Viscosity Measurements

For the determination of the equilibrium viscosities at low temperatures close to the glass transition, the three-point beam-bending (3PBB) method is used in a Netsch 602 thermo-mechanical analyzer (TMA) [149]. A constant load is applied to a beam with a rectangular cross section by a fused silica probe with a wedge-shaped geometry. During the experiment the resulting deflection rate is measured. This technique allows the determination of viscosities in the range of 10^7 to 10^{14} Pa s [149] using the relation

---

[4] Here, % corresponds to energy percent and due to different, unknown energies of formation of the phases this can not be assigned to wt% or vol%.

$$\eta = -\frac{gL^3}{144 I_c \nu} \left[M + \frac{\rho A L}{1.6} \right] \tag{3.9}$$

where g is the gravitational constant, I_c the cross-section moment of inertia, ν the mid-point deflection rate, M the applied load, ρ the density of the glass, A the cross-sectional area and L the support span of the experimental apparatus. Using different thermal protocols (isothermal holding and continuous heating) the viscosity of the undercooled liquid can be measured in vicinity of the glass transition. During isothermal holding the relaxation of the sample to reach the equilibrium state causes a change of the viscosity. The resulting viscosity data is fitted using a Kohlrausch-Williams-Watts (KWW) stretched exponential function [71, 150]

$$\eta(t) = \eta_a + \eta_{eq-a} \left(1 - exp \left[- \left(\frac{t}{\tau} \right)^{\beta} \right] \right) \tag{3.10}$$

where $\eta(t)$ is the viscosity, η_a the value of the amorphous phase before relaxation and η_{eq-a} the amplitude during the relaxation process. t is the time and τ the characteristic relaxation time. β corresponds to the stretching exponent of the exponential function. The temperature dependence of η or τ are then described by equation 2.8 and 2.9, respectively.

3.2.3 Viscosity Measurements of the High Temperature Liquid

The method of choice for the measurement of the viscosity or surface tension of highly reactive liquids, such as zirconium or titanium, is a container-less method. Here, contamination by crucible walls are completely avoided and due to the avoidance of heterogeneous nucleation a higher undercooling is achievable. In case of electromagnetic levitation (EML) a metallic sample (6 - 8 mm diameter) is processed container-less in a high-frequency alternating magnetic field. A schematic illustration of the setup is shown in Fig. 3.4. One induction coil is used to levitate the sample by an external Lorentz force (positioning circuit) and the second coil is used for the heating of the sample (heating circuit).

In case of dynamic measurements, the molten sample is forced to an oscillation by a short heating pulse, resulting in a deflection of the droplet in two directions in space (X and Y). The decay behavior, which is determined using video data or the sample coupling electronics (SCE), enables the calculation of the viscosity and surface tension [154–157]. In comparison to an electrostatic levitator (ESL), where the measurements

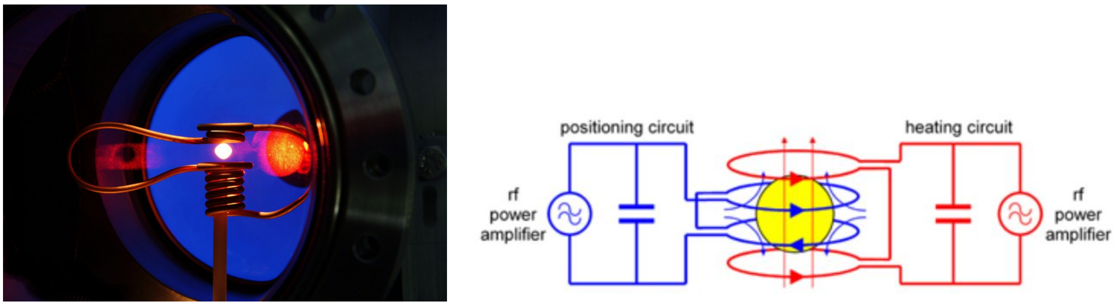

(a) (b)

FIGURE 3.4: a) Image of a levitated molten metallic droplet in an electromagnetic levitator (EML). Taken from Ref. [151]. b) Setup of the coil system in an electromagnetic levitator (EML). The positioning circuit is used for levitation of the sample and the heating circuit is used for the temperature control and for forcing an oscillation of the liquid droplet. Taken from Refs. [152, 153].

are carried out in vacuum environment (see section 3.3.2), in case of EML experiments the sample is processed in an inert gas (Ar) atmosphere, allowing the processing of easily evaporating samples. However, the gravitational field of the earth can cause a deformation of the liquid droplet, preventing an accurate measurement of the viscosity and surface tension. It is for this reason, that it is necessary to conduct the experiment in different facilities, operating in microgravity. In this work, measurements are carried out in a "reduced-gravity aircraft", which follows an parabolic flight path, providing roughly 23 s of microgravity at each parabola during free falling. In Fig. 3.5a the processing parameters, temperature, coil voltage and gravitation are shown. After heating the sample with a voltage of 10 V above its liquidus temperature, three oscillations are forced with different short voltage pulses during microgravity.

The collected data are analyzed using the "oscillating drop technique" revisited in Ref. [157]. Therefore, the dynamic viscosity η of the liquid sample can be calculated from the damping constant Γ of the decay of a forced oscillation by

$$\eta(T) = \frac{3m\Gamma(T)}{20\pi r_0(T)} \tag{3.11}$$

where m and r_0 correspond to the mass and the radius of the sample, respectively. The oscillation or rather the damping behavior can be described by a damped cosine function by

$$r(t) = r_0 + Acos(\omega t)exp(-\Gamma t) \tag{3.12}$$

where r(t) is the radius, which changes during the oscillation, and ω corresponds to the angular frequency. A is the amplitude of the oscillation.

The surface tension σ can then be calculated from the frequency of the oscillation via

$$\sigma = \frac{3\pi m}{32\omega^2}. \tag{3.13}$$

Both, equation 3.11 and 3.13, are valid for a weak damping ($\Gamma << \omega$) and for viscosities below $\eta_{crit} = 0.76\sqrt{\sigma r_0 \rho}$. However, by fitting the experimental data from the EML experiments at microgravity with a function in the form of equation 3.12, $\eta(T)$ and $\sigma(T)$ of the high temperature liquid can be calculated. In Fig. 3.5b, the fitting procedure of an oscillation of the $Ti_{60}Zr_{15}Cu_{17}S_8$ alloy is shown. In the inset the initial deflection of the droplet is shown, which decays because of the damping of the sample.

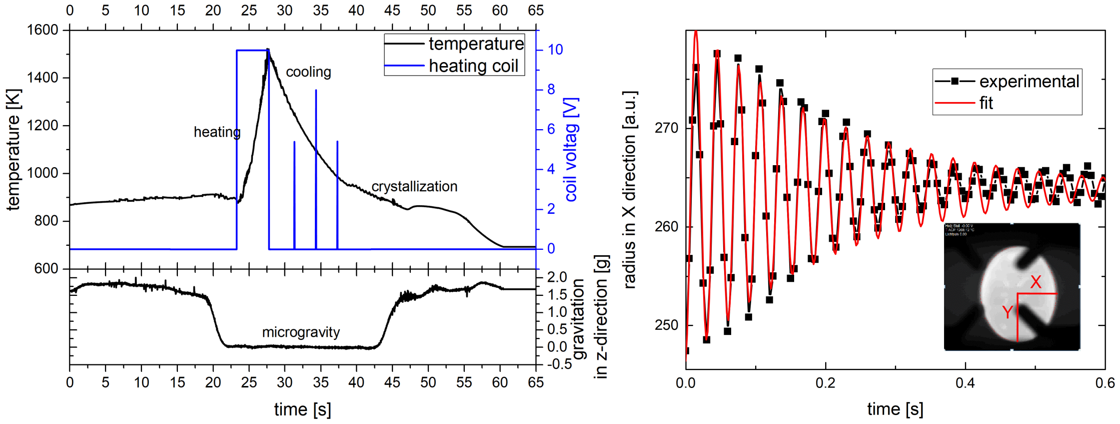

(a) (b)

Figure 3.5: a) Temperature, voltage and gravity as a function of temperature. The temperature is measured using a pyrometer. The voltage corresponds to the heating circuit, which is also used to set three pulses to force an oscillation of the droplet upon free cooling in microgravity. b) Decay behavior of the radius of a liquid droplet in X direction, during a forced oscillation in microgravity. The data points are fitted with a damped cosine function. The inset shows the detection of the radius of the droplet with a high frequency camera.

3.3 Structural Investigations and Phase Identification

As already pointed out, the structure of the liquid phase has a significant impact on the process of glass formation. In particular, the evolution of different structural metrics with temperature is one major topic in this thesis. Furthermore, the crystalline phases that limit the thermal stability and compete with the glassy phase upon quenching are of certain interest for the development of new bulk glass forming compositions. In simple terms, the underlying principle behind the methods used for the structural investigations is the interaction of photons or electrons with the atomic structure. In the following, the different methods used in this work are explained briefly, whereby the main focus is set to the data analysis.

3.3.1 Conventional X-ray Diffraction

In case of X-ray diffraction experiments, a focused X-ray photon beam is used to investigate the atomic structure. According to Bragg and Laue, under certain conditions the incident X-ray beam is diffracted constructively or destructively by the atomic structure. Highly periodic atomic structures, like crystals, fulfill these diffraction conditions at their lattice planes, resulting in the formation of sharp diffraction peaks (Bragg peaks). The intensity level and location of the diffraction peaks are characteristic for each specific crystal structure. For a detailed description of the experimental setup and the theoretical background the reader is referred to Ref. [158]. However, less periodic structures like the glassy or the liquid structure, which show only short-to-medium range order, do not produce any sharp Bragg diffraction peaks. Here, a diffuse distribution of the intensity is observed. These intensity "halos" can be attributed to the atomic shells, reflecting the possibility to find an atom at a certain atomic distance (see section 2.3).

A PANalytical X'Pert Pro/ PANalytical Empyrean X-ray diffractometer (XRD) with a Bragg-Brentano geometry ($\theta - 2\theta$) and copper as tube anode material (CuK_α radiation) is used to identify crystalline phases and to prove the amorphous character of the samples. For this, the samples are grind and cut to enable the measurement in the cross-section with the lowest cooling rate. Diffraction patterns of the crystalline equilibrium phases were simulated using the PowderCell 2.3 software [159]. For this, it is assumed that the phases are present in their ideal structural state and the influence of the high cooling rates, which may have an impact on the composition or atomic structure, are neglected.

In order to compare the diffraction pattern measured with different beam sources or rather wavelength λ, the diffraction angle θ is converted to the wave vector Q, which is independent from λ, by

$$Q = 4\frac{\pi}{\lambda} sin(\theta\frac{\pi}{180}) \tag{3.14}$$

which can be derived from Bragg's law and Laue's equation.

3.3.2 High Energy Synchrotron X-ray Experiments

In-situ high energy synchrotron X-ray experiments are carried out at the hard X-ray diffraction beamline P02 at the German electron synchrotron (DESY) operating at a fixed energy of 60 keV (0.207 Å) and at the high intensity beamline ID11 at the European synchrotron radiation facility (ESRF) operating at an energy of 100 keV (0.124 Å). Here, only the experimental setup and the data analysis is reviewed briefly. For a detailed description of the theoretical backgrounds of the scattering experiments, the reader is referred to Ref. [160].

In case of the experiments done at the DESY, the influence of temperature changes on the structure of as-cast samples is investigated in transmission mode in the high and low temperature regime. The experiments are conducted with a heating and cooling rate of 0.33 K/s in three different furnaces: a ceramic heater, a lamp furnace and a Linkam furnace. The first two furnaces enable measurements from room temperature up to 1473 K, whereas the Linkam furnace has a temperature limit of 873 K, but a higher temperature accuracy. In the lamp furnace and the ceramic heater the sample has to be placed in SiO_2 tubes (1 mm in diameter and a wall thickness of 0.01 mm), reducing the accuracy of the temperature control and introducing an additional background to the diffraction data, which has to be corrected. However, high temperature measurements of the equilibrium liquid phase are performed only for the $Pd_{31}Ni_{42}S_{27}$ alloy, since no reactions with the silica tube are observed. The samples (1 mm rods) are placed inside the quartz capillaries and are covered with B_2O_3 in order to reduced sample contamination by the atmosphere. Additionally, the capillaries are flushed with high purity argon. Highly accurate low temperature measurements are carried out for Ti-, Zr- and Pd-alloys in the Linkam furnace on roughly 0.25 mm thick plate-shaped samples, which are directly attached to the silver heating plate in the furnace, using copper conductive paste. In all experiments, a beamsize of 0.5 mm x 0.5 mm is used and the diffracted intensity is detected with a Perkin Elmer XRD1621 CsI bonded amorphous silicon detector (2048 pixels x 2048 pixels). The exact wave length slightly varies for each beam time and is determined, by using a calibration standard, to 0.20712 Å, 0.20745 Å and 0.20669 Å for the measurements in the lamp furnace, the ceramic heater and the Linkam furnace, respectively.

At the ESRF an electrostatic levitator (ESL) is used to process highly reactive samples container-less in a high vacuum environment in their equilibrium liquid. In an ESL the sample is levitate using a static electrical field between two electrodes. Four auxiliary electrodes, which are aligned laterally, position the sample in the electrostatic field (Fig. 3.6a). The position is controlled by two positioning lasers, which have an lateral offset of

90 degrees. The sample surface is additionally charged with an ultraviolet lamp to enable the levitation in the electrostatic field. Heating takes place by two diode lasers with a power of 25 W and the temperature is detected with a pyrometer. Spherical samples with a diameter of 2 - 3 mm are heated manually above their liquidus temperature. A detailed description of an ESL can be found elsewhere [161, 162]. After a sufficient overheating is reached, and no crystalline reflexes are visible in the diffraction pattern, the sample is cooled by switching of the heating lasers until crystallization occurs. An exemplary temperature profile is shown in Fig. 3.6b. The beam size in the experiment is chosen to be 0.5 mm x 0.5 mm and the exact wave length is determined to be 0.123984 Å. For the detection of the diffraction pattern a custom-built detector, which is provided at the beamline, is used.

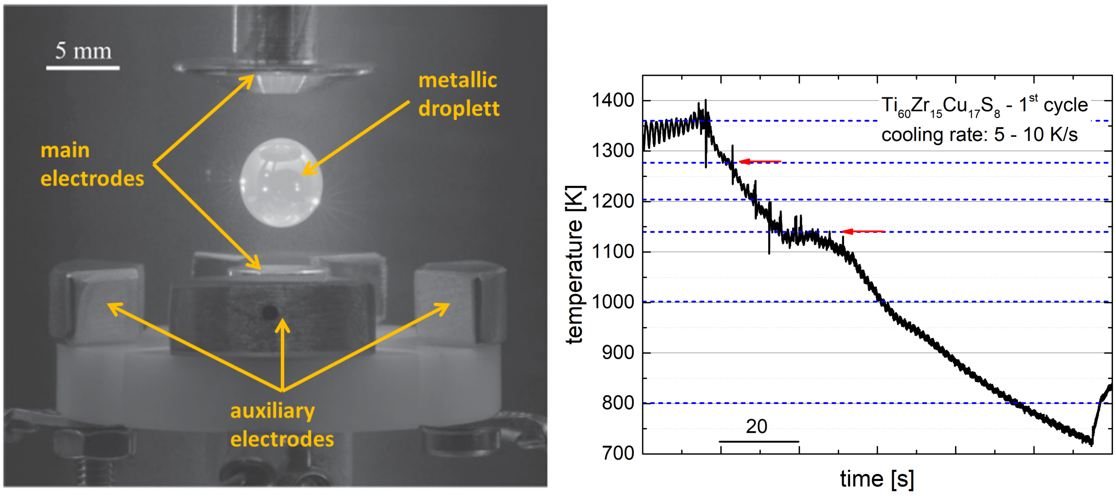

(a)

(b)

FIGURE 3.6: a) Image of the electrode system in an electrostatic levitator (ESL). Taken from Ref. [162]. b) Temperature profile of a cooling cycle during an ESL measurement. Upon free cooling a maximum cooling rate of roughly 10 K/s is achieved. The blue dashed lines mark the temperatures at which a diffraction pattern is analyzed for the identification of the crystalline phases. The red arrows highlight the recalescences of the crystallization processes.

For the integration of the two dimensional raw X-ray diffraction patterns the Fit2D [163], the PyFAI [164] and the Dawn [165, 166] analysis software was used, yielding the raw intensity $I_{raw}(Q)$. Using PDFgetX2 the total structure factor S(Q) and the total reduced pair distribution function G(r) were obtained after subtraction of the furnace background and correction of $I_{raw}(Q)$ [167] . S(Q) and G(r) were afterwards interpolated with a cubic spline for the determination of the peak maxima (Fig. 3.7a). A detailed description of the data processing can be found in Ref. [51]. As described in section 2.3, in some cases a splitting of the diffraction peaks can be observed. For an accurate determination of the peak positions a Bi-Gaussian fit is used in this work (Fig. 3.7b).

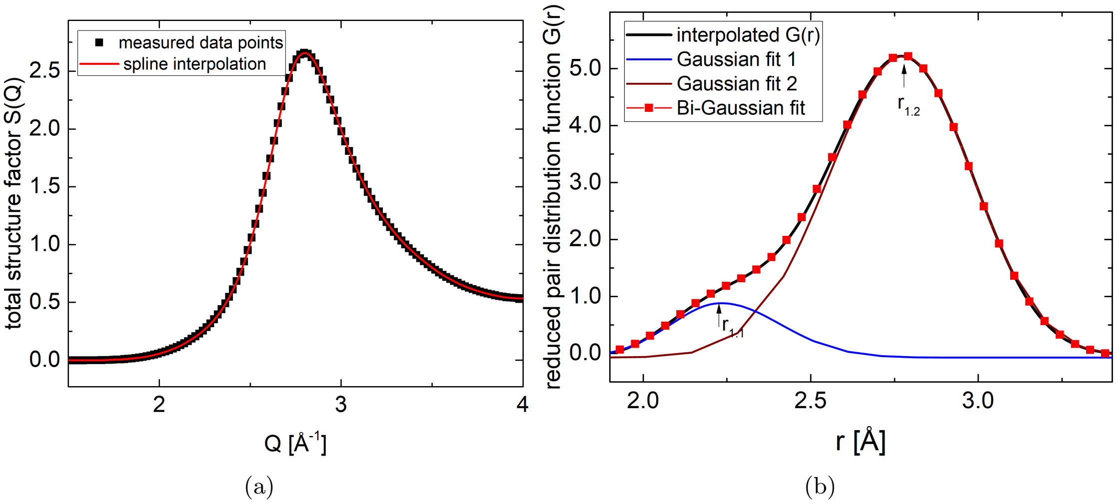

(a) (b)

FIGURE 3.7: a) Spline interpolation of the first sharp diffraction peak in the total structure factor S(Q) of a Pd-based BMG. b) Bi-Gaussian fit of the interpolated first sharp diffraction peak in the total pair reduced distribution function G(r) of a Pd-based BMG.

3.3.3 Scanning Electron Microscopy

The imaging in a scanning electron microscope (SEM) results from the interaction of a primary electron beam with the near-surface atoms of the sample. Secondary electrons (SE) and back scattered electrons (BSE) are detected, leading to different contrasts. Additionally, a reasonable analysis of the chemical composition is possible using Electron dispersive X-ray spectroscopy (EDX). A detailed description of the principles of a SEM and the working principles of the detectors can be found elsewhere [168].

In this work, microstructural analysis and analysis of the fracture surfaces of the samples are conducted by field emission scanning electron microscopy (Zeiss NT Ltd. Sigma VP). EDX was used to determine the compositions of crystalline and amorphous phases. Therefore, especially partially crystalline as-cast samples, in which the primary crystals are frozen-in in an amorphous matrix, are analyzed in order to confirm the identifications done by the analyzes of the diffraction pattern.

3.4 Mechanical Properties

The elastic and plastic deformation behavior of the different alloying systems are analyzed using three-point flexural beam bending tests, which are carried out with a Shimadzu testing machine at a deflection rate of 0.3 mm/min and a support span of L = 15 mm. Under bending load, the formation of a single catastrophic shear band is prevented, since at the neutral plane of the beam the shear band propagation is stopped and the further deformation results in the formation of new shear bands. The beam-shaped samples for the tests are ground and polished to the appropriate geometry, reducing the influence of the casting surface finish. The strain and stress at the beam surface are calculated according to the Euler–Bernoulli beam theory by

$$\sigma = \frac{3FL}{2bh^2} \tag{3.15}$$

$$\epsilon = \frac{6Dh}{L^2} \tag{3.16}$$

where F is the applied load and b and h are the width and the height of the beam, respectively. D corresponds to the deflection at the center of the beam.

Young's modulus, E, offset yield strength (0.2 %), $\sigma_{yield}^{0.2\%}$, and total flexural strength, σ_{total}, of the novel glass forming compositions are determined as shown in Fig. 3.8. Additionally, the elastic strain limit ϵ_{el}, the fracture strain ϵ_{frac} and the total strain to failure ϵ_{total} are obtained.

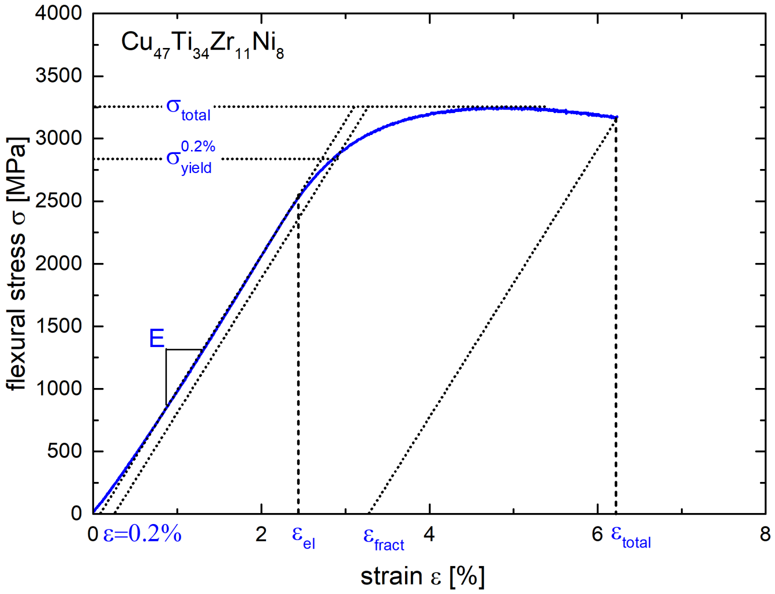

FIGURE 3.8: Experimentally determined engineering stress-strain curve of the bulk glass forming alloy $Cu_{47}Ti_{34}Zr_{11}Ni_8$. The elastic modulus E refers to the slope of the stress-strain curve below the elastic strain limit ϵ_{el}. The yield strength is determined at 0.2 % of plastic deformation ($\sigma_{yield}^{0.2\%}$). Additionally, the total strain to failure ϵ_{total}, the flexural fracture strength σ_{total} and the fracture strain ϵ_{frac} can be determined.

In addition, hardness measurements are conducted using a Wolpert Wilson 930 N universal hardness tester and a Vicker's indenter with a load of 49.03 N (HV5) for selected alloys in each alloying system. The size of the hardness indents is analyzed with an Olympus BH-2 optical microscope.

Poisson's ratio ν is measured using an Olympus 38DL Plus ultrasonic thickness gauge. Therefore, the longitudinal and shear wave velocities are determined according to

$$V = \frac{d}{t_{trans}/2} \tag{3.17}$$

where V are the longitudinal or the shear sound velocity, d the sample thickness and t_{trans} the round trip transition time.

From the transversal and longitudinal shear velocities, Poisson's ratio ν can be calculated by

$$\nu = \frac{1 - 2(V_T/V_L)^2{}^2}{2 - 2(V_T/V_L} \tag{3.18}$$

where V_T and V_L are the shear and the longitudinal wave velocity, respectively. For an accurate measurement of ν the samples are grind to a plane parallel shape. The volumetric mass densities ρ, which are determined by Archimedes measurements, are used to calculate Young's modulus according to

$$E = \frac{V_L^2 \rho (1 + \nu)(1 - 2\nu)}{1 - \nu}. \tag{3.19}$$

3.5 Electrochemical Characterization

The corrosion behavior of novel Ti- and Zr-based alloys is characterized using a custom built three-electrode electrochemical flat cell, which is connected to a Zahner IM6ex electrochemical testing system. A platinum foil and a saturated calomel electrode (SCE) are taken as counter and reference electrode, respectively. The surface area of the samples, being in contact with the electrolyte, is 1.13 cm^2, corresponding to 12 mm in diameter. Analytical-grade reagents and single distilled water are used for the synthesis of a borate buffered solution ($H_3BO_3[0.3M], Na_2B_4O_7 - \Delta 10 H_2O[0.075M]$) with 0.1 M NaCl (pH 8.4). The experiments were conducted at ambient conditions in a Faraday cage with a voltage scan rate of 0.17 mV/s. In Fig. 3.9 the polarization curve of the Ti-based bulk metallic glass forming alloy $Ti_{50}Zr_{25}Cu_{17}S_8$ is shown. In the first step, the potential was continuously increased up to 1.4 V. At roughly -0.37 V (E_{corr}), the change from an anodic to a cathodic behavior can be observed, which is manifested by a singularity. A further increase of the voltage results in the formation of a passive layer and thus, a passive region with a nearly constant current (i_{pass}). At around 1 V an increasing current is observed, which can be attributed to a decreasing stability of the passive layer or rather a charge transport (E_{break}). In the second step the potential is decreased again in order to investigate the re-passivation behavior. In the "down" scan another singularity can be observed at 0.35 V, which is attributed to the reconstruction of the passive layer on the sample surface (E_{pp}), being connected to a change to an anodic behavior.

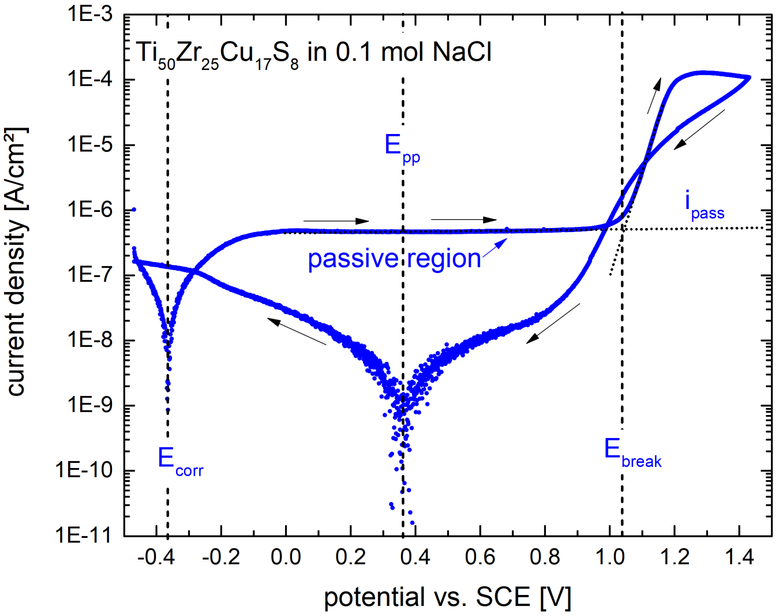

FIGURE 3.9: Experimentally determined dynamic polarization curve of a Ti-based bulk metallic glass. When sweeping up the potential from a negative value, the behavior changes from anodic to cathodic behavior at E_{corr}. At roughly -0.1 V the system reaches a passive region at which i_{pass} is constant. A further increase of the voltage results in a breakdown of the passive layer for electron transport at E_{break}. Here, the current increases by about two orders of magnitude. After decreasing the voltage again, at about 0.35 V (E_{pp}) the sample is re-passivated due to the reconstruction of a stable passivation layer.

Chapter 4

Development and Processing of Sulfur-Bearing Bulk Metallic Glasses

This chapter deals with the results of the development of new bulk metallic glasses containing sulfur as key element. First of all, sulfide systems are reviewed and different rules for the selection of relevant sulfide systems, in which glass formation can be suggested, are proposed. Subsequently, the findings about glass formation in the ternary Pd-Ni-S and the quinary Ti-Zr-Ni-Cu-S system are presented. Additionally, the influence of higher amounts of oxygen is evaluated for the novel developed Ti-based alloys and a completely new die-casting process is designed for the processing of bulk metallic glasses.

4.1 Sulfur in Metallic Systems

Sulfur (S) is a non-metallic element and belongs to the group of chalcogens (O, S, Se, Te, Po). It occurs inter alia as metal sulfide (sulfur-metal compound) and is one of the most common elements on earth. In general, metal sulfides can be divided in three different types regarding their binary phase diagrams [169]:

1. type-1 binary sulfide systems are characterized by two liquid immiscibility fields, one on the metal-rich side and one on the sulfur-rich side, which are separated by a congruently melting binary compound (Fig. 4.1a).

2. type-2 binary sulfide systems show a deep eutectic at the metal-rich side of the phase diagram and have one liquid immiscibility field at the sulfur-rich side. The eutectic reaction and the immiscibility gap are separated by a congruently melting binary compound (Fig. 4.1b).
3. type-3 binary sulfide systems display one liquid immiscibility field at the metal-rich side and an eutectic reaction in the compositional space between the immiscibility gap and a congruently melting phase (Fig. 4.1c).

In particular, the type-2 binary systems are of certain interest for the development of novel bulk glass forming alloys, since at the deep eutectic the metallic liquid is stabilized in comparison to the crystalline structure (see section 2.2.1). Moreover, sulfur has a small atomic diameter of 103 pm, which is close to the value of phosphorous (102 pm) [86]. Thus, the addition of sulfur to metallic liquids might result in an increase of the packing density, leading to more sluggish kinetics and a higher GFA (see section 2.2.1).

As already pointed out in section 3.1, the processing of sulfur is less complicated in comparison to the processing of P, which is a common constituent in BMGs, since S has no toxic modification. S has a stable liquid phase at ambient pressure, strongly reducing the evaporation during alloying. However, so far sulfur was not considered as potential element in metallic glass forming alloys, although it is well known in other disciplines in materials science.

Besides the general rules for the selection of promising compositions for the design of metallic glass forming alloys (see section 2.2.1), possible constituents for sulfur-bearing metallic glass forming alloys are identified according to the following two criteria:

1. The binary phase diagrams of the constituents are of type-1 or type-2 according to Ref. [169].
2. The alloys contain at least one element, which can be processed together with S in a silica tube such as Fe, Co, Ni, Cu or Pd.

On the basis of these rules, more than 500 different compositions have been produced in the frame of this work and several novel bulk glass forming compositions have been discovered. In the following sections, some metallic systems, in which glass formation is observed, are presented.

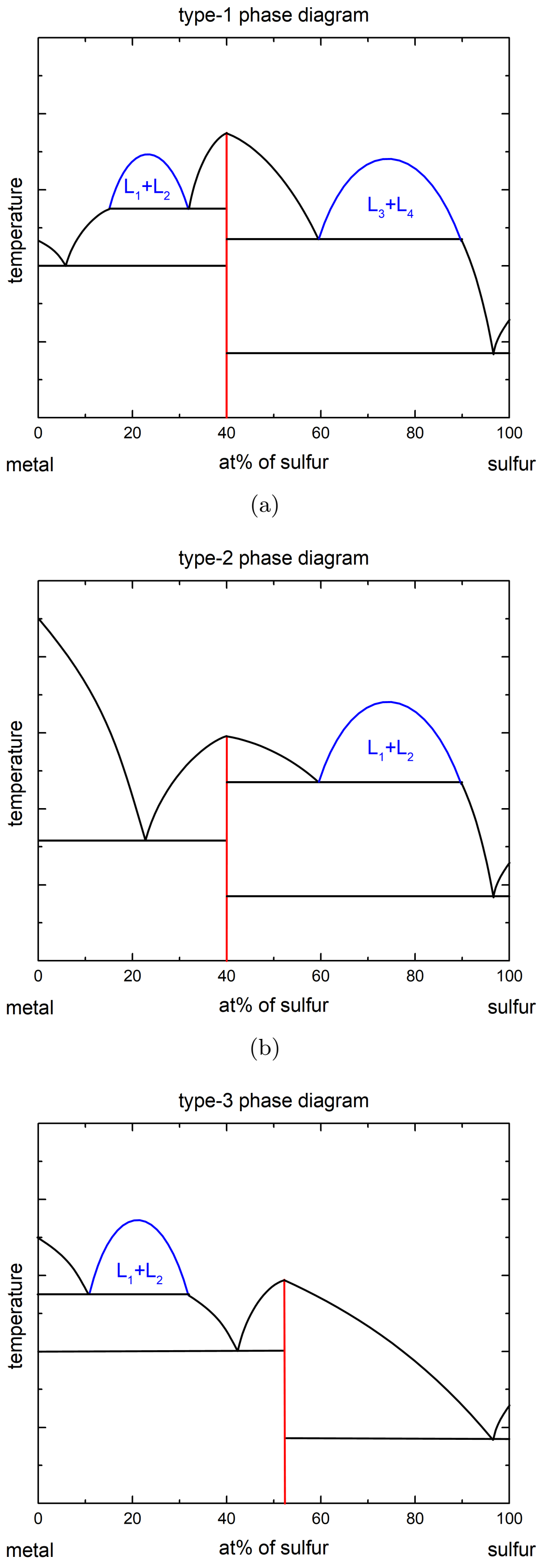

(a)

(b)

(c)

FIGURE 4.1: a) Type-1 binary sulfide phase diagram. b) Type-2 binary sulfide phase diagram. c) Type-3 binary sulfide phase diagram. In the style of Ref. [169]. To simplify the diagrams, no solubility of the respective other element is assumed for the solid solutions and the intermetallic compound is assumed to be stoichiometric.

4.2 The Ternary Pd-Ni-S System

Among all ternary bulk metallic glass former, the best glass forming alloys are found in the ternary Pd-Ni-P system, with critical casting diameters of several centimeter [170–173]. The Pd-Ni-P system fulfills the criteria proposed by Inoue (see section 2.2.1), since the enthalpies of mixing are highly negative (for the main constituents Pd and P), the atomic diameters vary by more than 12 % and the GFA can further be tuned by the addition of further elements [26]. As already mentioned, S has a similar atomic diameter as P. Furthermore, Pd as well as Ni do not react with silica tubes (low affinity to Si and O) and show deep eutectics with sulfur. Hence, both elements are suitable for the alloying procedure described in section 3.1 and fulfill the two criteria proposed in section 4.1. It is for this reason, that the ternary Pd-Ni-S system is the first alloying system that is selected for an in-depth investigation in this work.

In Fig. 4.2 the binary Ni-S and Pd-S phase diagrams are shown (type-2 phase diagrams according to Ref. [169]), exhibiting deep eutectics at roughly 33 at% and 28 at% of sulfur [174–176], where the liquid phase is stabilized down to roughly 913 K and 898 K, respectively. These temperatures are far below the melting points of pure Pd ($T_m(Pd) =$ 1828 K) and Ni ($T_m(Ni)$ = 1728 K). Pd and Ni show a complete range of liquid and solid solution in the binary phase diagram [177]. Thus, in comparison to the Ni-P and Pd-P systems, where the eutectic reactions are located at roughly 20 at% of P (16/18 at% and 1051 K for Pd-P [178] and 19 at% and 1164 K for Ni-P [179]), the eutectic reactions in the sulfur-containing systems are located at higher S-contents. This shift might be explained by the difference in the electronegativities and valency between S and P, since the existence and positions of eutectics is not only influenced by the atomic diameters but also by the distribution of the electronegativities and valency [12, 180].

However, as a starting point for the preparation of samples and the development of novel bulk metallic glasses, compositions in the range of 20 to 36 at% S and 20 to 59 at% Pd are synthesized. According to Ref. [182], the corresponding alloys are found to be in the three phase field of the binary phases Ni_3S_2 - Pd_4S - (Ni,Pd) or in the two phase field Ni_3S_2 - Pd_4S (Fig. 4.3). Hence, these crystalline phases are expected to compete with glass formation and restrict the GFA and GFR. The primary precipitating phases are identified in section 5.1.3.

In a first step, samples with a thickness of 300 μm are cast in order to evaluate the processing route (Fig. 3.1) and to determine the GFR or rather observe whether glass formation takes place in this alloying system. The alloys are characterized by DSC measurements up to 873 K in alumina pans (Fig. 4.4, Tab. 4.1, Tab. 5.2). Because of the low liquidus temperature [182], it is possible to determine the glass transition temperature,

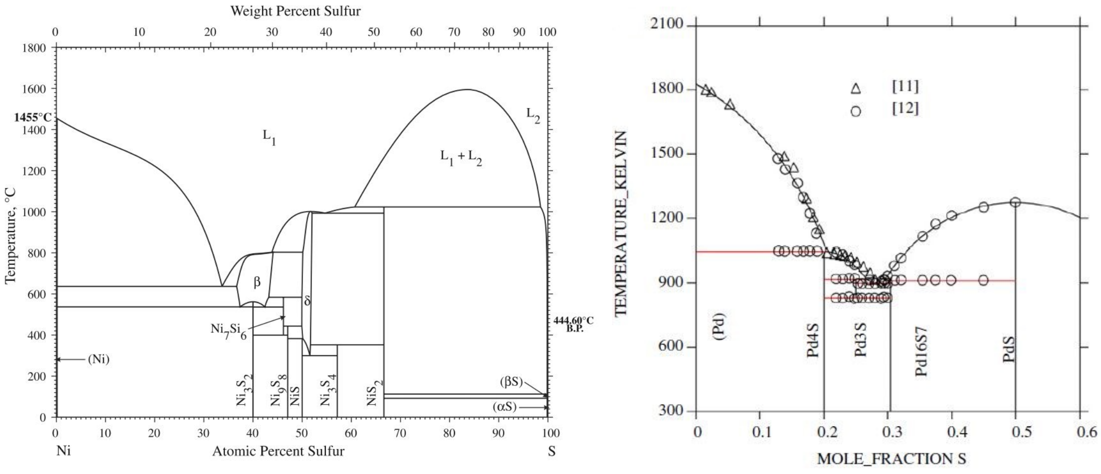

(a) (b)

FIGURE 4.2: a) Binary phase diagram of nickel and sulfur (type-2 - see section 4.1). A deep eutectic reaction can be observed at the metal-rich side at about 33 at% of sulfur. Taken from Ref. [181]. b) Binary phase diagram of palladium and sulfur. A deep eutectic reaction can be observed at the metal-rich side at about 29 at% of sulfur. Taken from Ref. [176].

the crystallization events and the melting behavior in one step in a DSC. The results are shown in Fig. 4.4a and b for alloys with an equal Pd to Ni ratio ($Pd_{32+\frac{x}{2}}Ni_{32+\frac{x}{2}}S_{36-x}$-axis in Fig. 4.3) and alloys with a constant S-content of 27 at% ($Pd_{40.5-x}Ni_{32.5+x}S_{27}$-axis in Fig. 4.3), respectively. Alloys within the GFR (Fig. 4.3) show a pronounced glass transition followed by different crystallization events. The reduced glass transition temperature (t_{rg} - see section 2.2.1) is about 0.58 in this compositional region and changes only slightly with composition. By integration of the crystallization and melting peaks the characteristic enthalpies can be determined (see section 3.2.1.1). The ratio between the enthalpy of crystallization upon heating ΔH_x and the enthalpy of fusion ΔH_f is about 0.5, indicating a fast decrease of the enthalpy from the equilibrium liquid to the glassy state. From ΔH_f, the entropy of fusion ΔS_f can be calculated (equation 2.5), yielding information about the driving force for crystallization $\Delta G^{l-x}(T)$ at small undercoolings. The values range from 13.3 to 14.9 kJ g-$atom^{-1}$ K^{-1} and are rather high for a bulk glass forming system.

The GFR for 300 μm samples is determined to be in a sulfur-range of 24 to 30 at% and a nickel-range of 32 to 50 at%. These results are summarized in Fig. 4.3. Empty circles correspond to samples with a crystalline proportion according to XRD measurements, whereas amorphous samples (filled circles) show no sharp Bragg diffraction peaks in XRD measurements. In Fig. 4.5a XRD pattern of some glassy alloys are shown. The maximum critical diameter achieved by copper mold casting is determined to be 2 mm for the $Pd_{37}Ni_{37}S_{26}$ alloy.

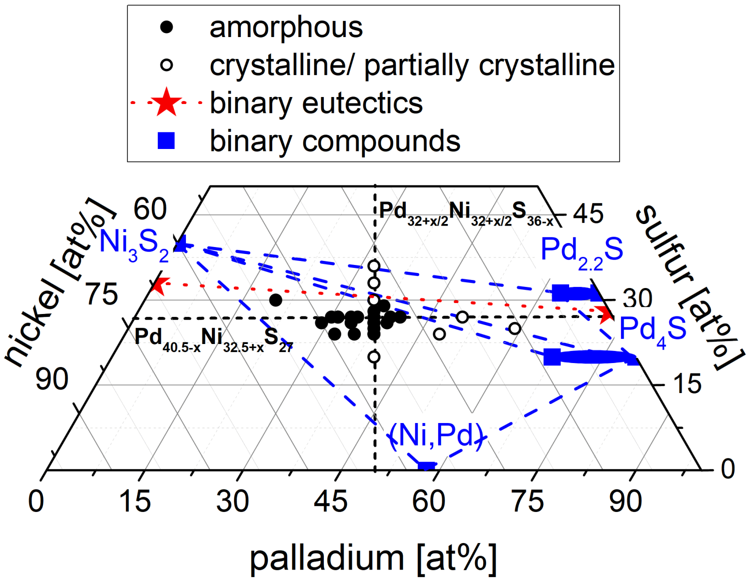

FIGURE 4.3: Glass forming region (GFR) in the ternary Pd-Ni-S system. The open circles correspond to partially or fully crystalline samples, whereas the filled circles represent fully amorphous samples with a thickness of 300 μm. The dashed blue lines mark the equilibrium phase fields at 673 K according to Ref. [182]. Furthermore, the $Pd_{32+\frac{x}{2}}Ni_{32+\frac{x}{2}}S_{36-x}$-axis and the $Pd_{40.5-x}Ni_{32.5+x}S_{27}$-axis are displayed as black dashed lines. Figure and figure caption are adapted from Ref. [8].

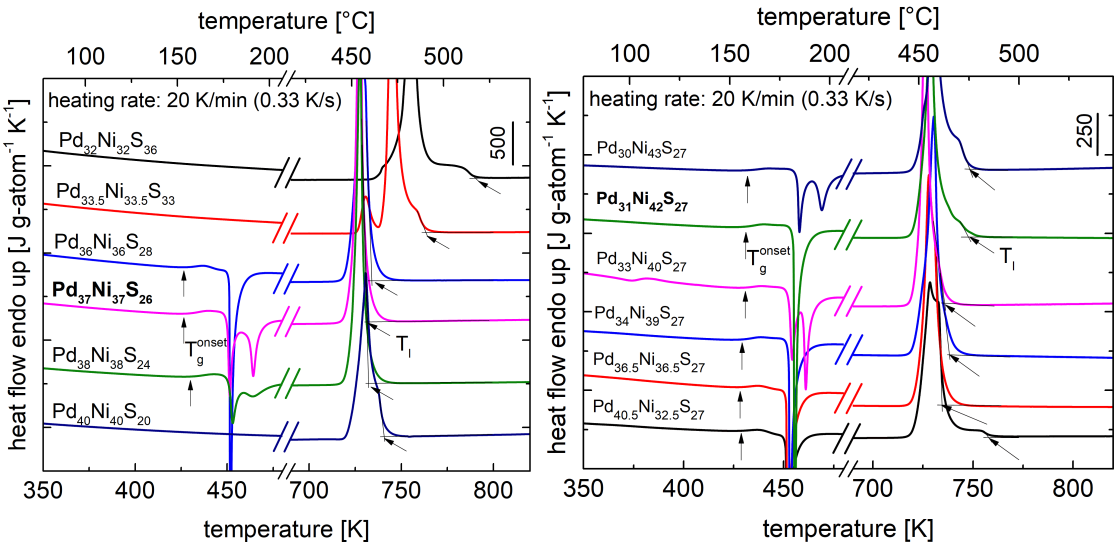

(a)

(b)

FIGURE 4.4: a) DSC measurements with a heating rate of 0.33 K/s of alloys on the $Pd_{32+\frac{x}{2}}Ni_{32+\frac{x}{2}}S_{36-x}$-axis. The glass transition temperature T_g and the liquidus temperature T_l are indicated. Adapted from Ref. [8]. b) DSC measurements with a heating rate of 0.33 K/s of alloys on the $Pd_{40.5-x}Ni_{32.5+x}S_{27}$-axis. The glass transition temperature T_g^{onset} and the liquidus temperature T_l are indicated.

The best compromise between the thermal stability or rather the extend of the SCLR (ΔT_x (0.33 K/s) = 27.2 K - see section 3.2.1.1) and the GFA is found for the $Pd_{31}Ni_{42}S_{27}$ alloy (Fig. 4.5b), showing a critical diameter of 1.5 mm (Fig. 4.5a). ΔT_x is of certain interest for the measurement of the thermo-physical properties of the deeply undercooled liquid, which are shown in section 5.1. A high energy synchrotron X-ray pattern of a 0.75 mm rod of $Pd_{31}Ni_{42}S_{27}$ is shown in the inset in Fig. 4.5b, clearly proving the amorphous structure of the sample.

In summary, several novel bulk glass forming alloys have been produced in the ternary Pd-Ni-S system. Hence, sulfur is shown to be a possible constituent in metallic glass forming compositions. Later in this work, the particular $Pd_{31}Ni_{42}S_{27}$ alloy is characterized regarding its thermo-physical and mechanical properties, which are both in turn linked to structural changes of the amorphous phase upon cooling. These results are then discussed in the context of the experimentally determined thermal stability and GFA.

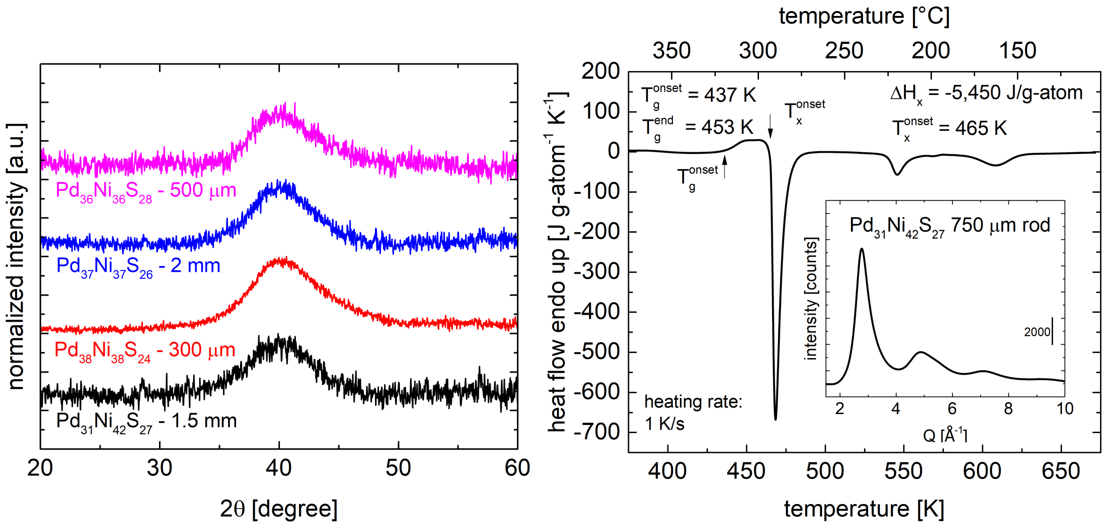

(a)

(b)

Figure 4.5: a) XRD pattern of samples in the Pd-Ni-S with a varying thickness. Taken from Ref. [8]. b) DSC scan of of $Pd_{31}Ni_{42}S_{27}$. The characteristic temperatures and enthalpies are indicated. The inset shows the integrated high energy synchrotron X-ray diffraction pattern of a 0.75 mm rod of $Pd_{31}Ni_{42}S_{27}$. Adapted from Ref. [7].

TABLE 4.1: Characteristic temperatures of different alloys in the Pd-Ni-S system determined by continuous DSC measurements with a heating rate of 0.33 K/s. By subtraction of the onset of the glass transition T_g^{onset} from the onset of crystallization T_x^{onset} the extend of the supercooled liquid region ΔT_x can be calculated. The liquidus temperature T_l and the T_g^{onset} yield the reduced glass transition temperature t_{rg}. T_m corresponds to the solidus temperature. Data taken from Ref. [8].

Alloy Composition $[at\%]$	T_g^{onset} $[K]$	T_x^{onset} $[K]$	T_m $[K]$	T_l $[K]$	ΔT_x $[K]$	t_{rg}
$Pd_{32}Ni_{32}S_{36}$	—	—	752.2	789.9	—	—
$Pd_{33.5}Ni_{33.5}S_{33}$	—	—	726.6	763.1	—	—
$Pd_{36}Ni_{36}S_{28}$	425.9	438.9	721.1	734.2	13.0	0.580
$Pd_{37}Ni_{37}S_{26}$	425.9	449.2	721.7	730.8	23.3	0.582
$Pd_{38}Ni_{38}S_{24}$	428.8	450.7	721.8	732.5	21.9	0.586
$Pd_{40}Ni_{40}S_{20}$	—	—	723.3	744.0	—	—
$Pd_{31}Ni_{42}S_{27}$	429.8	457.0	725.5	756.0	27.2	0.569

TABLE 4.2: Enthalpy of crystallization ΔH_x and entalpy of fusion ΔH_f of different alloys in the Pd-Ni-S system measured with a heating rate of 0.33 K/s. Using equation 2.5, the entropy of fusion ΔS_f can be calculated from ΔH_f. D_c corresponds to the critical diameter of a sample to achieve an X-ray amorphous structure. Data taken from Ref. [8].

Alloy Composition $[at\%]$	ΔH_x $[kJ$ g-$atom^{-1}]$	ΔH_f $[kJ$ g-$atom^{-1}]$	ΔS_f $[kJ$ g-$atom^{-1}$ $K^{-1}]$	d_c $[mm]$
$Pd_{32}Ni_{32}S_{36}$	—	13.1	16.6	—
$Pd_{33.5}Ni_{33.5}S_{33}$	—	12.9	16.9	—
$Pd_{36}Ni_{36}S_{28}$	6.0	10.9	14.9	0.3
$Pd_{37}Ni_{37}S_{26}$	5.8	10.4	14.2	2
$Pd_{38}Ni_{38}S_{24}$	5.1	9.7	13.3	0.3
$Pd_{40}Ni_{40}S_{20}$	—	8.1	10.7	—
$Pd_{31}Ni_{42}S_{27}$	5.5	11.1	14.7	1.5

4.3 The Quasi-ternary Ti-(Zr)-Ni-(Cu)-S System

4.3.1 The Ternary Ti-Ni-S System

Ti-based alloys are of great interest for many fields of application, due to the low density of Ti in combination with the extraordinary mechanical properties and corrosion resistance [183]. In case of the binary Ti-S system, another promising phase diagram can be found (Fig. 4.6a). Here, a eutectic reaction is observed at a S-content of 14 at% and 1485 K. Indeed, the eutectic temperature is much higher in comparison to the Ni-S and Pd-S system, but still rather low for the Ti-rich side of a binary system. However, the alloying of pure Ti and pure S in a silica tube is impeded by the high affinity of Ti to O and Si and the processing of S in an arc furnace is not possible due to the low boiling point. It is for this reason, that an element such as Ni or Pd has to be added to the Ti-S system, which is suitable for the production of a sulfide pre-alloy that can be used in an arc furnace. Pd has a high mass density (11.99 gcm^{-3}) and is rather expensive and thus, its use is not expedient in a Ti-based alloy, which is aimed to be used as structural material. In contrast, Ni is already well known in crystalline Ti-alloys (such as shape memory alloys like TiNi), being less expensive and having a significantly lower mass density (8.91 gcm^{-3}). Furthermore, the binary Ti-Ni system is well known as a starting point for the alloy development of glass forming compositions, since Ni shows a smaller atomic diameter than Ti (r_{Ti}=142 pm; r_{Ni}=128 pm) [86], a highly negative heat of mixing with Ti (ΔH_{mix}^{Ni-Ti}= -35 kJ mol^{-1}) [184]) and the binary phase diagram displays a very deep eutectic at 25 at% Ni of 1215 K (Fig. 4.6b).

In the binary Ti-Ni system, the formation of amorphous phases was observed in the range of 28-50 at% Ni, using the melt spinning technique (sample thickness of a few micrometers)[188]. However, due to the formation of the solid solution or binary, (cubic) intermetallic compounds such as Ti_2Ni, the GFA of Ti-rich alloys is strongly limited in these binary systems. In the past, further elements (e.g. Cu, Si, B, Be, Al, Sn) were added in order to increase the confusion, suppress for the formation of the crystalline phases [189] and increase the packing density of the liquid phase [26], leading to a higher GFA. The best ternary glass formers are found to be in the Ti-Ni-Si [190], Ti-Ni-Al [191], Ti-Ni-Sn [192], Ti-Ni-Cu [193] and Ti-Fe-Si systems [194]. So far, S has not been added to the binary Ti-Ni system to increase the GFA in this alloying system. On this account, the ternary Ti-Ni-S system is chosen as starting point for the alloy synthesis. The ternary phase diagram of Ti-Ni-S or rather its liquidus projection is not available to identify the possible GFR.

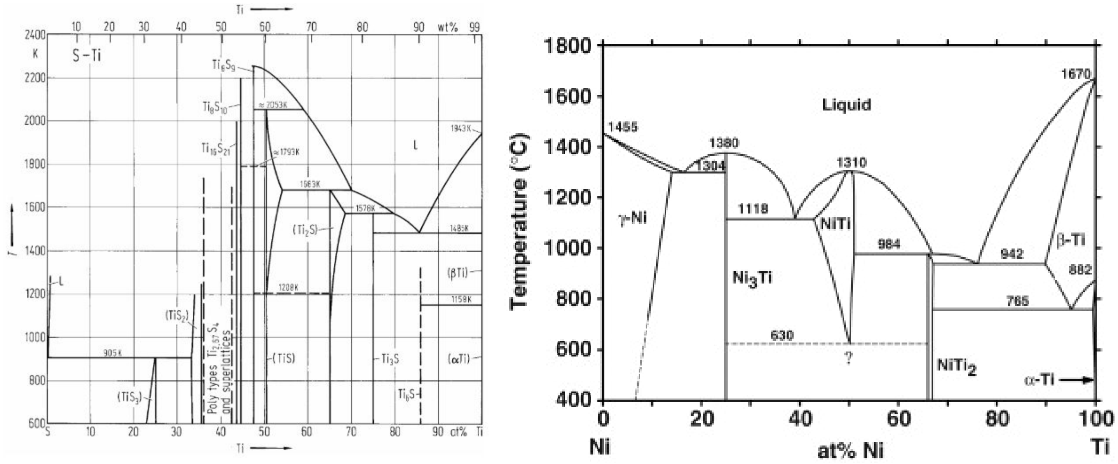

(a) (b)

Figure 4.6: a) Binary phase diagram of titanium and sulfur (type-2 - see section 4.1). A deep eutectic reaction can be observed at the metal-rich side at about 14 at% of sulfur. Taken from Ref. [185]. b) Binary phase diagram of titanium and nickel. A deep eutectic reaction can be observed at the Ti-rich side at about 25 at% of nickel. Taken from Ref. [186].

For the determination of the GFR, 500 μm samples have been produced in the range of 0 to 15 at% of sulfur and 60 to 80 at% Ti, which are analyzed using XRD and DSC. In Fig. 4.7, the compositions that are produced and characterized in the ternary system, the binary intermetallic compounds from the binary equilibrium phase diagrams as well as the GFR are illustrated. The empty circles and the half filled circles correspond to crystalline and partially crystalline samples, respectively. The green diamond marks the composition of an X-ray amorphous sample. Partially crystalline samples show crystallization events upon heating in DSC, but also sharp diffraction peaks in XRD, which correspond to crystalline proportions. The DSC and XRD measurements of alloys on the $Ti_{75}Ni_{25-x}S_x$-axis (x = 5, 6, 7, 8, 9.5, 11) and the $Ti_{70+x}Ni_{23-x}S_7$-axis (x = 2.5, 5, 7.5, 10) are shown in Fig. 4.8 and Fig. 4.9. It is evident, that the alloys do not display a pronounced glass transition temperature, but for some alloys several exothermic events can be observed upon heating. As already mention, a proper identification of amorphous phases is only possible in combination with XRD measurements. The introduction of S for Ni in the binary $Ti_{75}Ni_{25}$ alloy results in the destabilization of the binary intermetallic compound Ti_2Ni and the formation of an icosahedral phase at sulfur contents of more than 5 at% of S (Fig. 4.9a). The formation of such an icosahedral phase was proven by different authors in Ti-Ni alloys upon rapid quenching [195–198]. Here, the icosahedral phase shows the same signature in X-ray diffraction patterns. For the alloy $Ti_{75}Ni_{17}S_8$ no Bragg diffraction peaks are observed in the XRD pattern, proving the amorphous nature of the structure. Higher amounts of sulfur lead to the formation of new crystalline phases upon rapid quenching. Additionally, the Ni to Ti ratio is changed

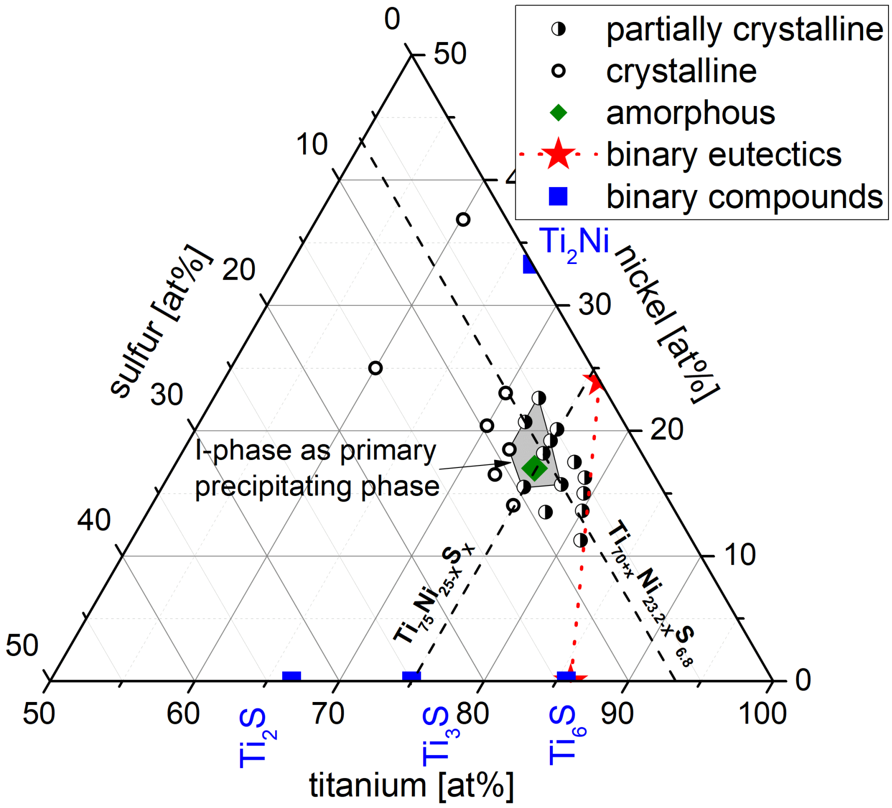

FIGURE 4.7: Glass forming region (GFR) in the ternary Ti-Ni-S system. The open circles correspond to crystalline and the half filled circles to partially amorphous samples with thickness of 500 μm. The green diamond highlights the composition $Ti_{75}Ni_{17}S_8$, where a X-ray amorphous sample with 500 μm is obtained by copper mold casting. The blue squares mark the binary equilibrium phases obtained from the phase diagrams in Ref. [185] and [187]. The binary eutectics are highlighted with red stars and the red dashed line is used to guide the eye. Additionally, the $Ti_{75}Ni_{25-x}S_x$-axis and the $Ti_{70+x}Ni_{23-x}S_7$-axis, which are shown in Fig. 4.8 and Fig. 4.9, are displayed as black dashed lines. Adapted from Ref. [9].

at a sulfur-content of 7 at% in order to investigate the influence on the GFA. A change of this ratio does not prevent the formation of the Bragg peaks in the X-ray pattern. Hence, this ratio does not result in a higher GFA. Finally, the $Ti_{75}Ni_{17}S_8$ alloy exhibits with a critical diameter of 500 μm the highest GFA in the ternary Ti-Ni-S system. These results are verified using high energy synchrotron X-ray radiation in transmission (inset in Fig. 4.10a). In samples with a thickness of 750 μm of $Ti_{75}Ni_{17}S_8$, which is slightly above its critical casting thickness, the formation of a complex crystalline mixture of inter alia Ti_2Ni and an icosahedral phase can be observed (Supp. Fig. A.1). Thus, a clear identification of the primary phase, restricting glass formation is not possible at this point. The crystallization processes of the quinary alloys is investigated and discussed in detail in section 5.2.3 and section 6.2.2.

In Fig. 4.10b a DTA measurement at a rate of 0.33 K/s of initially amorphous $Ti_{75}Ni_{17}S_8$ is shown. The sample is first heated up to 1400 K and subsequently cooled down to 973

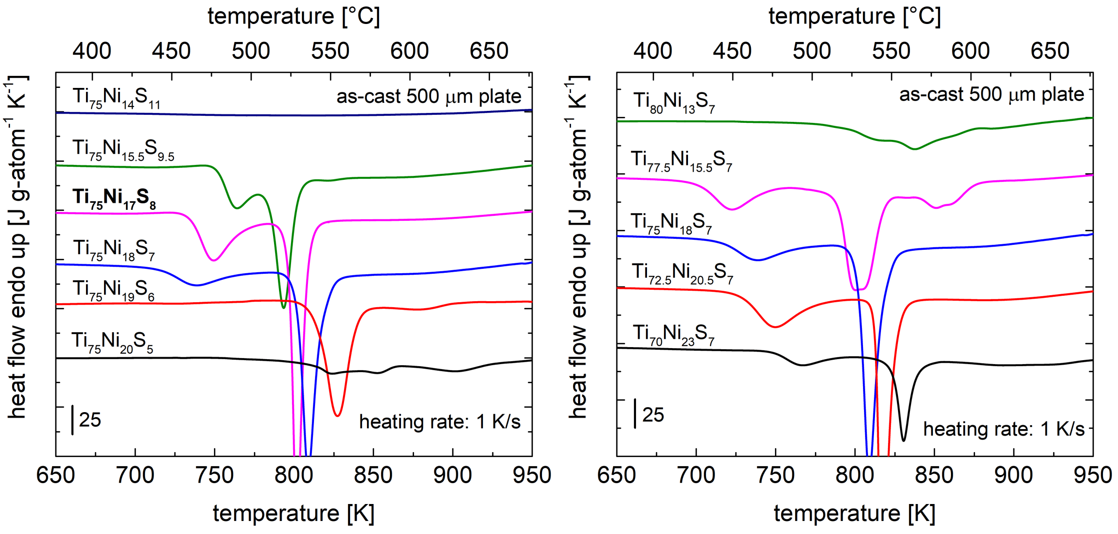

(a) (b)

FIGURE 4.8: a) DSC measurements with a heating rate of 1 K/s of 500 μm plates of alloys on the $Ti_{75}Ni_{25-x}S_x$-axis. b) DSC measurements with a heating rate of 1 K/s of 500 μm plates of alloys on the $Ti_{70+x}Ni_{23-x}S_7$-axis. Both figures are adapted from Ref. [9].

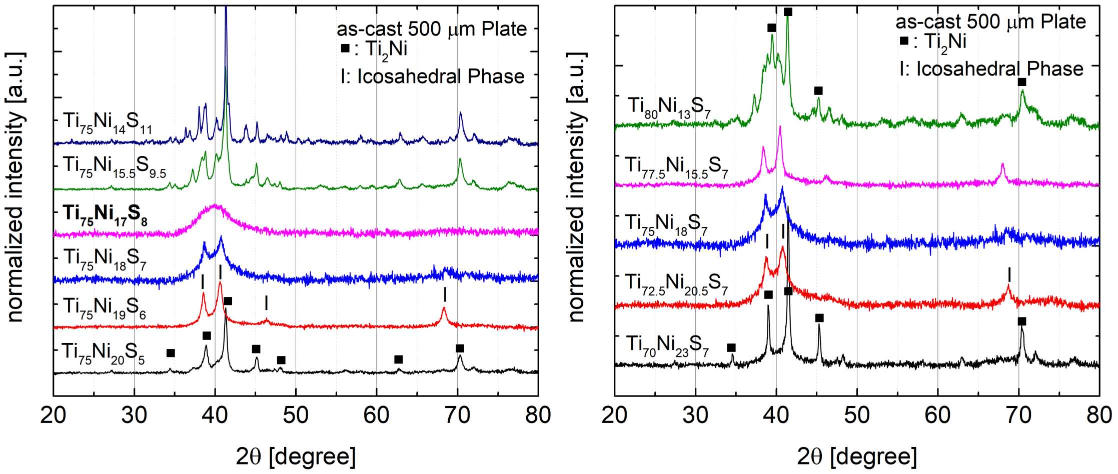

(a) (b)

FIGURE 4.9: a) XRD pattern of samples on the $Ti_{75}Ni_{25-x}S_x$-axis with a thickness of 500 μm. The crystalline diffraction peaks of some compounds are indicated. b) XRD pattern of samples on the $Ti_{70+x}Ni_{23-x}S_7$-axis with a thickness of 500 μm. The crystalline diffraction peaks of some compounds are indicated. Both diagrams are adapted from Ref. [9].

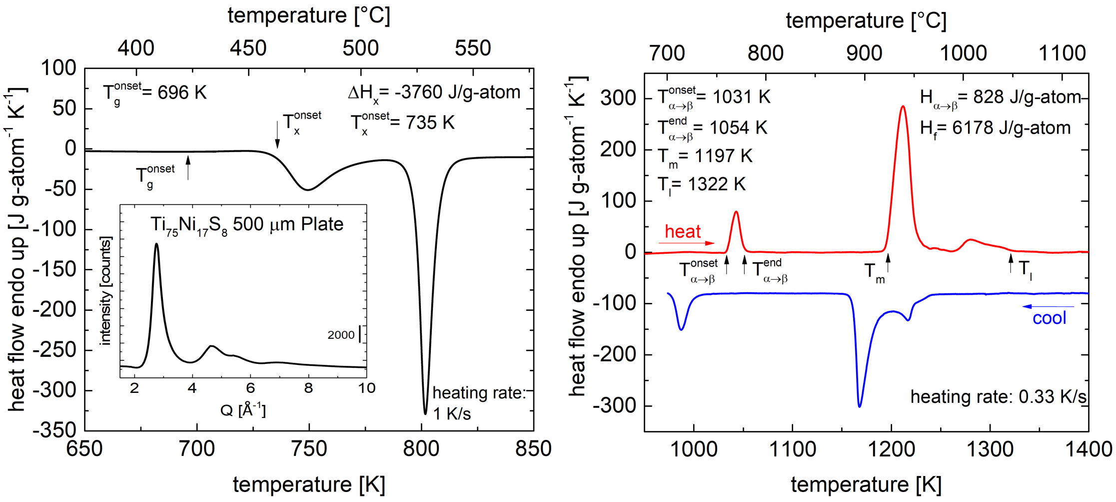

(a) (b)

FIGURE 4.10: a) DSC trace measured with a heating rate of 1 K/s of a 500 μm plate of $Ti_{75}Ni_{17}S_8$. The enthalpy of crystallization ΔH_x and the glass transition temperature T_g^{onset} as well as the onset of crystallization T_x are indicated. The inset shows a high energy synchrotron X-ray diffraction pattern of a 500 μm plate. Adapted from Ref. [7]. b) DTA trace up to 1400 K of initially amorphous $Ti_{75}Ni_{17}S_8$ measured with a heating/ cooling rate of 0.33 K/s. The melting temperature T_m and the liquidus temperature T_l are indicated. Below the melting temperature, an endothermic (exothermic) experiment can be observed upon heating (cooling), which is suggested to correspond to the $\alpha \leftrightarrow \beta$ transformation of the crystalline solid solution.

K. Upon heating an endothermic event below the solidus temperature can be observed at 1031 K, which is suggested to correspond to the α - β transformation of the crystalline solid solution. This transformation occurs at 1155 K for pure titanium and at 1038 K in the binary Ti-Ni system. Further heating results in the melting of the sample at 1197 K (T_m), ending at 1322 K (T_l). Upon cooling a two step crystallization process can be observed at an undercooling of roughly 100 K, followed by the β - α transformation. The rather high melting interval results in a low value of t_{rg} of 0.53, if the slight kink in the heat flow in Fig. 4.10 is allocated to the glass transition temperature ($T_g^{onset}(1K/s) = 696K$).

In summary, a maximum critical diameter of 500 μm is observed for the $Ti_{75}Ni_{17}S_8$ alloy, having a low thermal stability upon heating from the glassy state and a relatively high liquidus temperature.

4.3.2 Ti-based Alloys in the Ti-Zr-Cu-Ni-S system

In order to increase the GFA of the ternary $Ti_{75}Ni_{17}S_8$ alloy, additional elements are added. As already discussed in section 2.2.1, a higher number of elements can result in a higher GFA. The first additional element that is selected is Cu. Cu has a nearly equal atomic diameter as Ni (r_{Cu} = 127 pm; r_{Ni} = 128 pm) [86] and displays an almost neutral enthalpy of mixing with Ni (ΔH_{mix}^{Cu-Ni} = 4 kJmol^{-1}) [184]. This is reflected by the formation of a solid solution over the complete compositional range of Cu and Ni. Additionally, Cu shows, like Ni, a negative heat of mixing with Ti (ΔH_{mix}^{Cu-Ti} = -9 kJmol^{-1}) [184]. The binary Cu-S system is a type-1 sulfide system [169], displaying two immiscibility fields, which are departed by fcc digenite (D_g), being the high temperature intermetallic compound $Cu_{2-\delta}S$ with a higher solubility limit for S (Fig. 4.11) [169, 199].

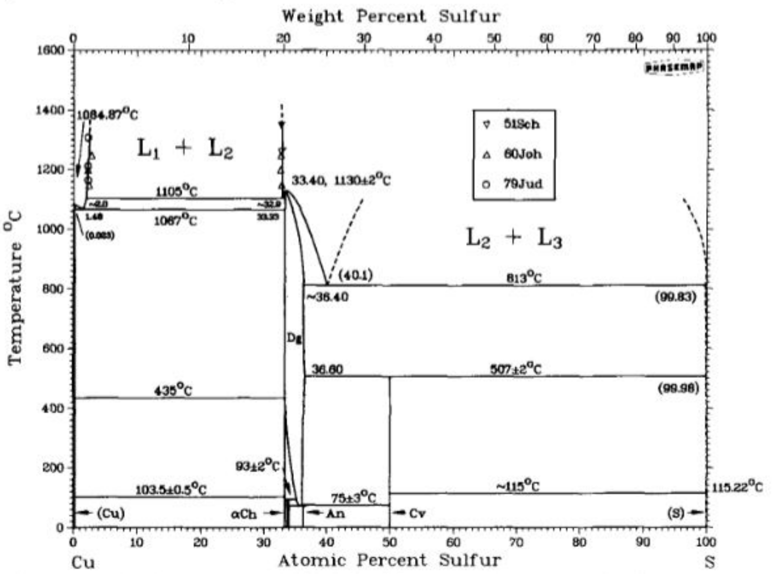

FIGURE 4.11: a) Binary phase diagram of copper and sulfur (type-1 - see section 4.1). Two immiscibility fields in the liquid phase can be observed at the metal-rich side and the sulfur-rich side. Taken from Ref. [199].

The influence of the substitution of Ni by Cu is analyzed by DSC measurements of 300 μm plates (Fig. 4.12a) and XRD measurements on 500 μm plates (Fig. 4.12b). The addition of Cu leads to an increasing thermal stability, which is manifested by a pronounced glass transition temperature in DSC measurements and the development of a stable supercooled liquid region for higher Cu contents. The addition of Cu leads to a slight increase of the liquidus and solidus temperature (Fig. 4.13) and decrease of the glass forming ability as can be seen from the XRD measurements of the 500 μm plates (Fig. 4.12b). Thus, the Ni - Cu substitution shows a contrary effect on the thermal stability and GFA.

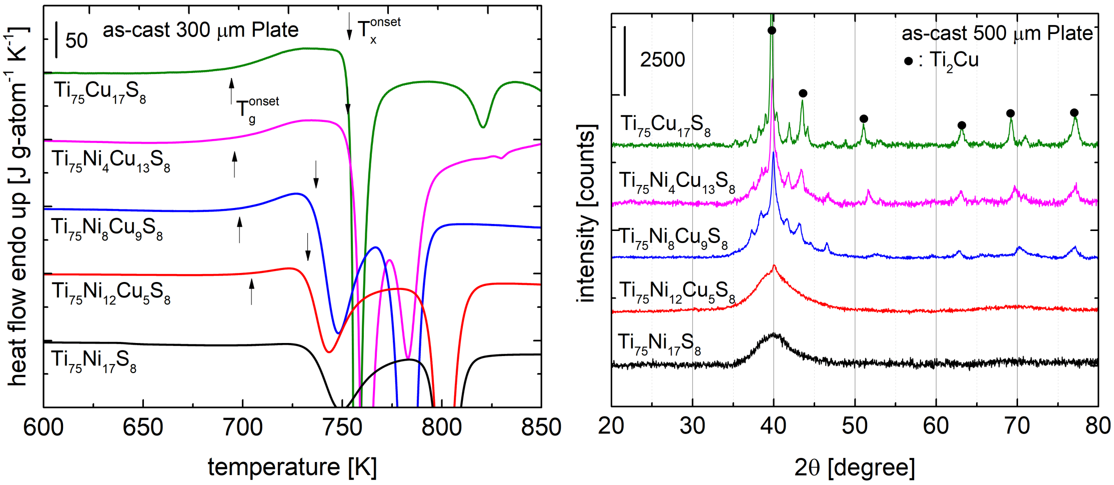

(a) (b)

FIGURE 4.12: a) DSC measurements of $Ti_{75}Ni_{17-x}Cu_xS_8$ (x = 5, 9, 13, 17) at 1 K/s. The onset of the glass transition T_g^{onset} and the onset of crystallization T_x^{onset} are indicated with arrows. b) XRD measurements of $Ti_{75}Ni_{17-x}Cu_xS_8$ (x = 5, 9, 13, 17). The Ti_2Cu phase is indicated with black dots. Both diagrams are adapted from Ref. [9]

An element, which is well known to be a substitute for Ti in bulk glass forming alloys, is Zr [200]. Although the atomic diameter of Zr is higher than that of Ti (r_{Zr} = 158 pm) [86], their binary phase diagram displays the formation of a solid solution over the entire compositional space [201, 202]. Furthermore, the enthalpy of mixing of Ti and Zr is equal to zero among each other (ΔH_{mix}^{Ti-Zr} = 0 kJmol^{-1}) [184], but highly negative with Ni (ΔH_{mix}^{Ni-Ti} = -35 kJmol^{-1}; ΔH_{mix}^{Ni-Zr} = -49 kJmol^{-1}) [184], also indicating a good exchangeability. The binary phase diagram S-Zr is to the knowledge of the author not reported in literature.

Samples with different Zr-contents are produced with a varying casting thickness and are characterized using DSC, DTA and XRD, in order to evaluate the effect on the GFA and thermal stability. At this point only Ti-based alloys are considered. The formation of Zr-based BMGs is shown later in section 4.3.3. In Fig. 4.13a DSC measurements at a heating rate of 1 K/s of $Ti_{75-x}Zr_xNi_{17}S_8$ (x = 5, 10, 15, 25, 35) alloys are shown. The addition of Zr results in a shift to lower temperatures and a smearing out of the first crystallization event, indicating a lower thermal stability. Melting detection experiments revealed that the liquidus temperature T_l is strongly increased by the substitution of Ti by Zr, whereas the solidus temperature is shifted to lower values. Hence, the melting interval is significantly increased and t_{rg} drops below 0.5 (0.47 for $Ti_{60}Zr_{15}Ni_{17}S_8$). It has to be noted, that the high reactivity of the melts with both, the crucible and the atmosphere, impede the accurate determination of the liquidus temperature T_l and the enthalpy of fusion ΔH_f. However, the critical casting thickness is increased by the substitution of Ti by Zr. At a Zr-content of 35 at% the critical diameter is increased to almost 3 mm (Supp. Fig. A.2). Only a small portion of an icosahedral phase exists besides the amorphous phase as concluded from DSC and XRD measurements (see section 3.2.1.4).

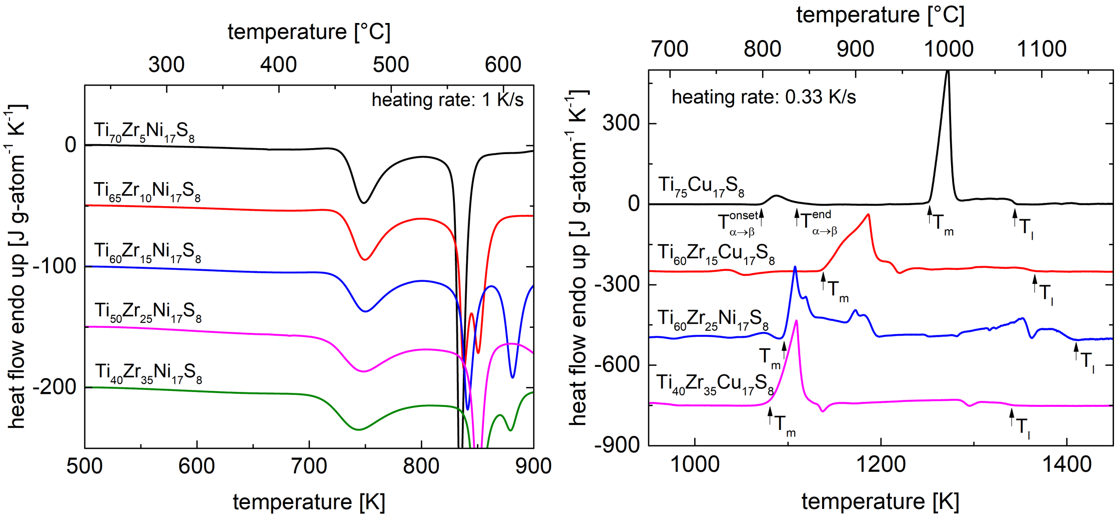

(a) (b)

FIGURE 4.13: a) DSC measurements of $Ti_{75-x}Zr_xNi_{17}S_8$ (x = 5, 10, 15, 25, 35) at 1 K/s. b) DTA measurements of various alloys in the Ti-Zr-Ni-Cu-S system at 0.33 K/s. T_m and T_l as well as the onset ($T^{onset}_{\alpha\to\beta}$) and the end ($T^{end}_{\alpha\to\beta}$) of the $\alpha \leftrightarrow \beta$ transformation are indicated with arrows.

In a next step the simultaneous substitution of Ti and Ni and thus, the extension to a quinary system, is investigated. Therefore, alloys with four different Zr-contents (5, 15, 25, 35 at%) and two different copper contents (5, 17 at%) are analyzed to obtain overall tendencies of the simultaneous substitution (Fig. 4.14a-d). Already small additions of Cu (5 at%) significantly increase the GFA and for a Zr-content of 35 at% X-ray amorphous samples with a diameter of 3 mm can be obtained. The complete substitution of Ni by Cu results in a slight decrease of the GFA for low Zr-contents but for Zr-contents of 25 at% and 35 at% an equal GFA is achieved. Interestingly, the addition of Cu leads again to a stabilization of the undercooled liquid upon heating from the glassy state. Thus, the findings and results from the individual substitution of Ni with Cu and Ti with Zr in the Ti-Ni-S system are also valid in case of a simultanous substitution of Ni and Ti. Moreover it is evident, that the substitution of Ni with Cu in all alloys leads to an increase in ductility, since the Cu-free alloys are highly sensitive to failure during cutting of the samples. The mechanical properties are presented in detail in section 5.2.5.

In summary, quarternary alloys in the Ti-Zr-Cu-S system show the best compromise between GFA and thermal stability. The thermal properties and the GFA are summarized in table 4.3.

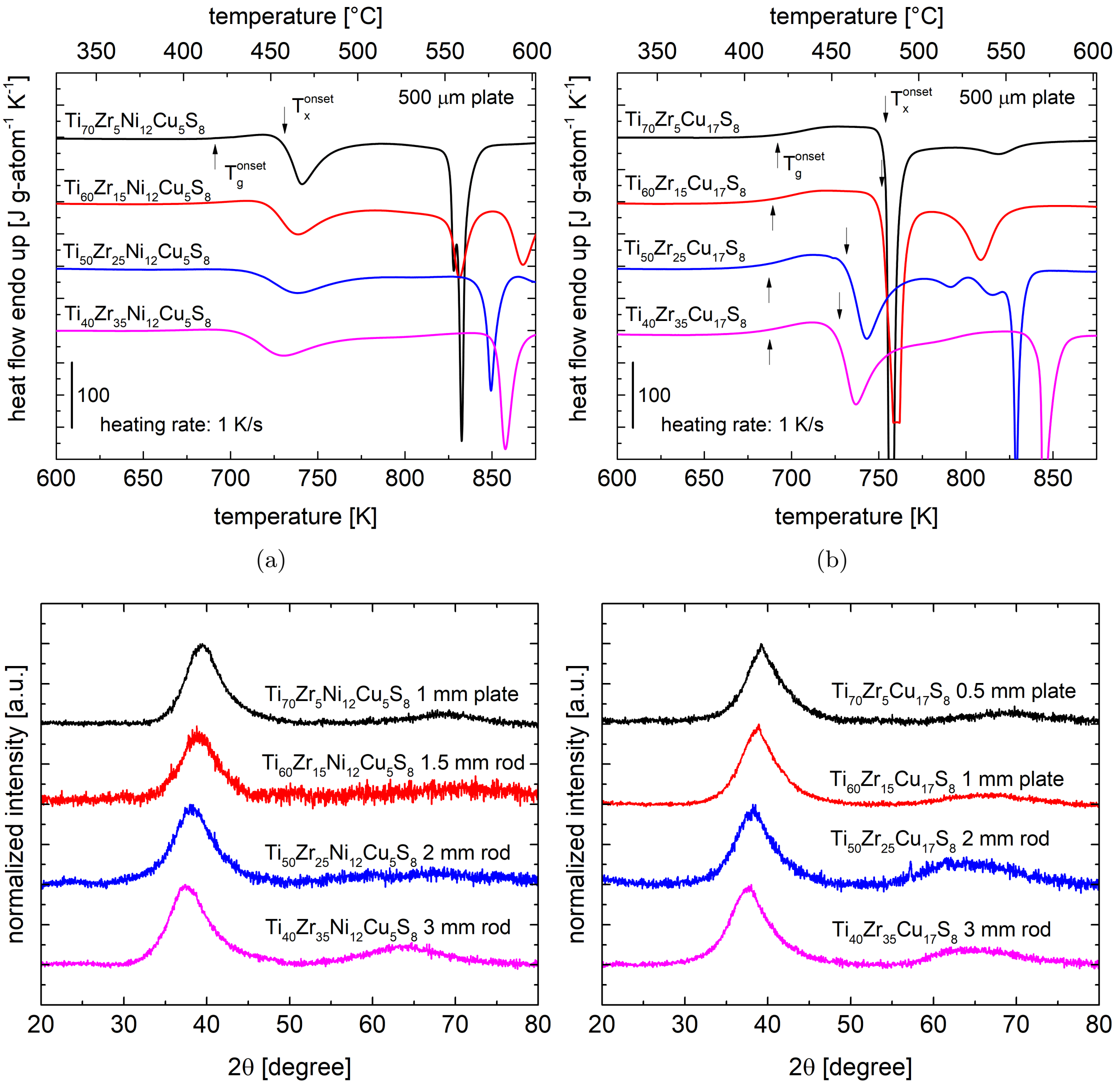

(a) (b)

(c) (d)

FIGURE 4.14: a) DSC measurements of $Ti_{75-x}Zr_xNi_{12}Cu_5S_8$ (x = 5, 15, 25, 35) at 1 K/s. The onset of the glass transition T_g^{onset} and the onset of crystallization T_x^{onset} are indicated with arrows. Adapted from Ref. [7]. b) DSC measurements of $Ti_{75-x}Zr_xCu_{17}S_8$ (x = 5, 15, 25, 35) at 1 K/s. The onset of the glass transition T_g^{onset} and the onset of crystallization T_x^{onset} are indicated with arrows. Taken from Ref. [7]. c) XRD measurements of $Ti_{75-x}Zr_xNi_{12}Cu_5S_8$ (x = 5, 15, 25, 35) with varying diameters. Taken from Ref. [9]. d) XRD measurements of $Ti_{75-x}Zr_xCu_{17}S_8$ (x = 5, 15, 25, 35) with varying diameters. Taken from Ref. [9].

Table 4.3: Characteristic temperatures of different alloys in the Ti-Zr-Ni-Cu-S system determined by continuous DSC measurements with a heating rate of 1 K/s. By subtraction of the onset of the glass transition T_g^{onset} from the onset of crystallization T_x^{onset} the extend of the supercooled liquid region ΔT_x can be calculated. T_m and T_l correspond to the solidus and liquidus temperature measured at 0.33 K/s, respectively. d_c is the critical diameter for which fully amorphous samples can be obtained by copper mold casting. Taken from Ref. [7, 9].

Alloy Composition $[at\%]$	T_g^{onset} $[K]$	T_x^{onset} $[K]$	T_m $[K]$	T_l $[K]$	ΔT_x $[K]$	t_{rg}	d_c $[mm]$
$Ti_{75}Ni_{17}S_8$	—	735	1197	1322	—	—	0.5
$Ti_{75}Cu_{17}S_8$	690	751	1253	1346	61	0.513	< 0.5
$Ti_{70}Zr_5Ni_{17}S_8$	—	730	—	—	—	—	< 1
$Ti_{60}Zr_{15}Ni_{17}S_8$	—	728	1096	1409	—	—	< 2
$Ti_{50}Zr_{25}Ni_{17}S_8$	—	717	—	—	—	—	< 2
$Ti_{40}Zr_{35}Ni_{17}S_8$	—	714	—	—	—	—	< 3
$Ti_{70}Zr_5Ni_{12}Cu_5S_8$	693	729	—	—	36	—	1
$Ti_{60}Zr_{15}Ni_{12}Cu_5S_8$	—	722	—	—	—	—	1.5
$Ti_{50}Zr_{25}Ni_{12}Cu_5S_8$	—	713	—	—	—	—	2
$Ti_{40}Zr_{35}Ni_{12}Cu_5S_8$	—	707	—	—	—	—	3
$Ti_{70}Zr_5Cu_{17}S_8$	688	753	—	—	65	—	0.5
$Ti_{60}Zr_{15}Cu_{17}S_8$	675	752	1135	1365	77	0.495	1
$Ti_{50}Zr_{25}Cu_{17}S_8$	673	730	1082	1340	57	0.502	2
$Ti_{40}Zr_{35}Cu_{17}S_8$	671	724	1080	1343	54	0.499	3

4.3.3 Zr-based Alloys in the Ti-Zr-Cu-Ni-S system

If the Zr-content in $Ti_{75-x}Zr_xNi_{17}S_8$ is further increased (x > 37.5 at%), the system changes to a Zr-based system. In Fig. 4.15a the DSC traces at 1 K/s of several Zr-based alloys with a thickness of 500 μm are shown. Here, a significant rise of the thermal stability is observed for Zr-contents higher than 55 at%. Unfortunately, this increase is accompanied by a drastic drop of the GFA. Samples with 70 and 75 at% of Zr do not show any considerable crystallization events upon heating, indicating a fully crystalline microstructure. For instance, the $Zr_{65}Ti_{10}Ni_{17}S_8$ alloy shows an extend of the SCLR of $\Delta T_x = 67K$, but a critical casting thickness below 500 μm. Care has to be taken by the interpretation of the DSC measurements of partially crystalline samples regarding the thermal stability. The formation of crystalline precipitations in the amorphous matrix could result in a change of the composition of the amorphous matrix, which could have in turn an effect on the thermal stability.

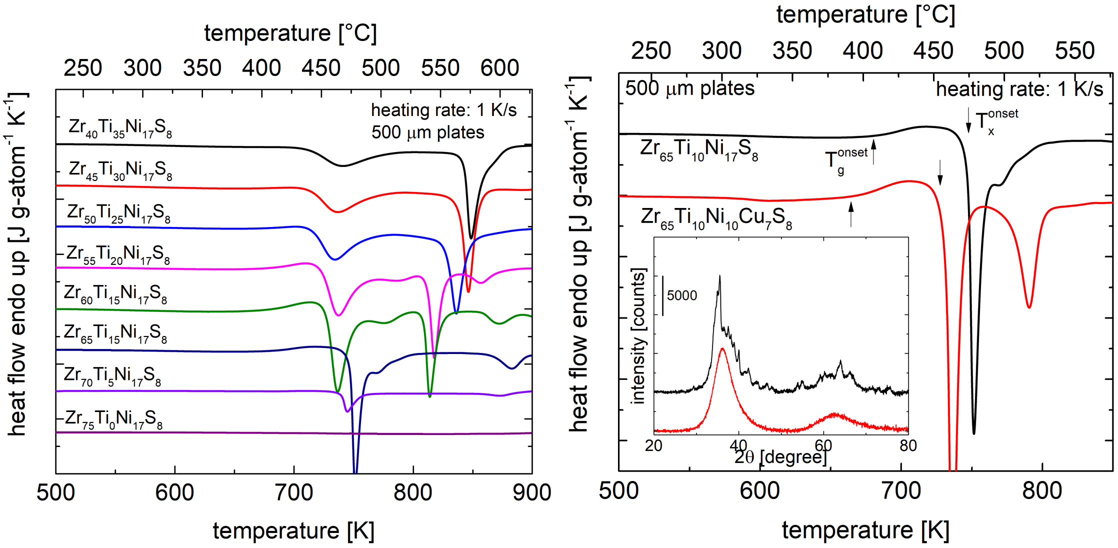

(a) (b)

FIGURE 4.15: a) DSC measurements of Zr-based alloys $Zr_{75-x}Ti_xNi_{17}S_8$ (x = 35, 30, 25, 20, 15, 10, 5, 0) at 1 K/s. b) DSC measurements of Zr-based alloys $Zr_{65}Ti_{10}Ni_{17-x}Cu_xS_8$ (x = 0, 7) at 1 K/s. The onset of the glass transition T_g^{onset} and the onset of crystallization T_x^{onset} are indicated with arrows.

In order to increase the GFA again, Cu is added for Ni (Fig. 4.15b). At a Cu content of more than 3 at% fully X-ray amorphous samples with a thickness of 500 μm are obtained. Like observed for the Ti-alloys, the increase in the GFA is accompanied by a reduction of thermal stability. However, an amount of 7 at% of Cu is added, since Cu is also expected to improve the mechanical properties regarding the ductility, as observed for the Ti-based alloys (see section 5.2.5).

A subsequent adjustment of the (Zr,Ti) to (Ni,Cu) ratio yields a further increase of the thermal stability with an unaffected critical casting thickness (Fig. 4.16a). Only for very high contents of (Ni,Cu) a drop of the GFA is observed. Additionally, the Zr-Ti ratio is iterated for an extension of the SCLR (Fig. 4.16b). Finally, $\Delta T_x(1K/s)$ is increased from 67 K for $Zr_{65}Ti_{10}Ni_{17}S_8$ up to 100 K for $Zr_{55.8}Ti_{13.2}Ni_{13.5}Cu_{9.5}S_8$.

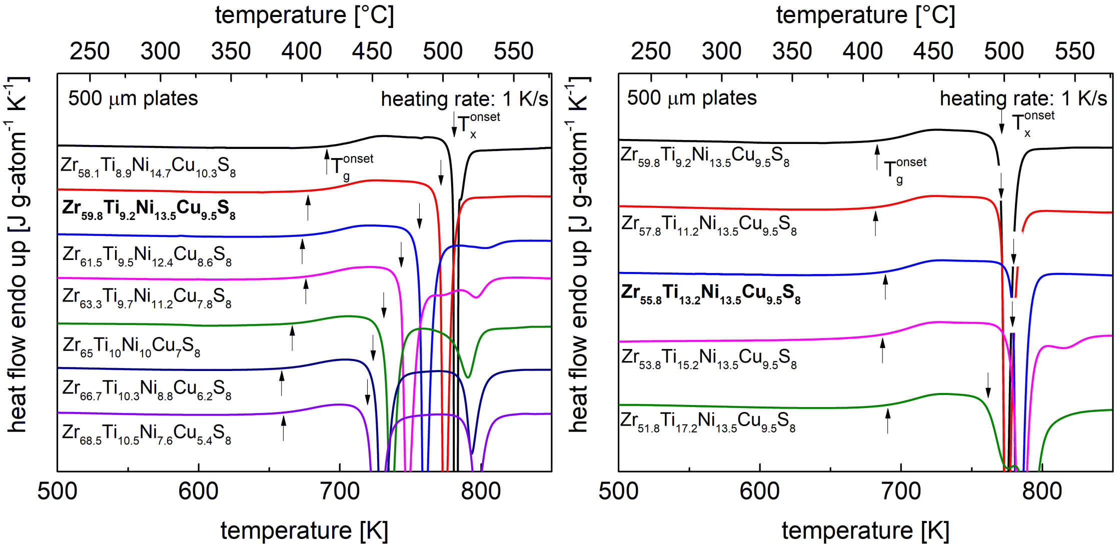

(a) (b)

FIGURE 4.16: a) DSC measurements of $(Zr_{0.87}Ti_{0.13})_{75+x}(Ni_{0.59}Cu_{0.41})_{17-x}S_8$ (x = 4, 2, 0, -2, -4, -6, -8) at 1 K/s. The onset of the glass transition T_g^{onset} and the onset of crystallization T_x^{onset} are indicated with arrows. b) DSC measurements of $Zr_{59.8-x}Ti_{13.2+x}Ni_{13.5}Cu_{9.5}S_8$ (x = 2, 4, 6, 8) at 1 K/s. The onset of the glass transition T_g^{onset} and the onset of crystallization T_x^{onset} are indicated with arrows.

In order to recover the GFA, the S-content is varied (Fig. 4.17). At a slightly reduced S-content of 7 at% the critical casting thickness rises above 1 mm (inset in Fig. 4.18) and reaches a value of almost 3 mm at a S-content of 6 at%. Interestingly, the GFA and the thermal stability behave always contrarily to each other in the Ti-Zr-Ni-Cu-S system. However, the best compromise between GFA and length of the SCLR are found for the $Zr_{56.5}Ti_{13.3}Ni_{13.6}Cu_{9.6}S_7$ alloy (Fig. 4.18a). As the Ti-based BMGs from section 4.3.2, the novel Zr-based, sulfur-containing alloy displays a broad melting interval and a rather high liquidus temperature of 1475 K (Fig. 4.18b), resulting in a t_{rg} of 0.46.

The characteristic temperatures to evaluate the thermal stability and the critical casting thickness of chosen compositions are summarized in table 4.4.

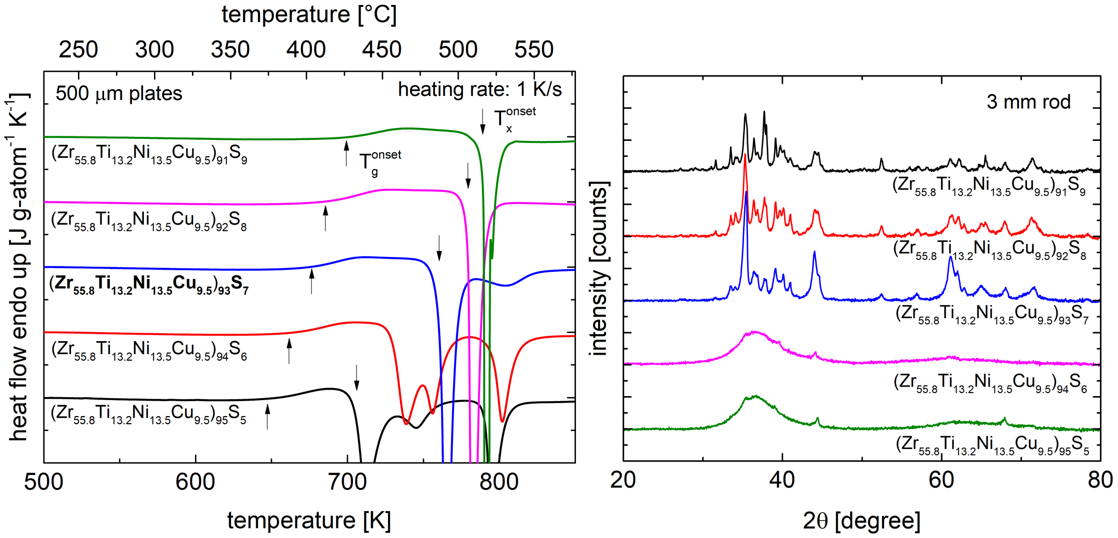

(a) (b)

FIGURE 4.17: a) DSC measurements of $Zr_{55.8}Ti_{13.2}Ni_{13.5}Cu_{9.5}S_8$ at 1 K/s with a varying S-content (5 - 9 at%). The onset of the glass transition T_g^{onset} and the onset of crystallization T_x^{onset} are indicated with arrows. b) XRD measurements of 3 mm rods of $Zr_{55.8}Ti_{13.2}Ni_{13.5}Cu_{9.5}S_8$ with a varying S-content (5 - 9 at%).

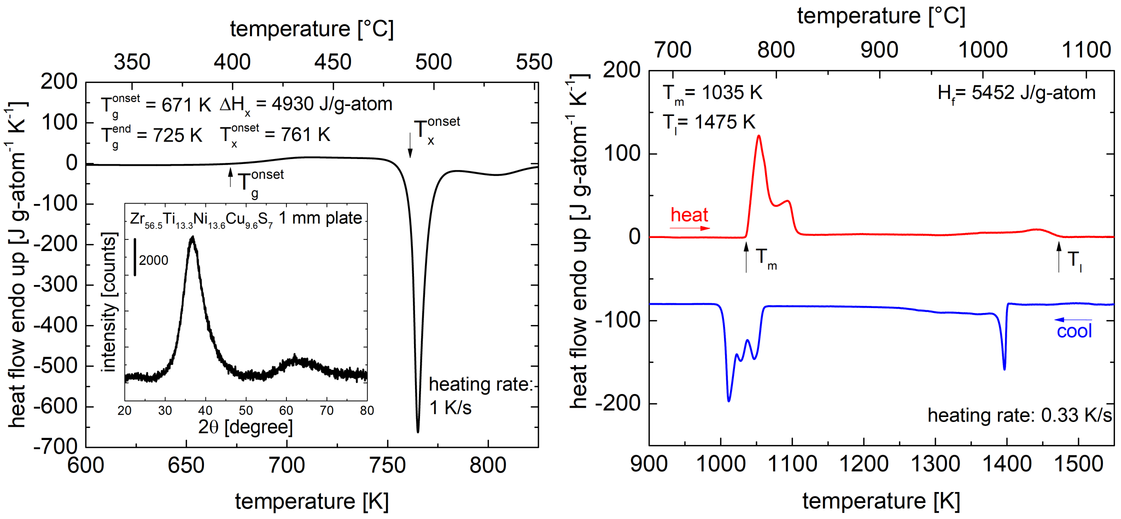

(a) (b)

FIGURE 4.18: a) DSC measurement of $Zr_{56.5}Ti_{13.3}Ni_{13.6}Cu_{9.6}S_7$ at 1 K/s. The inset shows a XRD measurement of a 1 mm plate. The characteristic temperatures and enthalpies are indicated. Taken from Ref. [7] b) DTA measurement of $Zr_{56.5}Ti_{13.3}Ni_{13.6}Cu_{9.6}S_7$ at 0.33 K/s. T_m and T_l are indicated with arrows.

TABLE 4.4: Characteristic temperatures of different Zr-based alloys in the Zr-Ti-Ni-Cu-S system determined by continuous DSC measurements with a heating rate of 1 K/s. By subtraction of the onset of the glass transition T_g^{onset} from the onset of crystallization T_x^{onset} the extend of the supercooled liquid region ΔT_x can be calculated. d_c is the critical diameter for which fully amorphous samples can be obtained by copper mold casting.

Alloy Composition $[at\%]$	T_g^{onset} $[K]$	T_x^{onset} $[K]$	ΔT_x $[K]$	d_c $[mm]$
$Zr_{65}Ti_{10}Ni_{17}S_8$	680	747	65	<0.5
$Zr_{65}Ti_{10}Ni_{10}Cu_7S_8$	664	727	63	0.5
$Zr_{59.8}Ti_{9.2}Ni_{13.5}Cu_{9.5}S_8$	676	770	94	0.5
$Zr_{55.8}Ti_{13.2}Ni_{13.5}Cu_{9.5}S_8$	682	782	100	1
$Zr_{56.5}Ti_{13.3}Ni_{13.6}Cu_{9.6}S_7$	671	761	90	>1

4.4 Processing of S-bearing Bulk Metallic Glasses

This section deals with the processing of the novel Ti-based and Zr-based glass forming alloys on an industrial scale. Therefore, the effect of industrial grade raw materials on the glass forming ability (GFA) is investigated and a new die-casting or rather injection molding method, which is customized for the processing of BMGs, is developed. Furthermore, the improvement of the process-ability of already known bulk glass forming alloy compositions by addition of sulfur is presented.

4.4.1 Influence of Industrial Grade Material

The processing under industrial-related conditions requires the use of industrial grade materials and the processing in industrial achievable atmospheres (lower vacuum/ low purity inert gas atmosphere). Both result in a "contamination" of the alloy by elements like oxygen. Commonly, a higher oxygen content drastically alters the GFA and mechanical properties of BMGs [203–207]. For example, the use of low purity zirconium (roughly 10 000 ppm) results in a reduction of the critical casting thickness of the Zr-based bulk metallic glass $Zr_{59.3}Cu_{28.8}Al_{10.4}Nb_{1.5}$ of about a factor of three [206, 207]. Hence, one major objective in the development of BMGs is a high robustness against oxygen impurities. On this account, the newly developed Ti-based bulk glass forming alloys are produced from industrial grade raw materials (Cu80S20, Zr R60702 and titanium ASTM grade 1). Assuming the maximum oxygen contents from the specifications of these raw materials, the master-alloy has an O-content of up to 0.55 at%. However, DSC measurements (Fig. 4.19a) and high energy synchrotron X-ray diffraction experiments (Fig. 4.19b) of $Ti_{40}Zr_{35}Cu_{17}S_8$ reveal that the use of industrial grade material has neither an impact on the GFA nor on the thermal stability. This proves the high robustness of the novel alloys against oxygen impurities and suggests a good process-ability under industrial-related conditions.

4.4.2 Die-Casting of Bulk Metallic Glasses

As already pointed out in section 2.6, in contrast to conventional, crystalline alloys, (bulk) glass forming alloys do not undergo volume shrinkage as observed during crystallization. This features the unique molding accuracy of BMGs and microstructures on the nanometer scale can be replicated [134]. Hence, BMGs are predestined for the near-net shape processing by high pressure die-casting or injection molding. To date available injection molding machines for BMGs are modified polymer injection molding machines still encountering several issues during the processing of glass forming alloys.

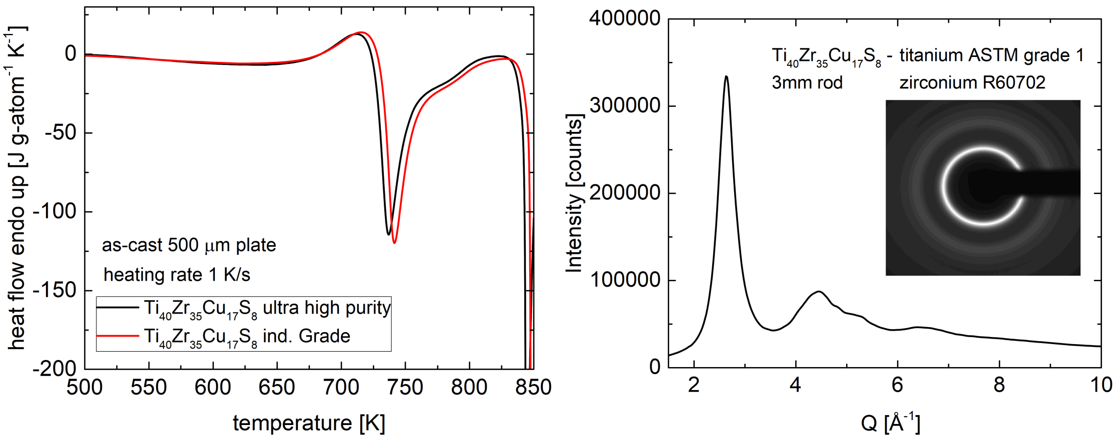

(a) (b)

FIGURE 4.19: a) DSC trace of a 500 μm plate of ultra high-purity $Ti_{40}Zr_{35}Cu_{17}S_8$ and $Ti_{40}Zr_{35}Cu_{17}S_8$ produced from industrial grade materials. b) High energy synchrotron X-ray diffraction pattern of a 3 mm rod of $Ti_{40}Zr_{35}Cu_{17}S_8$ produced from industrial grade materials. The absence of Bragg diffraction peaks proves the amorphous character of the sample. Both taken from Ref. [9].

For the production of fully amorphous parts with the ideal properties high cooling rates and a high overheating of several hundreds of Kelvin has to be realized [208]. Furthermore, a contamination of the melt by a crucible material should be avoided to reduce the effect of heterogeneous nucleation. Commonly, the cold crucible technique (also termed skull melting) is used for the processing of highly reactive metallic melts. Here, the metal is positioned in a segmented water cooled copper crucible and inductively melted (Fig. 4.20a). However, the cold crucible technique is limited to a relatively low overheating (roughly 20 K - Fig. 4.20b) [209]. The commercially available injection molding machines are built on this principle and thus, are limited to a small number of near-eutectic glass forming compositions. Hence, especially compositions with a broad melting behavior, like the novel Ti- and Zr-alloys, may not be allowed to be processed by this technique.

In the frame of this thesis, a novel concept based on the laboratory scale principles is develop and a prototype is built, enabling the production of BMG parts on an industrial scale with laboratory quality. The working principle is schematically shown in Fig. 4.21a and a produced part is illustrated in Fig. 4.21b. A feedstock material (about 10 to 40 g) is placed on top of the mold. Here, the ingot is melted using an electric arc in order to achieve maximum overheating over several hundred degrees. Subsequently, the electrode moves away and the melt is forced by a piston into the mold. In order to force the melt into the mold, a tongued sleeve encloses the molten ingot before the piston gets in contact with the melt. This principle is filed in a patent (DE 10 2018 115 815.7).

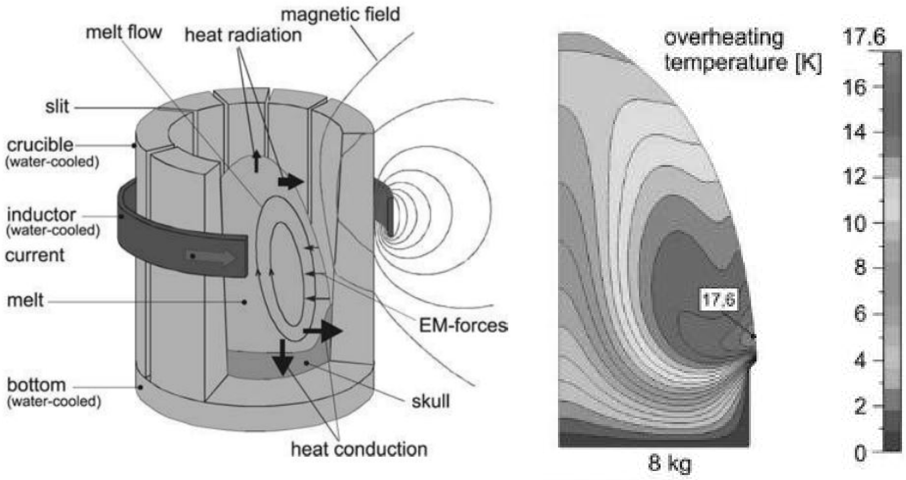

(a) (b)

FIGURE 4.20: a) Schematic illustration of an induction furnace with cold crucible. b) Overheating of a TiAl melt (8 kg) in a cold crucible using a high frequency generator with an electric power of 190 kW and a frequency of 10 kHz. Both taken from Ref. [209].

(a) (b)

FIGURE 4.21: a) Inside view of the vacuum chamber of the novel developed die-casting/injection molding process. b) Part of $Ti_{40}Zr_{35}Cu_{17}S_8$ produced by the novel developed die-casting process.

4.4.3 Minor Additions of Sulfur

As already mentioned, the glassy state of BMGs enables an unique process-ability using techniques like selective laser melting (SLM - also termed 3D printing) [137–139] or thermoplastic forming (TPF) [134, 210–212]. Besides the GFA, the thermal stability or rather the length of the SCLR (ΔT_x) plays a key role for these processes.

In this work, a positive effect on ΔT_x is observed if sulfur is added in small amounts to well-known BMGs such as Vitreloy 101 ($Cu_{47}Ti_{34}Zr_{11}Ni_8$), Vitreloy 105 ($Zr_{52.5}Ti_5Cu_{17.9}Ni_{14.6}Al_{10.0}$) or binary $Ni_{62}Nb_{38}$ (Fig. 4.22). In all cases, the SCLR is extended by about 15 K, significantly improving their process-ability. However, this effect is examined in detail elsewhere [213].

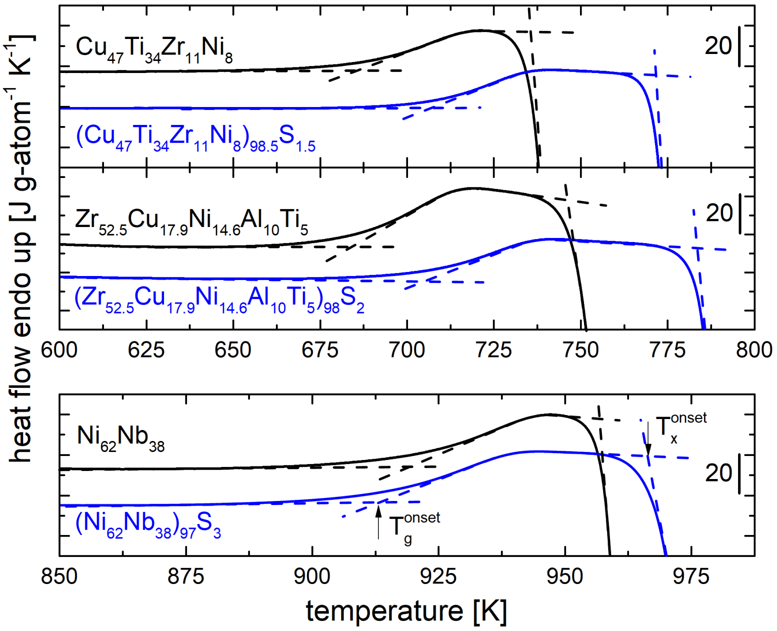

Figure 4.22: Comparison of the thermal stability upon heating at 1 K/s of several bulk metallic glass-forming systems (black lines) and their sulfur-bearing counterparts (blue lines). The dashed tangents indicate the onset of the glass transition T_g^{onset} and the onset of crystallization onset T_x^{onset}. Taken from Ref. [7].

Chapter 5

Characterization of Sulfur-bearing Bulk Metallic Glasses

In this chapter, the thermo-physical, structural, mechanical and electrochemical properties of the novel sulfur-bearing bulk metallic glasses are investigated in order to understand the process of glass formation and to reveal potential fields of application.

5.1 Characterization of $Pd_{31}Ni_{42}S_{27}$

As already pointed out, Pd-based alloys in the Pd-Ni-P system represent the best bulk metallic glass formers known so far [171, 214]. Here, the GFR is usually located at relative high amounts of metalloid elements like P, B or Si of about 20 at%. Although a similar role of S and P in the amorphous structure can be suggested due to their similar atomic diameters, the underlying process for glass formation seems to be different. This is inter alia manifested by a shift of the GFR to higher contents of sulfur of roughly 25 - 30 at% [8]. Because of the high amount of sulfur, the glass forming alloys in the Pd-Ni-S system are at the edge between metallic and non-metallic glasses, namely sulfide or chalcogenide glasses. Hence, the role of sulfur in this novel metallic glass forming system is of certain interest in order to supplement the overall picture about the process of glass formation. Therefore, the different thermodynamic, kinetic and structural characteristics of the novel Pd-Ni-S system are investigated. Additionally, the mechanical properties of the novel alloys are analyzed and correlations to the thermo-physical and structural properties are examined.

5.1.1 Thermodynamics of $\mathbf{Pd_{31}Ni_{42}S_{27}}$

In Fig. 5.1a the results of the molar heat capacity measurements $c_p(T)$ are shown, covering a temperature range of about 700 K (189.5 K - 863 K) (see section 3.2.1.2). The characteristic temperatures, which are obtained by DSC measurements with a heating rate of 0.33 K/s, are indicated with arrows (see section 4.2). At low temperatures the molar heat capacity of the glassy phase $c_p^{glass}(T)$ is slightly higher than that of the crystalline mixture $c_p^{x-tal}(T)$. At room temperature both values ($c_p^{x-tal}(293K) =$ 24.61 J g-$atom^{-1}$ K^{-1}; $c_p^{glass}(293K) = 24.94$ J g-$atom^{-1}$ K^{-1}) are, in agreement with Dulong-Petit's law, close to the value of 3R = 24.94 J g-$atom^{-1}$ K^{-1}. In contrast to the glassy phase, the data of the crystalline mixture $c_p^{x-tal}(T)$ shows a λ-shaped kink at 399.5 K that is allocated to the Curie temperature, where a transition from ferromagnetism to paramagnetism takes place. A similar observation was made in the $Pd_{40}Ni_{40}P_{20}$ bulk glass forming alloy, but here the transition takes place at 513 K, which is about 115 K higher than for $Pd_{31}Ni_{42}S_{27}$ [215]. This agrees with the higher glass transition temperature (583 K) and the higher liquidus temperature (974 K) of the phosphorous-bearing alloy. However, in both cases the λ-transition was only observed in the crystalline state. In vicinity of the glass transition, $c_p^{glass}(T)$ increases upon heating, which is attributed to an unfreezing of the structure [30]. At 440 K and 60.2 J g-$atom^{-1}$ K^{-1}, the molar heat capacity reaches the level of the supercooled liquid $c_p^{liquid}(T)$. This value is rather high in comparison to the well-known phosphorous-bearing bulk glass forming alloys $Pd_{40}Ni_{40}P_{20}$ and $Pd_{40}Cu_{30}Ni_{10}P_{20}/$ $Pd_{43}Cu_{27}Ni_{10}P_{20}$ with c_p-values close to T_g of 49.1 J g-$atom^{-1}$ K^{-1} [173] and roughly 46 J g-$atom^{-1}$ K^{-1} [216], respectively.

The measured value of $c_p(T)$ in the supercooled liquid region close to T_g is much higher than the values measured for the equilibrium liquid above the liquidus temperature, which are in the range of 40 J g-$atom^{-1}$ K^{-1}. Thus, upon cooling from the equilibrium liquid, the molar heat capacity increases steadily with decreasing temperature.

From the resulting functions of the molar heat capacity, the enthalpy difference between the (undercooled) liquid phase and the crystalline mixture ΔH^{l-x} can be calculated according to equation 2.4. The course of the enthalpy difference is illustrated in Fig. 5.1b. According to Kirchhoff's rule the integral of the molar heat capacity difference is related to the difference of the heat of crystallization ΔH_x and the heat of fusion ΔH_f by

$$\Delta H_f - \Delta H_x = \int_T^{T_l} \frac{c_p^{l-x}(T)'}{T'} dT' \tag{5.1}$$

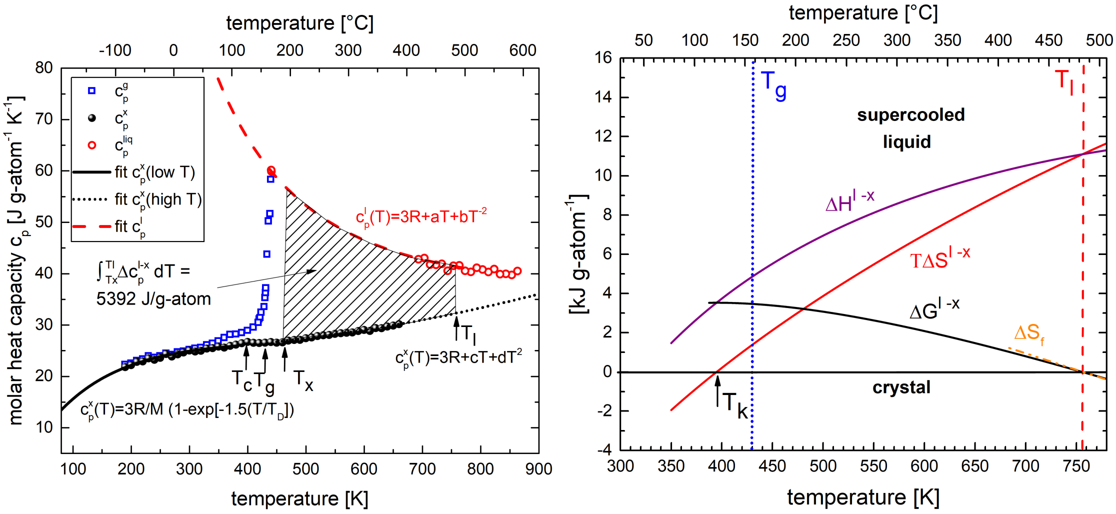

(a)

(b)

FIGURE 5.1: a) Molar heat capacity $\Delta c_p(T)$ of the glass, the crystalline mixture and the (undercooled) liquid of $Pd_{31}Ni_{42}S_{27}$. b) Difference of the enthalpy ΔH^{l-x}, entropy ΔS^{l-x} and Gibbs free energy ΔG^{l-x} between the crystalline mixture and the undercooled liquid.

yielding the values 5.6 kJ g-$atom^{-1}$ for $\Delta H_f - \Delta H_x$ and 5.4 kJ g-$atom^{-1}$ for the integral, respectively, validating the accuracy of the c_p measurements.

Fig. 5.1b also shows the temperature-scaled entropy difference between the crystalline mixture and the (undercooled) liquid phase $T\Delta S^{l-x}$, which was calculated according to equation 2.4. The high value of the enthalpy of fusion (11.1 kJ g-$atom^{-1}$ [8]) in combination with the low liquidus temperature of the alloy results in an extraordinarily high entropy of fusion (14.7 J g-$atom^{-1}$ K^{-1} [8]), causing a dramatic drop of the entropy in the supercooled liquid region and yielding the slope of ΔG^{l-x}. In comparison, the related Pd-based systems $Pd_{40}Ni_{40}P_{20}$, $Pd_{40}Cu_{30}Ni_{10}P_{20}$ and $Pd_{43}Cu_{27}Ni_{10}P_{20}$, show entropy of fusion values in the range of 5 - 11.8 J g-$atom^{-1}$ K^{-1} (Δ $H_f = 6$ kJ g-$atom^{-1}$ - 10.4 kJ g-$atom^{-1}$)[1] [45, 216], being about 40 % lower.

From the course of ΔS^{l-x} Kauzmann's temperature can be determined below which the entropy of the disordered, amorphous solid would be lower than that of the ordered crystal [65] (see section 2.2.2.4). Kauzmann's temperature of $Pd_{31}Ni_{42}S_{27}$ ($T_K = 394.8$ K) is 35 K below the onset of the glass transition measured at 0.33 K/s ($T_g(0.33K/s) =$ 429.8 K [8]). This temperature difference is in comparison to the Pd-Ni-P system ($T_g - T_K = 83$ K [215]) rather small, which is reasonable because of the faster drop of entropy in the sulfur-bearing system.

---

[1] Note, that for some bulk glass forming alloys the enthalpy of fusion ΔH_f and thus, also the entropy of fusion ΔS_f, differ significantly between the melting from the as-cast amorphous state and the slower cooled crystalline state. Here, the ΔH_f from the glassy state is chosen (first melting), since it is assumed that this value is less affected by the cooling rate.

From the enthalpy and entropy difference between the crystal and the (undercooled) liquid, also the Gibbs free energy difference ΔG^{l-x} can be calculated, using equation 2.4. ΔG^{l-x} is depicted in Fig. 5.1b, showing a value of roughly 3.5 J g-$atom^{-1}$ at the glass transition temperature, which is comparably high for a bulk glass forming system [148]. This difference in the Gibbs free energy is the first decisive contribution for the process of nucleation and growth as it describes the driving force for the formation of the crystalline mixture in the liquid phase (see section 2.2.2.1).

TABLE 5.1: Fitting parameters a, b, c and d of the c_p data of $Pd_{31}Ni_{42}S_{27}$ calculated from equation 3.2 and 3.3.

Alloy Composition [$at\%$]	a x 10^{-3} [J g-$atom^{-}1$ K^2]	b x 10^6 [J K g-$atom^{-1}$]	c x 10^{-3} [J g-$atom^{-}1$ K^2]	d x 10^{-6} [J g-$atom^{-}1$ K^2]
$Pd_{32}Ni_{32}S_{36}$	7.59 ± 0.24	6.1 ± 0.079	-4.3 ± 0.46	18.49 ± 0.8

TABLE 5.2: Fitting parameters M and T_D of the c_p data of $Pd_{31}Ni_{42}S_{27}$ calculated from equation 3.4. T_K is Kauzmann's temperature. T_c (x-tal) corresponds to the Curie temperature of the crystalline mixture, which is manifested by a kink in the c_p data in Fig. 5.1a.

Alloy Composition [$at\%$]	M (x-tal)	T_D (x-tal) [K]	T_c (x-tal) [K]	T_K [K]
$Pd_{32}Ni_{32}S_{36}$	0.927 ± 0.006	172.1 ± 4.6	399.5	394.8

5.1.2 Kinetics of $Pd_{31}Ni_{42}S_{27}$

The second crucial contribution to the process of glass formation (or rather the nucleation and growth process of the crystal), are the dynamics of the liquid phase. As described in section 2.2.2.2, the temperature sensitivity of the dynamics of the (undercooled) liquid, e.g. the dynamic viscosity η(T) or the structural (α-) relaxation time τ_α(T), can be described via a VFT-type equation (equation 2.8 and 2.9) [30].

In a first step, the fragility index m and the fragility parameter D* can be estimated from DSC scans using two different approaches (see section 2.2.2.2 and 3.2.1.3).
The first approach considers the jump of the molar heat capacity at the glass transition temperature $\Delta c_p^{l,g-x}(T_g)$, which was shown to correlate with the kinetic fragility of the liquid, when it is normalized to the entropy of fusion ΔS_f (equation 3.7) [47]. In order to erase irreversible contribution to the heat flow in a DSC scan, a "pre-treatment" is conducted prior heating the sample until crystallization occurs, leading to a more reliable determination of $\Delta c_p^{l,g-x}$ (Fig. 5.2a) [8]. Here, it has to be stressed that the cooling rate during the casting process influences the fictive temperature and thus $\Delta c_p^{l,g-x}$. On this account, the sample is heated with 0.33 K/s above T_g^{end} within the SCLR and subsequently cooled with 0.33 K/s. Finally, $\Delta c_p^{l,g-x}$ is read to be 30 ± 2 J g-$atom^{-1}$ K^{-1} at $T_g^{onset}(0.33\ K/s)$ and ΔS_f is determined to be 14.7 kJ g-$atom^{-1}$ K^{-1}. Equation 3.7 yields a fragility index of m = 73 ± 5 for the DSC trace of the $Pd_{31}Ni_{42}S_{27}$ alloy shown in Fig. 5.2a, corresponding to a fragility parameter D* of 10.3 ± 0.9 (equation 2.11). The error results from the reading error of $\Delta c_p^{l,g-x}(T_g^{onset})$. From Fig. 5.1 a more precise value of $\Delta c_p^{l,g-x}$ can be read, which is determined to be 35.1 J g-$atom^{-1}$ K^{-1}, leading to an even higher fragility index m of 95.5 corresponding to a D* of 7.4.
A second estimation of the kinetic fragility of the deeply undercooled liquid was proposed by Wei et al. [41]. In his work, the slope of the heat flow at T_g of a T_g-scaled DSC scan measured with 1 K/s is correlated with the fragility parameter D* according to equation 3.8 (see section 3.2.1.3). The 1^{st} derivation of the T_g-scaled DSC scan is displayed in Fig. 5.2b, in which the maximum slope at T_g can be read. The reading error is emphasized as grey bar, leading to a D* value of 7.2 ± 0.7, which corresponds to a fragility index m of 98 ± 8 (equation 2.11).

In summary, both estimations indicate a high temperature sensitivity of the viscosity or rather relaxation time in the low temperature regime.

However, for a more precise determination of the kinetic fragility and in order to validate the two approaches described above, further experiments are carried out. Due to the low thermal stability upon heating from the glassy state, which is manifested by a limited

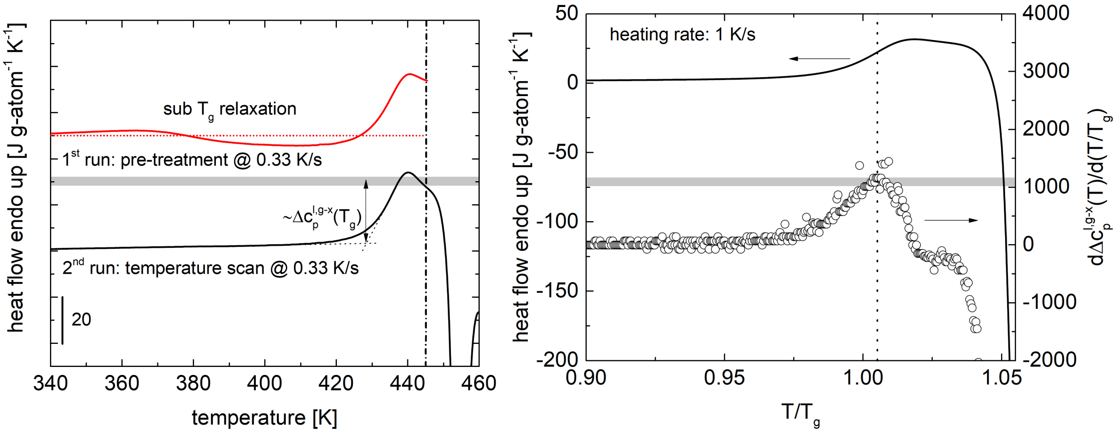

(a) (b)

FIGURE 5.2: a) DSC scans at 0.33 K/s of $Pd_{31}Ni_{42}S_{27}$. The first run (upper curve) displays a pre-treatment up to 446 K in order erase the thermal history of the sample. The second run (lower curve) shows a scan until crystallization occurs. The baseline is shown as dotted line. The gray bar indicates the error for the reading of the heat capacity. b) T_g-scaled DSC scan at 1 K/s of a pre-treated sample. The pre-treatment was carried out in the same manner as shown in a). The lower curve shows the 1^{st} derivative for the determination of the slope at the glass transition. The grey bar indicates the reading error. Figure and figure description are taken from Ref. [8]

length of the supercooled liquid region (SCLR: $\Delta T_x = T_x^{onset} - T_g^{onset}$), different difficulties are encountered when measuring the structural relaxation time or the dynamic viscosity.

The method of choice for the direct determination of the equilibrium viscosity at a specific temperature is the measurement of the deflection rate in a thermo-mechanical analyzer (TMA) in isothermal mode (see section 3.2.2). The expected high kinetic fragility in combination with the low thermal stability makes the determination of the dynamic viscosity or the structural relaxation time rather difficult. The latter one limits the temperature range to higher temperatures, whereas the high kinetic fragility results in a rapidly increasing viscosity, limiting the temperature range to lower temperatures. However, the resulting isothermal TMA measurements are shown in Fig. 5.3a together with the corresponding KWW fits (equation 3.10), covering a temperature range of only 10 K but a viscosity range of two orders of magnitude (10^{12} - 10^{14} Pas). The values of the equilibrium viscosity η_{eq} are displayed in Fig. 5.3c. Unfortunately, another issue is encountered during the isothermal measurements. The $Pd_{31}Ni_{42}S_{27}$ alloy does not reach a stable equilibrium value of the viscosity as can be seen in Fig. 5.3a. This effect might originate from phase separation as observed in several other bulk glass forming alloys [217–219] or from a smeared out crystallization (see section 5.1.3), both resulting in a continuously increasing viscosity. Thus, the equilibrium viscosity η_{eq} depends on the size of the time interval that is considered for the KWW fit. Similar observations can be made in case of the Ti- and Zr-based alloys in the Ti-Zr-Cu-Ni-S system in section 5.2.2.

On this account, the viscosity of the alloy is determined, using the scanning mode of the TMA. Different rates (0.083 K/s, 0.5 K/s, 1 K/s, 1.33 K/s) allow to get access to a wider temperature range due to the rate dependence of the glass transition.
In a first procedure, each scan is fitted solely using equation 2.8 like illustrated in Fig. 5.3c for a heating rate of 0.083 K/s. At this rate D* is determined to 8.96 ± 0.009 and T_0 to $341 \pm 0.08K$, respectively. For each rate at least two different measurements are carried out, yielding an average value of the fragility parameter D* of 7.6 ± 1.5 and of T_0 of $353.8 \pm 15K$. As viscosity limit at infinite temperature η_0 the value 4.1×10^{-5} Pa s was calculated according to the relation $\eta_0 = N_A \hbar / V$, where N_A corresponds to Avogadro's constant, $\hbar$ to the Planck constant and V to the molar volume [37].
In a second procedure, an equilibrium value of the viscosity is read from the TMA scan above the end of the respective glass transition ($T_g^{end} < T < T_x$). T_g^{end} and T_x are determined in a DSC scan with the same heating rate. This data set of the equilibrium viscosities is summarized in a T_g-scaled viscosity over temperature plot (Angell-Plot) in Fig. 5.3d. The equilibrium viscosities determined in scanning mode cover a temperature range of roughly 20 K. Fitting of this set of data using equation 2.8 leads to a fragility parameter D* of 8.3 ± 0.8 and a T_0 of $347 \pm 8K$.

In addition to the TMA measurements, the structural relaxation times were measured by evaluating the shift of the fictive glass transition temperature by applying different heating rates. As already pointed out in section 3.2.1.3, Angell et al. showed that the fictive glass transition temperature is equal to the onset of the glass transition measured in DSC, if the heating rate is identical to the cooling rate at which the glassy structure is frozen-in [36, 73, 220]. Evenson et al. showed this for the first time for bulk metallic glass forming alloys in Ref. [145]. Therefore, a pre-treatment is performed prior to each measurement with a specific rate as shown in Fig. 5.2a. Heat flow curves measured with different heating rates subsequent to the pre-treatment are shown in the Fig. 5.3b. It is evident, that the width of the glass transition increases slower with increasing heating rate than the heating rate itself, resulting in smaller relaxation times at higher onset temperatures. Equation 3.5 enables the calculation of the corresponding transition times. Using equation 2.7 the relaxation times can be allocated to equilibrium viscosities with a proportionality factor $G_{\tau-\eta}$ of $9.15 \times 10^8 \pm 3.48 \times 10^8$ GPa and are shown together with the equilibrium viscosities at T_g^{end} in Fig. 5.3d. This proportionality factor $G_{\tau-\eta}$ is proportional but not equal to G_∞, since the relaxation time τ is not equal to the Maxwell relaxation time as stated in Ref. [39, 221]. G_∞ is expected to be in the order of 1×10^{10} Pa [222], which would result in much higher viscosity values and a discrepancy

between the measured equilibrium viscosities and the calculated ones from the T_g-shift method. However, the solely fitting of the relaxation times using equation 2.9 yields a D* of 8.9 ± 2.2 and a T_0 of $341.5 \pm 16.8K$ with a τ_0 of 4.5×10^{-14} s (equation 2.7 with $\eta_0 = 4.1 \times 10^{-5}$ Pa s and $G_{\tau-\eta} = 9.15 \times 10^8$ GPa).
The rate dependence of the glass transition temperature can also be analyzed by plotting the logarithm of the heating rate normalized by the standard heating rate q_s (= 0.33 K/s) over the onset of the fictive temperature normalized by the fictive temperature at 0.33 K/s (see section 3.2.1.3). This is illustrated in the inset in 5.3b, yielding a fragility index m of 82.2 ± 17.7 (equation 3.6), which corresponds to a D* of 8.8 ± 2.3.

All in all, all approaches for the fragility determination point towards a fragile kinetic behavior (D* of 8.3 in average) and hence, a high sensitivity of the viscosity to temperature changes. The results of the analysis of the kinetic data are summarized in table 5.3.

Table 5.3: Fragility parameter D* and fragility index m of $Pd_{31}Ni_{42}S_{27}$ determined by different methods. For a detailed description of the methods the reader is referred to the experimental section (see section 3.2.1.3 and section 3.2.2).

Approach	Fragility index m	Fragility parameter D^*
Slope-Fragility method (Wei et al.)	98 ± 8	7.2 ± 0.7
c_p method (DSC scan) (Wang et al.)	73 ± 5	10.3 ± 0.9
c_p method (c_p data) (Wang et al.)	95.5	7.4
TMA scans 1	94 ± 15	7.6 ± 1.5
TMA scans 2	87 ± 7	8.3 ± 0.8
T_g-shift method (Busch et al.)	82 ± 16	8.9 ± 2.2
T_g-shift method (Angell et al.)	82.8 ± 17.7	8.8 ± 2.3
average value	88	8.3

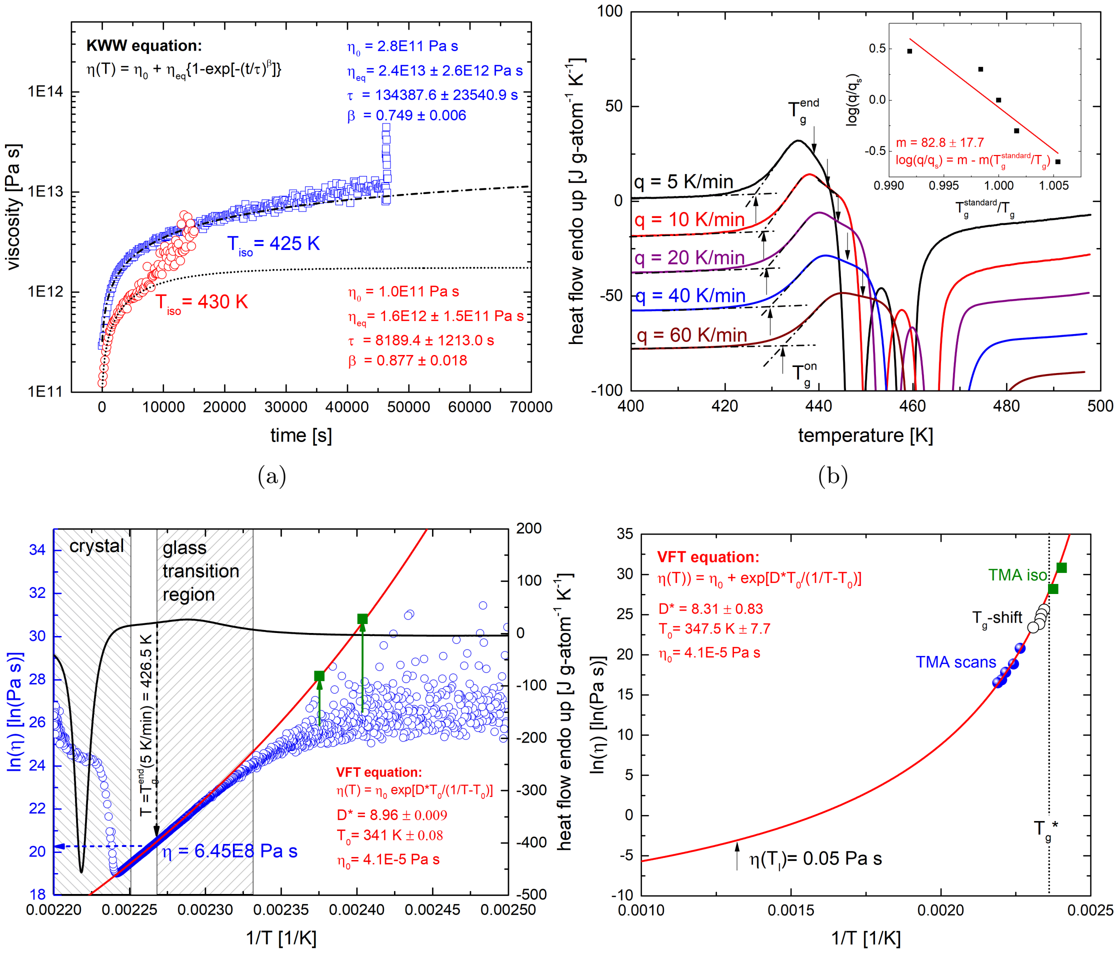

(a) (b)

(c) (d)

FIGURE 5.3: a) Isothermal TMA measurement of $Pd_{31}Ni_{42}S_{27}$ at 430 K and 425 K. The data is described using equation 3.10. b) DSC scans of $Pd_{31}Ni_{42}S_{27}$ at different heating rates. Prior to each measurement, the sample is heated above T_g^{onset} of each specific rate within the SCLR ($T_{pre-treatment} = f(q) \approx T_g^{end}(q)$). The inset shows the determination of the fragility index m by the method described in Ref. [36]. c) Continuous TMA measurement of $Pd_{31}Ni_{42}S_{27}$ at 0.083 K/s. The red curve corresponds to the VFT fit (equation 2.8). For fitting only the data points of the supercooled liquid are taken into account. The green squares correspond to the equilibrium viscosities determined by isothermal measurements. d) Viscosity over inverse temperature plot of $Pd_{31}Ni_{42}S_{27}$ with the viscosity values determined by the methods shown in a) - c). The VFT fit of the viscosities determined by TMA scans is shown as red line.

5.1.3 Crystallization Behavior of $\mathbf{Pd_{31}Ni_{42}S_{27}}$

In order to determine the isothermal and continuous TTT diagrams, which both provide information about the critical cooling rate, isothermal and continuous crystallization experiments are conducted upon cooling from the equilibrium liquid as well as upon heating from the glassy state.

In case of the continuous cooling and heating experiments with different rates, the onsets of the first crystallization events are determined by the tangent method (Fig. 5.4a,b). At high temperatures, the crystallization process is nucleation controlled and hence, is a highly statistical process. In contrast, the growth controlled nature of the crystallization process in the low temperature regime results in a more smeared-out manner of the crystallization events with a strongly reduced scattering. On this account, at least 5 cycles were measured in the high temperature regime in order to determine the experimental error of $\pm 3\sigma$. The continuous cooling experiments reveal, that a cooling rate as low as 0.083 K/s already leads to an undercooling of almost 100 K, which is, with respect to the small temperature interval between the melting temperature T_m = 725.5 K [8] (see section 4.2) and the glass transition temperature T_g(0.33 K/s) = 425.6 K [8] (see section 4.2) of ~300 K, a rather high undercooling. Upon continuous heating, another interesting feature is evident. Lower heating rates ($<$ 1 K/s) yield a splitting of the exothermic crystallization event.

The results of the isothermal crystallization experiments are presented in Fig. 5.4c and Fig. 5.4d. Here, the crystallization time $t_{iso}^{1\%}$, at which 1 % of the total crystallization enthalpy is released, is determined by integration of the first exothermic crystallization peak. Like for the continuous experiments, at least five measurements are carried out in the high temperature regime in order to determine the experimental error of the crystallization times. Like in case of the continuous experiments, a good "supercoolability" is observed.

From the isothermal and continuous crystallization experiments the crystallization enthalpies can be obtained as a function of temperature (or heating rate) by integration of the heat flow curves. These enthalpies can be used for the validation of the enthalpy curve H(T) (Fig. 5.1b), which is calculated from the molar heat capacity measurements (Fig. 5.1a). In general, the crystallization enthalpy decreases with decreasing holding temperature as expected from the calculated enthalpy curve in Fig. 5.1b. However, care has to be taken by the determination of the total amount of enthalpy release in the low temperature isothermals. After a certain holding time, some enthalpy could still be stored in the sample, since the holding time was not sufficiently high for all processes to occur and the equilibrium crystalline state is not reached. Hence, subsequent to the

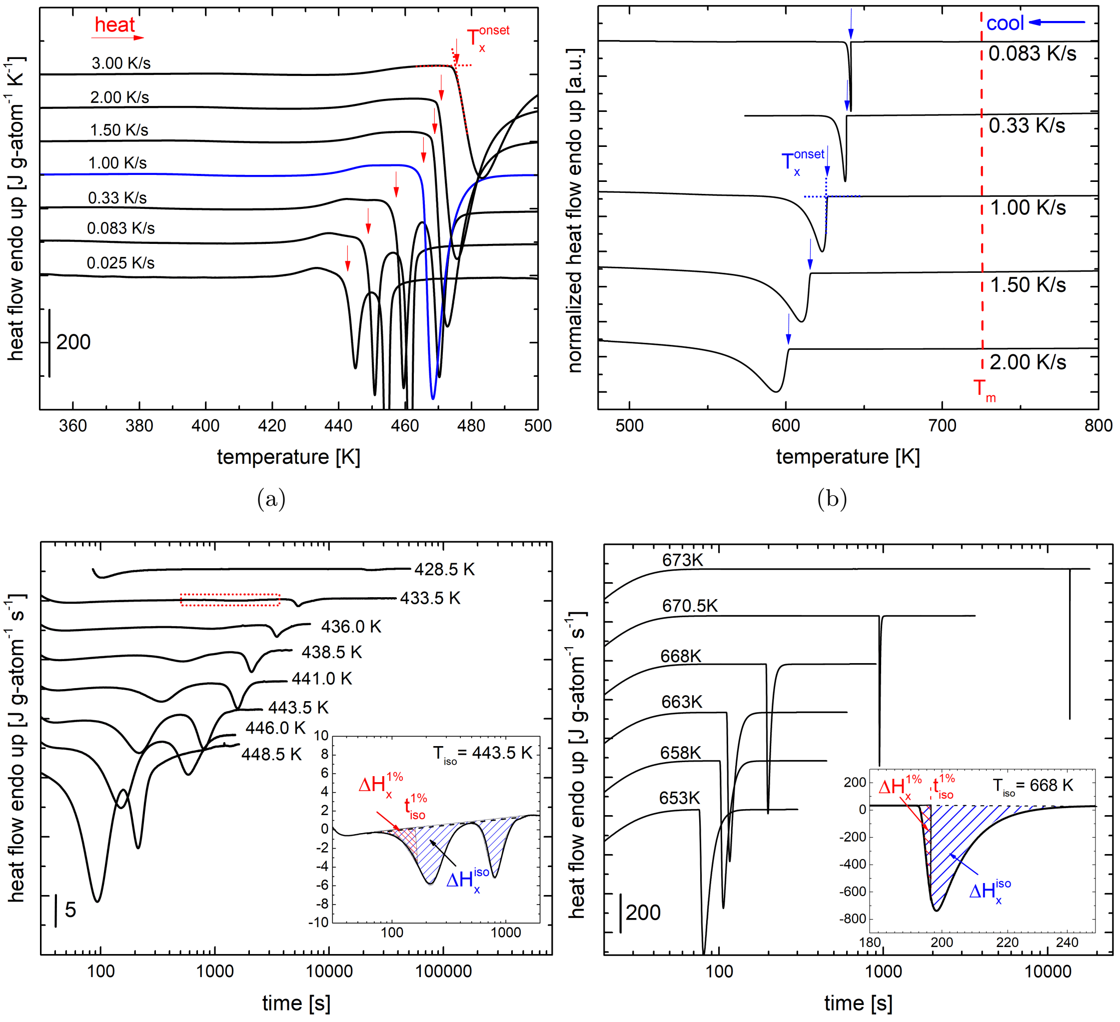

(a)

(b)

(c)

(d)

FIGURE 5.4: a) Continuous DSC measurements of glassy $Pd_{31}Ni_{42}S_{27}$ at different heating rates. The onset of crystallization T_x^{onset} is determined by the tangent method and indicated by a red arrow. At heating rates below 1 K/s (marked in blue) the crystallization sequence is decoupled in two distinct events. For higher rates only one exothermic event is evident. b) Continuous DSC measurements of molten $Pd_{31}Ni_{42}S_{27}$ at different cooling rates. During the measurements the sample was covered with B_2O_3. The solidus temperature T_m is emphasized by a red dashed line. The corresponding onset of crystallization T_x^{onset} is marked by a blue arrow. c) Isothermal DSC measurements of glassy $Pd_{31}Ni_{42}S_{27}$ at different temperatures in the low temperature regime. The time $t_{iso}^{1\%}$ at which 1 % of the total crystallization enthalpy ΔH_x is released, is determined by integration according to the inset. The first crystallization event gets smeared out at lower temperatures (dotted square). d) Isothermal DSC measurements of molten $Pd_{31}Ni_{42}S_{27}$ at different temperatures in the high temperature regime. $t_{iso}^{1\%}$ is determined as shown in the inset. Like in case of the continous measurements, the measurements the sample was covered with B_2O_3 during the measurement.

isothermal treatment, the samples are heated continuously up to the solidus temperature to record the residual enthalpy in the sample [63]. Considering this procedure, the crystallization enthalpy data of the isothermal as well as the continuous measurements are within the error intervals of the enthalpy curve as shown in Fig. 5.5. The error interval results from the determination of the enthalpy of fusion [8] (see section 4.2).

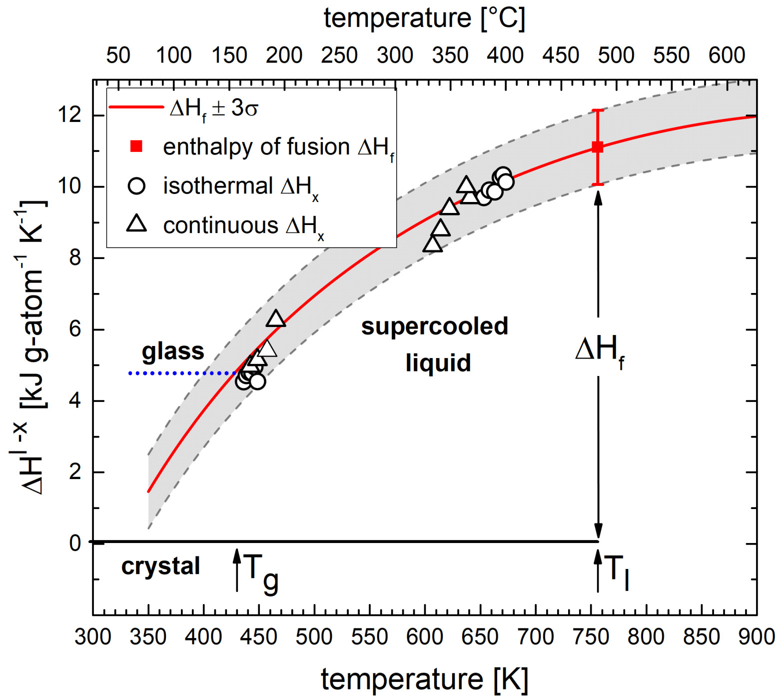

FIGURE 5.5: Enthalpy difference between the (supercooled) liquid and the crystalline mixture. The measured crystallization enthalpies from the isothermal and continuous crystallization experiments are within the ±3σ error interval of the enthalpy of fusion ΔH_f.

For the interpretation of the crystallization times and the differences between the crystallization processes upon heating and cooling, the identification of the primary precipitating phases and the crystallization sequence are of great interest. Therefore, in-situ high energy synchrotron experiments are carried out to identify the crystalline phases by means of their diffraction pattern. The description of the experimental setup can be found in section 3.3.2 or Ref. [8]. According to the ternary phase diagram reported in Ref. [182], the $Pd_{31}Ni_{42}S_{27}$ alloy is located in the ternary phase field of the binary intermetallic compounds Pd_4S and Ni_3S_2 and the solid solution (Pd,Ni). Thus, in case of equilibrium, one of these phases might be the primary crystalline phase. Although other, probably metastable, phases might be formed during quenching, the most straight forward approach is to compare the experimentally obtained diffraction pattern with the diffraction pattern of the equilibrium crystalline phases, which are simulated with the PowderCell 2.3 software [159] (see section 3.3.1).

The evolution of the diffraction pattern upon continuous cooling/ quenching from the equilibrium liquid and upon continuous heating from the glassy state are displayed in Fig. 5.6. The diffraction pattern of the liquid and the glassy phase do not show crystalline Bragg peaks, proving the amorphous character of these phases. After heating the initially amorphous, as-cast sample above the onset of crystallization, Bragg diffraction peaks are formed, which correspond most likely to the binary intermetallic compounds Pd_4S and Ni_3S_2 (Fig. 5.6a). The diffraction pattern of these phases were simulated using the Powder Cell software [159] and the crystallographic data were taken from Ref. [223] and [224] for Pd_4S and Ni_3S_2, respectively. The temperature/ time resolution of the setup is not sufficient to resolve the exact sequence of the formation of these two phases. However, under these heating conditions, the formation of the solid solution (Pd,Ni) is not observed.
When cooling the sample with 0.33 K/s from 1021 K the first diffraction peaks are observed at an undercooling of about 35 K (Fig. 5.6b). The positions of the peaks are in good agreement with the diffraction patterns observed upon heating, suggesting the simultaneous formation of the binary intermetallic compounds Pd_4S and Ni_3S_2. Only the intensity distribution differs between patterns obtained upon heating from the glassy state and during cooling from the equilibrium liquid. This may result from the shape, size and distribution of the crystalline phases in the amorphous matrix.
Subsequently, the sample is heated again to the stable equilibrium liquid and then quenched by a flow of compressed air to achieve higher cooling rates. During this a proper recording of the temperature is not possible. However, even during quenching, the formation of both phases, Pd_4S as well as Ni_3S_2, is observed (Fig. 5.6c).

In summary, the continuous experiments reveal that upon cooling as well as upon heating the intermetallic compounds Pd_4S and Ni_3S_2 are formed simultaneously. The formation of the solid solution (Pd,Ni) and the cubic high temperature modification of $Ni_{3\pm x}S_2$ is not observed upon cooling and quenching, which might result from a supersaturation of the intermetallic compounds. This is reasonable since the solid solution displays nearly no solubility for sulfur, but especially the intermetallic compound Pd_4S shows a high compositional stability range [182].

Although it is revealed that in continuous experiments the crystallization sequence upon heating and cooling is equivalent (simultaneous formation of Pd_4S and Ni_3S_2), the sequences can differ in cases of isothermal experiments because of transient nucleation effects. The isothermal heat flow curve in Fig. 5.7 of the isothermal crystallization at 443.5 K displays two distinct exothermic events, which might correspond to a decoupled formation of Pd_4S and Ni_3S_2. For a correct interpretation, in-situ isothermal synchrotron experiments were carried out. From Fig. 5.7 it is evident, that after roughly

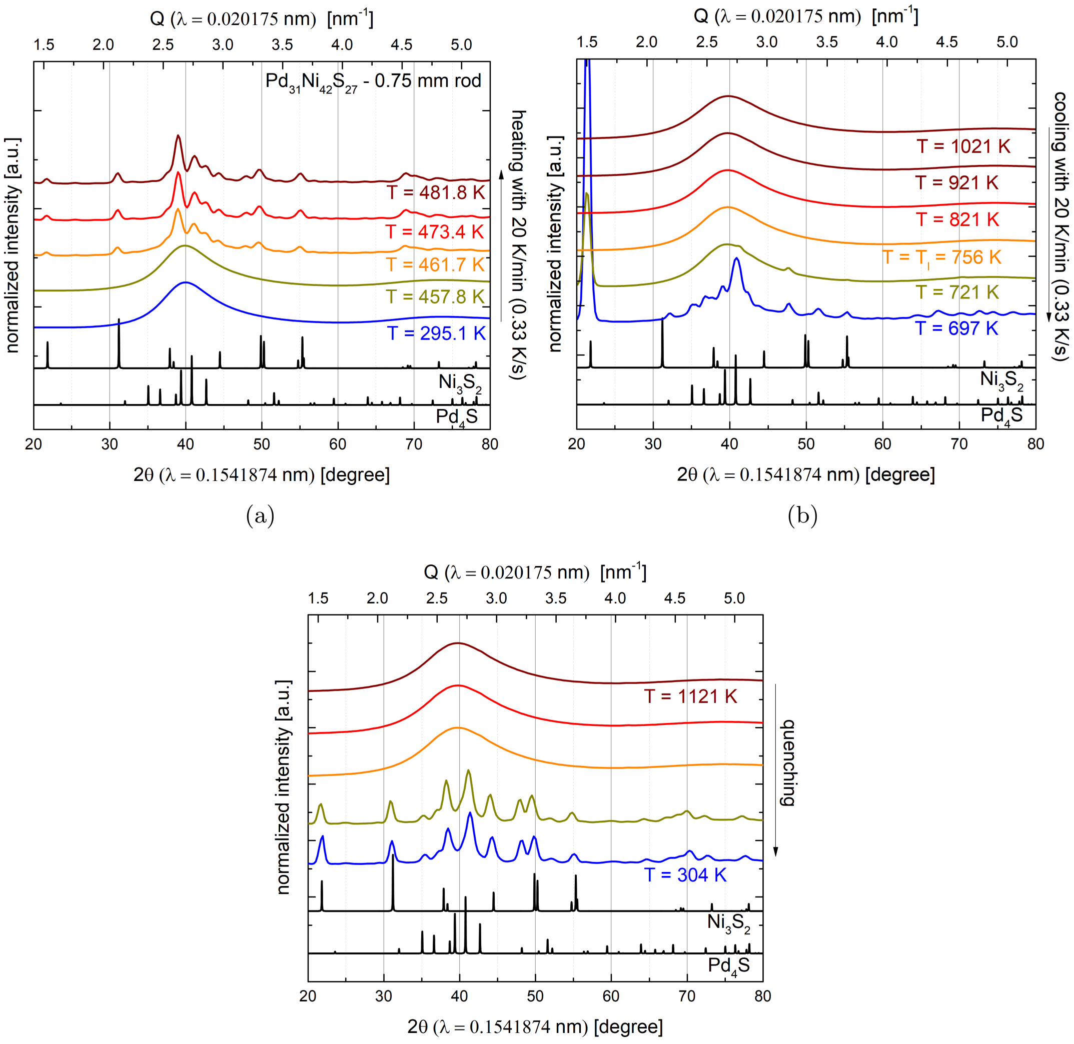

(a)

(b)

(c)

FIGURE 5.6: In-situ X-ray diffraction pattern of a 0.75 mm rod upon a) heating from the glassy state at 0.33 K/s b) cooling from the equilibrium liquid at 0.33 K/s and c) quenching from the equilibrium liquid. In addition, the simulated diffraction patterns of the crystalline equilibrium phases Ni_3S_2 and Pd_4S are shown. In all cases, Ni_3S_2 and Pd_4S form simultaneously. Figure and figure description are taken from Ref. [8].

100 s the FSDP are formed in I(Q). These reflexes can be attributed to the formation of the intermetallic compound Pd_4S. Subsequently, the formation of Ni_3S_2 is observed. Thus, the crystallization sequences under continuous heating/cooling conditions differ from that in case of isothermal experiments or rather in isothermal experiments the formation of both phases is decoupled at low temperatures. At high temperatures no difference in the crystallization sequences is expected since only one distinct peak is observed in the caloric experiments (Fig. 5.4b,d).

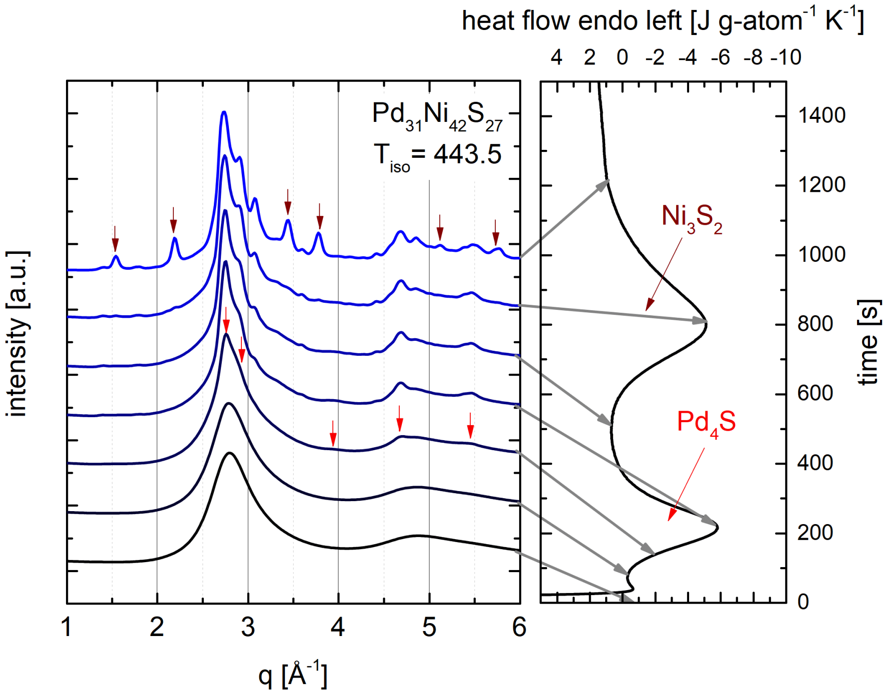

FIGURE 5.7: In-situ X-ray diffraction pattern of an as-cast 0.5 mm plate of $Pd_{31}Ni_{42}S_{27}$ isothermally hold at 443.5 K. In case of isothermal experiments, a two step crystallization process is observed. The red and the brown arrows indicate the Bragg peaks of the primary (Pd_4S) and secondary crystallizing phase (Ni_2S_3).

5.1.4 Structure of liquid and glassy $\mathbf{Pd_{31}Ni_{42}S_{27}}$

Besides the temperature dependence of the thermodynamics and kinetics, the changes of the atomic structure with temperature is of great interest. In Fig. 5.8 the change of the total structure factor S(Q) and the reduced pair distribution function G(r) upon heating from the glassy state to the equilibrium liquid is shown. Between 440 K and 873 K the crystalline mixture is formed and hence, data about the amorphous phase in this temperature range is not accessible in this experimental setup.

The first FSDP in S(Q) is located at around 2.8 $\AA^{-1}$ for both, the high and the low temperature regime (Fig. 5.8a). A significant difference can be observed at the second sharp diffraction peak (SSDP) in S(Q). In comparison to the high temperature liquid, the glassy phase and the low temperature liquid show a degeneration of the SSDP. Fourier transformation of the total structure factor S(Q) yields the reduced pair distribution function G(r), leading to real space information of the superpositioned atomic distances (see section 3.3.2). G(r) shows several significant differences between the low temperature undercooled liquid and the high temperature equilibrium liquid (Fig. 5.8b). The FSDP of G(r) is located at roughly 2.8 $\AA$ and shows a slight offset between the high temperature liquid and the low temperature liquid. At low temperatures a pre-peak is clearly visible at roughly 2.2 $\AA$, which is not present in the high temperature liquid.

Additionally, a change upon cooling can be observed at higher atomic distances. In the low temperature regime, the appearance of a shoulder at the SSDP in G(r) is present and the peak maximum splits up into two distinct maxima.

All in all, the analysis of the reciprocal and real space information of the atomic structure points towards structural changes on the way from the high temperature equilibrium liquid to the low temperature glassy state. These differences are analyzed and discussed later in this work (see section 6.4).

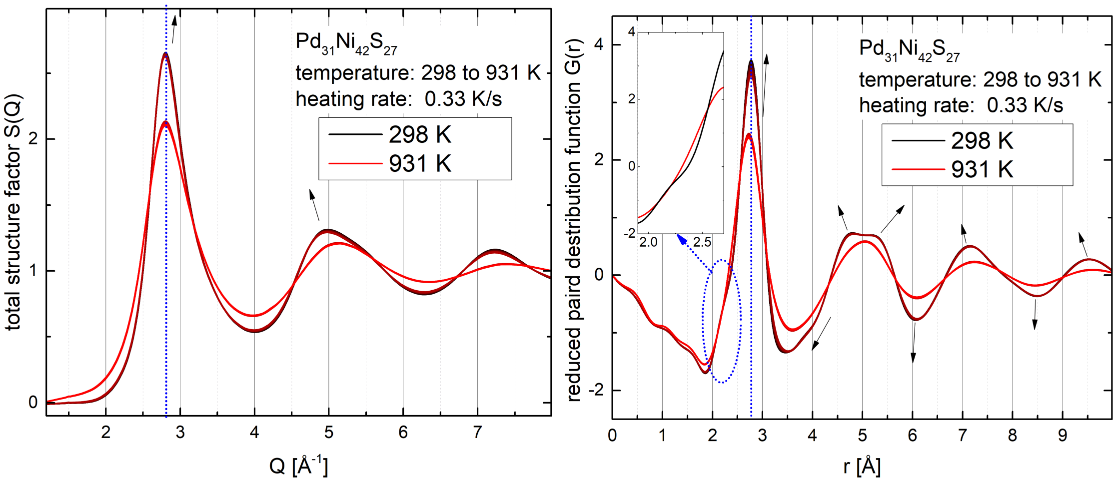

(a)

(b)

FIGURE 5.8: a) Total structure factor S(Q) of $Pd_{31}Ni_{42}S_{27}$ upon heating from the glassy state. b) Reduced pair distribution function G(r) of $Pd_{31}Ni_{42}S_{27}$ upon heating from the glassy state. For both, the changes of the peak positions and shapes are indicated with arrows.

5.1.5 Mechanical Behavior of $\mathbf{Pd_{31}Ni_{42}S_{27}}$

Vickers hardness measurements (HV5) are conducted on plate-shaped samples of Pd_{31} $Ni_{42}S_{27}$ with a thickness of 0.9 mm. The hardness value is determined to be 400 ± 8 HV5. Around the indents the formation of shear bands is not observed, pointing towards a brittle mechanical behavior of the sample.

For the evaluation of the elastic and plastic deformation behavior, three-point bending flexural tests are conducted on plate-shaped samples with a cross section of 0.9 x 4 mm^2. In Fig. 5.9 the resulting engineering stress - strain curves are displayed. The sample fails at a maximum stress of about 700 MPa and a total strain to failure of 0.95 %. The resulting Young's modulus is determined to be 75 GPa. As shown by Johnson et al., an elastic limit of about 2 % is usually expected for metallic glasses [108]. Assuming this value for the elastic limit, a yield strength of about 1.5 GPa is expected for an elastic modulus of 75 GPa (intersection point of the dashed and the dotted line in Fig. 5.9). Thus, the sample fails before reaching its nominal yield strength, revealing a high sensitivity to fracture and hence, a brittle mechanical behavior. For comparison, hardness measurements and three-point flexural bending tests are carried out for the well-known $Pd_{43}Cu_{27}Ni_{10}P_{20}$ bulk glass forming alloy. Vickers hardness is measured to be 501 ± 12 HV5 and the engineering stress - strain curve of a plate shaped sample of $Pd_{43}Cu_{27}Ni_{10}P_{20}$ reveals an offset yield strength of roughly 2.1 GPa at an elastic limit of 2 %. Young's modulus is determined to be 102 GPa. At the end of the linear elastic regime, the sample undergoes plastic deformation, revealing a ductile mechanical behavior. The sample fails at a maximum stress of 2.7 GPa and a total strain to failure of 3.06 %.

The fracture surfaces of both alloys are analyzed using scanning electron microscopy (SEM). Secondary electron (SE) images of both samples from Fig. 5.9 are displayed in Fig. 5.10. Lower magnitude images of the fracture surface of $Pd_{31}Ni_{42}S_{27}$ show a smooth morphology. Only in higher magnitude images a "dimple-like" morphology on the nanometer scale can be revealed (Fig. 5.10 a). By comparison, the fracture sample of $Pd_{43}Cu_{27}Ni_{10}P_{20}$ shows "river-like" or "vain-like" pattern on the micrometer scale (Fig. 5.10 b). The respective scale of these features gives information about the localization of the plastic deformation and the resulting ductility. A more localized deformation results in a more brittle behavior [225–228], confirming the findings in the three-point bending flexural tests, that the $Pd_{31}Ni_{42}S_{27}$ shows a more brittle mechanical behavior than $Pd_{43}Cu_{27}Ni_{10}P_{20}$, which is most likely linked to a lower fracture toughness.

An additional feature, which is visible in the SE images, are micropores in the fracture surface (Supp. Fig. A.3). These micropores result from the casting procedure and

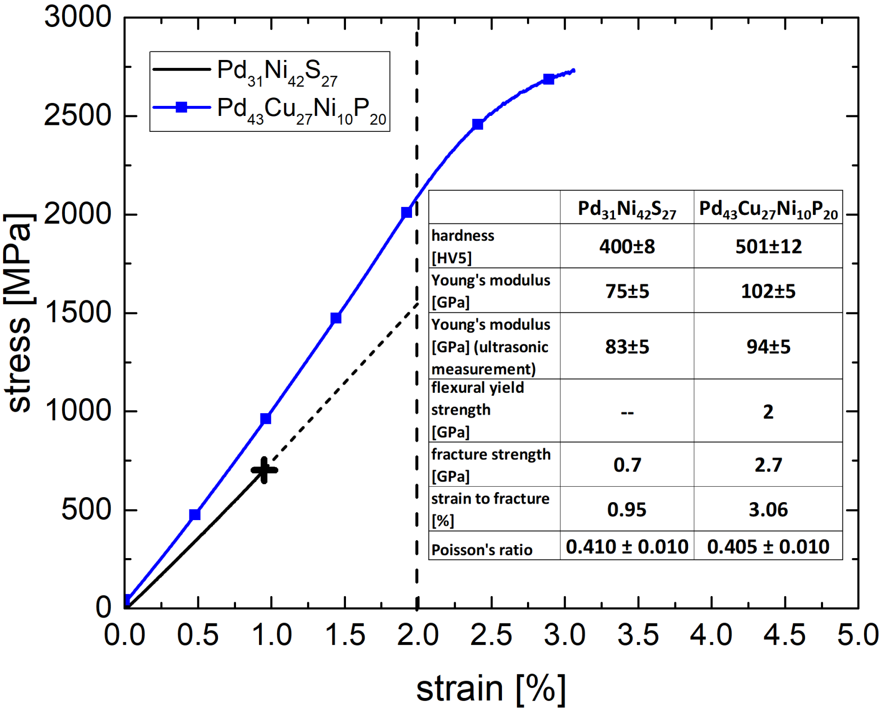

	$Pd_{31}Ni_{42}S_{27}$	$Pd_{43}Cu_{27}Ni_{10}P_{20}$
hardness [HV5]	**400±8**	**501±12**
Young's modulus [GPa]	**75±5**	**102±5**
Young's modulus [GPa] (ultrasonic measurement)	**83±5**	**94±5**
flexural yield strength [GPa]	**--**	**2**
fracture strength [GPa]	**0.7**	**2.7**
strain to fracture [%]	**0.95**	**3.06**
Poisson's ratio	**0.410 ± 0.010**	**0.405 ± 0.010**

FIGURE 5.9: Engineering stress-strain curve of a plate-shaped sample of $Pd_{31}Ni_{42}S_{27}$ measured in a three-point-beam bending setup at a deflection rate of 0.3 mm/min. The flexural elastic limit of less than 1% indicates the brittle mechanical behavior in flexural bending. Figure and figure description are taken from Ref. [8].

can initiate a critical crack and a subsequent failure. Therefore, the sample can fail before reaching its yield strength [229–232] like observed in case of the $Pd_{31}Ni_{42}S_{27}$ alloy. A similar behavior was observed inter alia in three-point flexural beam bending experiments of Mg-based alloys by Chang et al. [232]. In their study they showed that in case of a bending load the samples fail at an average stress of 308 ± 45% MPa, whereas the samples reach a compressive yield strength of 896 ± 6%. Thus, bending mode is more sensitive to scattering of fracture strength than compressive mode, originating from the higher sensitivity to inclusions and micro-pores in case of tension stresses. For a more precise determination of the avarge bending strength, a Weibull analysis would be neceassary, but because of the high material costs of Pd and the poor mechanical properties, this alloy does not show promising properties for the industrial application and it is for this reason that the number of bending tests performed in this work was limited.

Besides the hardness measurements and the three-point bending flexural tests, the longitudinal and transversal ultrasonic sound velocities are measured in order to determine Young's modulus and Poisson's ratio. E and ν are determined to be 95 ± 5 GPa and 0.405±0.01 as well as 83±5 GPa and 0.410±0.01 for $Pd_{43}Cu_{27}Ni_{10}P_{20}$ and $Pd_{31}Ni_{42}S_{27}$, respectively. The values of Young's modulus are in good agreement with that obtained from the three-point flexural beam bending tests.

The data obtained from mechanical testing are summarized in the table in Fig. 5.9.

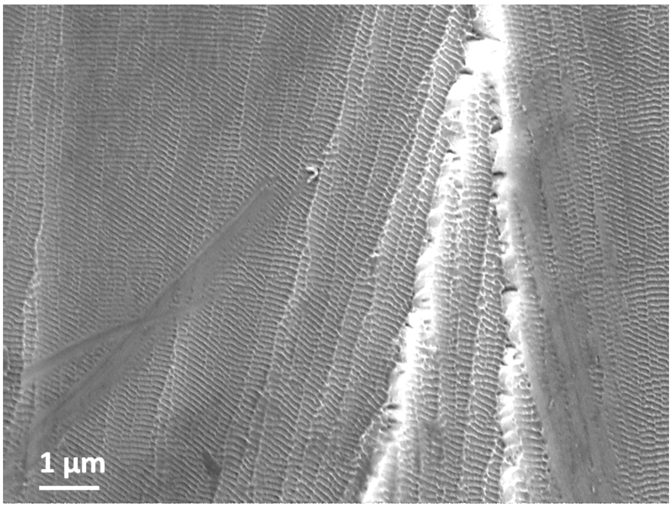

(a)

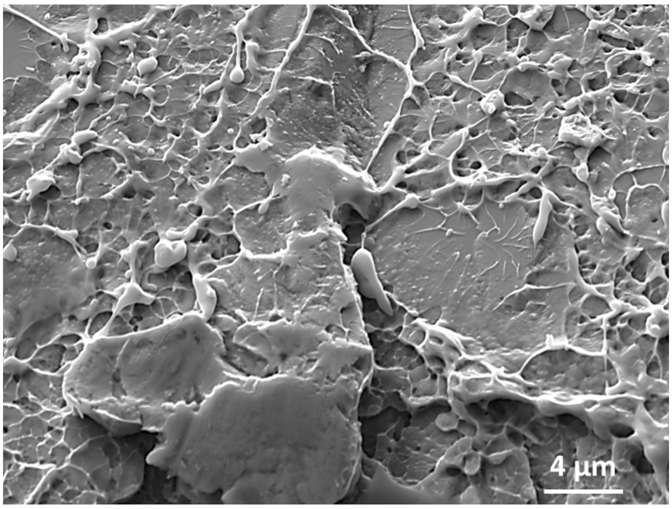

(b)

FIGURE 5.10: SE images of the fracture surface of a) $Pd_{31}Ni_{42}S_{27}$ and b) $Pd_{43}Cu_{27}Ni_{10}P_{20}$. The scale of the features in the fracture surface indicates a more brittle behavior of the S-bearing alloy, since the plastic deformation is more localized. Adapted from Ref. [8].

5.2 Characterization of Sulfur-bearing Ti- and Zr-based Bulk Metallic Glasses

Among all BMGs, in particular Zr-based and Ti-based bulk glass forming alloys have drawn the attention of the industry for the use as structural material. The novel developed Ti-based BMGs may be even more interesting for application due the suitable constituents and the high Ti-content. Thus, an in-depth characterization of their properties is necessary. For this, different alloys are chosen from the previous chapter, with the main focus on the Ti-rich $Ti_{60}Zr_{15}Cu_{17}S_8$ and the Zr-rich $Zr_{56.5}Ti_{13.3}Ni_{13.6}Cu_{9.6}S_7$. In combination with crystallization experiments and structural investigations, the thermo-physical properties may allow to understand the process of glass formation, yielding new strategies for the alloy design in this novel alloying system. So far, the limited glass forming ability and thermal stability of Ti-based glass forming alloys did not allow a proper characterization of their thermo-physical properties, so that in the frame of this work the thermo-physical properties of this subgroup of BMGs are determined for the first time. The obtained thermo-physical properties are inter alia required for simulation studies of casting processes for future applications.

To reveal the superiority of the novel Ti- and Zr-based glass forming alloys over commercially used glassy and crystalline alloys, the mechanical and electrochemical properties are measured, since the high strength-to-density ratio in combination with the high corrosion resistance are the main reasons for the use of (crystalline) Ti-alloys such as Ti6Al4V.

5.2.1 Thermodynamics of $\mathbf{Ti_{60}Zr_{15}Cu_{17}S_8}$ and $\mathbf{Zr_{56.5}Ti_{13.3}Ni_{13.6}Cu_{9.6}S_7}$

In Fig. 5.11 the results of the heat capacity measurements in vicinity of the glass transition of the $Ti_{60}Zr_{15}Cu_{17}S_8$ and the $Zr_{56.5}Ti_{13.3}Ni_{13.6}Cu_{9.6}S_7$ glass forming alloys are shown. Arrows mark the characteristic temperatures obtained by DSC and DTA measurements at 0.33 K/s (see section 4.3). Using equation 3.3 the molar heat capacity of the solids (glass/ crystal) can be described. At 348 K the values of $c_p^{glass}(T)$ and $c_p^{x-tal}(T)$ are determined to 26.2 J g-$atom^{-1}$ K^{-1} and 25.8 J g-$atom^{-1}$ K^{-1} for $Ti_{60}Zr_{15}Cu_{17}S_8$ and 26.9 J g-$atom^{-1}$ K^{-1} and 26.8 J g-$atom^{-1}$ K^{-1} for $Zr_{56.5}Ti_{13.3}Ni_{13.6}Cu_{9.6}S_7$, respectively. It is evident that the molar heat capacity of the glassy state is in both cases slightly higher than that of the crystalline state. Nevertheless, all values are close to the value of 3R = 24.94 J g-$atom^{-1}$ K^{-1} and thus, are in good agreement with Dulong-Petit's law.

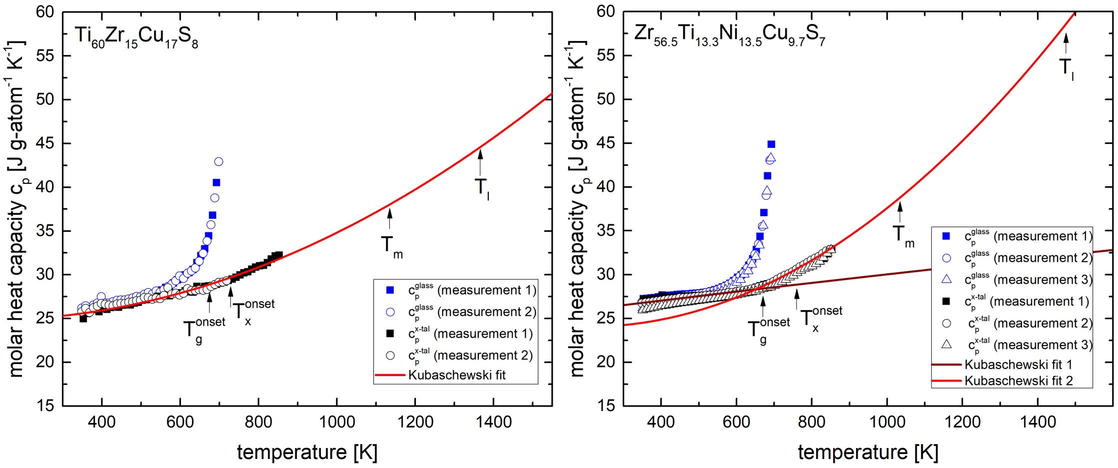

(a) (b)

FIGURE 5.11: Molar heat capacity $c_p(T)$ of a) $Ti_{60}Zr_{15}Cu_{17}S_8$ and b) $Zr_{56.5}Ti_{13.3}Ni_{13.6}Cu_{9.6}S_7$. For both alloys, $c_p(T)$ of the glass and of the crystal increases with temperature. In vicinity of T_g^{onset} the value of $c_p^{glass}(T)$ increases rapidly. The low thermal stability ($\Delta T = T_x^{onset} - T_g^{onset}$) does not allow a proper determination of the molar heat capacity of the deeply undercooled liquid. The solidus temperature T_m and the liquidus temperature T_l are also indicated.

For both alloys the molar heat capacity of the crystalline mixture ascends with temperature. Extrapolation of the data of $Ti_{60}Zr_{15}Cu_{17}S_8$ (Fig. 5.11a) yields a value of 38 J g-$atom^{-1}$ K^{-1} at the solidus temperature T_m, which is rather high in comparison to other bulk glass forming alloys [233]. In case of $Zr_{56.5}Ti_{13.3}Ni_{13.6}Cu_{9.6}S_7$ (Fig. 5.11b), a kink can be observed in the $c_p^{x-tal}(T)$ data at about 650 K. Here, fitting of the data below 650 K leads to a value of 30 J g-$atom^{-1}$ K^{-1} at T_m, whereas fitting above 650 K leads to a value of 38 J g-$atom^{-1}$ K^{-1}.

The molar heat capacity of the glass increases rapidly when reaching the glass transition temperature. Different initial temperatures have been chosen as starting points for the step-method in order to measure the molar heat capacity of the deeply undercooled liquid. However, the low thermal stability of both alloys prohibits a proper determination of the molar heat capacity of the undercooled liquid. The highest value of $c_p^{glass}(T)$ is measured to be 42.9 J g-$atom^{-1}$ K^{-1} and 44.8 J g-$atom^{-1}$ K^{-1} for $Ti_{60}Zr_{15}Cu_{17}S_8$ and $Zr_{56.5}Ti_{13.3}Ni_{13.6}Cu_{9.6}S_7$, respectively. These values are in good agreement with these observed for other Zr- and Cu-Ti-based bulk metallic glasses, such as Vitreloy 105 ($Zr_{52.5}Ti_5Cu_{17.9}Ni_{14.6}Al_{10}$) or Vitreloy 101 ($Cu_{47}Ti_{34}Zr_{11}Ni_8$), which also show values of about 45 J g-$atom^{-1}$ K^{-1} in the supercooled liquid region [233].

Because of the high reactivity of Ti- and Zr-based melts, an accurate measurement of the heat capacity of the equilibrium liquid is hardly possible. In case of $Ti_{60}Zr_{15}Cu_{17}S_8$ and $Zr_{56.5}Ti_{13.3}Ni_{13.6}Cu_{9.6}S_7$, the broad melting interval ($T_l - T_m$) makes the determination of $c_p^l(T)$ above the liquidus temperature T_l even more complicated. In order to estimate the Gibbs free energy difference between the liquid and the crystal, the enthalpy of fusion or rather the entropy of fusion can be used (see section 4.3). Unfortunately, the strong reactions between the melt and the crucible and/or atmosphere, do not allow an accurate determination of ΔH_f, since the reactions are changing the total value of the enthalpy and impeding the determination of the baseline. It is for this reason, that the thermodynamic functions of the liquid phase are not accessible using the methods of this work and the Gibbs free energy difference between the liquid and the crystal can not be determined. For the future, experiments on the International Space Station (ISS) are proposed to the European Space Agency (ESA).

5.2.2 Kinetics of $Ti_{60}Zr_{15}Cu_{17}S_8$ and $Zr_{56.5}Ti_{13.3}Ni_{13.6}Cu_{9.6}S_7$

Using the approach proposed by Wei et al. (see section 3.2.1.3) [41], the kinetic fragility at low temperatures[2] can be estimated by equation 3.8. There, the slope of the heat flow at T_g^{onset} of a DSC measurement at 1 K/s is evaluated. The first derivative of a DSC measurement at 1 K/s normalized by the onset of the glass transition temperature T_g^{onset} is shown in Fig. 5.12a and Fig. 5.12b for $Ti_{60}Zr_{15}Cu_{17}S_8$ and $Zr_{56.5}Ti_{13.3}Ni_{13.6}Cu_{9.6}S_7$, respectively. The corresponding values of the fragility parameter D^* are 27.6 ± 2.5 and 26.8 ± 2.5, indicating a strong kinetic behavior. The second approach described in section 3.2.1.3, which was proposed by Wang et al. [47], can not be used in this alloying system, since the entropy of fusion is not accessible due to the above discussed issues regarding the reactivity of the melt and the high liquidus temperature.

The low temperature structural relaxation times are determined using the different T_g-shift methods described in section 3.2.1.3.
For this, as-cast samples of $Ti_{60}Zr_{15}Cu_{17}S_8$ and $Zr_{56.5}Ti_{13.3}Ni_{13.6}Cu_{9.6}S_7$ are heated with different rates (0.083 - 3 K/s) from room temperature to the supercooled liquid region above the end of the glass transition T_g^{end} and are then cooled down to room temperature using the same rate as upon heating. Subsequently, the samples are heated again with the same rate above T_x^{onset}. Due to this procedure, the onset temperature of the glass transition T_g^{onset} coincidences with the fictive temperature $T_g^{fictive}$ and the rate dependence of $T_g^{fictive}$ can be evaluated [36, 73, 145, 220]. The resulting DSC traces are displayed in Fig. 5.13. In order to emphasize the effect of the standard treatment, scans of as-cast samples are shown as dashed lines. The resulting transition times τ_{trans} are calculated using equation 3.5 and are shown in Fig. 5.15 together with the equilibrium viscosities. Solely fitting of the transition times with equation 2.9 leads

---

[2] Assuming a fragile-to-strong transition of the liquid (see section 2.2.2.2), the temperature sensitivity of the relaxation quantities of the high temperature equilibrium liquid and the deeply undercooled liquid in vicinity of the glass transition can differ.

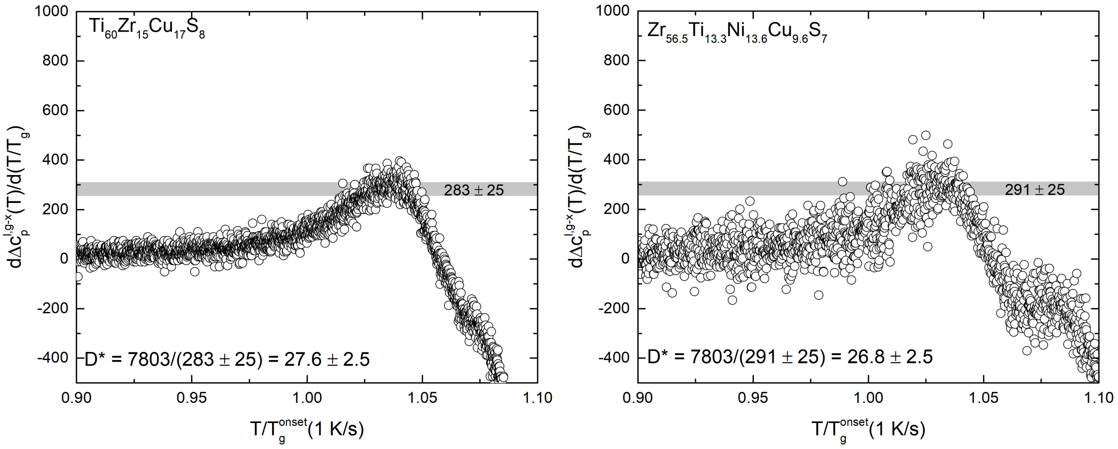

(a) (b)

FIGURE 5.12: First derivative of the heat flow of a DSC measurement at 1 K/s normalized by the onset of the glass transition temperature T_g^{onset} for a) $Ti_{60}Zr_{15}Cu_{17}S_8$ and b) $Zr_{56.5}Ti_{13.3}Ni_{13.6}Cu_{9.6}S_7$. From the slope at T_g^{onset} the fragility of the alloy can be estimated according to equation 3.8. Both alloys are estimated to exhibit a strong kinetic behavior.

to a fragility parameter D^* of roughly 55 for both alloys (dotted lines in Fig. 5.15), which is enormously high for a metallic glass forming liquid.

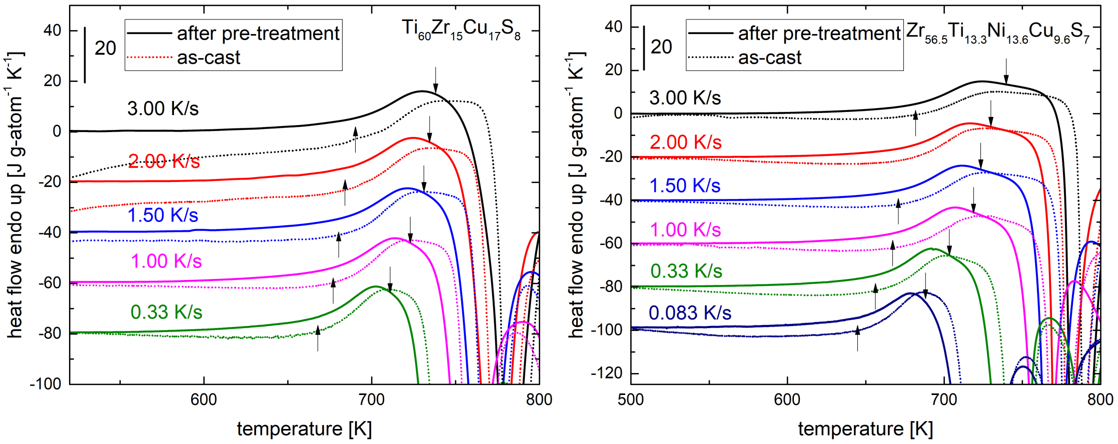

(a) (b)

FIGURE 5.13: DSC traces of 500 μm plates of a) $Ti_{60}Zr_{15}Cu_{17}S_8$ and b) $Zr_{56.5}Ti_{13.3}Ni_{13.6}Cu_{9.6}S_7$ with different thermal histories (as-cast and pre-treated) and with varying heating rates. The arrows indicate the onset and the end of the glass transition. The change of the width (T_g^{end}-T_g^{onset}) yields the structural relaxation time τ_α, which is attributed to T_g^{onset} of the respective rate. For both alloys a low temperature sensitivity of τ_α or rather τ_{trans} is revealed by this method (Fig. 5.15a,b).

The evaluation of the rate sensitivity of $T_g^{fictive}$ by the method proposed by Angell et al. (see section 3.2.1.3) [36], also yields fragility parameters between 40 to 50 (Fig. 5.14). Hence, not the method itself indicates a very strong kinetic behavior but the rate dependence of $T_g^{fictive}$. This effect is discussed later in this section.

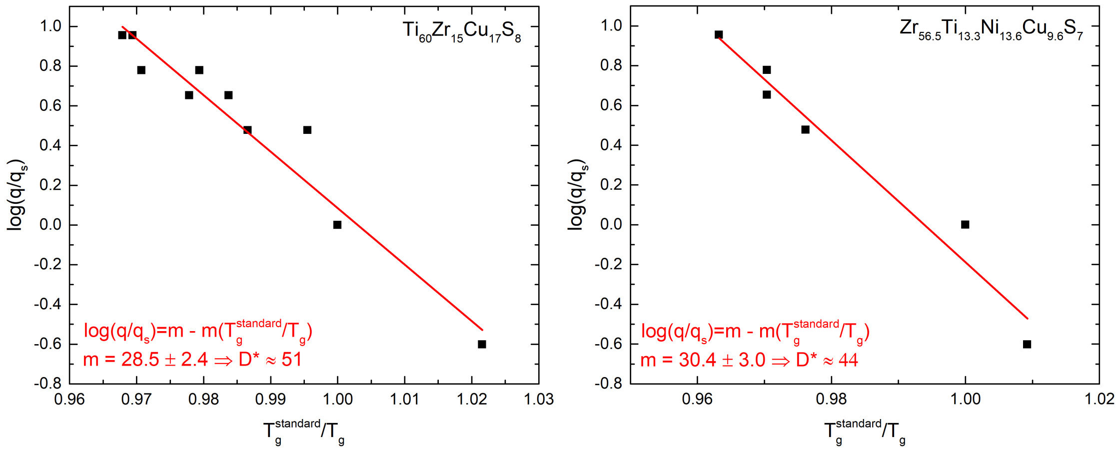

(a) (b)

FIGURE 5.14: Evaluation of the rate dependence of $T_g^{fictive}$ for c) $Ti_{60}Zr_{15}Cu_{17}S_8$ and d) $Zr_{56.5}Ti_{13.3}Ni_{13.6}Cu_{9.6}S_7$ according to Ref. [36], revealing a strong kinetic behavior for both alloys.

For a more accurate description of the low temperature fragility, the equilibrium viscosities are measured using a thermo-mechanical analyzer (TMA) (see section 3.2.2). In Fig. 5.15a and Fig. 5.15b the results of the isothermal TMA measurements are shown. The equilibrium viscosities are determined using equation 3.10. At some temperatures a kink is observed before reaching a stable plateau value of the viscosity, which is attributed to a phase separation of the deeply undercooled liquid or a smeared out crystallization. Such a behavior is commonly observed for Zr-based BMGs [217–219]. In practice, the KWW fit is carried out only for times below this event. In some cases, however, an continuous increasing viscosity is observed and the onset of the phase separation or crystallization is not detectable. Therefore, the crystallization times from the isothermal crystallization experiments measured in DSC (see section 5.2.3) are taken into account to estimate the onset of crystallization and to improve the quality of the fitting. Finally, fitting of the equilibrium viscosities with a VFT-type equation (equation 2.8), yields D^* values of 26.9 and 30.2 for $Ti_{60}Zr_{15}Cu_{17}S_8$ and $Zr_{56.5}Ti_{13.3}Ni_{13.6}Cu_{9.6}S_7$, respectively (Fig. 5.15c,d). These values are in the range of other Zr- or Cu-Ti-based BMGs [53, 217, 218, 234].
In Fig. 5.15c and Fig. 5.15d also a continuous TMA measurement with 0.33 K/s is shown for each alloy. Here, a discontinuity of the viscosity is observed at temperatures above T_g^{onset} (marked with a black arrow). For comparability also a DSC scan at 0.33 K/s is displayed in Fig. 5.15c and d. The transition times from the T_g-shift measurements are converted into viscosities using equation 2.7. As proportionality factor $G_{\tau-\eta}$[3] a value of 6.5×10^8 GPa and 3×10^8 GPa is determined by shifting the relaxation times on the values of the VFT fit of the equilibrium viscosities.

---

[3] $G_{\tau-\eta}$ is proportional but not equal to the high frequency shear modulus G_∞ as discussed in section 5.1.2 and Ref. [39, 221].

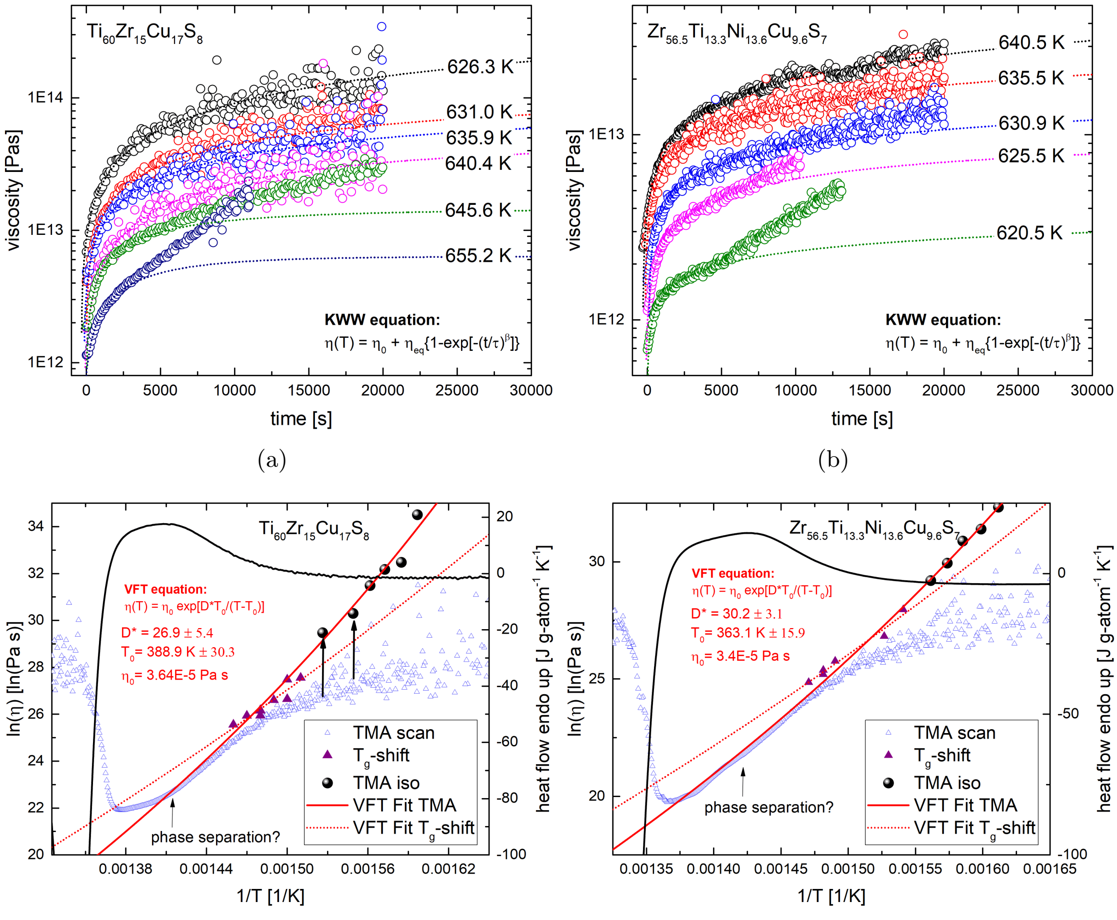

(a) (b)

(c) (d)

FIGURE 5.15: a) and b) display isothermal low temperature equilibrium viscosity measurements of $Ti_{60}Zr_{15}Cu_{17}S_8$ and $Zr_{56.5}Ti_{13.3}Ni_{13.6}Cu_{9.6}S_7$, respectively. The TMA measurements are fitted using the KWW equation. In c) and d) a continuous TMA measurement at 0.33 K/s is shown together with relaxation times from the T_g-shift measurements and the equilibrium viscosities from the isothermal TMA measurements for $Ti_{60}Zr_{15}Cu_{17}S_8$ as well as $Zr_{56.5}Ti_{13.3}Ni_{13.6}Cu_{9.6}S_7$. In addition, a DSC scan at 0.33 K/s is plotted on the right y-axis. Fitting of the equilibrium viscosities from the TMA measurements with a VFT equation reveals a rather high fragility parameter D^* of 26.9 and 30.2 for $Ti_{60}Zr_{15}Cu_{17}S_8$ and $Zr_{56.5}Ti_{13.3}Ni_{13.6}Cu_{9.6}S_7$, respectively. The temperature dependence of the relaxation times points towards even higher fragility parameters, which might be attributed to phase separation or crystallization during the thermal treatment of the samples.

Viscosities of the high temperature equilibrium liquid are measured using the oscillating drop method in an electromagnetic levitator (EML) in microgravity (TEMPUS) [154–157]. Thereby, a molten metallic droplet is levitated in a electromagnetic field under microgravity and from forced oscillations the dynamic viscosity and the surface tension can be calculated. A detailed description of the procedure can be found in section 3.2.3. In Fig. 5.16a the oscillation of the radius in one direction in space of a liquid droplet of $Ti_{60}Zr_{15}Cu_{17}S_8$, which is forced by a electromagnetic pulse, is shown. From the decay behavior the damping constant can be determined (equation 3.12), yielding the viscosity of the liquid (equation 3.11). An equal analysis can be conducted for the sample coupling electronics (SCE), which can be seen as an answer function of the electronics to the oscillations of the sample (Fig. 5.16b). Finally, the viscosity is plotted versus temperature in Fig. 5.17a. Here, a rather high viscosity is measured in vicinity of the liquidus temperature, which is about two orders of magnitude higher than the viscosity of a pure metal at its melting point [43]. An increased viscosity due to a crystalline proportion in the liquid phase is excluded on the basis of synchrotron experiments in the liquid state (see section 5.2.3). Moreover, the onset of crystallization is visible in the recordings of the high frequency camera during the TEMPUS experiments.

Besides the damping behavior, the frequency of the oscillation can be analyzed, which yields information about the surface tension of the sample via equation 3.13. In Fig. 5.17b, the surface tension is shown as a function of temperature. The average value of 1 N/m is rather low in comparison to liquid Zr or Ti(-alloys), which display values of about 1.5 N/m [156, 235, 236]. As stated in Ref. [237], the high surface activity of elements (e.g. O, P) could cause a compositional gradient, influencing the viscosity measurement by the oscillating drop method and hence, the method has to be verified for these kind of alloys. A reduction of the surface tension from 1.575 to 1.475 N/m by the addition of about 1 at% of O was observed in case of the Zr-based BMG $Zr_{59.3}Cu_{28.8}Al_{10.4}Nb_{1.5}$ [238]. For this alloy the viscosity of the equilibrium liquid has been measured by the container-less oscillating drop method and by container-based Couette rheometer measurements [239], suggesting that the oscillating drop method is valid for the determination of the viscosity and surface tension when surface active elements are present [238, 239].

The equilibrium viscosities of the deeply undercooled liquid in vicinity of the glass transition temperature as well as the viscosities of the equilibrium liquid are shown together in a T_g-scaled Arrhenius plot (Angell plot - Fig. 5.18). Using equation 2.8 the data in the low and high temperature regime are fitted simultaneously[4], yielding a D^* value of 19.6. Interestingly, the fit describes the course of the experimental determined viscosity

---

[4] Only the high temperature viscosity data from the visual data analysis are used in one direction of space (Fig. 5.16) in order to prevent a too strong weighting of the high temperature data.

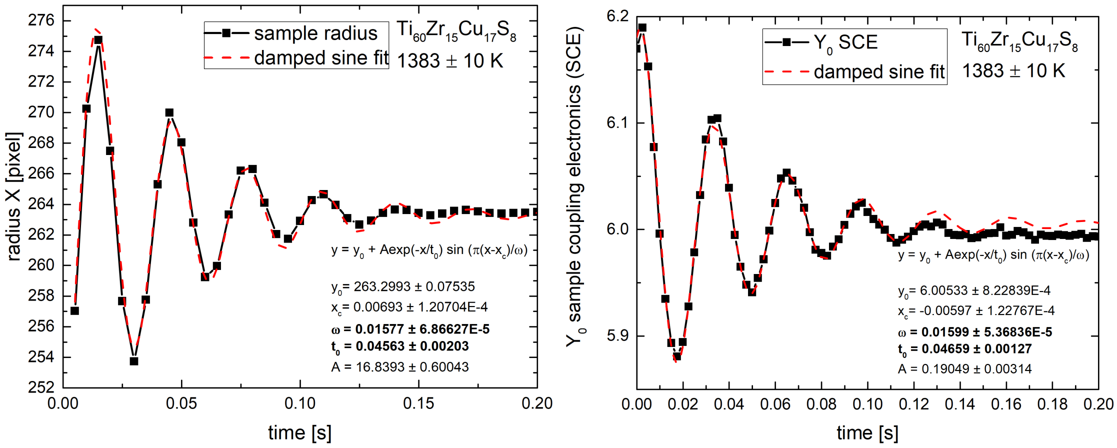

(a) (b)

FIGURE 5.16: a) Decay behavior of the forced oscillation of the radius in one direction in space (X) of a molten droplet of $Ti_{60}Zr_{15}Cu_{17}S_8$ at 1383 K measured under microgravity. The parameters of the damped sine function, which was used for fitting of the experimental data, are shown in the inset. b) Damping behavior of the sample coupling electronics (SCE), which corresponds to the answer of the positioning regulation of the magnetic field to the forced oscillation of the liquid droplet. Fitting of the data points with a damped sine function yields the damping constant t_0 and the frequency ω. Both fits reveal a similar damping behavior of the sample.

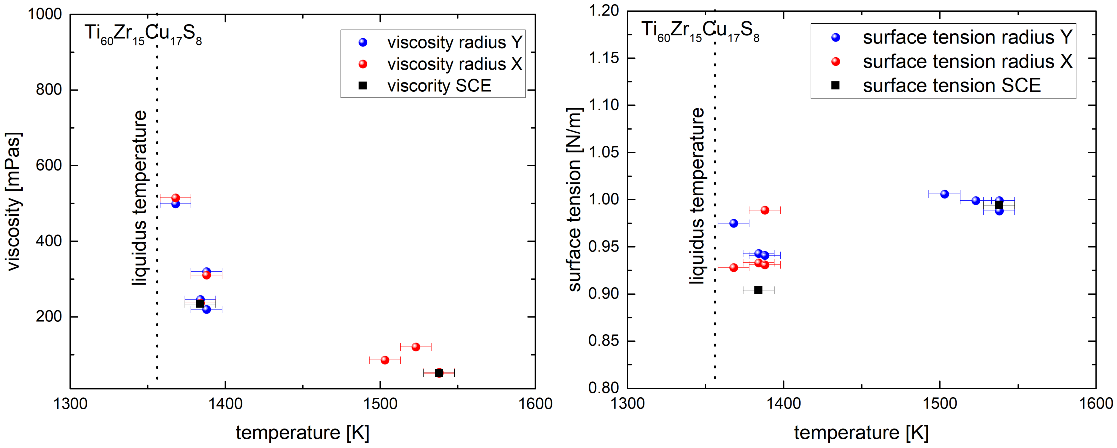

(a) (b)

FIGURE 5.17: a) Calculated viscosities of the equilibrium liquid of $Ti_{60}Zr_{15}Cu_{17}S_8$ at different temperatures above its liquidus temperature. Upon cooling the viscosity increases. In vicinity of the liquidus temperature the viscosity reaches values of above 500 mPas, which is comparably high for a metallic liquid. b) Surface tension of liquid $Ti_{60}Zr_{15}Cu_{17}S_8$ at different temperatures above its liquidus temperature. The values are below 1 N/m in average, indicating a rather low surface tension.

over fifteen orders of magnitude rather well. Such an behavior is very unusural, since in many bulk glass forming alloys like Zr-, Fe- or Au-based systems, a discrepancy between the temperature dependence of the low and the high temperature liquid is observed, beeing attributed to a so-called fragile-to-strong transition (see section 2.2.2.2). Therfore usurally a single VFT fit is not able to describe viscosity of the low and the high temperature liquid.

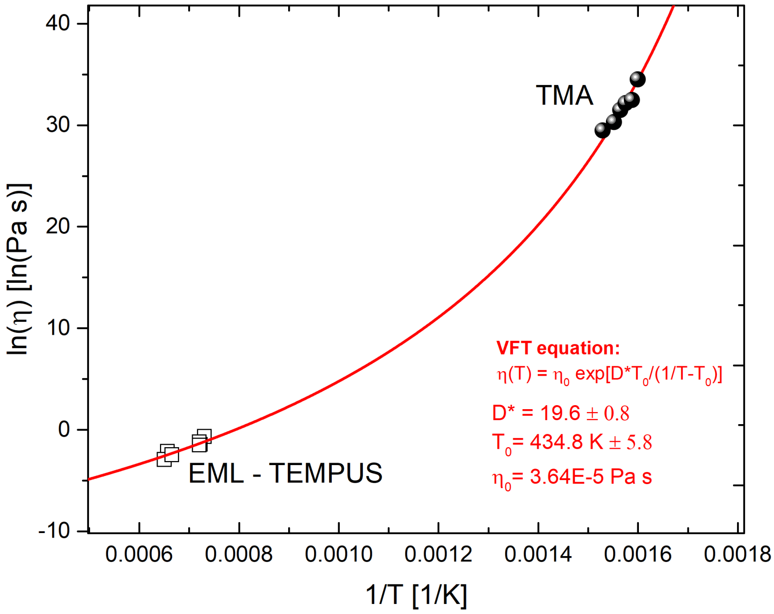

FIGURE 5.18: Angell plott of the high and low temperature viscosity of $Ti_{60}Zr_{15}Cu_{17}S_8$. A VFT fit ($D^* = 19.6$; T_0= 434.8 K) is able to describe the course of the viscosity with temperature over fifteen orders of magnitude and no discrepancy is observed between the high and the low temperature liquid.

5.2.3 Crystallization Behavior of Ti- and Zr-based Alloys

In order to identify the crystallization sequence upon rapid cooling and heating, crystallization experiments are conducted. The knowledge about the primary precipitating phases upon heating and cooling may facilitate new strategies for the improvement of the glass forming ability and thermal stability. Therefore, caloric and X-ray diffraction measurements are combined.

As already pointed out, the high reactivity of the Ti- and Zr-rich melts does not allow the measurement of the equilibrium liquid, when in contact with a crucible material. Therefore, caloric experiments are only conducted in the low temperature regime upon heating from the glassy state. Already the continuous measurements of the T_g-shift measurements provide a first insight in the process of crystallization or rather the crystallization sequence (Fig. 5.13). At slow heating rates, both alloys show at least two distinct events in the heat flow curves, being attributed to different crystallization events, whereas at higher rates the second event is getting smaller. At 3 K/s no second event is observed anymore for the specific $Zr_{56.5}Ti_{13.3}Ni_{13.6}Cu_{9.6}S_7$ alloy. Interestingly, at very low heating rates a third event can be observed at low temperatures, drastically decreasing the thermal stability. However, the Zr-based alloy shows a strongly increasing thermal stability with increasing heating rate (Fig. 5.13b). In contrast, T_g^{onset} and T_x^{onset} shift more or less in the same manner for $Ti_{60}Zr_{15}Cu_{17}S_8$ (Fig. 5.13a) and hence, the thermal stability does not increase significantly with the heating rate.

A similar observation can be made in case of isothermal measurements. At lower temperatures a clear shoulder is visible in the heat flow curve, which vanishes at higher temperatures (Fig. 5.19). Such a change of the number of distinguishable events in the DSC measurements might result on the one hand from a change in the crystallization sequence and on the other hand from the fact that at higher temperatures or heating rates the crystallization events are smeared out because of the thermal inertia of the sample.

For the identification of the crystalline phases, which correspond to the exothermic events in the DSC experiments, in-situ high energy synchrotron experiments are conducted upon heating with 0.33 K/s from the glassy phase (see section 3.3.2). The identification of crystallization products upon heating from the glassy state or rather at low temperatures is a particular challenge, since the size of these crystallites is very small (in the range of nm) due to the strongly reduced kinetics in this temperature regime [240]. According to the Scherrer equation, the small size of the crystallites results in a broadening of the Bragg diffraction peaks of the corresponding crystal structure, making the identification more difficult.

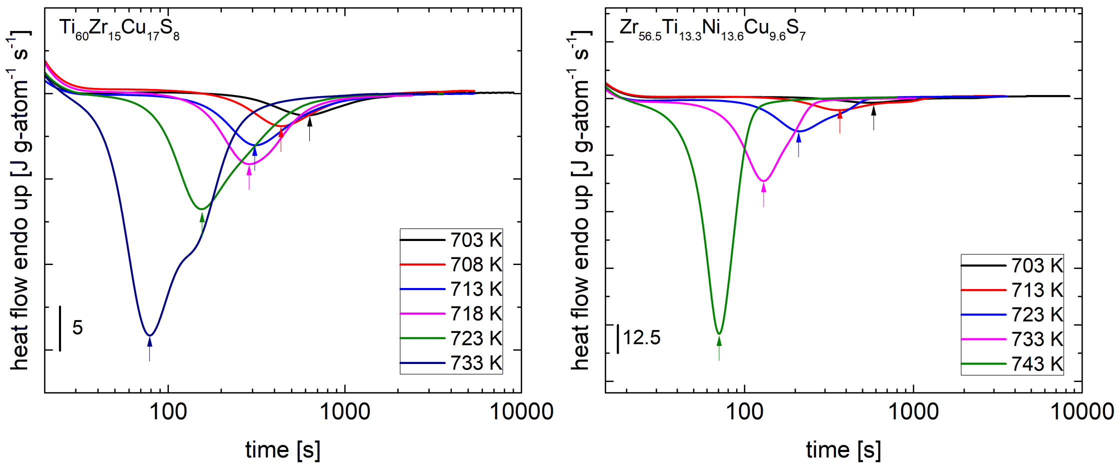

(a)

(b)

FIGURE 5.19: Isothermal heat flow curves of a) $Ti_{60}Zr_{15}Cu_{17}S_8$ and b) $Zr_{56.5}Ti_{13.3}Ni_{13.6}Cu_{9.6}S_7$ at different temperatures. The arrows indicate the peak time of the first crystallization event.

In Fig. 5.20 the results are shown for three different compositions, covering a range of 60 to 13.3 at% of Ti. In all cases, a fully amorphous pattern is observed before heating the sample, proving its glassy structure. Heating above T_x^{onset} (see section 4.3) leads to the formation of several Bragg diffraction peaks due to the formation of the primary precipitating crystalline phase. Referring to literature data about the crystallization behavior of $Ti_{45}Zr_{35}Ni_{20-x}Cu_x$ alloys, these peaks most likely correspond to an icosahedral or rather quasi-crystalline structure for all three alloys [195, 197, 241, 242]. The formation of quasi-crystalline structures as primary precipitating phase upon heating from the glassy state was already observed in several Zr-, and Ti-based bulk glass forming alloys [198, 243].

Further heating results in the formation of additional Bragg diffraction peaks, most likely resulting from the formation of new crystalline phases. For the identification one has to reconsider the phase diagrams from section 4.3. All three alloys are located in the Ti-/ Zr-rich corner of the quasi-ternary (Ti,Zr)-(Cu,Ni)-S phase diagram, close to the binary compounds Ti_2S, Ti_3S (Ti_8S_3), Ti_2Ni, Zr_2Ni, Ti_2Cu, Zr_2Cu and the solid solution. Since the ternary Ti/Zr-Ni-S and Ti/Zr-Cu-S phase diagrams are not available, only the binary phase diagrams are considered.

From intensive studies about the ternary Ti-Zr-Cu system, it is known, that the Cu-bearing compounds are stable over the iso-compositional line ($(Ti, Zr)_2Cu$, (Ti, Zr)) and hence, Ti and Zr are interchangeable in the crystalline structure [244]. The work of Chebotnikov and Molonkov revealed a shift of the Bragg diffraction peaks to smaller values of 2θ for higher Zr-contents [244], which is reasonable due to the larger atomic diameter of Zr. Furthermore, the formation of different laves phases is observed. However, for the Ti-rich alloys, $Ti_{60}Zr_{15}Cu_{17}S_8$ and $Ti_{40}Zr_{35}Cu_{17}S_8$, the peaks at higher temperatures are most likely attributed to the quasi-binary $(Ti, Zr)_2Cu$ intermetallic compound. Due to the high number of peaks, an allocation of the diffraction pattern of $Zr_{56.5}Ti_{13.3}Ni_{13.6}Cu_{9.6}S_7$ at 843.8 K to one of the expected crystalline structures is unfeasible on the basis of the available results.

The identification of the primary precipitating phases upon rapid cooling is even more challenging since the short time scales or fast dynamics make in-situ experiments rather difficult and upon cooling different solid state reaction can change the microstructure and disable an ex-situ analysis of the primary phase.
However, the ex-situ analysis of partially crystalline as-cast samples with diameters higher than the critical diameter is still one approach to identify the primary crystalline phase. These samples can be analyzed using techniques like X-ray diffraction to reveal the crystalline structure and by EDX measurements to identify the composition of the crystalline phases that are embedded in the glassy matrix. X-ray pattern of partially crystalline as-cast samples of $Ti_{60}Zr_{15}Cu_{17}S_8$, $Ti_{40}Zr_{35}Cu_{17}S_8$ and $Zr_{56.5}Ti_{13.3}Ni_{13.6}Cu_{9.6}S_7$ are shown in Fig. 5.21a. For the Ti-based alloys, the $(Ti, Zr)_2$-Cu phase can be most likely indicated by means of the Bragg diffraction peaks. This is in good agreement with the XRD pattern of quasi-ternary Ti-Cu-Ni-S alloys in Fig. 4.12 in section 4.3.2. Due to the substitution of Ti with Zr the peak positions are suggested to shift to lower values of q.
High magnification BSE images of the 4 mm rod and the ingate of $Ti_{40}Zr_{35}Cu_{17}S_8$ are shown in Fig. 5.21b. In the center of the rod, a needle-like dark phase can be observed, which is supposed to be embedded in the amorphous matrix[5]. The BSE contrast results mainly from the difference of the mean atomic number Z of the different phases. A higher value of Z leads to a higher scattering of the electrons of the primary electron beam, resulting in a brighter appearance. Since the crystallites appear dark, a lower atomic number is concluded, which is in agreement with the EDX measurements, which reveal an enrichment of S and Ti in the dark phase ($Ti_{45.96}Zr_{34.80}Cu_{6.71}S_{12.53}$). At the edges of this phase, another dark phase can be observed, but the determination of the composition is not possible since the interaction bulb of the primary electron beam is larger than the crystal size and thus, the lateral resolution of the EDX method is not sufficient. However, in the first glance, a phase with a composition close to the Ti_2Cu phase is not present, not confirming the XRD results.
The crystalline microstructure of the ingate allows a proper analysis of the composition of the respective phases, since the lower cooling rate results in a course microstructure,

---

[5] The matrix is assigned to be amorphous, since the sample shows high enthalpy of crystallization in DSC and still an amorphous halo in XRD.

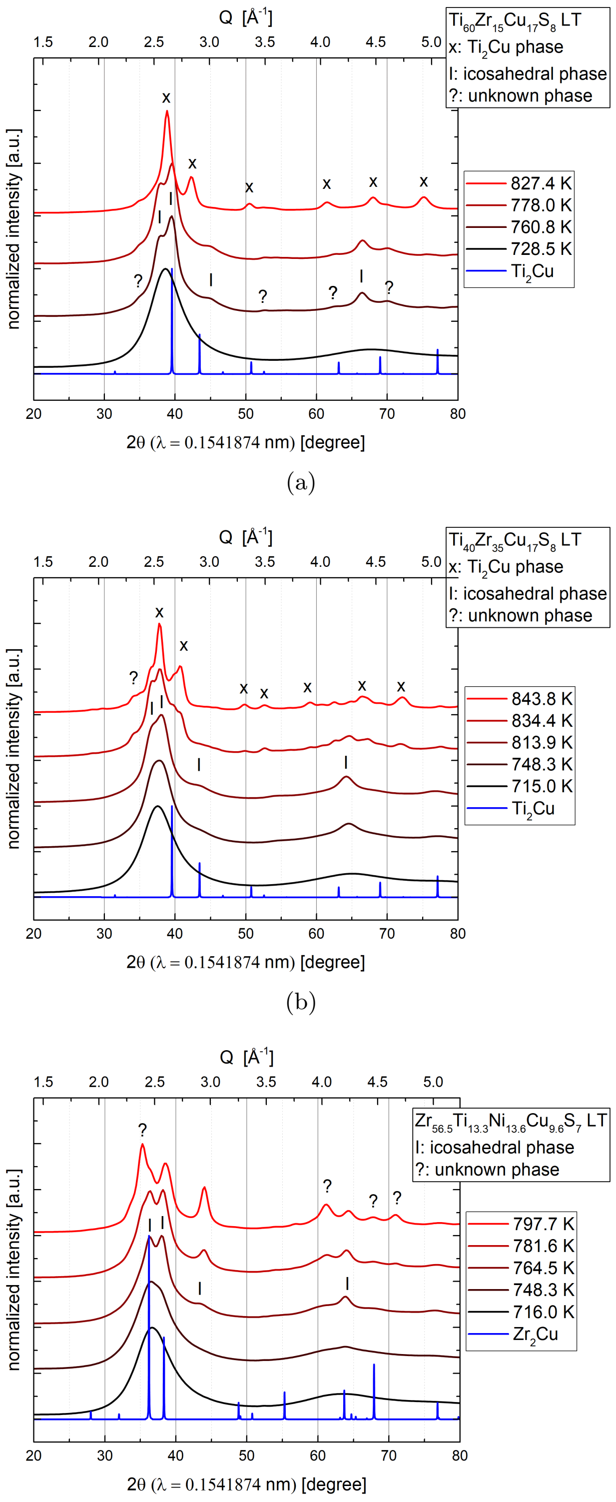

(a)

(b)

(c)

Figure 5.20: In-situ high energy synchrotron X-ray diffraction pattern of a) $Ti_{60}Zr_{15}Cu_{17}S_{8}$, b) $Ti_{40}Zr_{35}Cu_{17}S_{8}$ and c) $Zr_{56.5}Ti_{13.3}Ni_{13.6}Cu_{9.6}S_{7}$ upon heating from the glassy state at 0.33 K/s. In addition, the simulated diffraction patterns of the most likely attributable primary crystalline phases are shown. In all cases, the primary crystallization product exhibits an icosahedral or rather quasi-crystalline structure. The corresponding Bragg diffraction peaks are indicated with "I".

reducing the error of the EDX measurement (Fig. 5.21c). Here, it is evident that the dark needle-shaped phase has a S content of about 20 at%. Furthermore the second dark phase seems to have a rather low S content but is enriched in Ti (up top 58.76 at%). In between the dark needles, which are surrounded by the second dark phase, a fine bright microstructure can be observed. The composition is measured to Ti 35.52 at%, Zr 36.52 at%, Cu 25.51 at% and S 2.46 at%. This phase is associated with the Ti_2Cu phase identified in the XRD measurements. In case of the 4 mm rod, the microstructure is assumed to be even more fine and hence, might be not visible in the SEM image in Fig. 5.21b. These results imply, that the primary S-rich phase is hardly or rather not detectable using X-ray diffraction experiments. The simulated diffraction pattern of Ti_2S and Ti_8S_3 are shown in Fig. A.4. From this it is eveident, that under the same diffraction conditions the scattered intensities of the sulfide phases are significatnyl lower due to the more complex crystal structures in comparison to Ti_2Cu.

As already mentioned, an alternative approach is the in-situ analysis of the crystallization sequence. For this, in-situ X-ray diffraction experiments are carried out upon free cooling ($\approx$ 5-10 K/s) from the equilibrium liquid in an electrostatic levitator (ESL). The ESL circumvents reaction of the samples with a crucible and also reduces heterogeneous nucleation to a minimum, benefiting undercooling. Diffraction pattern at elevated temperatures are shown in Fig. 5.22a and the corresponding temperature profile during the measurement is shown in Fig. 3.6b. The temperatures of the diffraction pattern are highlighted as blue dashed lines. At 1360 K no Bragg peaks are visible in the two dimensional pattern, proving that the sample is in its equilibrium liquid state. Cooling below this temperature results in the formation of the first sharp Bragg peaks and a small recalescence can be suspected in the pyrometer data. At 1277 K the degeneration of the FSDP can be observed and at 1204 K the peaks are stronger pronounced. Further cooling leads to the formation of a pronounced crystalline diffraction pattern, which does not change upon further cooling. Below 1140 K the structure is again most likely $(Ti, Zr)_2Cu$. The onset at about 1360 K agrees with the liquidus temperature determined in the DTA measurements (1365 K) and confirms the broad melting range. The low undercooling during the ESL measurements is suggested to originate from the rather low overheating during the processing. A higher overheating is prevented by evaporation of the sample. The diffraction experiments also validate the viscosity measurements of the equilibrium liquid above 1360 K and exclude an effect of precipitating crystals on the viscosity. However, at this point the primary phase at 1277 K can not be indicated.

A BSE image of the microstructure of the sample processed in the ESL is shown in Fig. 5.22b. In general, the microstructure is equal to that of the ingate of the $Ti_{40}Zr_{35}Cu_{17}S_8$ alloy (Fig. 5.21c). Again a sulfur-rich dark phase (Ti 61.25/61.04 at%, Zr 15.95/16.24

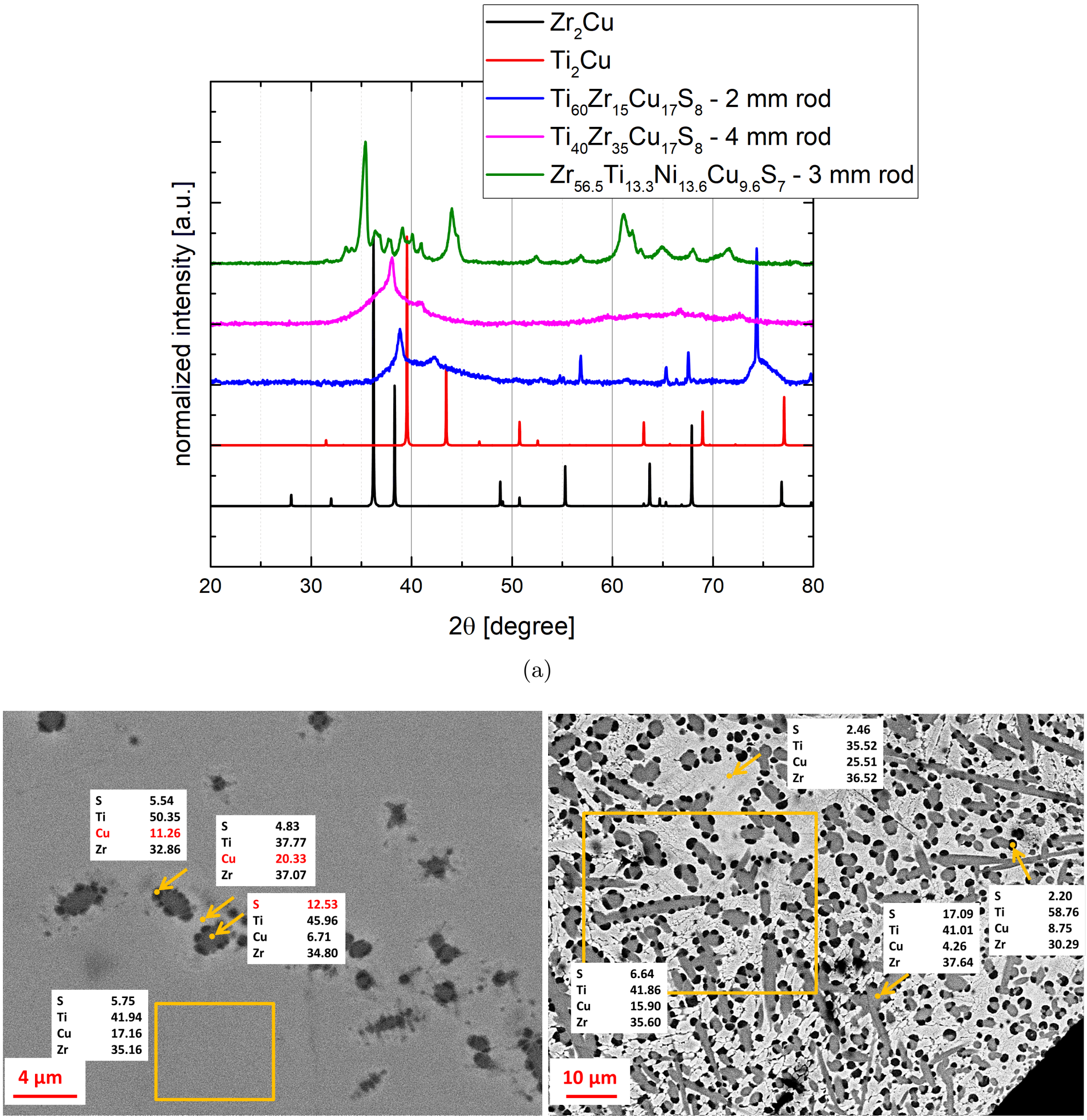

(a)

(b)

(c)

FIGURE 5.21: a) X-ray diffraction pattern of as-cast partially crystalline rods of $Ti_{60}Zr_{15}Cu_{17}S_8$, $Ti_{40}Zr_{35}Cu_{17}S_8$ and $Zr_{56.5}Ti_{13.3}Ni_{13.6}Cu_{9.6}S_7$. Furthermore the simulated diffraction patterns of the crystalline Ti_2Cu [245] and the Zr_2Cu phase [246] are shown. The simulation was carried out with the Powder Cell software [159]. In case of the Ti-based alloys, the Bragg peaks in the diffraction pattern can be attributed to Ti_2Cu, but in case of $Zr_{56.5}Ti_{13.3}Ni_{13.6}Cu_{9.6}S_7$ the crystalline phases can not be identified. b) BSE image of the microstructure of the 4 mm rod of $Ti_{40}Zr_{35}Cu_{17}S_8$. Small crystallites can be observed that are embedded in an amorphous matrix. c) BSE image of the microstructure of an ingot of $Ti_{40}Zr_{35}Cu_{17}S_8$. The slower cooling rates results in the formation of a course, crystalline microstructure. Here, the needle-shaped phase shows a strong enrichment in sulfur, whereas two other phases are visible, which are depleted in sulfur.

at%, Cu 2.41/2.52 at%, S 20.38/20.20 at%), a sulfur-depleted dark phase (Ti 77.77 at%, Zr 10.44 at%, Cu 9.18 at%, S 2.62 at%) and a sulfur-depleted, Cu-rich phase are observed (Ti 45.92 at%, Zr 28.86 at%, Cu 24.81 at%, S 0.40 at%). The latter two ones are allocated to β-Ti (=(Ti, Zr)) and Ti_2Cu, whose signature can be observed in the diffraction pattern (Supp. Fig. A.1). The role of the different phases in the process of glass formation is discussed in detail in section 6.2.2.

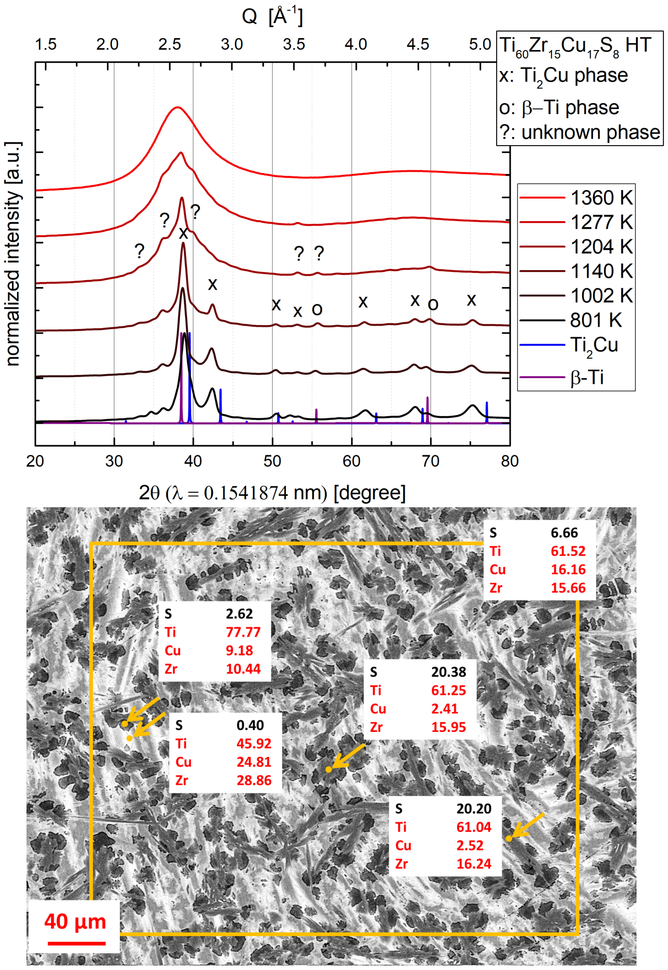

FIGURE 5.22: a) In-situ high energy synchrotron X-ray diffraction pattern of $Ti_{60}Zr_{15}Cu_{17}S_8$ upon free cooling from its equilibrium liquid. The experiments are carried out in an electrostatic levitator (ESL). At 1277 K the first sharp Bragg diffraction peaks are evident. Further cooling results in the formation of the binary intermetallic compound Ti_2Cu. The simulated diffraction pattern of Ti_2Cu [245] and β-Ti [247] are shown in blue and purple, respectively. b) BSE image of the microstructure of $Ti_{60}Zr_{15}Cu_{17}S_8$ after the processing in the ESL. Again, the needle-shaped phase show a significant enrichment in sulfur (roughly 20 at%), whereas other areas show a strong depletion in sulfur. The areas or spots where EDX measurements are performed are marked with yellow dots/arrows.

5.2.4 Structure of Ti- and Zr-based Bulk Metallic Glasses

The in-situ high energy synchrotron X-ray experiments also allow the investigation of the amorphous structure of the glass and to some extend of the undercooled liquid and the high temperature equilibrium liquid.

Fig. 5.23a displays the total structure factor S(Q) of the glassy phase of the three different alloys $Ti_{60}Zr_{15}Cu_{17}S_8$, $Ti_{40}Zr_{35}Cu_{17}S_8$ and $Zr_{56.5}Ti_{13.3}Ni_{13.6}Cu_{9.6}S_7$. It is evident and reasonable that the higher Zr-content leads to a shift of the diffraction peaks to lower values of Q due to a larger atomic diameter of Zr over Ti. Furthermore, a split of the SSDP in S(Q) can be observed for all alloys, which is less pronounced for the Zr-based alloy.

The corresponding reduced pair distribution function G(r) shows a shift of the peaks to higher values of r (Fig. 5.23b). Interestingly, the Zr-based alloy exhibits a shoulder at the lower r side of the FSDP, which is not observed for the Ti-based alloys. The SSDP in G(r) shows a shoulder at higher values of r.

The temperature sensitivity for both, S(Q) and G(r) is analyzed and discussed in detail in section 6.2.3.

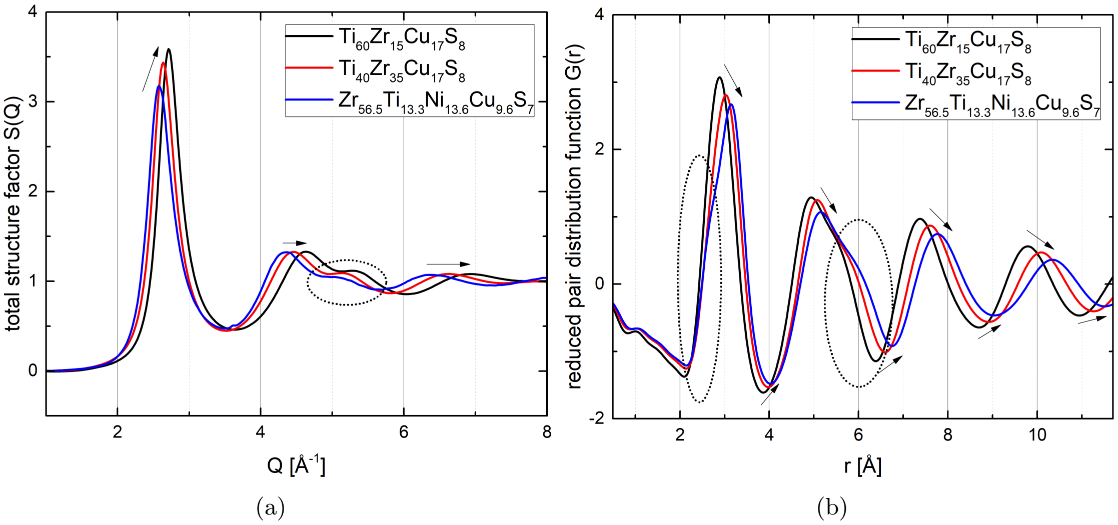

(a) (b)

FIGURE 5.23: a) Total structure factor S(Q) of glassy $Ti_{60}Zr_{15}Cu_{17}S_8$, $Ti_{40}Zr_{35}Cu_{17}S_8$ and $Zr_{56.5}Ti_{13.3}Ni_{13.6}Cu_{9.6}S_7$ at room temperature. A higher Zr-content results in a shift of the peaks to lower values of Q. b) Reduced pair distribution function G(r) of glassy $Ti_{60}Zr_{15}Cu_{17}S_8$, $Ti_{40}Zr_{35}Cu_{17}S_8$ and $Zr_{56.5}Ti_{13.3}Ni_{13.6}Cu_{9.6}S_7$ at room temperature. Here, a shift of the peaks to higher values of r is observed for alloys with a higher Zr-content (black arrows).

As shown in section 5.2.3, in-situ experiments are also carried out in the high temperature regime for the specific $Ti_{60}Zr_{15}Cu_{17}S_8$ glass forming alloy. Fig. 5.24a shows S(Q) of the equilibrium liquid at 1360 K in comparison to that of the glassy phase at 323 K.

Here, it can be observed, that the FSDP is shifted to higher Q values upon cooling. The split of the SSDP in S(Q) is already slightly present in the equilibrium liquid and gets more pronounced for the glassy structure.

The corresponding G(r) is shown in Fig. 5.24b. A high temperature sensitivity of G(r) can be observed at higher values of r, which is manifested by a splitting of the SSDP. The shift of the peak positions are indicated with black arrows.

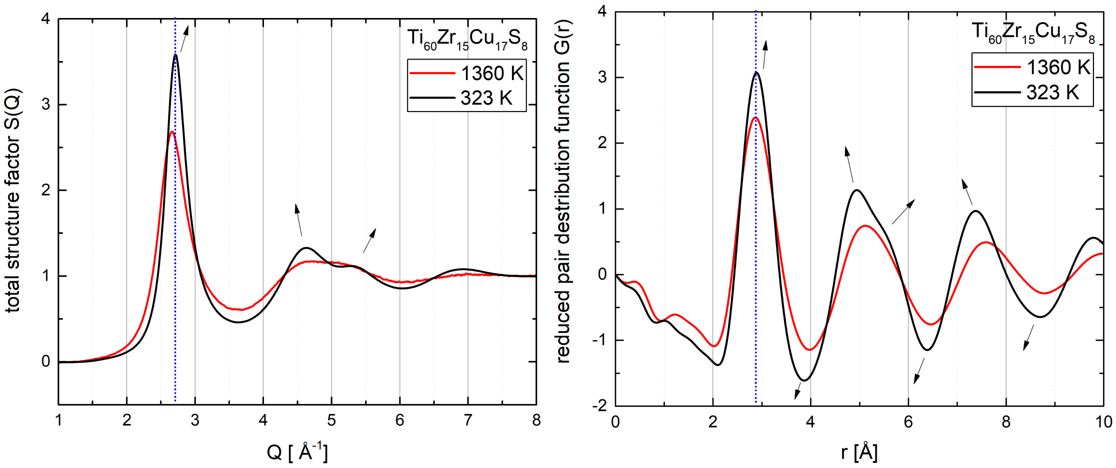

(a)

(b)

FIGURE 5.24: a) Total structure factor S(Q) of liquid and glassy $Ti_{60}Zr_{15}Cu_{17}S_8$ at 1360 K and 323 K, respectively. The shift of the peak position and the change of the shape are highlighted with arrows. b) Reduced pair distribution function G(r) of liquid and glassy $Ti_{60}Zr_{15}Cu_{17}S_8$ at 1360 K and 323 K, respectively. The shift of the peak position and the change of the shape with temperature are highlighted with arrows.

5.2.5 Mechanical Behavior of novel Ti-based Bulk Metallic Glasses

As described in section 2.4, the amorphous atomic structure of BMGs and the accompanying absence of lattice defects and other microstructural features leads to unique mechanical properties. In Fig. 5.25 three-point bending engineering stress-strain curves of different sulfur-bearing Ti- and Zr- based glass forming alloys are presented in comparison to crystalline Ti6Al4V. First of all it is evident that the amorphous alloys show similar Young's moduli ($\approx$ 100 GPa) as the crystalline titanium alloy (103 GPa). The novel Ti- and Zr-based alloys reach an flexural offset yield strength at a strain of 0.2 % of roughly 3 GPa and hence, are about two times stronger than crystalline Ti6Al4V. Furthermore, for all amorphous alloys the uniquely high elastic strain limit of about 2.5 % is observed[6]. As proposed in section 4.3.2, the introduction of Cu to the alloys has a drastic influence on the ductility. For example the $Ti_{40}Zr_{35}Ni_{17}S_8$ alloy fails before reaching its expected yield strength value (Fig. 5.25a), whereas the alloys with a Ti-content of 40 at% in combination with Cu undergo pronounced plastic deformation in bending (Fig. 5.25b). Such a behavior is of great importance for the application, since plastic deformation signals a failure before the fracture strength is reached. The ductility is also reflected in the fracture surfaces. More brittle alloys show a "glassy" or mirror-like fracture surface, whereas the more ductile ones display a dull surface.
Another interesting feature of the novel Ti-based alloys is their robustness against oxygen impurities. In section 4.3.2 it is shown that the GFA is not altered by the use of industrial grade materials. Usually, also the mechanical performance of BMGs is strongly affected by higher oxygen contents [205, 248–250]. However, in Fig. 5.25b three-point bending curve of the $Ti_{40}Zr_{35}Cu_{17}S_8$ alloy, which was synthesized from industrial grade raw materials (titanium ASTM grade 1, zirconium R60702), is shown. It displays a similar behavior than the sample produced from ultra high purity reagents, also indicating the robustness against oxygen impurities.

In addition to the three-point bending flexural tests, hardness measurements are carried out. In their as-cast state, the amorphous alloys achieve hardness values of up to 550 HV5 and hence, are about 200 HV harder than crystalline Ti6Al4V. The fact that subsequent heat treatments are unnecessary for BMGs to reach such high hardness and strength values is one of their major advantages over crystalline alloys.

By measuring the transversal and longitudinal ultrasonic sound velocity of the samples, Young's modulus and Poisson's ratio can be determined using equation 3.19 and 3.18. The volumetric mass density ρ is measured according to the Archimedes method. In

---

[6] The elastic strain limit in bending mode is higher due to the uneven state of stress. Here, the strain in the extreme fiber is considered.

general, the elastic moduli are in good agreement with these from the three-point bending tests. Poisson's ratio of the alloys is of about 0.39 and increases slightly with an increasing Zr-content. As reported in Ref. [251] and Ref. [252] , a higher value of ν points towards a more ductile mechanical behavior, being in good agreement with the findings about the Ti-alloys in this work.

All in all, the novel developed alloys show an extraordinary strength-to-density ratio and a high hardness in the as-cast state in combination with an ultra high elasticity in comparison to crystalline Ti-alloys. The use of industrial grade materials does not significantly alter these properties and hence, these Ti-BMGs might be capable to outperform crystalline Ti-alloys in several fields of application. The mechanical properties are summarized in table 5.4 and table 5.5.

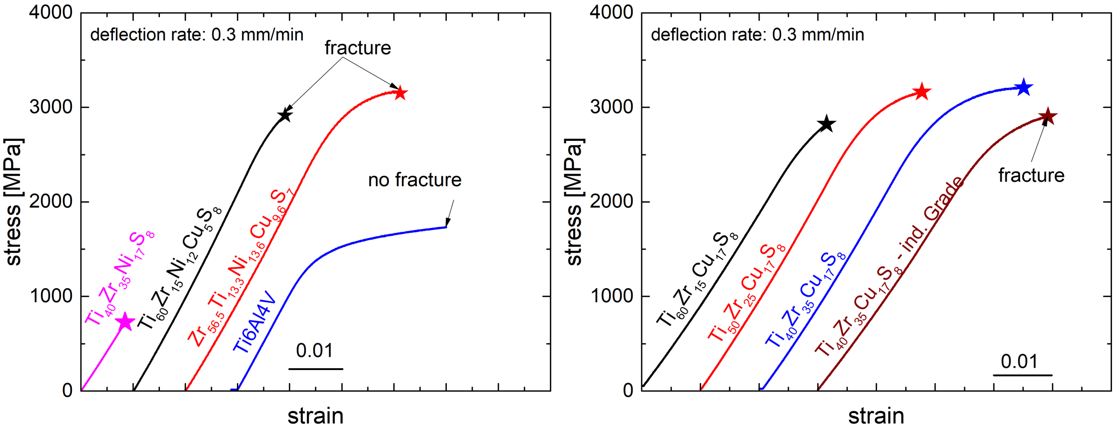

(a) (b)

FIGURE 5.25: a) Engineering stress - strain curves of different glassy Ni-and S-bearing Ti-/Zr-alloys in comparison to crystalline Ti6Al4V measured by three-point flexural beam bending tests. The Cu-free BMG $Ti_{40}Zr_{35}Ni_{17}S_8$ shows a low fracture strength in comparison to the Cu-containing Ti- and Zr-based BMGs, which exhibit a twice that high fracture strength than crystalline Ti6Al4V. b) Engineering stress - strain curves of different Ni-free, S-bearing Ti-based metallic glasses under bending load. All alloys show a high fracture strength followed by a plastic regime. Even the sample of $Ti_{40}Zr_{35}Cu_{17}S_8$, which is produced from industrial grade raw materials, shows an excellent mechanical performance. Data are taken from Ref. [7, 9].

Table 5.4: Mechanical properties of amorphous sulfur-bearing Ti-based alloys of this work in comparison to crystalline Ti6Al4V and amorphous Vitreloy 101. HV5 is the hardness on Vicker's scale and σ_{yield}, $E_{bending}$ and $\sigma_{fracture}$ correspond to the offset yield strength (0.2 %), Young's modulus and the fracture yield strength, respectively, which are measured in three-point beam bending. ϵ_{el} is the elastic strain limit and ϵ_{total} the total strain to failure. The more detailed definition can be found in section 3.4.

Alloy Composition $[at\%]$	HV5	σ_{yield} $[GPa]$	$\sigma_{fracture}$ $[GPa]$	$E_{bending}$ $[GPa]$	ϵ_{el} [%]	ϵ_{total} [%]
$Ti_{40}Zr_{35}Ni_{17}S_8$	—	0.7	0.7	89	0.8±0.1	0.8±0.1
$Ti_{60}Zr_{15}Ni_{12}Cu_5S_8$	555±8	2.9±0.1	2.9±0.1	108	2.4±0.1	2.9±0.1
$Ti_{60}Zr_{15}Cu_{17}S_8$	547±6	2.8±0.1	2.8±0.1	98	2.5±0.1	3.1±0.1
$Ti_{50}Zr_{25}Cu_{17}S_8$	524±12	3.0±0.1	3.1±0.2	98	2.5±0.1	3.8±0.1
$Ti_{40}Zr_{35}Cu_{17}S_8$	509±17	3.0±0.2	3.2±0.2	96	2.6±0.1	4.5±0.1
$Ti_{40}Zr_{35}Cu_{17}S_8$ ind. Grade	524±8	2.7±0.2	3.0±0.2	92	2.6±0.1	3.8±0.1
$Zr_{56.5}Ti_{13.3}Ni_{13.6}Cu_{9.6}S_7$	498±8	2.9±0.1	3.2±0.1	100	2.5±0.1	4.1±0.1
$Cu_{47}Ti_{34}Zr_{11}Ni_8$ (Vit101)	576±5	2.8±0.1	3.2±0.1	105	2.4±0.1	6.2±0.1
$Ti_{86.2}Al_{10.2}V_{3.6}$ (Ti6Al4V)	340±5	1.4±0.2	—	103	0.5	no frac.

Table 5.5: Mechanical properties of amorphous sulfur-bearing Ti-based alloys of this work in comparison to crystalline Ti6Al4V and amorphous Vitreloy 101. V_L and V_T are the longitudinal and transversal sound velocities. ρ is the volumetric mass density determined by Archimedes' measurements, ν corresponds to Poisson's ratio and E_{US} to Young's modulus determined by ultrasonic measurements.

Alloy Composition $[at\%]$	V_L $[mm\mu^{-1}s^{-1}]$	V_T $[mm\mu^{-1}s^{-1}]$	ρ $[g/cm^3]$	E_{US} $[GPa]$	ν
$Ti_{60}Zr_{15}Cu_{17}S_8$	—	—	5.5±0.1	—	—
$Ti_{50}Zr_{25}Cu_{17}S_8$	5.62±0.11	2.45±0.02	5.7±0.1	95	0.38±0.01
$Ti_{40}Zr_{35}Cu_{17}S_8$	5.43±0.05	2.33±0.02	5.9±0.1	89	0.39±0.01
$Ti_{40}Zr_{35}Cu_{17}S_8$ ind. Grade	5.49±0.1	2.40±0.02	5.9±0.1	97	0.38±0.01
$Zr_{56.5}Ti_{13.3}Ni_{13.6}Cu_{9.6}S_7$	5.24±0.17	2.14±0.07	6.8±0.1	89	0.40±0.01
$Cu_{47}Ti_{34}Zr_{11}Ni_8$ (Vit101)	5.43±0.08	2.27±0.03	6.9±0.1	105	0.39±0.01
$Ti_{86.2}Al_{10.2}V_{3.6}$ (Ti6Al4V)	6.59±0.05	4.4±0.1	3.11±0.06	115	0.35±0.01

5.2.6 Corrosion Behavior of novel Ti-and Zr-based Alloys

Because of their chemical and structural homogeneity, often a high corrosion resistance is expected for BMGs. However, most BMGs are rather complex alloys, which have shown to tend to chloride-induced pitting corrosion. The pitting corrosion is attributed to the large standard electrode potential difference between the constituents, like for example between Cu and Zr [122, 253].

Fig. 5.26a,b displays potentiodynamic polarisation curves of some novel Ti- and Zr-based BMGs in a 0.1 M NaCl borate buffered solution. Additionally, the results from two commercially available BMGs Vitreloy 101 ($Cu_{47}Ti_{34}Zr_{11}Ni_{8}$), Vitreloy 105 ($Zr_{52.5}Ti_{5}$-$Cu_{17.9}Ni_{14.6}Al_{10}$) and the crystalline Ti6Al4V ($Ti_{86.2}Al_{10.2}V_{3.6}$) alloy are shown for comparison. Vitreloy 101 and Vitreloy 105 are chosen since they both have the same main constituents (Ti, Zr, Cu, Ni). The characteristic values[7] of each alloy are summarized in Table 5.6. The passive current density i_{pass} of the sulfur-bearing alloys is slightly higher in comparison to the Vitreloy alloys and Ti6Al4V, but it is reached for all alloys at about 0 V vs. SCE and thus, the process for passivation is assumed to take place at the same period of time. Ti6Al4V, which is known to have a very high corrosion resistance, displays a passive region up to 1.015 ± 0.003 V vs. SCE. Here, the current density increases because the oxidation of water takes place. A similar behavior is observed for the $Ti_{50}Zr_{25}Cu_{17}S_{8}$, but the step of the current density i is higher, which might be caused by a different defect state and conductivity of the passivation layer [127].
Vitreloy 101 and Vitreloy 105 show a shorter passive region until a drastic increase of the current density occurs. This increase is attributed to pitting corrosion [122, 125, 253–257]. In comparison, the $Ti_{40}Zr_{35}Cu_{17}S_{8}$ and the $Zr_{56.5}Ti_{13.3}Ni_{13.6}Cu_{9.6}S_{7}$ show an intermediate passive region, whereby the pitting potential E_{pit} of $Ti_{40}Zr_{35}Cu_{17}S_{8}$[8] is nearly as high as the breakdown potential E_{break} of Ti6Al4V and $Ti_{50}Zr_{25}Cu_{17}S_{8}$.

From these results different tendencies can be derived. On the one hand the substitution of Ti with Zr results in a decrease of the corrosion resistance, but on the other hand the (Ti,Zr) to the Cu (Ni) ratio is even more crucial. A high amount of Cu and even Ni seems to drastically reduce the corrosion resistance because of a stronger tendency for pitting corrosion. As discussed in section 4.3, commonly, Ti-based bulk glass forming alloys show high contents of Cu and/or Ni (up to 50 at%). These relatively high amounts of Cu lead to a high sensitivity for pitting corrosion, especially in chloride-containing electrolytes, since the formation of CuO and pitting corrosion is favored by a high Cu-content in Ti- and Zr-alloys due to the large difference in the standard electrode

---

[7] The definition of the characteristic values is shown in detail in section 3.5.

[8] In this study it is observed, that for $Ti_{40}Zr_{35}Cu_{17}S_{8}$ the surface quality has a strong influence whether pitting corrosion takes place or not. Similar findings are proposed in Ref. [258].

potential [122, 125, 253–257]. This becomes apparent when considering Vitreloy 101. Often a higher corrosion resistance is expected due to the high amount of Ti, but in fact the corrosion resistance is lower than that of Vitreloy 105 due to the high Cu content. Here it has to be noticed that Vitreloy 105 also has a not negligible amount of Al, whose effect is not investigated in this work. However, the corrosion resistance of Vitreloy 101 is lower than that of all other alloys analyzed in this work. The higher corrosion resistance of the Ti- and Zr- alloys is not attributed to the amount of S, since S additions to Vitreloy 101 do not significantly increase its corrosion resistance as shown elsewhere.

Fig. 5.27 shows images of the surfaces of the samples subsequent to the potentiodynamic polarization measurements. On the surfaces of the alloys, which display a rapid increase during the voltage sweep during the polarization measurements, corrosion pits are clearly visible. The size of the corrosion pits in $Ti_{40}Zr_{35}Cu_{17}S_8$ (Fig. 5.27a) is strongly increased in comparison to these in Vitreloy 101 (Fig. 5.27c) because of the higher potential at which pitting corrosion is initialized. In contrast, the total number of pits is strongly reduced. Alloys that do not show an indication for pitting corrosion in Fig. 5.27b,d, only show a color change of the surface due to the passivation layer.

In Fig. 5.26c a subsequent reverse scan of the polarization curve after reaching the transpassive region is presented for $Ti_{50}Zr_{25}Cu_{17}S_8$ and Ti6Al4V. For both alloys a negative hysteresis of the current density can be observed, which is allocated to the change from an anodic to a cathodic reaction. Such a behavior is attributed to a re-passivation of the surface.

Altogether, the electrochemical polarization experiments reveal that the novel Ti- and Zr-based glass forming alloys exhibit an excellent passivation behavior.

TABLE 5.6: Electrochemical properties obtained by potentiodynamic polarization measurements. E_{corr} corresponds to the corrosion potential, i_{pass} is the passive current density. E_{pit} and E_{break} correspond to the pitting or breakdown potential, respectively, depending on the underlying electrochemical mechanism.

Alloy Composition $[at\%]$	E_{corr} $[V vs. SCE]$	i_{pass} $[Am^{-2}]$	E_{pit} or E_{break} $[V vs. SCE]$	E_{corr} - E_{pit} or E_{break} $[V vs. SCE]$
$Ti_{50}Zr_{25}Cu_{17}S_8$	- 0.35	5.4E-7	1.03	1.38
$Ti_{40}Zr_{35}Cu_{17}S_8$	- 0.35	7.7E-7	0.96	1.31
$Cu_{47}Ti_{34}Zr_{11}Ni_8$ (Vit101)	- 0.22	2.5E-7	0.03	0.25
$Ti_{86.2}Al_{10.2}V_{3.6}$ (Ti6Al4V)	- 0.27	3.4E-7	1.02	1.29
$Zr_{56.5}Ti_{13.3}Ni_{13.6}Cu_{9.6}S_7$	- 0.33	4.3E-7	0.57	0.88
$Zr_{52.5}Ti_5Cu_{17.9}Ni_{14.6}Al_{10}$ (Vit105)	- 0.31	3.9E-7	0.06	0.37

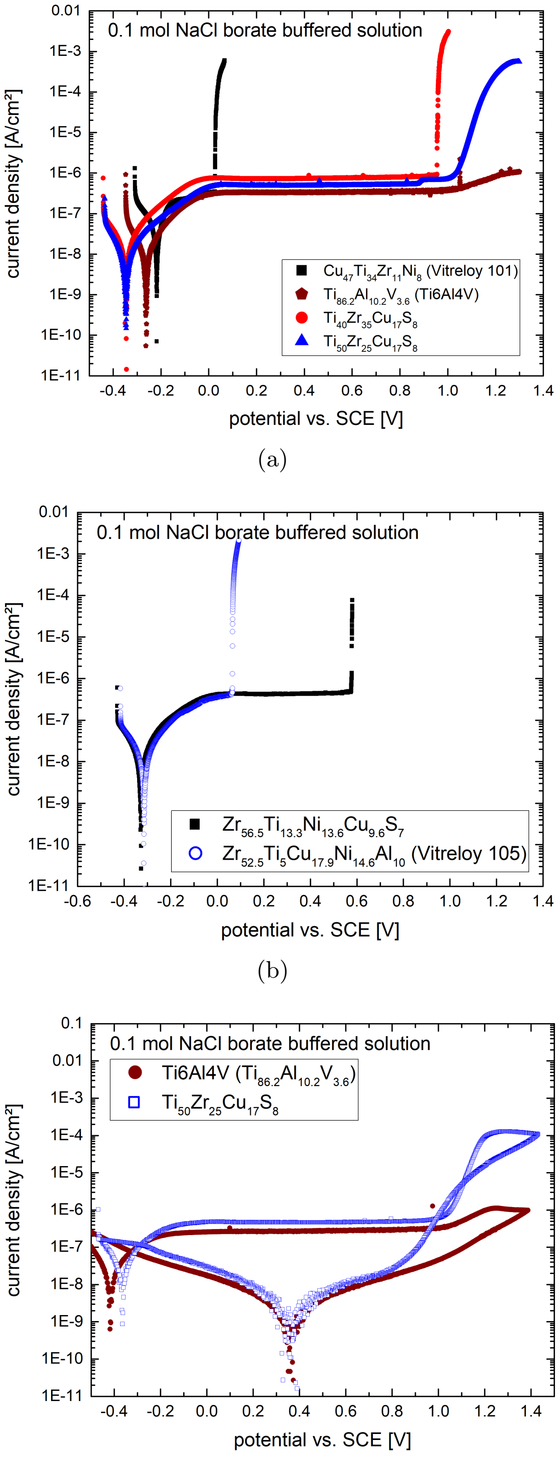

(a)

(b)

(c)

FIGURE 5.26: a) Potentiodynamic polarization curves in a borate buffered 0.1 M NaCl solution of a) amorphous $Ti_{40}Zr_{35}Cu_{17}S_8$, $Ti_{50}Zr_{25}Cu_{17}S_8$, $Cu_{47}Ti_{34}Zr_{11}Ni_8$ (Vitreloy 101) in comparison to crystalline Ti6Al4V and of b) amorphous $Zr_{56.5}Ti_{13.3}Ni_{13.6}Cu_{9.6}S_7$ in comparison to amorphous $Zr_{52.5}Ti_5Cu_{17.9}Ni_{14.6}Al_{10}$ (Vitreloy 105). c) Reversed potentiodynamic polarization curves of $Ti_{50}Zr_{25}Cu_{17}S_8$ in comparison to crystalline Ti6Al4V in a borate buffered 0.1 M NaCl solution. Both alloys show a repassivation before reaching the initial corrosion potential E_{corr}.

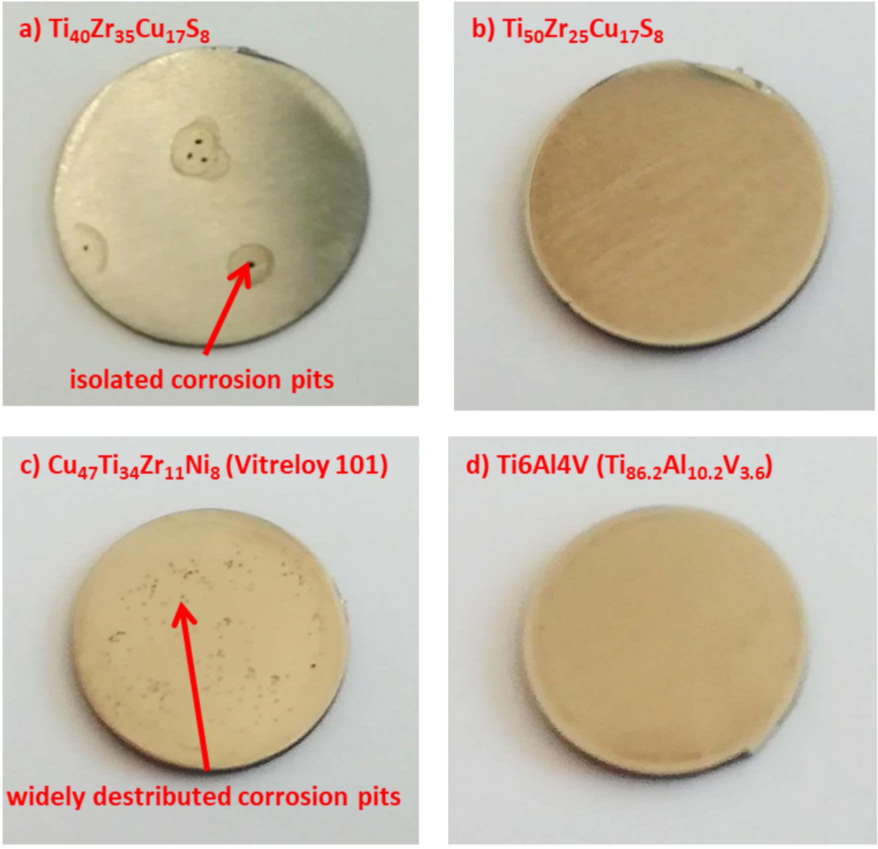

FIGURE 5.27: Pictures of the sample surfaces after the potentiodynamic polarization measurements of a) amorphous $Ti_{40}Zr_{35}Cu_{17}S_8$ b) amorphous $Ti_{50}Zr_{25}Cu_{17}S_8$ c) amorphous $Cu_{47}Ti_{34}Zr_{11}Ni_8$ and d) crystalline Ti6Al4V. Figure and figure caption are taken from Ref. [9].

Chapter 6

Glass formation in Sulfur-bearing Metallic Systems

In this chapter, the process of glass formation in the Pd-Ni-S and the Ti-Zr-Ni-Cu-S system is discussed on the basis of the findings in the previous chapters. The underlying reasons for the stabilization of the liquid phase regarding kinetic and the thermodynamic contributions are examined and links between the thermo-physical behavior, the mechanical properties and the structural evolution of the liquid phase upon cooling are analyzed. Finally, the findings about the sulfur-containing alloys in the respective systems are compared to literature data of sulfur-free bulk glass forming alloys.

6.1 Glass formation in the Ternary Pd-Ni-S System

Although glass formation is observed in a wide compositional range in the ternary Pd-Ni-S system, the maximum GFA in the Pd-Ni-S system is determined to be only 2 mm by copper mold casting and hence, about one order of magnitude lower than in the topologically equivalent Pd-Ni-P system (see section 4.2). In this section, the differences regarding the process of glass formation are elaborated and the different roles of sulfur and phosphorous on the mechanical properties are discussed. Finally, the temperature dependence of the structure is analyzed in order to reveal links to the thermo-physical and mechanical properties.

6.1.1 Estimation of the Glass Formation in the Ternary Pd-Ni-S System

As described in section 2.2, metallic glass formation typically takes place close to deep eutectic reactions. Here, the liquid phase is stabilized down to lower temperatures with respect to the crystalline structure. This stabilization can originate from thermodynamic and kinetic contributions, namely the interfacial energy (γ^{x-l}), the driving force for crystallization ($\Delta G^{l-x}(T)$) and the dynamics of the liquids ($\eta(T)$).
The liquidus temperature at the metal-rich side of the Pd-Ni-S system reaches a minimum value of roughly 730 K at about 26 at% S. Together with the narrow range of melting, this implies that the alloys are close to an eutectic trough and that the liquid is strongly stabilized when looking at the melting points of pure Pd and Ni. With a varying sulfur-content a change of the slope of the liquidus line is observed, also pointing towards an eutectic reaction at 26 at% (Fig. 6.1a). It is noticeable, that only close to this S-content, bulk glass formation is observed.

One parameter to estimate the GFA under consideration of the liquidus temperature T_l and the glass transition temperature T_g is the reduced glass transition temperatures t_{rg} proposed by Turnbull [24]. The value of t_{rg} of the Pd-Ni-S alloys is about 0.58 (see section 2.2.1), pointing towards a moderate GFA. In comparison, the Pd-Ni-P system shows a value of t_{rg} of up to 0.67, but exhibits a critical diameter of up to 2 cm [12, 170, 171]. Thus, the difference of the GFA between these two systems is reflected by t_{rg}. One could suggest that, if only t_{rg} and T_l are considered, the weaker GFA in the Pd-Ni-S system originates from the low T_g, since T_l is even lower than in the phosphorous-bearing system. One hypothesis for this difference would be a different atomic mobility of sulfur and phosphorous in the amorphous metallic solid.

Another parameter that is used to estimate the GFA in a glass forming system is the length of the SCLR (ΔT_x). In this system, the general tendency that a higher thermal stability upon heating from the glassy state correlates with the GFA is observed. Similar observations were made in other bulk glass forming systems [259, 260]. However, as observed for the sulfur-bearing Ti-alloys (see section 4.3), this correlation does not hold for all bulk glass forming metallic systems. For the validity of this correlation, the crystallization sequence or rather the primary precipitating phases plays an important role. In case of the $Pd_{31}Ni_{42}S_{27}$ alloy, the crystallization sequences are identical in continuous heating and cooling experiments and hence, a high thermal stability of the glassy phase allows conclusions about the thermal stability of the liquid or rather the GFA, if a shift of the crystallization nose to longer crystallization times in a TTT diagram is assumed. However, in comparison to the $Pd_{40}Ni_{40}P_{20}$ alloy, $Pd_{31}Ni_{42}S_{27}$ possesses a rather low thermal stability, which might also originate from a higher mobility of sulfur than of phosphorous.

Both, t_{rg} and ΔT_x point towards a low GFA, but these concepts can not be used for the description of the process of glass formation or rather the location of the GFR in this system. Therefore, the decisive thermodynamic and kinetic contributions have to be considered.

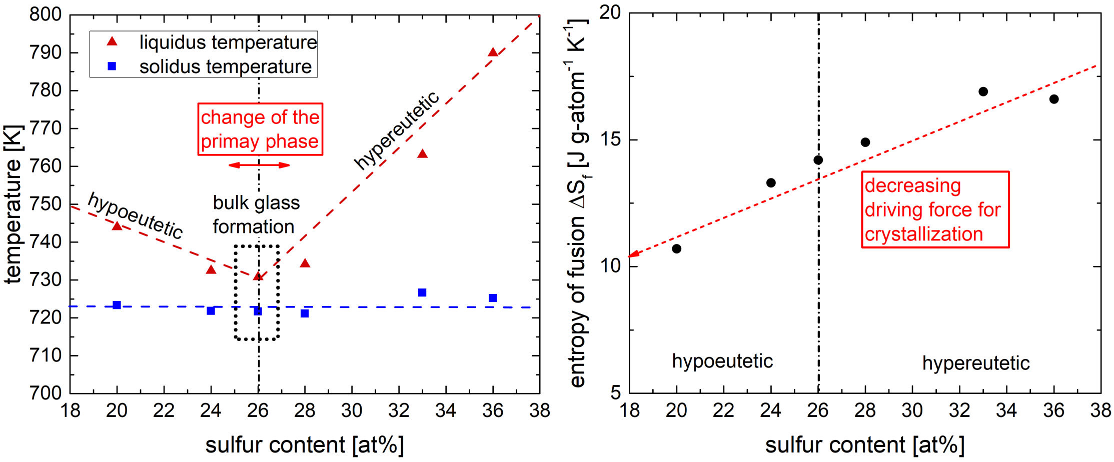

(a) (b)

FIGURE 6.1: a) The solidus and liquidus temperatures as a function of the sulfur-content. The schematically highlighted kink in the slope of the liquidus line indicates a change of the primary precipitating phase. Figure and figure description are adapted from Ref. [8]. b) Entropy of fusion ΔS_f as a function of the sulfur-content. A decreasing driving force for crystallization is estimated for lower values of S.

Interestingly, the driving force for crystallization, estimated from the entropy of fusion ΔS_f, and the critical diameter d_c behave opposite, since the ΔS_f decreases for lower values of sulfur (Fig. 6.1b), but glass formation diminishes rapidly. This effect is attributed to a change of the primary phase at the minimum of the liquidus temperature. Here, at a sulfur content of 26 at% the system changes from hypoeutectic to hypereutectic (Fig. 6.1a), which is suggested to be accompanied by a change of the primary crystalline phase. In particular, the interfacial energy γ^{x-l} depends on the crystalline phase and, in turn, strongly influences the process of glass formation. From the phase diagrams in section 4.2, the formation of the solid solution (Ni,Pd) is assumed to cause the sudden drop of the GFA. A similar observation was made by Schroers and Co-workers in the Au-Si glass forming system [261].

Besides a change of the primary phase or rather the interfacial energy γ^{x-l}, a drastic change of the kinetics ($\eta(T)$) might be possible as proposed inter alia in a Ni-based bulk glass forming system by Johnson et al. [17]. However, if the slope-fragility method (see section 5.1.2) is valid, all alloys in the Pd-Ni-S system exhibit a rather fragile kinetic behavior as estimated from the DSC measurements (see section 4.2), since all alloys display a short glass transition region. Hence, a change of fragility is not suggested to cause the drop of the GFA.

6.1.2 On the Glass Forming Ability in the Ternary Pd-Ni-S System

For an exact description of the GFA and an understanding of the location of the GFR, the $Pd_{31}Ni_{42}S_{27}$ alloy has been investigated comprehensively regarding its thermo-physical properties.

The driving force for crystallization of $Pd_{31}Ni_{42}S_{27}$

The high entropy of fusion ($\Delta S_f = 14.7$ J g-$atom^{-1}K^{-1}$ - see section 4.2) causes a fast rise of the Gibbs free energy difference $\Delta G^{l-x}(T)$ upon cooling the liquid below the liquidus temperature [8]. This fast rise is, in turn, compensated by the strong increase of the molar heat capacity when undercooling the liquid (Fig. 5.1). As already discussed elsewhere, the increase of the molar heat capacity is rather unexpected regarding the Debye model for the molar heat capacity, but commonly observed in undercooled metallic liquids [28]. It is attributed to the fast decrease of the configurational entropy according to Turnbull and Chen [28] and a decreasing free-volume due to the formation of a short range order (SRO) as proposed by Busch et al. [29]. The huge difference of c_p between the crystal/glass and the liquid in vicinity of T_g is typical for more fragile systems and tends to a lower glass forming ability [29]. However, $\Delta G^{l-x}(T)$ reaches a maximum value of approximately 3.5 kJ g-$atom^{-1}$ at T_g, which is about twice as high in comparison to the alloy $Pd_{43}Cu_{27}Ni_{10}P_{20}$ [63], but close to the value of $Pd_{40}Ni_{40}P_{20}$ [45]. Such a value of $\Delta G^{l-x}(T)$ at T_g is high for a bulk metallic glass former, but not extraordinarily high. In Fig. 6.2 the course of $\Delta G^{l-x}(T)$ of different bulk metallic glass formers is shown. For example, the Fe-based bulk glass forming alloy $Fe_{67}Ni_{3.5}Cr_{3.5}Mo_6P_{12}C_{5.5}B_{2.5}$ with a GFA of up to 13 mm shows an even higher value than the alloy of this work, but ΔS_f of $Fe_{67}Ni_{3.5}Cr_{3.5}Mo_6P_{12}C_{5.5}B_{2.5}$ is only 8.95 J g-$atom^{-1}K^{-1}$ [54]. Hence, the maximum of the Gibbs free energy is, if considered individually, not the limitation for a high GFA. Furthermore it has to be noted, that the driving force for crystallization dominates the high temperature regime of the nucleation and growth process, so that the slope at T_l ($= \Delta S_f$) is more crucial and not the maximum value of the Gibbs free energy difference at T_g. In case of an equal entropy of fusion, the absolute value of $\Delta G^{l-x}(T)$ depends of the relation between T_l and T_g. These findings again tend to the fact that a high atomic mobility might limit the GFA in this system.

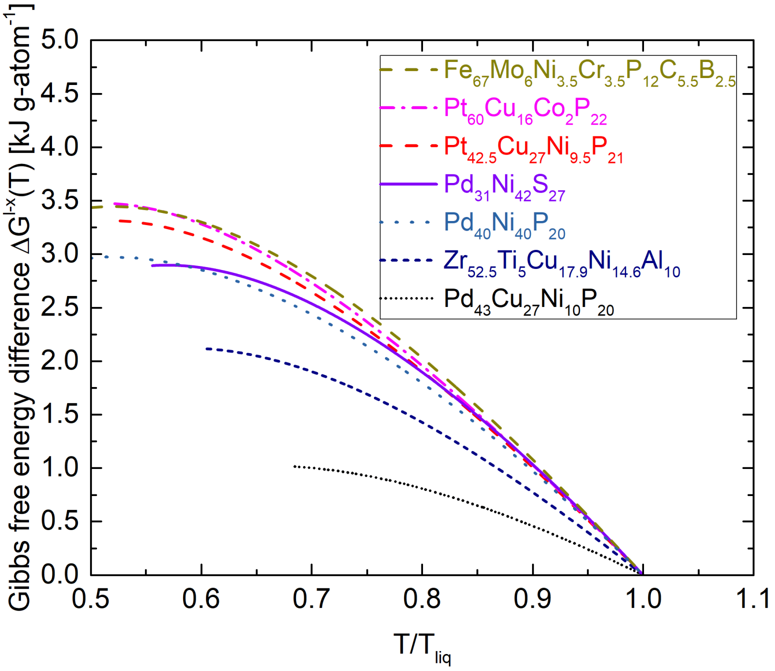

FIGURE 6.2: Gibbs free energy difference $\Delta G^{l-x}(T)$ for different bulk metallic glass formers. It is evident, that the value of $\Delta G^{l-x}(T = T_g)$ of $Pd_{31}Ni_{42}S_{27}$ is comparably high. Data taken from Ref. [39, 45, 54, 216, 233].

On the kinetically fragile behavior of $Pd_{31}Ni_{42}S_{27}$

The determined values of the fragility parameter D* and the fragility index m clearly indicate a fragile kinetic behavior (D*= 8.3; m = 86). Several methods were used in order to provide reliable data, which can be used for the description of the GFA. Both parameters are in good agreement with the estimations in section 5.1.2, which yield a value of D*= 7.2 ± 0.7 and a m = 74 ± 5, proving the quality the proposed correlations [8].

The high temperature sensitivity results in a lower melt viscosity at the liquidus temperature, tending to a lower GFA of the alloy as can be seen in Fig. 6.3. Here, the temperature-dependence of different metallic and non-metallic glass former is shown. It is evident, that the estimated value of the dynamic viscosity at T_l[1] is more than two orders of magnitude lower for $Pd_{31}Ni_{42}S_{27}$ ($T_g^*/T_l = 0.56 \rightarrow \eta(T = T_l) = 0.05$ Pas) in comparison to the kinetically stronger metallic glass formers $Pd_{40}Ni_{40}P_{20}$ ($T_g^*/T_l = 0.57 \rightarrow \eta(T = T_l) = 1.47$ Pas) [45, 262] and $Pd_{40}Cu_{30}Ni_{40}P_{20}$ ($T_g^*/T_l = 0.656 \rightarrow \eta(T = T_l) = 21.1$ Pas) [45, 216, 263]. This difference in viscosity originates not only from the temperature sensitivity of each alloy but on the different ranges of $T_l - T_g^*$. However, the low viscosity or rather the high diffusivity in vicinity of T_l may be the reason for the limited GFA of 1.5 mm by copper mold casting [8]. The value of the melt viscosity

---

[1] If it is assumed that no fragile-to-strong transition occurs in-between T_g and T_l (see section 2.2.2.2).

$\eta(T = T_l)$ is even that low (comparable to a pure metal) that it comes to a surprise that bulk glass formation takes place at all, when considering the high value of ΔS_f.

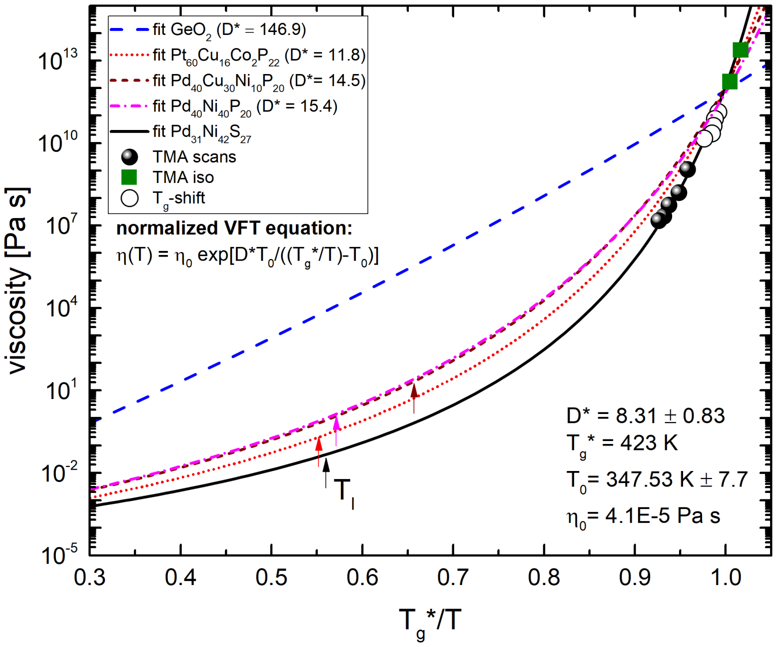

FIGURE 6.3: Angell plot of different bulk glass forming alloys. $Pd_{31}Ni_{42}S_{27}$ displays the most fragile kinetic behavior among all glass formers shown here, implying a very low viscosity at its liquidus temperature. The liquidus temperatures of the respective alloys are emphasized with arrows. Data taken from Ref. [39, 45, 216, 262–264].

Crystallization experiments of $Pd_{31}Ni_{42}S_{27}$

In the continuous crystallization experiments an undercooling of more than 100 K is achieved using a cooling rate of only 0.083 K/s (Fig. 6.4). In comparison to that, the Pt-based $Pt_{60}Cu_{16}Co_2P_{22}$ alloy, having a similar driving force for crystallization, but a higher fragility parameter of D* $= 11.8$ ($T_g^*/T_l = 0.55 \rightarrow \eta(T = T_l) = 0.19$ Pas) [39] (Fig. 2.6), achieves only an undercooling of about 30 K under the same conditions during the crystallization experiments [63]. The high GFA in this alloying system ($d_c = 16$ mm [64]) is supposed to originate from a high interfacial energy and the suppression of the primary phase at higher cooling rates [63], but nonetheless the undercooling observed for $Pd_{31}Ni_{42}S_{27}$ is several times higher although having a much lower GFA. One reason for the limited undercooling in the Pt-based alloys was proposed by Gross et al. in Ref. [63]. Due to the temperature limit of the DSC the Pt-based alloys could only be overheated for about 100 K above the liquidus temperature. It has been shown by Rim et al. that, in case of Zr-based bulk glass forming alloys, an overheating threshold of several hundreds of K has to be overcome to dissolve persistent crystalline structure in the metallic liquid [208]. However, because of the lower liquidus temperature of $Pd_{31}Ni_{42}S_{27}$ a higher overheating of more than 200 K is achieved in a DSC. Another noteworthy finding in the study of Gross et al. was that the exothermic signal of the crystallization process in the continuous cooling experiments show a pronounced pre-peak, which is attributed to the passing of a two phase field (liquid + crystal). Hence, a driving force for crystallization is already present although not all stable crystalline phases are undercooled and the formation is kinetically frustrated. In contrast, the heat flow curves upon continuous cooling from the equilibrium liquid of $Pd_{31}Ni_{42}S_{27}$ show one distinct exothermic peak (Fig. 5.4) and the in-situ high energy synchrotron X-ray experiments of $Pd_{31}Ni_{42}S_{27}$ revealed that upon heating and cooling the binary intermetallic compounds Pd_4S and Ni_3S_2 are formed simultaneously, supporting the results of the caloric experiments.

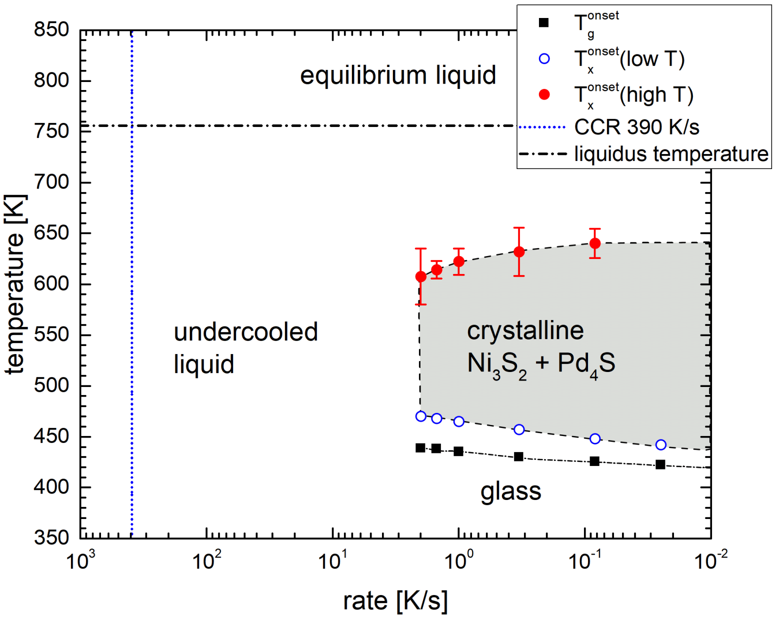

FIGURE 6.4: Continuous time-temperature-transformation (TTT) diagram of $Pd_{31}Ni_{42}S_{27}$. The onset of crystallization in the low temperature temperature regime (T_x^{onset}(low T)), the onset of crystallization in the high temperature regime (T_x^{onset}(high T)) and the onset of the glass transition (T_g^{onset}) are determined using the tangent method (see section 3.2.1.1 and section 5.1.3). In addition, the critical cooling rate calculated from equation 2.1 and the liquidus temperature are marked as blue dotted line and black dashed-dotted line, respectively.

Using equation 2.1, the critical cooling rate for $Pd_{31}Ni_{42}S_{27}$ is calculated to 390 K/s (Fig. 6.4), assuming a critical diameter of 1.5 mm [8]. However, the course of the onsets of crystallization would suggest a significantly lower critical cooling rate, which is in good agreement with the undercooling ability at low cooling rates. One explanation for this discrepancy might be that the experimentally determined GFA of 1.5 mm underestimates the actual GFA. The glass forming ability of metallic glasses can be deteriorated by shear induced crystallization and by heterogeneous nucleation at the mold walls. Both occur in case of copper mold casting. Hence, it might be possible that other casting techniques like water quenching results in a higher GFA. The discrepancy between copper mold casting and water quenching in silica tubes was inter alia shown by Granata et al. for the Pd-Cu-Si system [265]. Here, the critical diameter could be enhanced by a factor of roughly 2 (from 6 mm diameter to 10 mm diameter) when the suction casting process is compared to water-quenching of B_2O_3 fluxed master alloys. Another example can be found in the Fe-P-B-Si-C system, here the GFA is reduced significantly by suction casting over water quenching [266]. However, the continuous TTT diagram does not allow a fitting procedure of the data points due to the non-steady state conditions and the critical cooling rate is not accessible due to the limited cooling rates of the DSC.

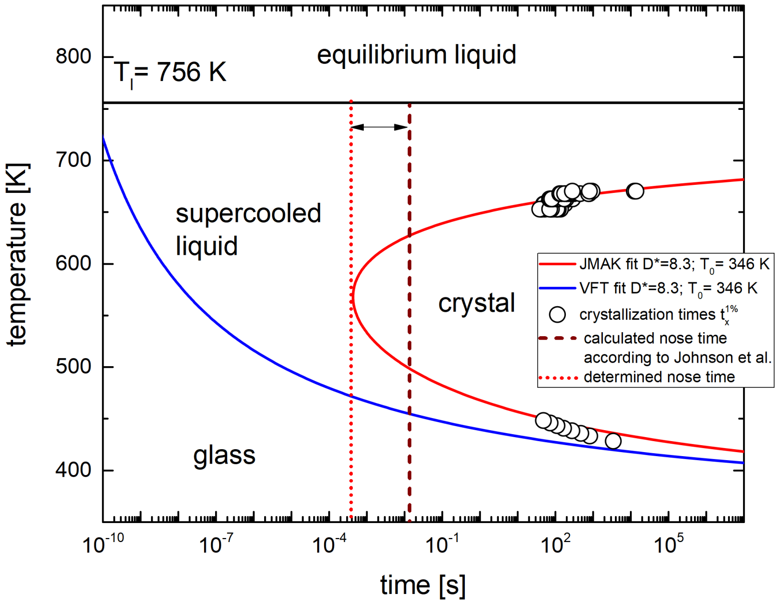

FIGURE 6.5: Isothermal TTT diagram of $Pd_{31}Ni_{42}S_{27}$. The crystallization times at which 1 % of the crystallization enthalpy is released ($t_x^{1\%}$ - open circles) are determined by integration of the isothermal heat flow curves (Fig. 5.4). The data is described using equation 2.18 together with the thermo-physical parameters determined in section 5.1 (solid red line). Additionally, the VFT fit determined in section 5.1.2 is shown as solid blue line. The dashed brown line represents the minimum crystallization time from Ref. [62] and the solid black line highlights the liquidus temperature.

In contrast, the shape of the isothermal TTT diagram can be described using classical nucleation theory [267], as shown by different authors for a variety of bulk metallic glass forming alloys [63, 221, 268–270]. For this, the time $t_x^{i\%}$, at which a defined proportion i of the nucleation process has been occurred, can be expressed according to the JMAK (Johnson-Mehl-Avrami-Kolmogorov) equation (equation 2.18 in section 2.2.2.3). Thus, it is possible to fit the data points in the isothermal TTT diagram using the experimentally determined parameters of the dynamic viscosity, the molar heat capacity and the enthalpy of fusion. In case of the isothermal experiments, steady-state conditions are maintained and transient nucleation effects (time-dependence of the nucleation rate - equation 2.16) do not occur. Transient nucleation and its effects on the glass forming ability are discussed later in this section. A temperature dependence of γ^{x-l} is neglected for the fitting procedure.

Using a D* of 8.3 and a T_0 of 346 K and the fitting constants in table 5.2 for the description of the molar heat capacity, the isothermal crystallization times at which 1% of the total crystallization enthalpy is released ($t_x^{1\%}$), can be fitted (Fig. 6.5). This yields the fitting parameters A (equation 2.16) of 1.84×10^{46} and the interfacial energy γ^{x-l} of $0.107 \pm 4.2 \times 10^{-4}$ J m^{-2}. This value is comparable to the value determined for $Pt_{42.5}Cu_{27}Ni_{9.5}P_{21}$ in Ref. [63] of 0.11 J m^{-2} and hence, considerably higher in comparison to Zr-based alloys (γ^{x-l} =0.01 - 0.04 J m^{-2} [221, 271, 272]) and Pd-P (γ^{x-l}=0.079 J m^{-2} [269]/ 0.067 J m^{-2} [268]) based alloys. Such a high interfacial energy agrees well with the observations in the continuous TTT diagram, in which a high undercooling is observed at moderate cooling rates.

However, the description of the experimental data via equation 2.18 has two drawbacks:

> (1) On the one hand, the fitting function (equation 2.18) is not able to describe the curvature and slope of the crystallization time in vicinity of the glass transition (Fig. 6.5). As shown in the magnification of the low temperature regime in Fig. 6.6, the fit deviates by about one order of magnitude in the crystallization time at temperatures around 430 K.
>
> During the experimental determination of the values of the molar heat capacity the experimental errors are relatively small, whereas the kinetic constants show larger experimental errors because of the limited thermal stability upon heating. However, a better fitting by variation of the kinetic constants within the experimental errors (T_0 and D*), is only possible via an independent change of T_0 and D* (Supp. Fig. A.5). In fact, T_0 and D* are dependent variables in the VFT equation and hence, an invalid fitting procedure due to inaccurate input values can be excluded.
>
> However, the slope of the crystallization times is steeper than the fitting function and the curvature is almost zero (Fig. 6.6). Similar observation were made by Masuhr et al. in Ref. [221] for the Zr-based alloy Vitreloy 1, where the crystallization times in the low temperature regime could only be described assuming an Arrhenius-like behavior of the diffusivity. Their data suggests a violation of the Stokes-Einstein relation (equation 2.6) in the deeply undercooled liquid because of a decoupling of the diffusivity of the different atomic species. These experimental findings were picked up by Tanaka, who postulated a possible resolution of the Kauzmann paradox [65, 67]. In his theory, a decoupling of the translational and rotational diffusivity leads, in turn, to a decoupling of the structural relaxation time τ_α and the relaxation time for material transport τ_D, whereby the latter one governs the crystallization process. In contrast to τ_α, τ_D shows an Arrhenius-like behavior with a temperature-independent activation energy [67]. The decoupling

takes place at a bifurcation temperature T_B, which is below the melting temperature, but above the VFT-temperature T_0 (= 346 K). Thus, at a lower metastable limit T_{LML} (gray dot in Fig. 6.6) the structural relaxation time crosses the crystallization time ($\tau_\alpha = t_x$) and hence, no “equilibrium” supercooled liquid is accessible below T_{LML} ($T_g \geq T_x$).

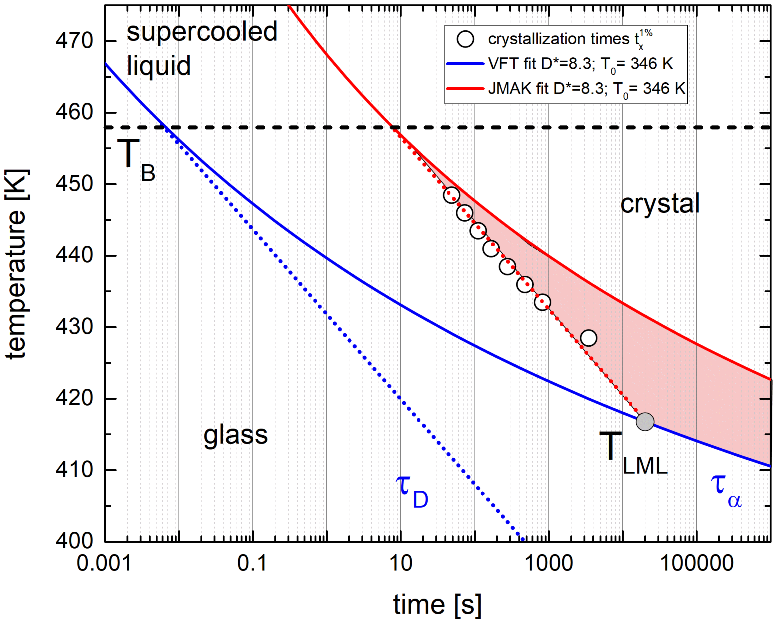

Figure 6.6: Magnification of the low temperature regime of the isothermal TTT diagram of $Pd_{31}Ni_{42}S_{27}$. It is evident, that the JMAK fit (equation 2.18) deviates from the exact course of the crystallization times ($t_x^{1\%}$ - open circles). At the bifurcation temperature T_B, a kink of the courses of the JMAK and the VFT fit might be caused by the decoupling of the relaxation time for material transport τ_D and the structural relaxation time τ_α. At the lower metastable limit T_{LML}, $t_x^{1\%}$ might intersect with τ_α, being an explanation for the avoidance of Kauzmann's paradox because of crystallization. In the style of Ref. [67].

Another explanation for the deviation of the fitting function and the experimental data at low temperatures might be a change of the primary phase in the isothermal experiments. Although it was revealed that in continuous experiments the crystallization sequence upon heating and cooling is equivalent (simultaneous formation of Ni_3S_2 and Pd_4S), the sequences differs in cases of isothermal experiments (Pd_4S is formed first - see section 5.1.3). The underlying reason might be transient nucleation or different growth rates of both phases at low temperatures. Transient nucleation assumes that in an undercooled liquid, that is free of any crystalline clusters, the nucleation frequency rises from zero to its steady-state level via a sigmoidal function of time and hence, is a function of both, time and temperature (I= f(T,t)). The time to reach the steady-state level is termed incubation time. The different growth rates might originate on the one hand from a breakdown of the Stokes-Einstein relation and the accompanied decoupling of the diffusivities as discussed above. On the other hand different nucleation states (in terms of quenched-in nuclei) of the glassy phase, which are caused by different transient nucleation effects of the individual phases, can cause different growth rates.

Regardless of the underlying reason, if the primary phases in the high and the low temperature regime differ from each other, both regimes have to be fitted solely [70, 240]. However, fitting of the onsets of the second crystallization events results in a similar shape of the nose (Supp. Fig. A.6).

(2) On the other hand, the CCT and TTT diagram show discrepancies to each other regarding the calculated GFA and with respect to the experimentally determined GFA (compare Fig. 6.5 and Fig. 6.4). According to Johnson et al. the minimum in the crystallization time τ_x^* in a TTT diagram ("nose time") can be calculated from [62]

$$\tau_x^* = 0.00419(10d_c)^{2.54} \tag{6.1}$$

where d_c is the critical diameter in cm. In their work, the nose time is not assigned to the type of TTT diagram (isothermal or continuous). However, using an experimental diameter of 1.5 mm, equation 6.1 yields a τ_x^* of 0.0138 s for $Pd_{31}Ni_{42}S_{27}$ (Fig. 6.5). It is evident, that the fit according to equation 2.18 suggests an about thirty times lower value of τ_x^* and hence, a higher GFA is expected from the model of Johnson. This is the opposite tendency as estimated from the CCT diagram in Fig. 6.4, which indicates a higher GFA as observed in the experiments. Such a difference between the isothermal and the continuous TTT diagram might also be explained due to the effect of the incubation time in case of transient nucleation [273]. Johnson et al. suggested that the incubation time of the nucleation rate is somehow included in the reduced glass transition temperature t_{rg} or the fragility index m and hence, included in their model [62]. However, since the solidus and the liquidus temperature are independent from the heating rates and since the transient nucleation rate can be significantly lower in case of high cooling rates, the steady-state approach could be insufficient for the determination of the GFA in some systems. For instance, in a study of Kelton and Greer on the nucleation rate in the $Au_{81}Si_{19}$ and the $(Au_{85}Cu_{15})_{77}Si_9Ge_{14}$ alloys, the transient nucleation rate is shown to be several orders of magnitude lower than the steady-state nucleation rate, implying that the consideration under steady-state conditions is not applicable for the evaluation of the GFA [274].

All in all, the high kinetic fragility in combination with the high driving force for crystallization strongly limit the GFA. Glass formation is suggested to take place because of a high interfacial energy between the liquid an the crystalline solid. The interfacial energy is also suggested to determine the location of the GFR in this system, which is a function of the sulfur-content. This is concluded since estimations of the kinetic fragility indicate an unchanged fragility index D^* and estimations of the driving force for crystallization by the entropy of fusion indicate even a decreasing ΔG^{l-x} for lower S-contents (below 26 at% - Fig. 6.1b). Thus, these two parameters point towards a higher GFA for lower S contents, but the experimental GFA diminishes, which is assumed to be caused by a change of the interfacial energy or rather the primary precipitating phase.

Our findings suggest that the process of glass formation is on the one hand facilitated by a strong rate dependence of the nucleation process (transient nucleation) and on the other hand is sensitive to heterogeneous nucleation and shear induced crystallization during the casting process, so that a higher experimental GFA is expected when using the water quenching technique.

6.1.3 Structural Changes on the Pathway to Glassy $\mathbf{Pd_{31}Ni_{42}S_{27}}$

In order to reveal effects of temperature changes on the total structure factor S(Q) and the reduced pair distribution function G(r) and to reveal links to the thermo-physical properties, the temperature dependence of the peak positions and the temperature-induced changes of the shapes of the peaks are analyzed and discussed with respect to data of other bulk glass forming liquids.

The total structure factor S(Q)

At a first glance, the overall shape of S(Q) is typical for a metallic liquid/glass, implying a non-directional bonding of the atoms in the liquid structure. In contrast, covalent glasses (oxide glasses and chalcogenide glasses), show a different shape of S(Q) due to network structure [51, 275]. Hence, despite the high content of sulfur in $Pd_{31}Ni_{42}S_{27}$, S(Q) suggests that it is structurally a metallic glass.

In general, the analysis of the first sharp diffraction peak (FSDP) in S(Q) yields information about the MRO in bulk metallic glasses and bulk glass forming liquids [276]. Some alloys, with a pronounced MRO, exhibit a pre-peak at lower Q values at the left side of the FSDP in S(Q) [39, 94, 277–282]. The FSDP in S(Q) shows a uniform shape without a pronounced pre-peak at lower values of Q (Fig. 5.8) in both, the low- and the high-temperature regime. A similar structural signature can be observed for phosphorous-containing Pd-based alloys in the (Pd,Pt)-Cu-Ni-P system [39, 283]. Here, the substitution of Pd by Pt leads to the formation of a pre-peak at low Q-values of S(Q) [39, 283]. However, it has to be pointed out that the total structure factor represents the superposition of the weighted partial structure factors. Thus, the pre-peak might not be detectable in S(Q) due to the superposition, but is present in some partial, binary structure factors.

The peak position of the FSDP in S(Q) yields also information about dilatation behavior in the glassy state [103, 284]. The thermal volume expansion coefficient in the glassy state γ_{glass}^{X-ray} is calculated to be $2.8 \times 10^{-5} K^{-1}$, being in the same order of magnitude as observed for other bulk metallic glasses [285] (Fig. 6.7a). Additionally, the evolution with temperature of the position of the FSDP in S(Q) in the (supercooled) liquid phase is interesting. It should be noted that in the liquid state, it does not represent the thermal expansion coefficient, because of the gained degrees of freedom. Within the glass transition region (T ∼ 420 K), the value of $(Q_1(323K)/Q_1)^3$ shifts to significantly higher values. The inset of Fig. 6.7a shows the total structure factor of the last data point in the SCLR in vicinity of T_g, proving that the strong peak shift is not caused by crystallization. In the equilibrium liquid, $(Q_1(323K)/Q_1)^3$ is decreasing with temperature. A linear fit of the data in the HT-liquid points towards the value in the SCLR. Such a double kink in the temperature dependence of Q_1^{-3} and a negative slope in the equilibrium liquid is a rather unusual feature and commonly not observed in Zr-, Au-, Pd- or Pt-based alloys [40, 56, 283, 285]. In isothermal experiments at 443.5 K it is observed that as a precursor of crystallization the maximum of the FSDP in I(Q) shifts to lower Q values (Fig. 6.7b), which might be the reason for the anomalous behavior of Q_1 in the SCLR as observed in Fig. 6.7a, but it does not explain the anomalous behavior in the equilibrium liquid. One hypothesis could be ascribed to the role of sulfur, since for example the viscosity of pure sulfur increases with increasing temperature due to ring-opening polymerization [286, 287].

In contrast to the high-temperature equilibrium liquid, the second peak of S(Q) of the low-temperature liquid shows a non-uniform shape (Fig. 5.8a). This change of the shape can be attributed to the formation of short-range order upon cooling from the equilibrium liquid [93, 241]. Sachdev et al. showed that in case of an ideal icosahedral ordering the ratio of $Q_{2.1}/Q_1$ and $Q_{2.2}/Q_1$ are 1.71 and 2.04, respectively [93]. In order to determine reliable values of the peak positions $Q_{2.1}$ and $Q_{2.2}$, a bigausian fit is used as shown in Fig. 3.7b. The peak position of the FSDP is located at 2.798 Å^{-1} at 300 K. Hence, for $Pd_{31}Ni_{42}S_{27}$ the ratios are 1.74 and 1.95 being slightly different from an ideal icosahedral structure. However, independent from the exact geometry of the SRO, the formation of SRO during cooling is in good agreement with the strong increase of the molar heat capacity in Fig. 5.1.

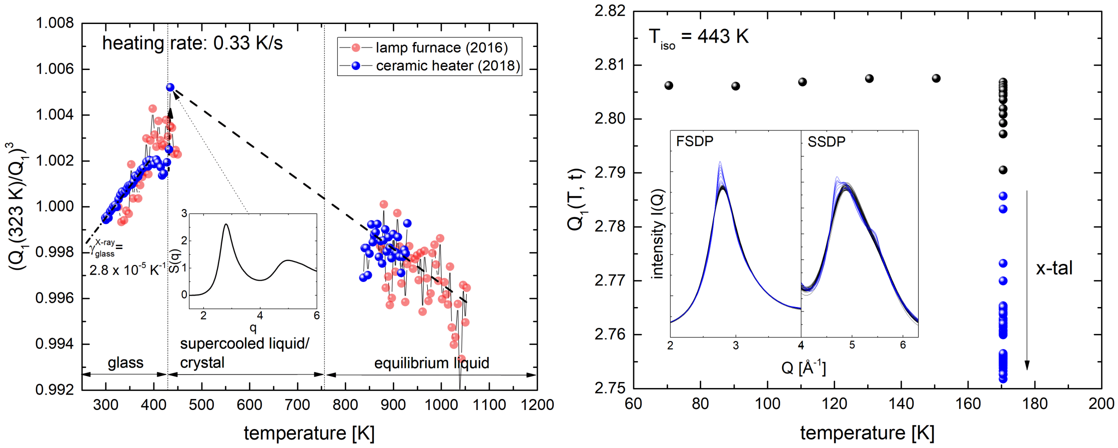

(a) (b)

FIGURE 6.7: a) Temperature dependence of $(Q_1(323K)/Q_1)^3$ of $Pd_{31}Ni_{42}S_{27}$. The data was acquired during two independent beam times in different experimental setups. At low temperatures the thermal volume expansion coefficient γ_{glass}^{X-ray} is calculated to be $2.8\times10^{-5}\ K^{-1}$ according to Ref. [103]. Upon heating a strong increase is observed in vicinity of the glass transition temperature. In the high temperature regime a negative "expansion" is observed. b) Evolution of Q_1 of $Pd_{31}Ni_{42}S_{27}$ at 443 K with time. Q_1 shifts to smaller values in the SCLR until crystallization occurs.

The reduced pair distribution function G(r)

Real space information about the averaged and superpositioned atomic distances can be obtained by analyzing the reduced pair distribution function G(r). As already pointed out, the position of the FSDP (r_1) of G(r) is located at roughly 2.8 Å, exhibiting a pre-peak at about 2.2 Å in the low-temperature regime (Fig. 5.8b). In order to determine reliable values of the peak positions, a bigausian fit as shown in Fig. 3.7b is used. The maximum at 2.78 Å indicates that G(r) is mainly dominated by the Pd-Pd interaction, since Pd has an atomic radius of 1.42 Å [86], leading to a theoretical interatomic distance of Pd-Pd of 2.82 Å. The appearance of the pre-peak at 2.23 Å can be ascribed to contributions with a smaller scatterings lengths like S-S (2 x 1.03 Å = 2.06 Å [86]) or Ni-S (1.03 Å + 1.26 Å = 2.29 Å [86]). Here it has to be mentioned again, that only the reduced pair distribution functions are analyzed so that some features might vanish due to the superposition of the partial pair distribution functions.

Upon heating, the FSDP shifts to lower r-values and the pre-peak vanishes (Fig. 6.8a). The shift to lower r-values with increasing temperature is commonly observed in bulk glass forming liquids and attributed to an increasing coordination number [288, 289], although intuitively a shift to higher values is expected because of an increasing bond length. Ding et al. ascribed this behavior to the asymmetry of the FSDP [290]. A kink of r_1 is observed when reaching the end of the glass transition T_g^{end}, which results in a faster decrease with temperature. The data of the equilibrium liquid follows the same trend. It is conspicuous that the position of the second sharp diffraction peak r_2 decreases upon heating when reaching T_g^{end} and subsequently increases again. This feature is reproduceable in two different experimental setups. In the high temperature regime, r_2 is located at much higher values due to merging of the two distinct maxima visible in the glassy state. This asymmetry of the SSDP in G(r) is discussed in the next paragraph.

As proposed in Ref. [104], the temperature dependence of the peak positions r_3 and r_4 can be used to determine the structural fragility index m_{str}, which correlates with the kinetic fragility (see section 2.3). Unfortunately, the quality of the diffraction data does not allow a proper determination of these two peak positions in the equilibrium liquid. It is evident, that the difference between the two independent measurements is rather high and hence, an interpretation of the temperature sensitivity of the peak positions is not reasonable. In the low temperature regime, the thermal stability of the alloy or rather the extend of the SCLR is to short to determine m_{str}.

As discussed above, in the glassy structure a degeneration of the SSDP can be observed, which is not visible in the equilibrium liquid. The shape of the SSDP yields information about the connection between the local representative structural units (RSU), which plays an important role for the formation of the medium range order of the glassy structure [100, 101]. The RSU may share one, two, three or four atoms [100, 101]. On the basis of geometrical considerations, the most probable positions of the second nearest neighbors for each cluster connection scheme can be calculated from the average bond length as 2 r_1 (1-atom connection), $\sqrt{3}\ r_1$ (2-atom connection), $\sqrt{(8/3)}\ r_1$ (3-atom connection) and $\sqrt{2}\ r_1$ (4-atom connection) [96, 97, 101]. The calculated values are marked as grey vertical lines in Fig.6.8b (compare to Fig. 2.12). The positions of the four features in the low-temperature regime at the SSDP partially match with the calculated values of the second nearest neighbor positions, which can be ascribed to the fact that the the actual nearest neighbor positions are not only influenced by the Pd-Pd interaction, dominating the position of the FSDP, but also by Ni and S with a smaller scattering length. However, upon cooling from the liquid phase the 4- and 3-atom connection, both corresponding to a face-sharing of the RSUs, seem to gain importance. The split of the SSDP might result also from the simultaneous formation of 1-atom connections [101]. As already described, the SSDP of the equilibrium liquid shows a uniform shape and no features are visible, suggesting that these connection schemes do not exist and are formed upon undercooling, like observed by Ding et al. in simulation studies [101].

Interestingly, the features observed in the SSDP of the glassy structure, are also present in G(r) of the crystalline structure. This implies that the medium range order of the liquid is also reflected in the crystalline structure. Similar observations are made in simulations studies about pure Ni and pure Fe. Here, the authors identified a "hidden topological order" in the glassy phase, which closely correlates with the crystalline structure [100, 102]. In our recent study on Pt- and Pd- based alloys, the influence of the substitution of Pd and Pt in $(Pd_{1-x}Pt_x)_{42.5}Cu_{27}Ni_{9.5}P_{21}$ on the liquid and glassy structure is investigated in detail [283]. Interestingly, the evolution of the shape of the SSDP in G(r) of $Pd_{31}Ni_{42}S_{27}$ resembles that of the Pt-based alloys and differs from the Pd-P alloys. The same difference accounts for G(r) of the corresponding crystalline structures (Fig. 6.21). It has to be stressed that also similarities of the temperature-dependence of the thermodynamic and kinetic properties are found for the Pt-P-based alloys and for the Pd-Ni-S alloy. Like $Pt_{42.5}Cu_{27}Ni_{9.5}P_{21}$, $Pd_{31}Ni_{42}S_{27}$ shows a high entropy of fusion, a rapidly increasing molar heat capacity at T_g and a very fragile kinetic behavior. Furthermore, both systems show very high values of the interfacial energy. Maybe the high interfacial energy, which is somehow connected to the entropy of fusion and the molar heat capacity, results from the more pronounced differences between the glassy/ crystalline structure and the equilibrium liquid in comparison to that of Pd-P-based alloys. Altogether this may imply that the temperature-sensitivity of the thermo-physical properties is somehow reflected in the degeneration of the SSDP in G(r). These thermodynamic and kinetic characteristic are, in turn, the reason for the glass formation in the respective systems and hence, the SSDP in G(r) may contain information about the process of glass formation itself. This is discussed in detail in section 6.4.

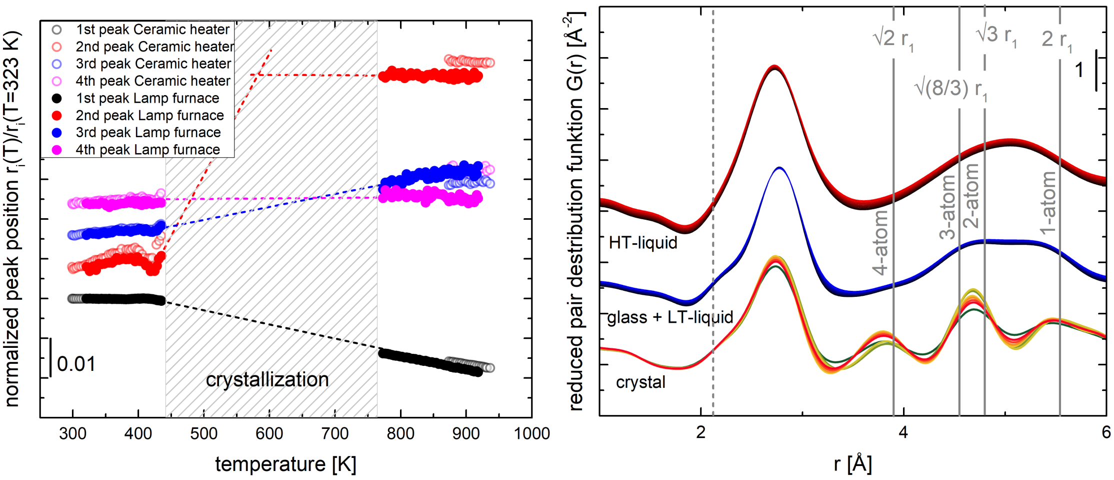

(a) (b)

FIGURE 6.8: a) Temperature dependence of the first four peak positions (r_1, r_2, r_3, r_4) of G(r) of $Pd_{31}Ni_{42}S_{27}$ normalized to the value at 323 K. The extrapolation of r_2 in the SCLR points towards an unexpected discontinuity, but this behavior can be explained by the difference of the shape of the second sharp diffraction peak (SSDP) of G(r) between the low and the high temperature liquid. The splitting of the SSDP causes a shift of the maximum. Additionally one can notice that r_3 and r_4 display a high scattering in the equilibrium liquid. b) Reduced pair distribution function G(r) of $Pd_{31}Ni_{42}S_{27}$ in the crystalline, glassy and the (undercooled) liquid state. It is evident that the glassy and the undercooled liquid show less smooth shape in G(r). At low values of r ($r < r_1$) a shoulder is visible and the shape of the 2^{nd} peak is degenerated. Interestingly, this degeneration agrees well with the shape of G(r) of the crystal. The positions of the 1-, 2-, 3- and 4-atom connections are displayed as gray vertical lines according to Ref. [101].

6.1.4 The Unexpected Brittle Behavior of $\mathbf{Pd_{31}Ni_{42}S_{27}}$

On the basis of different empirical correlations, a high ductility is expected for glassy $Pd_{31}Ni_{42}S_{27}$ due to the low kinetic fragility and the high Poisson ratio. For instance, Novikov et al. suggested that Poisson's ratio also correlates with the kinetic fragility [252, 291, 292]. In turn, it was proposed by Lewandowski et al. [251, 293] that Poisson's ratio is proportional to the ductility/ fracture toughness of a material. Thus, the temperature sensitivity of the thermo-physical properties or rather the dynamics of the liquid allow to draw conclusions about the plastic deformation behavior of the corresponding glass. For example, the Pt-based alloy $Pt_{57.3}Cu_{14.6}Ni_{5.3}P_{22.8}$ has a high Poisson's ratio and displays a rather low kinetic fragility (D*=13.6 ± 1) [39] in combination with a high ductility under bending and compressive loading [293].

However, the sulfur-bearing $Pd_{31}Ni_{42}S_{27}$ glassy alloy is characterized by a very low fragility (D* $\approx$ 8.3 / m $\approx$ 88) in combination with a high Poisson's ratio of 0.410 ± 0.010. These values agree perfectly with the correlation between Poisson's ratio ν and the fragility index m postulated in Ref. [292] ($\nu = -0.179 + 0.312 log(m)$), predicting a value

0.43 for ν. Hence, a very ductile mechanical behavior is expected for $Pd_{31}Ni_{42}S_{27}$, but the mechanical testing by three-point beam flexural bending (see section 5.1.5) clearly reveals a brittle mechanical behavior. Thus, the correlation between ν and the ductility is challenged.

It has to be mentioned that care has to be taken when interpreting the plastic behavior of a glassy alloy, because the ductility is strongly influenced by the amount of free-volume or rather the respective structural relaxation state of the sample [117, 294, 295]. The relaxation state is in turn a function of the cooling rate during the processing and hence, of the sample thickness. For instance, the Pd-based alloy $Pd_{43}Cu_{27}Ni_{10}P_{20}$ shows a high plasticity for thin samples but fractures in a brittle manner for thicker samples [117, 294]. It is for this reason that melt spun ribbons with a thickness of about 20 μm have been produced of $Pd_{31}Ni_{42}S_{27}$ in the frame of this work. Even the high cooling rates of about 10^6 K/s do not lead to a more ductile behavior of this alloy and hence, it is suggested that the alloy is intrinsically brittle.

The connection schemes of the representative structural units, which have been discussed above, are also thought to determine the mechanical behavior from simulation studies [101]. In case of the Pt-P and Pd-P based alloys in Ref. [283], the higher number of 2- and 4-atom connections in the structure of $Pt_{42.5}Cu_{27}Ni_{9.5}P_{21}$ is indeed reflected in a higher ductility in comparison to $Pd_{43}Cu_{27}Ni_{10}P_{20}$. Thus, from the similarities of the connection schemes of $Pd_{31}Ni_{42}S_{27}$ to the $Pt_{42.5}Cu_{27}Ni_{9.5}P_{21}$ alloy, also a ductile behavior is expected for $Pd_{31}Ni_{42}S_{27}$, but as discussed above, the three-point beam bending tests in section 5.1.5 clearly revealed a brittle mechanical behavior. Therefore, the cluster connection scheme does not allow conclusions about the mechanical behavior in the Pd-Ni-S system, at least for samples produced by copper mold casting.

One possible explanation for the unexpected brittle behavior might also be the casting technique used for the production of amorphous sample, as already discussed in case of the GFA in the end of section 6.1.2. It was shown for a Fe-based BMG that a significant difference in the mechanical behavior is observed, depending on the respective casting process [296]. In the referred work, a significantly higher compressive plasticity is observed for samples produced by the water quenching technique, which is attributed to originated from a higher cooling rate gradient in the sample, resulting in a more heterogeneous free volume distribution.

6.2 Glass Formation in the Quasi-ternary Ti-Zr-Ni-Cu-S System

This section deals with the results about the experimentally determined GFA, the findings about the thermo-physical properties and the information about the primary precipitating phases upon heating and cooling in the Ti-Zr-Ni-Cu-S system. These results are discussed in context of the state of the art of Ti-based BMGs and the findings in S-free BMG forming alloys. Subsequently, the evolution of the structure with temperature is investigated in detail in order to find links between the process of glass formation and the structure. Finally, the relevant properties for potential applications of this new class of Ti-based alloys are discussed.

6.2.1 State of the Art of Ti-based Bulk Metallic Glasses

In the following, the state of the art of Ti-based bulk metallic glasses is reviewed briefly in order to allow the reader a better assessment of the findings of this work. In Fig. 6.9 the critical casting thickness of Ti-based BMGs is shown as a function of the Ti-content. The first Ti-based BMGs with a high GFA were discovered in systems with Be, reaching critical diameters of up to 5 cm [297]. However, the high amount of toxic Be strongly limits their field of application. To date, the use of Be in alloys is considered critical and for future applications the use of this element is tried to be avoided. For example, substitute materials for beryllium bronze are developed for electronic applications or in mold making.
Be-free Ti-based bulk glass forming alloys show a drastically lower critical casting thickness. Especially alloys with high Ti-contents show a poor GFA. For instance, glass forming alloys with 55 at% display a critical diameter of only 2 mm, strongly limiting their range of application. However, at this point the properties of the most promising candidates for a widespread application are discussed briefly.

One of the most popular bulk glass forming alloys with a relatively high Ti-content is Vitreloy 101 ($Cu_{47}Ti_{34}Zr_{11}Ni_8$), which was discovered in the late 90's at Caltech by the Johnson group on the basis of the binary $Ti_{50}Cu_{50}$ composition [13]. The alloy consist in general of elements that are suitable for the industrial scale processing and the amount of expensive Zr is rather low in combination with a critical diameter of about 4 mm. Thus, this alloy is an interesting candidate for the use as structural material. Applications as implant material are not excluded, but the amount of 8 at% of Ni might be refused in this technological field. However, due to the high amount of Cu the alloy has a rather high density (6.9 g/cm^3). The high content of Cu also results in a lower

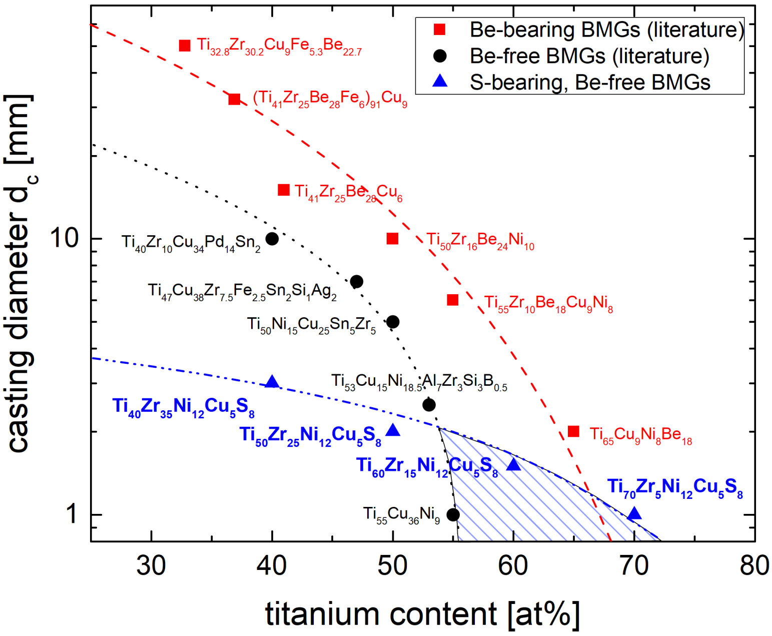

Figure 6.9: Critical casting diameters of Ti-based bulk glass formers as a function of their Ti-content. The dashed lines are trend-lines only used to guide the eye. Be-containing BMGs [297–301] (red squares, dashed line) generally show a higher GFA than Be-free alloys [18, 302–305] (black circles, dotted line). No bulk glass formation is observed for Be-free alloys with a Ti-content higher than 55 at%. The sulfur-bearing glass-forming alloys in this study (blue triangles, dash-dotted line) show bulk glass formation for Ti-contents up to 70 at% for the first time. The shaded area highlights the newly opened compositional range of bulk glass-formation for Be-free titanium alloys containing sulfur. Figure and figure description are taken from Ref. [7].

corrosion resistance compared to crystalline Ti-alloys (see section 5.2.6). The attempt to increase the amounts of Ti to more than 50 at% resulted in the study of Johnson et al. in a drastic decrease of the GFA and no bulk glass formation is reported [13].

In 2007 Inoue and Co-workers developed the $Ti_{40}Zr_{10}Cu_{36}Pd_{14}$ alloy also on the basis of the binary $Ti_{50}Cu_{50}$ alloy, achieving a critical diameter of up to 6 mm [306]. The critical diameter can be tuned to about 1 cm by addition of Sn [18, 307]. As-cast parts of these alloys have a high compressive strength and hardness of roughly 2 GPa and 550 HV, respectively [18, 306, 307]. However, the high amount of Pd leads to a high density (7.08 ± 0.02 g/cm^3 [308]) and high raw material costs, limiting their application. Again the high amount of Cu results in a higher susceptibility for the formation of corrosion pits [308].

Recently, another Ni-free Ti-based BMG was found in case of $Ti_{47}Cu_{38}Zr_{7.5}Fe_{2.5}Sn_2$-$Si_1Ag_2$ [305]. The alloy displays a GFA of up to 7 mm and comparable mechanical properties (ρ=6.3 g/cm^3, σ_{yield} =2 GPa, hardness=588 HV [305]) to the $Ti_{40}Zr_{10}Cu_{36}Pd_{14}$ alloy, but expensive elements such as Pd are excluded and thus, the alloy is more suitable for the industrial use on a large scale. More importantly, both alloys are Ni-free

Ti-based BMGs, showing high potentials for the application as implant material.

However, all three alloys have in common that they are developed on the basis of the binary Ti-Cu system around a ratio of $Ti_{50}Cu_{50}$. As discussed in section 5.2.6, the high difference in the nobility or rather the electrochemical potential results in a low corrosion resistance especially in chloride solutions [122]. Furthermore, the thermal stability of these alloys is rather low, impeding the liquid-like processing by thermoplastic forming [309] and also inhibiting an in-depth characterization of the thermo-physical properties of the deeply undercooled liquid.

6.2.2 On the Glass Forming Ability of new Ti-based Bulk Metallic Glasses

The novel Ti-based alloys, which have been designed in the frame of this work, show Ti-contents of up to 70 at% in combination with a critical casting thicknesses of 1 mm (Fig. 6.9). The particular $Ti_{40}Zr_{35}(Cu,Ni)_{17}S_8$ alloys exhibit a GFA of up to 3 mm. Furthermore, it is possible to exclude Ni in these alloys and the use of industrial grade raw materials does not alter the GFA and the mechanical properties. Again it is noticeable, that in the Ti-Zr-Cu-Ni system no bulk glass formation is observed at the Ti-rich side with Ti-contents of more than 55 at% [13]. Hence, sulfur is an indispensable component for glass formation in the Ti-Zr-Cu-Ni-S system.

The novel alloys have been developed on the basis of the binary Ti-Ni and Ti-S eutectics 4.3. Interestingly, the compositional modifications during the optimization of the GFA result in an extension of the melting interval and the best glass former are off-eutectic alloys, challenging the empirical rules for metallic glass formation (see section 2.2.1). The reduced glass transition temperature t_{rg} is only of about 0.5 and hence, bulk glass formation would not be suggested from the melting detection experiments. Interestingly, broad melting intervals of alloys can also be found in the Al-Ni-Y system [310]. Here the best glass former show high amounts of the main component Al of up to 86 at%, exhibiting a broad melting interval. However, in contrast to the S-bearing alloys the GFA of these Al-based MGs is rather poor.

Another finding in this study is that the alloys with the highest critical casting thickness exhibit the lowest thermal stability. Since these findings are contrary to the expectations from the empirical rules for metallic glass formation, the elaboration of the process of glass formation of the new Ti- and Zr-based BMGs is of great interest. So far, no thermo-physical data about Ti-based BMGs are available, since Ti-based BMGs have commonly a too low thermal stability for the measurements of thermo-physical quantities such as the molar heat capacity or the viscosity of the undercooled liquid. In this work, the thermo-physical properties of a Ti-based BMG with an Ti-content of 60 at% ($Ti_{60}Zr_{15}Cu_{17}S_8$) are measured and interpreted for the first time.

The driving force for crystallization

From the value of the molar heat capacity Δc_p^{l-x} at T_g (see section 5.2.1) and the low entropy of fusion ΔS_f of 5-8[2] (see section 4.3) an intermediate ascent of the driving force for crystallization $\Delta G^{l-x}(T)$ is concluded by comparing the results of this work with the data available for other Zr-based BMGs, which display a $\Delta c_p^{l-x}(T = T_g)$ of roughly 45 J g-$atom^{-1}$ K^{-1} in the equilibrium liquid and equal values for the entropy of fusion.

On the strong kinetic behavior in $Ti_{60}Zr_{15}Cu_{17}S_8$

The measurements of the dynamic viscosity $\eta(T)$ in vicinity of the glass transition and in the high temperature equilibrium liquid revealed a strong kinetic behavior over fifteen orders of magnitude, which can be well described by a VFT equation with a D^* of 19.6, T_0 of 434.8 K and an η_0 of 3.64$x10^{-5}Pas$ (Fig. 6.10). This is rather unexpected, since in several Zr-based BMGs a fragile-to-strong transition of the high temperature equilibrium liquid to the deeply undercooled liquid is observed [40, 50] (Fig. 2.4b). An apparently high viscosity above T_l because of a persisting crystalline phase in the melt or due to reactions can be excluded, since synchrotron experiments revealed that above 1360 K the melt contains no crystals. One explanation for the absence of a fragile-to-strong transition is that the transition temperature takes place above T_l as observed for Vitreloy 1 ($Zr_{41.2}Ti_{13.8}Cu_{12.5}Ni_{10}Be_{22.5}$). Such a behavior was also proposed in Angell's big picture for strong glass formers like SiO_2 or BeF_2 [311].
However, the kinetically strong behavior results in a high melt viscosity in vicinity of T_l ($\eta(T_l) \approx$ 500 mPas), favoring glass formation. For comparison, other bulk glass forming alloys like Vitreloy 101 and Vitreloy 105 show values for $\eta(T_l)$ of roughly 30 mPas and 120 mPas [213]. Sulfur-free alloys like $Ti_{37}Zr_{42}Ni_{21}$ and $Ti_{39.5}Zr_{39.5}Ni_{21}$ show melt viscosity of only about 50 mPas at the liquidus temperature [312, 313]. Thus, the high melt viscosity of $Ti_{60}Zr_{15}Cu_{17}S_8$ might be caused by the small sulfur atoms, resulting in a more densely packed structure, which is accompanied by a reduced atomic mobility.

As a result, the sluggish kinetics and the intermediate driving force are in good agreement with the observations for other Zr-based BMGs. As discussed by Gross et al. the process of glass formation in Zr-based BMGs is commonly evoked by a low driving force for crystallization in combination with sluggish kinetics manifested by a high fragility parameter in the range of 20 - 25 [63].

---

[2] As already pointed out, because of the high reactivity and the broad melting interval an exact determination of the entropy of fusion is not possible.

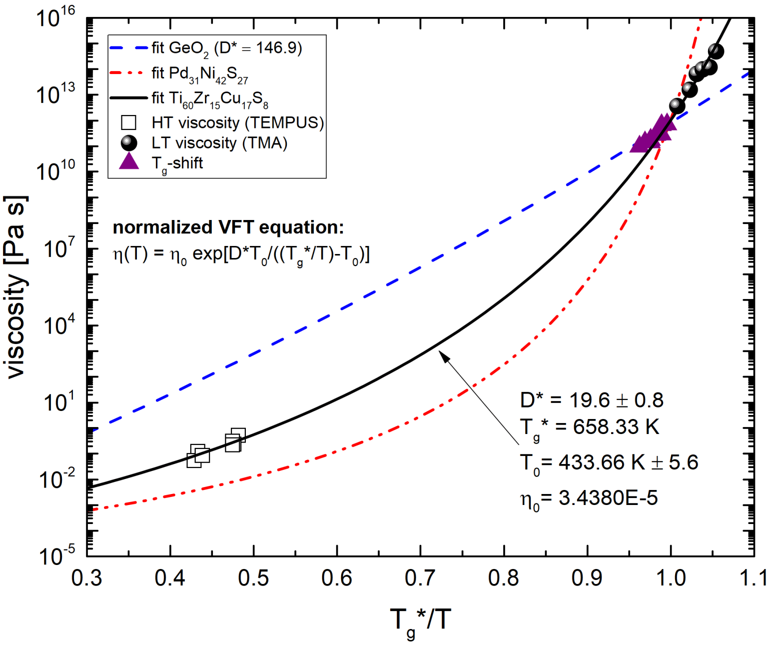

FIGURE 6.10: Angell plot of different bulk glass forming alloys. $Ti_{60}Zr_{15}Cu_{17}S_8$ shows a strong kinetic behavior over fifteen orders of magnitude, resulting in a high melt viscosity. Data about GeO_2 are taken from Ref. [38].

Estimation of the interfacial energy

Finally, the last contribution to the process of glass formation is the interfacial energy between the crystalline phase and the liquid phase γ^{x-l}. As already pointed out, this γ^{x-l} is hard to assess experimentally and hence, the fitting of the isothermal time-temperature-transformation (TTT) diagram is the most straight foreword approach. However, in case of highly reactive melts, this is only possible in container-less experiments like an electrostatic levitator (ESL). Unfortunately, this setup allows only moderate cooling rates and thus, the alloys need to have a very high GFA[3]. ESL experiments were conducted at the German aerospace center (DLR) in Cologne, but the cooling rate is not high enough and the high liquidus temperature causes a strong evaporation in the equilibrium liquid. Thus, in the frame of this work γ^{x-l} could not be determined. From literature one can see that Zr-based BMGs commonly have a rather low interfacial energy (γ^{x-l}=0.01 - 0.04 J m^{-2} [221, 271, 272]) in comparison to Pd- (γ^{x-l}=0.079 J m^{-2} [269]) and Pt-based BMGs (γ^{x-l}=0.11 J m^{-2} [63]) and hence, for the novel Ti-based BMGs also a low interfacial energy is expected.

In summary, the GFA in the novel Ti-Zr-Cu-Ni-S system is supposed to originate from the sluggish kinetics in the whole range of the undercooled liquid. The lower GFA in

---

[3] A critical cooling rate of less than 10 K/s, which corresponds to a critical casting thickness of more than 10 mm.

comparison to Zr-based BMGs might result from a higher driving force for crystallization, which is caused by the high liquidus temperature and the broad melting interval. About the role of the interfacial energy no conclusion can be drawn on the basis of the results of this work, but compared to literature, a low interfacial energy is expected.

Besides the glass forming ability, the thermal stability is decisive for the processing of BMGs by techniques like thermoplastic forming or selective laser melting. Assuming that a better GFA results from a shift of the nose in a TTT diagram to longer crystallization times, an increasing d_c should be connected to an increase of the thermal stability. Interestingly, a decoupling of both quantities is observed in the Ti-Zr-Cu-Ni-S system. Similar observation were made in the Zr-Ti-Cu-Ni-Be system [135, 314], where the alloys with the highest GFA also exhibit the lowest thermal stability. The authors suggested a change of the crystallization mechanism to cause this decoupling.

Crystallization sequences in the quasi-ternary Ti-Zr-Ni-Cu-S system

In order to understand the reason for the decoupling of the GFA and the thermal stability or rather the extend of the SCLR, the crystallization processes of the Ti-based alloys are discussed in detail:

Upon heating from the glassy state of the Ti-alloys (e.g. $Ti_{60}Zr_{15}Cu_{17}S_8$, $Ti_{40}Zr_{35}Cu_{17}S_8$) and the Zr-based alloy $Zr_{56.5}Ti_{13.3}Ni_{13.6}Cu_{9.6}S_7$, the primary phase is determined to an icosahedral phase (see section 5.2.3), which is followed by the formation of the intermetallic compound $(Ti, Zr)_2Cu$ in case of the Ti-based alloys. In Fig. 6.14a the crystallization sequence upon heating (curve (1)) is shown schematically as a TTT diagram. The formation of an icosahedral phases as primary phase upon heating is observed in several glassy systems [198, 243, 315], including for example Ti-Zr-Cu-Ni-Be alloys. These Ti-based, Be-containing alloys display a rather low thermal stability but a high GFA of up to 8 mm [183]. In contrast, the sulfur-bearing Ti-based alloys show a significantly higher thermal stability. From the T_g-shift measurements for the $Ti_{60}Zr_{15}Cu_{17}S_8$ and the $Zr_{56.5}Ti_{13.3}Ni_{13.6}Cu_{9.6}S_7$ alloy, it is evident that both alloys show a rather strong heating rate dependence of the thermal stability or rather the extend of the SCLR. Thus it is suggested, that the formation of the icosahdral phase has a rate dependence (Fig. 6.11a). Interestingly, the continuous TTT diagram (Fig. 6.11a) and the isothermal TTT diagram (Fig. 6.11b) are comparable for both alloys, pointing towards similar crystallization mechanisms, supporting the findings about the identical or at least similar primary phases. However, as already pointed out, the thermal stability is important for processes like thermoplastic forming or 3D printing of a BMG. These processes are well established for Zr-based BMGs but the lack in thermal stability of Ti-based BMGs impeded the processing of these alloys [309, 316]. To asses the thermal stability or rather the processing window of the novel Ti-based alloys, the crystallization temperatures and the crystallization times $t_x^{1\%}$ of a commercially used Zr-based BMG "AMZ4" ($Zr_{59.3}Cu_{28.8}Al_{10.4}Nb_{1.5}$) are added to Fig. 6.11b. It is evident, that the slope of $t_x^{1\%}$ of the S-bearing alloys is much steeper, but nevertheless, at higher temperatures, where the viscosities of the liquid are more suitable for the liquid-like processing by TPF [212], the crystallization times are comparable to the values of AMZ4.

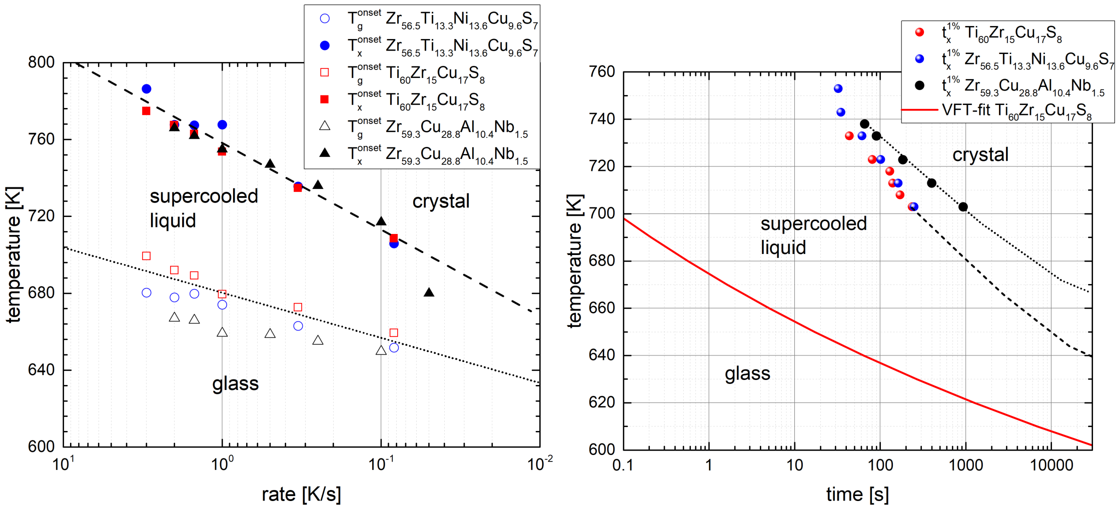

(a) (b)

FIGURE 6.11: a) Low temperature section of the continuous TTT diagram of $Ti_{60}Zr_{15}Cu_{17}S_8$ and $Zr_{56.5}Ti_{13.3}Ni_{13.6}Cu_{9.6}S_7$. Both alloys show a similar thermal stability. b) Low temperature section of the isothermal TTT diagram of $Ti_{60}Zr_{15}Cu_{17}S_8$ and $Zr_{56.5}Ti_{13.3}Ni_{13.6}Cu_{9.6}S_7$. The VFT fit of $Ti_{60}Zr_{15}Cu_{17}S_8$ is shown as solid red line. For a better interpretation an estimated course of the crystallization times $t_x^{1\%}$ is sketched as dashed line. It is evident, that both alloys show identical crystallization times, although the thermal stability in continuous measurements is different. Additionally, the characteristic temperatures and crystallization times of a commercially used Zr-based BMG "AMZ4" ($Zr_{59.3}Cu_{28.8}Al_{10.4}Nb_{1.5}$) are added. The data about AMZ4 is taken from Ref. [212].

Upon cooling of the Ni-free Ti-based alloys (e.g. $Ti_{60}Zr_{15}Cu_{17}S_8$, $Ti_{40}Zr_{35}Cu_{17}S_8$) the primary phase is identified to be a sulfur-rich phase, most likely followed by the formation of the (Ti,Zr) solid solution and the quasi-binary intermetallic compound Ti_2Cu (see section 5.2.3). The crystallization sequence upon cooling is shown schematically as curve (2) in Fig. 6.14a. Interestingly, the primary sulfur-rich phase is only detectable in SEM images but not identifiable in X-ray diffraction experiments. In Fig. 6.12a an SEM image of the microstructure of the center (lowest cooling rate) of an as-cast 3 mm rod of $Ti_{40}Zr_{35}Cu_{17}S_8$ is shown. Here, a small proportion (about 1 vol%, determined by image analysis) of dendrites is visible. Such an amount of crystallites is below the detection limit of conventional X-ray diffraction or caloric experiments, but should be detectable using high energy synchrotron X-ray diffraction experiments. Surprisingly, the sample from Fig. 6.12a shows no Bragg peaks in synchrotron diffraction pattern in Fig. 6.12b.

Regarding the composition of the black phase (about 20 at% S - see section Fig. 5.21), it is most likely a titanium sulfide phase like Ti_8S_3 or Ti_2S. The diffraction pattern of an as-cast 4 mm rod with a higher amount of crystallites shows clearly Bragg diffraction peaks of the Ti_2Cu phase (Fig. 5.21b). Hence, the primary sulfur-rich phase is not/ hardly detectable in X-ray diffraction experiments. One reason might be the rather complex unit cell of both phases (orthorhombic Pnnm; monoclinic C2/m), which lead to a very complex diffraction spectra [317, 318] (Fig. A.4). Another explanation would be that the phase is also amorphous. However, for an exact identification of the crystalline phases a more comprehensive study is necessary.

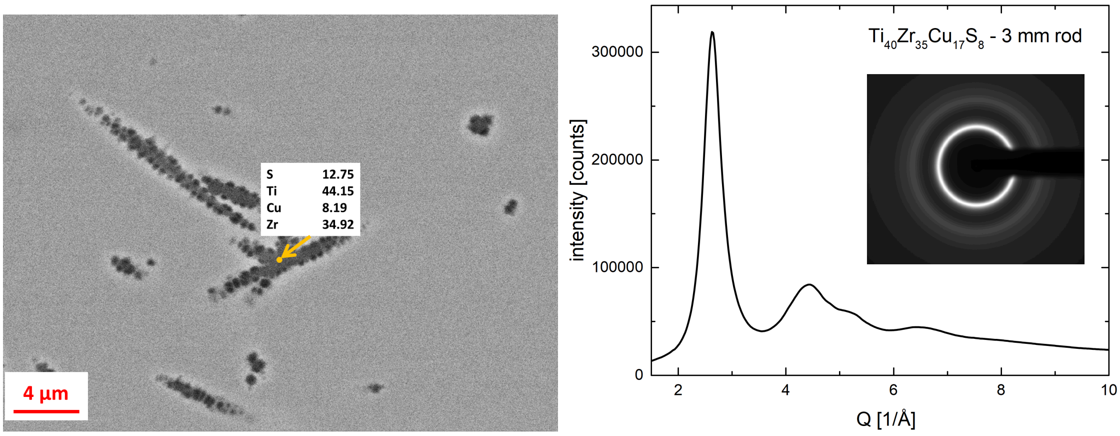

(a)

(b)

FIGURE 6.12: a) BSE image of the microstructure of the center of an as-cast 3 mm rod of $Ti_{40}Zr_{35}Cu_{17}S_8$. A small proportion of crystallites (sulfur-rich phase) can be observed, which is surrounded by a S-depleted bright zone. b) High energy synchrotron X-ray diffraction pattern of the sample shown in a). The small proportion of crystallites is not detectable in the diffraction experiments.

Interestingly, partially crystalline, as-cast samples with lower contents of Cu (e.g. Ti_{60}-$Zr_{15}Ni_{12}Cu_5S_8$, $Ti_{40}Zr_{35}Ni_{12}Cu_5S_8$) or rather Cu-free alloys (e.g. $Ti_{60}Zr_{15}Ni_{17}S_8$, $Ti_{40}Zr_{35}Ni_{17}S_8$) show Bragg peaks of an icosahedral phase like observed upon heating in XRD (Fig. 6.13b) although the black needle-shaped phase is clearly evident in SEM (Fig. 6.13a). From this, it is concluded that the substitution of Cu for Ni changes the second phase upon cooling from the icosahedral phase to Ti_2Cu (Fig. 6.14b). These results are supported by the findings of Kelton et al. for the S-free $Ti_{39.5}Zr_{39.5}Ni_{21}$ alloy, where the primary precipitating phase is identified to be an icosahedral phase [241]. This phase was also identified as primary phase in as-cast partially crystalline ribbons in the Ti-Zr-Ni system and the formation is more difficult if Cu is added to the alloy [242].

Altogether, the S addition in this system is suggested to cause the formation of a sulfide phase which delays the formation of the icosahedral phase or the Ti_2Cu phase, being accompanied by a higher undercool-ability. This, in turn, might originate from the higher melt viscosity of the S-bearing alloys. For instance, the melt S-free $Ti_{39.5}Zr_{39.5}Ni_{21}$ alloy at the liquidus temperature is about one order of magnitude lower than for $Ti_{60}Zr_{15}Cu_{17}S_8$ [312, 313].

As the sulfide phase is identified to be the primary phase, one could assume that the reduction of S in this alloy leads to a reduction of the number and sizes of the sulfide phase resulting in an even higher GFA, but it leads immediately to a pronounced formation of the secondary phase [319], again supporting the findings that sulfur is indispensable for glass formation in this alloying system.

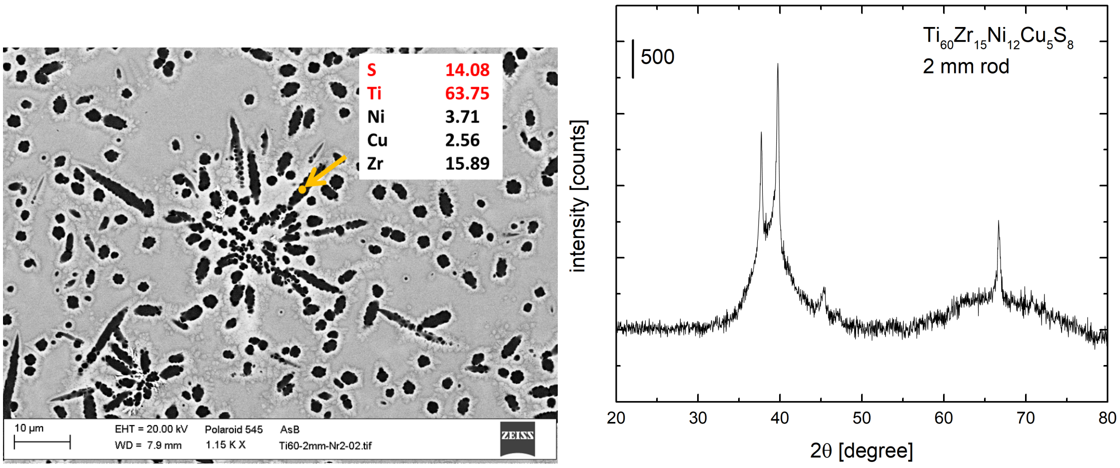

(a) (b)

FIGURE 6.13: a) BSE image of the microstructure of the center of an as-cast 2 mm rod (close to the ingate) of $Ti_{60}Zr_{15}Ni_{12}Cu_5S_8$. Dark dendrites with a higher amount of S and Ti are visible. b) X-ray diffraction pattern of the sample shown in a). The Bragg diffraction peaks are allocated to an icosahedral phase, which is formed around the black phase.

In summary, the substitutions (Zr for Ti and Cu for Ni) affect the GFA and thermal stability differently, because of the different primary phases upon heating an cooling. For instance, Cu results in a significant increase of the thermal stability but, the GFA is strongly reduced. Hence, the addition of Cu seems to make the crystallization of the icosahedral phase much more difficult, but benefits the formation of the sulfur-rich phase or rather the second crystallization product, since the S-rich phase is not detectable in XRD measurements. In contrast, Zr additions lead to an increase of the GFA, in other words, hinder the formation of the sulfide phase, whereas the icosahedral phase forms more easy, resulting in a reduced thermal stability (compare Fig. 6.14).

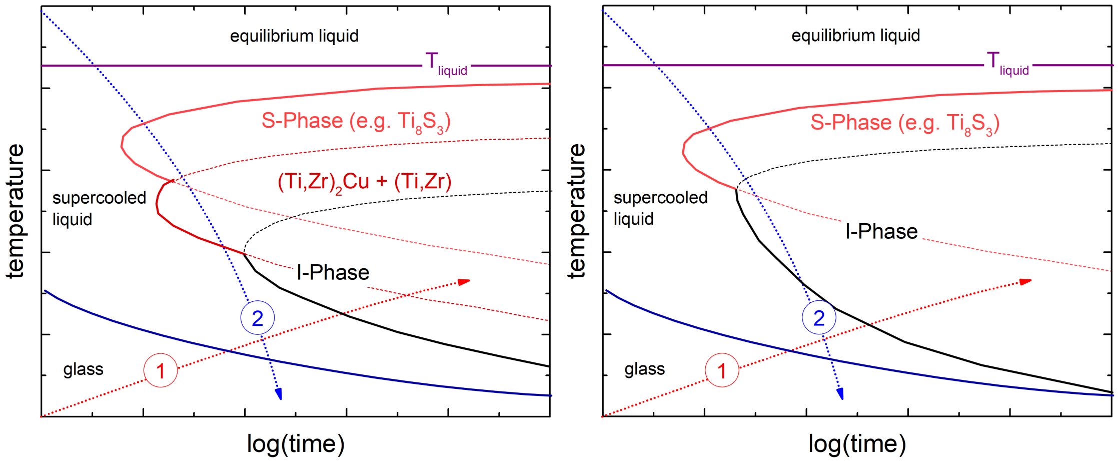

(a) (b)

FIGURE 6.14: Schematic illustration of the crystallization sequences upon heating from the glassy state and upon cooling from the equilibrium liquid for a) $Ti_{75-x}Zr_xCu_{17}S_8$ ($x \leq 35$) and b) $Ti_{75-x}Zr_xNi_{17-y}Cu_yS_8$ ($x \leq 35, y \leq 5$).

6.2.3 Temperature Dependence of the Structure of Sulfur-bearing Ti- and Zr-based Bulk Metallic Glasses

In this section, the evolution of the structure of different alloys in the Ti-Zr-Cu-Ni-S system are investigated in the glassy and the (supercooled) liquid state in order to reveal links to the strong kinetic behavior observed over fifteen orders of magnitude, being decisive for the process of glass formation in this system.

The total structure factor S(Q)

As described in section 5.2.4, the first sharp diffraction peak (FSDP) in the total structure factor S(Q) shows a uniform shape for the alloys $Ti_{60}Zr_{15}Cu_{17}S_8$, $Ti_{40}Zr_{35}Cu_{17}S_8$ and $Zr_{56.5}Ti_{13.3}Ni_{13.6}Cu_{9.6}S_7$, but the temperature dependence of the peak position of the FSDP Q_1 shows some differences (Fig. 6.15). The two Ti-based alloys show a rather similar behavior upon heating from the glassy state and the thermal volume expansion coefficient γ_{glass}^{X-ray} is calculated from the diffraction data to $3.4 \times 10^{-5} K^{-1}$ and $3.3 \times 10^{-5} K^{-1}$ for $Ti_{60}Zr_{15}Cu_{17}S_8$ and $Ti_{40}Zr_{35}Cu_{17}S_8$, respectively. These values are in good agreement with literature data of S-free BMGs [103]. In contrast, the Zr-based alloy shows an unusual behavior. At low temperatures, the thermal volume expansion γ_{glass}^{X-ray} is about one order of magnitude lower ($5.5 \times 10^{-6} K^{-1}$) and increases rapidly in vicinity of the glass transition temperature. The underlying reason for this abnormal behavior stays unclear at this point. The strong increase above T_g^{onset} might result from phase separation.

The in-situ measurements in the ESL allowed also the measurement of the equilibrium liquid of $Ti_{60}Zr_{15}Cu_{17}S_8$, using synchrotron radiation. Unfortunately, the experimental setup results in a high scattering, which is suggested to be caused by sample oscillation in the electrostatic field or the detector. Furthermore, the high liquidus temperature together with the tendency for evaporation limits the accessible temperature range above T_l. However, in comparison to the Pd-Ni-S system the value of Q_1(323 K)/Q_1(T))^3 is higher in the equilibrium liquid as in the deeply undercooled liquid in vicinity of T_g, which agrees with the findings in S-free Zr-based BMGs like Vitreloy 1 or Vitreloy 106a [40, 50]. In these system, this structural metric yields also information about a fragile-to-strong transition (see section 2.3), but the scattering is too high for any conclusions.

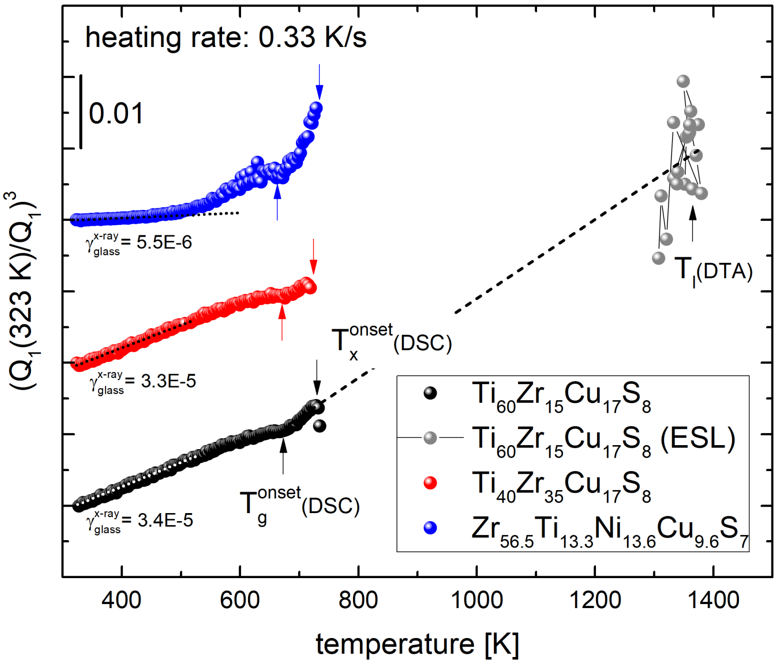

FIGURE 6.15: $(Q_1(323\text{ K})/Q_1(\text{T}))^3$ versus temperature plot of $Ti_{60}Zr_{15}Cu_{17}S_8$, $Ti_{40}Zr_{35}Cu_{17}S_8$ and $Zr_{56.5}Ti_{13.3}Ni_{13.6}Cu_{9.6}S_7$ measured at 0.33 K/s. The thermal volume expansion coefficient γ_{glass}^{X-ray} below T_g is determined to be $3.4 \times 10^{-5} K^{-1}$ and $3.3 \times 10^{-5} K^{-1}$ for the Ti-based alloys and $5.5 \times 10^{-6} K^{-1}$ for the Zr-based alloy. For $Ti_{60}Zr_{15}Cu_{17}S_8$ data of the equilibrium liquid are collected using electrostatic levitation (ESL).

From Fig. 5.24 it is evident, that the second sharp diffraction peak (SSDP) in S(Q) displays a strongly pronounced shoulder at higher values of Q. This feature is much stronger pronounced than for the $Pd_{31}Ni_{42}S_{27}$ alloy (see section 5.1.4). The shoulder is also apparent in the equilibrium liquid state for $Ti_{60}Zr_{15}Cu_{17}S_8$, but less pronounced. This feature is attributed to the existence and formation of short-range order. In fact, the existence of short-range order even above the liquidus temperature is in good agreement with the high melt viscosity in vicinity of T_l. As described for the $Pd_{31}Ni_{42}S_{27}$ alloy, the ratio of $Q_{2.1}/Q_1$ and $Q_{2.2}/Q_1$ are 1.71 and 2.04 in case of an ideal icosahedral ordering.

For $Ti_{60}Zr_{15}Cu_{17}S_8$ the ratios are 1.73 and 1.927 in the equilibrium liquid and 1.709 as well as 1.947 in the glassy state. Hence, the icosahdral ordering is suggested to get more pronounced upon cooling. Similar observations were made by Kelton et al. in case of the $Ti_{39.5}Zr_{39.5}Ni_{21}$ alloy [241]. In their work, also a pronounced icosahedral ordering is observed upon undercooling in in-situ high energy X-ray experiments.

This ordering tendency upon undercooling is also reflected by the increasing molar heat capacity [48] and the rate of loss of the excess entropy ΔS_{l-x}, which is proportional to the configurational contribution of the entropy [38]. One could suggest that the icosahedral ordering of the liquid phase is linked to the thermal stability, since an icosahedral phase is determined as primary precipitating phase. The values of $Q_{2.1}/Q_1$ and $Q_{2.2}/Q_1$ do not change significantly for $Ti_{40}Zr_{35}Cu_{17}S_8$ or $Zr_{56.5}Ti_{13.3}Ni_{13.6}Cu_{9.6}S_7$, and hence, conclusion about a relation between the structure and the thermal stability can not be drawn.

The reduced pair distribution function G(r)

The reduced pair distribution functions G(r) of the Ti-based alloys $Ti_{60}Zr_{15}Cu_{17}S_8$ and $Ti_{40}Zr_{35}Cu_{17}S_8$ are rather similar and show a uniform FSDP at r_1 and only a slight degeneration of r_2 (see section 5.2.4), which is less pronounced than in case of the Pd-based alloy (see section 5.1.4). This degeneration is formed upon cooling as observed in case of the Pd-based alloys. In contrast, in G(r) of the Zr-based alloy a distinctive shoulder is observed to lower r values at r_1.

The Ti-based alloys show a positive slope of $r_1(T)$ below T_g and a sudden change of the slope at T_g to a negative slope in the SCLR. Because of the lower thermal stability of the $Ti_{40}Zr_{35}Cu_{17}S_8$ alloy, the inflection point is not reached at T_g (Fig. 6.16). In contrast, the Zr-based alloy exhibits a negative slope of $r_1(T)$ with increasing temperature and a less pronounced peak at T_g, which might be caused because of the non-uniform shape of the FSDP. In contrast, for the peak positions at higher distances r_2, r_3 and r_4 the rate of change decreases when reaching the glass transition, but at T_g the slope increases again. This behavior is observed for the Ti- as well as the Zr-based alloys.

As described in section 2.3, the temperature-induced changes on the medium-range order length scale can be correlated with the kinetic fragility index m, assuming that the difference of the 3^{rd} and the 4^{th} atomic shell is represented by r_3 and r_4. The resulting difference in the volume dilatation of these two atomic shells is plotted over the T_g'[4] scaled temperature in Fig. 6.17. As shown in Fig. 2.13b, a lower sensitivity of ΔV_{4-3} (m_{str}) is observed for alloys with a lower kinetic fragility index m_{kin}. However,

---

[4] T_g' is defined in Ref. [104] as the onset temperature of the supercooled liquid region in DSC, which is manifested by a kink in the peak position r_1 (Fig. 6.16).

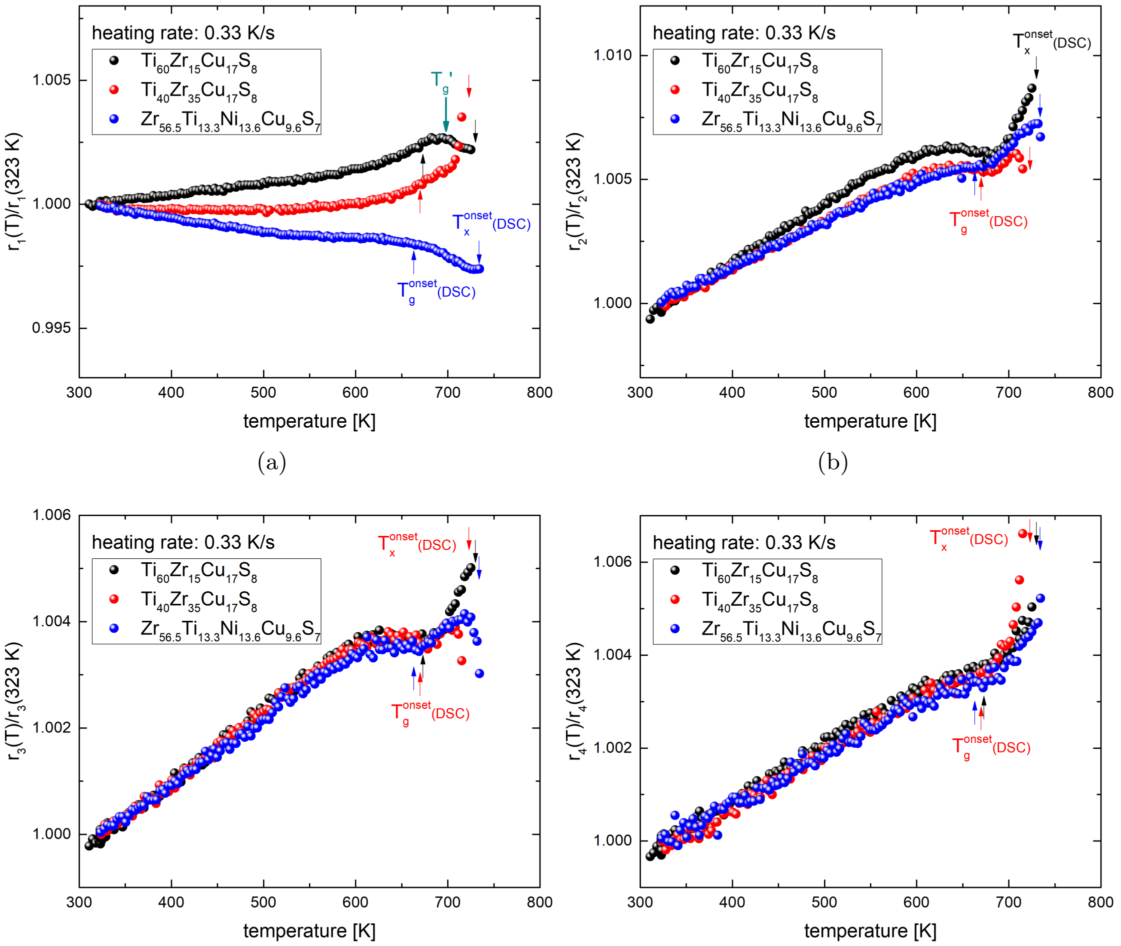

(a) (b)

(c) (d)

FIGURE 6.16: Change of the normalized peak positions r_1, r_2, r_3 and r_4 with temperature of $Ti_{60}Zr_{15}Cu_{17}S_8$, $Ti_{40}Zr_{35}Cu_{17}S_8$ and $Zr_{56.5}Ti_{13.3}Ni_{13.6}Cu_{9.6}S_7$. The onset of the glass transition T_g^{onset} and the onset of crystallization T_x^{onset} from DSC measurements with 0.33 K/s are indicated as arrows. Additionally, the onset of the SCLR obtained by DSC measurements is marked with T_g' in a).

the alloys of this work challenge the proposed correlation because they display a high temperature sensitivity of the structure but the viscosity measurements reveal a strong kinetic behavior. One explanation might be the tendency for phase separation of the alloys.

Another interesting finding is the evolution of the second peak in G(r) with temperature. G(r) of the equilibrium liquid, the glass and the crystalline structure are shown in Fig. 6.18. Here, a similar behavior as in the case of $Pd_{31}Ni_{42}S_{27}$ can be observed. The SSDP in G(r) shows a uniform shape in the equilibrium liquid, but a degeneration is visible, which is manifested by the formation of a shoulder at higher values of r. According to Ref. [100, 101], the shape of the SSDP yields information about the MRO or rather the connection schemes of the local representative structural units (RSU) (e.g. coordination

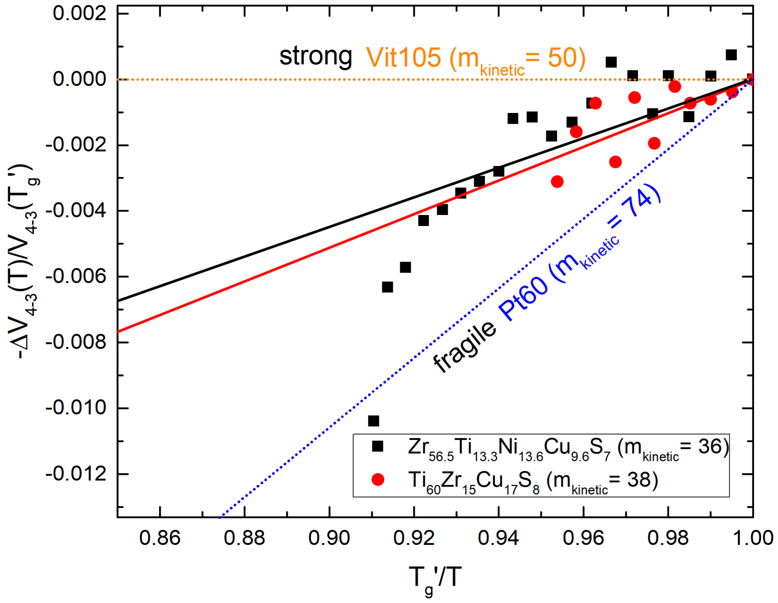

FIGURE 6.17: $-\Delta V_{4-3}(T)/V_{4-3}(T_g')$ versus T_g' scaled temperature plot of $Ti_{60}Zr_{15}Cu_{17}S_8$ and $Zr_{56.5}Ti_{13.3}Ni_{13.6}Cu_{9.6}S_7$. In S-free BMGs (i.a. Vit 105 ($Zr_{52.5}Ti_5Cu_{17.9}Ni_{14.6}Al_{10}$) or Pt60 ($Pt_{60}Cu_{16}Co_2P_{22}$)), a higher sensitivity of the volume dilatation of the 3^{rd} and the 4^{th} atomic shell correlates with the kinetic fragility parameter $m_{kinetic}$.

polyhedra) (see section 2.3 and 5.1.4). The positions of these second nearest neighbor atoms are calculated to be at 2 r_1 (1-atom connection), $\sqrt{3}$ r_1 (2-atom connection), $\sqrt{(8/3)}$ r_1 (3-atom connection) and $\sqrt{2}$ r_1 (4-atom connection) [96–98, 101] and are marked as gray vertical lines in Fig. 6.18. It is evident, that in the glassy structure the 1- and 2-atom connections are distinctively pronounced. Signatures of the higher order connections are in contrast to the $Pd_{31}Ni_{42}S_{27}$ alloy not evident. As these features are less pronounced in the reduced pair distribution function of the high temperature equilibrium liquid, these characteristics seem to form upon undercooling to the glassy state and are assumed as the formation of MRO [101].

However, more interesting is the fact that these features are also present in G(r) of the crystalline structure, like observed for the $Pd_{31}Ni_{42}S_{27}$ alloy (see section 5.1.4), implying that the connection scheme or rather the MRO is also reflected in the crystalline structure. This is in good agreement with the simulation studies on pure Fe in Ref. [102]. Combining these results with the results on the $Pd_{31}Ni_{42}S_{27}$ alloy, the presumption about the connection of structural data and the thermo-physical properties is intensified. As described in section 5.1.4, it might be possible that in the Pd-Ni-S system the high interfacial energy or the entropy difference between the liquid and the crystalline phase, is somehow reflected in a large structural difference between the equilibrium liquid and the crystalline structure, which in turn influences the MRO of the glassy phase. It is evident from Fig. 6.18 that the shape of the SSDP of G(r) of the equilibrium liquid is much closer to that of the crystalline structure compared to the one in the Pd-Ni-S system (Fig. 6.8b). If the interfacial energy in the Ti-Zr-Cu-S system is as low as observed in Zr-based systems [221, 271, 272], it would be possible to estimate the interfacial energy from the structural difference between the equilibrium liquid, the glass and the crystal. However, this is discussed in detail in section 6.4.

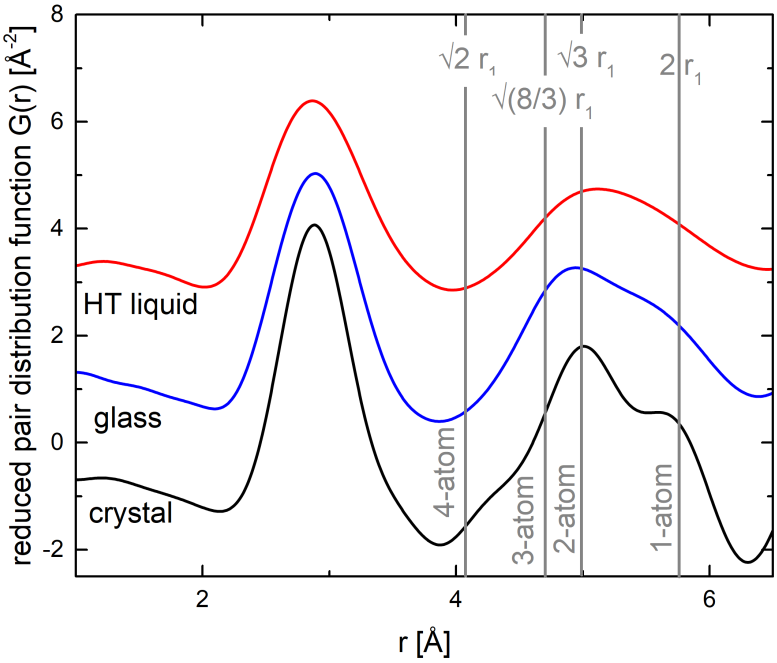

FIGURE 6.18: Reduced pair distribution function G(r) of $Ti_{60}Zr_{15}Cu_{17}S_8$ in the crystalline, glassy and the liquid state. The shape of the 2^{nd} peak is degenerated in the glassy state in comparison to that of the equilibrium liquid. As observed for the $Pd_{31}Ni_{42}S_{27}$ alloy, the degeneration is also visible in the shape of G(r) of the crystal. The gray vertical lines mark the positions of the 1-, 2-, 3- and 4-atom connections according to Ref. [101].

6.2.4 Properties of Ti-based Bulk Glass Forming Alloys and their Application

As-cast samples of $Ti_{60}Zr_{15}Cu_{17}S_8$ and $Ti_{40}Zr_{35}Cu_{17}S_8$ show a yield strength of up to 3 GPa in bending in combination with a hardness of about 500 HV (see section 5.2.5). More interestingly, the high yield strength is not accompanied with a brittle mechanical behavior. Only a small number of bulk glassy alloys shows bending ductility[5] and one major goal, besides an increasing GFA of an alloy, is the simultaneous improvement of plasticity. For example, minor additions are often added to improve both, the GFA and ductility [320]. In most studies the plasticity of BMGs is evaluated by compression tests, because BMGs show in general no plasticity in tension (see section 2.4). However, a more

---

[5] One has to be aware, that the sample geometry (process zone size) and the cooling rate affect the ductility of metallic glasses. (see section 2.4)

application oriented evaluation is achieved by bending tests, since most parts are subjected to tension and compression simultaneously. Because of the tensile stresses, only a small number of BMGs exhibit a pronounced plasticity under bending load. For example, a study of Schroers et al. revealed that the $Pt_{57.3}Cu_{14.6}Ni_{5.3}P_{22.8}$ alloy has an enormous plasticity (total strain to failure) in compression of more than 20 %, but only a plasticity of 3 % in bending tests. In comparison, alloys like $Ti_{47}Cu_{38}Zr_{7.5}Fe_{2.5}Sn_2Si_1Ag_2$ [305], $Ti_{40}Zr_{10}Cu_{36}Pd_{14}$ [18] and $Ti_{60}Zr_5Cu_9Ni_8Be_{18}$ [321] display a strain to failure of only 5 % under pure compression, but inter alia $Ti_{47}Cu_{38}Zr_{7.5}Fe_{2.5}Sn_2Si_1Ag_2$ does not show any plasticity in bending mode (Supp. Fig. A.7). Therefore, it is even more surprising that the novel Ti-based glassy alloys exhibit a total strain to failure of 4.5 % under bending load, tending to an even higher plasticity under compression.

Additionally, the high amount of Ti of the new alloy results in a low density as low as 5.5 g cm^{-3}. Because of this combination of properties, the new sulfur-bearing Ti-based BMGs are able to outperform crystalline Ti-alloys such as Ti6Al4V regarding their properties. This is emphasized in Fig. 6.19a.

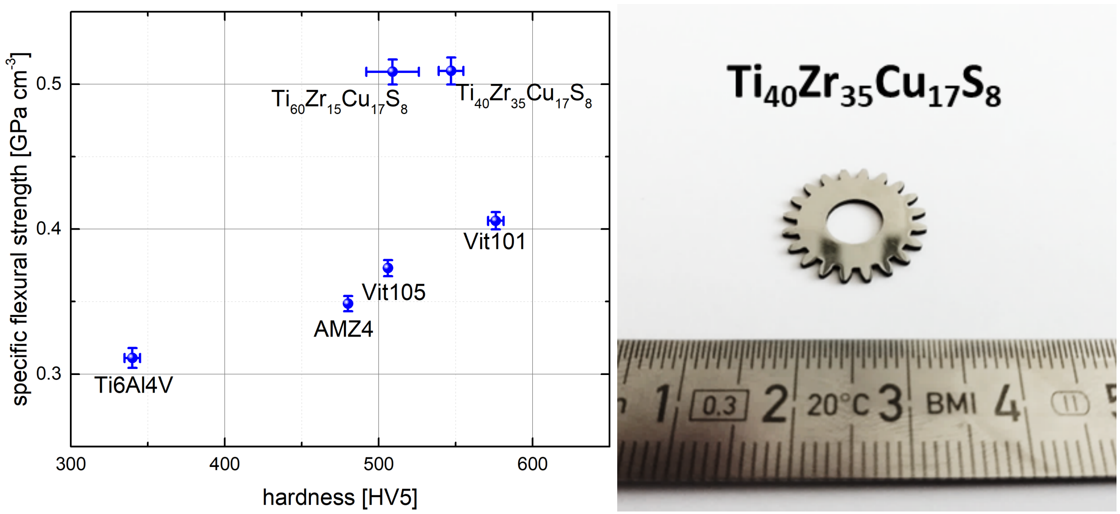

(a)

(b)

Figure 6.19: a) Specific flexural strength versus hardness plot of the novel Ti-based alloys in comparison to crystalline Ti6Al4V and commercially available BMGs. b) Gear produced from industrial grade $Ti_{40}Zr_{35}Cu_{17}S_8$.

At this point, the link between the mechanical and thermo-physical properties is picked up again. As proposed in Ref. [252, 291, 292, 322], the kinetic fragility is reflected in the mechanical properties e.g. Poisson's ratio via $\nu = -0.179 + 0.312log(m)$ [292]. According to this equation, a value of 0.34 can be calculated for ν from the experimentally determined fragility index m of 38 for $Ti_{60}Zr_{15}Cu_{17}S_8$. The measured value of ν is 0.38 and hence, the experimental correlation between m and ν is challenged. As already discussed, ν supposedly yields also information about the plasticity of an alloy and the value of 0.38 indeed predicts a rather ductile mechanical behavior[251]. However, the value of ν of $Pd_{31}Ni_{42}S_{27}$ is even higher ($\nu = 0.42$), which agrees with the kinetically fragile but contrasts with the mechanically brittle behavior. Thus, the findings of this work suggest that the correlation between ν, m_{kin} and the plasticity are not valid for S-bearing systems. Similar observation were made by Battezzati for different glass forming systems [323].

Besides their mechanical performance, the corrosion resistance is essential for the application of a metal in biomedical and industrial applications. Commonly, Zr- or Ti-based BMGs exhibit high contents of late transition metals such as Cu and/or Ni [127]. The high difference in the electrochemical potential between the late transition metals and the early transition metals (e.g. Ti, Zr) results in a high sensitivity for pitting corrosion in chloride-containing electrolytes [125]. However, the novel alloys show higher contents of Ti- and Zr (roughly 75 at%) together with the low contents of Cu and Ni (about 17 at%), leading to an extraordinarily high corrosion resistance. Interestingly, in Ref. [324], Huang et al. reported that BMGs with Cu-contents below 17.5 at% have a significantly higher corrosion resistance than alloys with higher Cu-contents, supporting the findings of this study. The potentiodynamic measurements in section 5.2.6 reveal that the novel sulfur-containing, amorphous Ti-alloys show an excellent passivation behavior, being comparable to crystalline Ti6Al4V.

Despite the superior mechanical and electrochemical properties, the high raw material price of available bulk glass forming alloys limited their widespread use. As shown in section 4.4, the alloys of this study can be produced from industrial purity raw materials (titanium ASTM grade 1, zirconium R60702, CuS 80/20) drastically reducing the raw material price of this alloy, being in the same range as crystalline Ti-based alloys such as Ti6Al4V. Additionally, it is proven in section 5.2.5, that the mechanical properties are not altered by the use of industrial grade raw material and hence, these new alloys are able to outperform crystalline alloys in manifold applications.

Besides the high material costs, the processing costs play a crucial role for the industrial application of BMGs. Most of the available alloys, which might be suitable for different applications, can only be processed on a laboratory scale. One reason is that the available techniques are not customized for the casting of BMGs and hence, only alloys with an exceptionally high GFA (Vitreloy 1, Vitreloy 105) can be processed. The framework conditions of an industrial processing are, in comparison to the processing on an laboratory scale, accompanied by quality cutbacks regarding the mechanical performance and glass forming ability. The high reactivity and the broad melting interval of the novel alloys is an additional challenge for a casting process. However, in this work, an industrial-scale process has been designed, which allows the processing of parts with cycle times below 1 minute from alloys, having a high liquidus temperature and being highly reactive (see section 4.4). In Fig. 6.19b a gear produced from industrial grade $Ti_{40}Zr_{35}Cu_{17}S_8$ is shown, which was eroded from an approximately 500 μm thick injection molded plate. The low cycle times of the casting process are not accompanied by quality cutbacks and thus, it is for the first time possible to process cheap BMG alloys with a low critical casting thickness but favorable properties on an industrial scale.

Besides the GFA, in particular, the mold fill- and flow-properties of an alloy play a key role for casting processes, which are governed by the dynamic viscosity and the surface tension. As already discussed above, the high melt viscosity enables bulk glass formation in this new system and hence, the surface tension σ, is of great interest for the evaluation of the cast-ability. In comparison to Zr- or Ti-(alloys) [156, 235, 236, 238], the sulfur-bearing liquids show an extraordinarily low surface tension of about 1 N/m (see section 5.2.2). For example, the sulfur-free alloy $Ti_{37}Zr_{42}Ni_{21}$ and $Ti_{39.5}Zr_{39.5}Ni_{21}$ show a surface tension of about 1.6 N/m [312, 313]. This reducing effect might result from the high surface activity of elements like S, O, N or C [325]. For example, the surface tension of pure iron is reduced from about 1.7 N/m to less than 1 N/m by the addition of 1 wt% of S (1.72 at%). However, due to the low surface tension, the novel alloys are assumed to be ideal casting alloys, allowing a better replication of the surface structures of the mold.

The same influence of S additions on the surface tension is suggested to be valid for other BMG forming systems, since already minor additions of S to Vitreloy 101 (+1.5 at%) and Vitreloy 105 (+2 at%) result in a drastic change of the wetting behavior in an electric arc furnace. Hence, minor additions of S to known glass formers is not only beneficial for the thermal stability but also to improve the cast-ability. Microalloying of elements to improve the cast-ability is a common method for casting of crystalline alloys (e.g. Na or Sr addition in aluminum cast alloys) [326]. Thus, the micro-alloying of S might have an enormous potential for the industrial processing of BMGs.

6.3 Parallels between different Sulfur-bearing Bulk Metallic Glasses

Although it is evident from the findings in this chapter that sulfur has not an universal role for the process of glass formation and the resulting properties such as the kinetic, thermodynamic or mechanical properties, still some similarities between the Pd- and the Ti-/Zr-based systems are observed.

It is conspicuous that all alloys with a high Ni-content such as $Pd_{31}Ni_{42}S_{27}$, $Ti_{60}Zr_{15}Ni_{17}S_8$ and also $(Ni_{0.62}Nb_{0.38})_{97}S_3$ show a very brittle mechanical behavior. The results about the Ni-Nb-S system (briefly shown in section 4.4.3) will be presented elsewhere. The brittle behavior of these alloys might originate from the bonding character between Ni and S. Small additions of Cu for Ni in the $Ti_{60}Zr_{15}Ni_{17}S_8$ system lead to a drastic improvement of the ductility (see section 5.2.5), which is suggested to be caused by the reduction of the number of the Ni-S bonds. However, these are only speculations and for a more concrete proposition a detailed investigation of the types of bonds is necessary. The equilibrium liquid phase of all S-bearing alloys shows a low surface tension or rather a high wet-ability on water-cooled copper, which is suggested to originated from the high surface activity of sulfur causing a drastic drop of the surface tension as revealed for $Ti_{60}Zr_{15}Ni_{17}S_8$. A lower surface tension is thought to be beneficial for the molding accuracy of the alloys in casting processes.

6.4 Evolution of the Liquid's Structure upon Undercooling

Another interesting finding in this work involves the evolution of the reduced pair distribution function G(r) of the (undercooled) liquid, glassy and crystalline phase. As already pointed out in section 2.3, different authors postulated, mainly on the basis of simulations, a link between the crystalline order and MRO in amorphous liquids and solids [98–102]. For instance, simulations revealed that the topological order in the glass is also reflected in the corresponding crystalline structure for pure Ni and Fe [100, 102] (Fig. 6.20). Wu et al. suggested that the entanglement of different hidden "crystalline" orders influences the glass forming ability of multi-component alloys due to a geometric frustration of the liquid [102]. However, in single component systems the crystallization takes place polymorphically and a defined crystalline structure can be assigned to the liquids structure. This is not the case for more complex, multi-component bulk glass forming alloys. Surprisingly, when looking at the experimental results of $Pd_{31}Ni_{42}S_{27}$ and $Ti_{60}Zr_{15}Cu_{17}S_8$, G(r) of the glassy phase shows significant accordance with that of the crystalline mixture. Moreover, one could suggest a link to the thermo-physical properties, since both alloys show different values of kinetic fragility D^*, the high interfacial energy γ^{x-l}, the excess heat capacity Δc_p^{l-x} as well as the entropy of fusion ΔS_f.

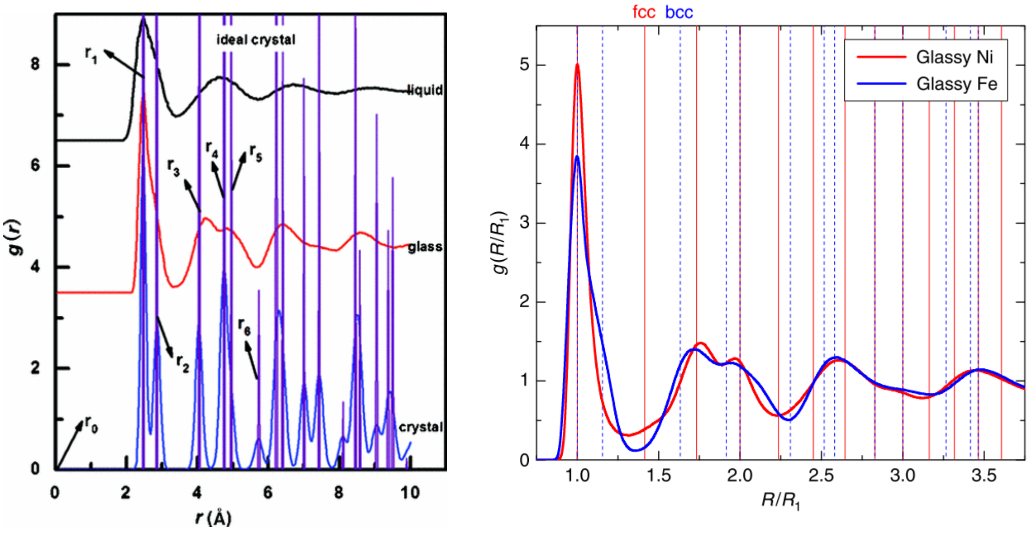

(a) (b)

Figure 6.20: a) Simulated pair distribution function of pure Fe in its liquid, glassy and crystalline state. Taken from Ref. [100]. b) Simulated pair distribution function of pure Ni and Fe in their glassy state normalized to the peak position of the first sharp diffraction peak (FSDP). The blue dashed lines indicated the peak positions of fcc Ni and the red solid lines the peak positions of bcc Fe. Taken from Ref. [102].

At this point, some thermodynamic and kinetic properties are discussed briefly in order to understand possible links to the structure.

As already pointed out, three different thermodynamic contributions determine the process of crystallization: ΔH_f, Δc_p^{l-x} and γ^{x-l}. The enthalpy of fusion ΔH_f yields the entropy of fusion ΔS_f (equation 2.5) and together with Δc_p^{l-x} the driving force for crystallization $\Delta G^{l-x}(T)$ (equation 2.4). In general, ΔS_f, representing the slope of $\Delta G^{l-x}(T)$ at the liquidus temperature, consist of vibrational and configurational contributions, whereby the letter ones originate from the configurational differences between the liquid and the corresponding crystal [38, 42]. As recently proposed by Smith et al. [327], the configurational part $S_{conf}(T)$ is the dominating contribution to the excess entropy $\Delta S^{l-x}(T)$[6] and hence, from a higher value of ΔS_f a higher configurational difference between the amorphous liquid and the ordered crystal can be concluded. Also the increase of $\Delta c_p^{l-x}(T)$ of the undercooled liquid upon cooling reflects the reduction of configurational entropy S_{conf} [28]. This rise of $\Delta c_p^{l-x}(T)$ or rather the vanishing $S_{conf}(T)$ is thought to be manifested by the formation of order in the liquid [29].

The last thermodynamic contribution γ^{x-l} is shown to correlate with ΔH_f or rather with ΔS_f for monoatomic metallic liquids but the proportionality factor is thought to depend i.a. on the respective crystal structure [31]. All in all, the three decisive thermodynamic contributions are linked to the structural differences between the liquid and the crystal and the increase of the order in the liquid phase.

Besides the thermodynamic contributions, the process of crystallization is governed by the atomic mobility. In general, the atomic mobility depends on the degree of order in the liquid phase: The more ordered the liquid is, the slower are the dynamics. As discussed in section 2.2.2.2, based on the theory proposed by Adam and Gibbs [44], a faster decreasing $S_{config}(T)$ (or $\Delta S^{l-x}(T)$) and a faster increase of $\Delta c_p^{l-x}(T)$ upon cooling, was revealed to point towards a kinetically fragile behavior [38, 43, 45, 47, 328]. This is, in turn, allocated to the rate of the increase of structural order in the undercooled liquid down to the glass transition [39, 46–48]. The structural ordering during undercooling is connected to a growth of the cooperatively rearranging regions in the theory of Gibbs and Adam and an increasing relaxation time [44]. Here it has to be mentioned, that $\Delta S^{l-x}(T)$ and $\Delta c_p^{l-x}(T)$ are both excess quantities and hence, they depend also from the value of the crystalline mixture. Nevertheless, also the kinetic contribution depends on the structure of both, the liquid and the crystal.

To give rise to the presumption that the above mentioned thermo-physical properties are somehow reflected in the structural differences between the liquid and the crystal, the reduced pair distribution functions G(r) of available data of S-free BMGs are analyzed in Fig. 6.21.[7] Again it has to be mentioned that in this work only the reduced pair distribution functions and not the partial PDFs are analyzed. Therefore, some characteristics

---

[6] $\Delta S^{l-x}(T_l) = \Delta S_f$

[7] The corresponding raw intensity data of the crystalline structures are shown in Fig. A.8.

in G(r) might get stronger pronounced or vanish due to the superposition of the partial PDFs. However, these alloys are chosen since they cover a wide range of ΔS_f (8 - 15 J g-$atom^{-1}$ K) [39, 45, 54, 216, 233, 329], $\Delta c_p^{l-x}(T_g)$ (J g-$atom^{-1}$ K) [39, 45, 54, 216, 233] as well as D^* (8.2 - 23.1) [45, 53, 54, 63, 329, 330] and for some a value of γ^{x-l} has been determined (0.01 - 0.11 J m^{-2})) [63, 268–272, 331].

By comparison of these eight bulk glass forming alloys showing different characteristics in their thermo-physical properties, the best qualitative agreement is found for ΔS_f (Tab. 6.1, Fig. 6.21): Alloys with the largest structural difference between the liquid and the crystal show the highest values for ΔS_f.

A correlation of the structural difference and the entropy of fusion would be reasonable, as if ΔS_f is considered to be proportional to the configurational entropy [38, 45, 327], a higher difference in the configurational entropy is linked to high structural differences. This hypothesis is supported when looking at the gain of the heat capacity of the undercooled liquid upon cooling (Fig. 6.22). $c_p^l(T_g)$-$c_p^l(T_l)$ is also suggested to refer to the loss of configurational entropy and indeed, qualitatively, a higher structural difference between the glass and the liquid is found for alloys with higher values of $c_p^l(T_g)$-$c_p^l(T_l)$. This is supported by the findings of Liu et al. in MD simulation studies and experimental diffraction experiments [99], suggesting that new atomic orders are formed during cooling from the equilibrium liquid to the glassy state.

However, in this work no quantitative evaluation of the structural difference is found and hence, no defined correlation can be calculated. A quantitative evaluation of the difference is hardly possible as G(r) of the crystal depends on the respective state of the microstructure and hence, is hardly comparable for different alloying systems. Nevertheless, these findings imply that for alloys with a high value of ΔS_f and ($c_p^l(T_g)$-$c_p^l(T_l)$) the liquid's structure has to undergo more complex changes to reach the crystalline state, whereas only slight changes of the liquid's structure are necessary for alloys with low values of ΔS_f and ($c_p^l(T_g)$-$c_p^l(T_l)$) to form the crystalline phases.[8] At this point the question arises, whether the thermo-physical properties of an undercooled liquid are to some extend predetermined by the specific crystalline structure and even whether some properties of the glassy phase might be derived from the crystalline phase. Therefore, a comprehensive investigation of this connection might be promising.

---

[8] Note, that for some bulk glass forming alloys the enthalpy of fusion and thus, also the entropy of fusion, differ significantly between the melting from the as-cast amorphous state and the slower cooled crystalline state. Here, the melting from the crystalline state subsequent to the crystallization at 0.33 K/s is chosen.

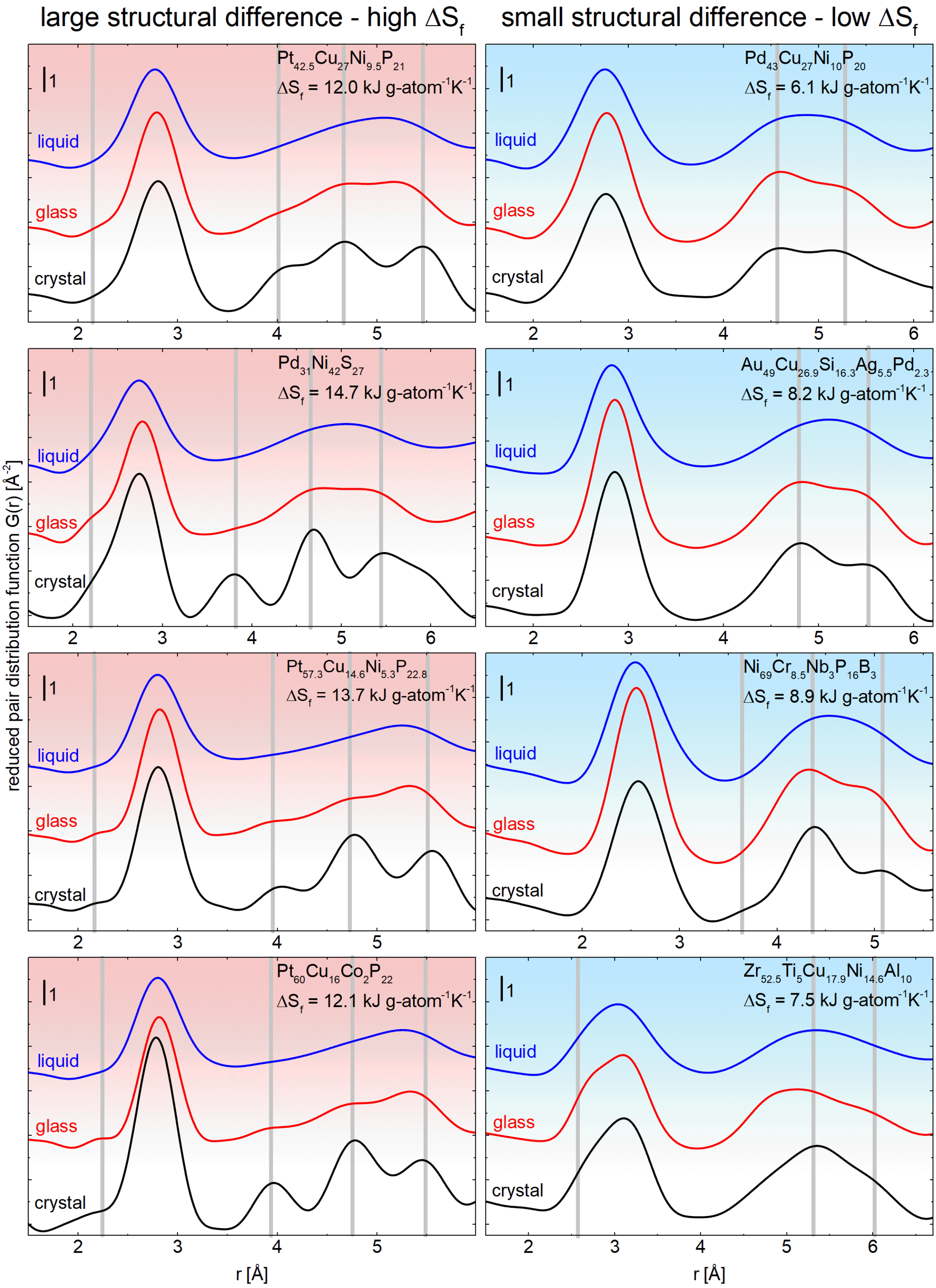

FIGURE 6.21: Reduced pair distribution function of the liquid, glassy and crystalline state of different bulk glass forming alloys. The gray vertical lines highlight the similarities between the crystalline and the glassy structure. The corresponding I(Q) data is shown in Fig. A.8.

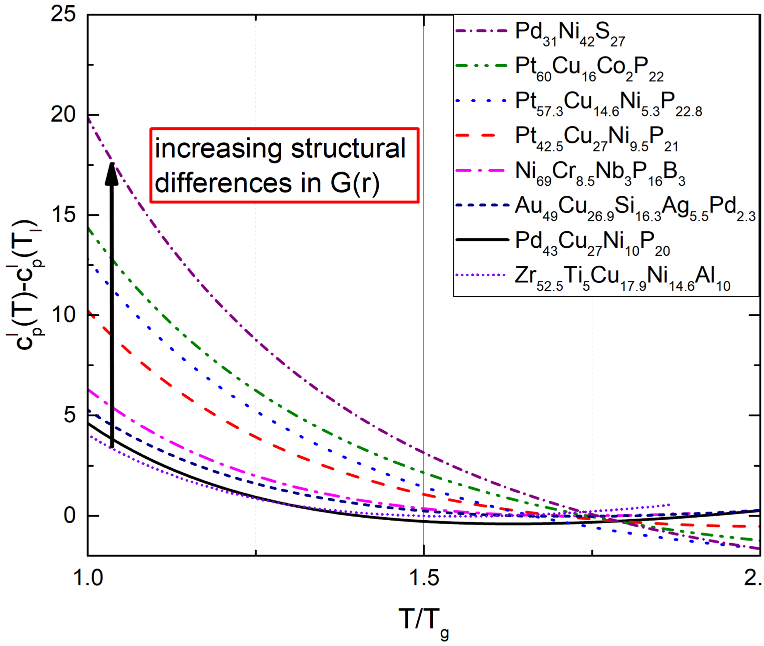

(a)

FIGURE 6.22: Difference of the molar heat capacity at glass transition temperature and the liquidus temperature ($c_p^l(T_g)$-$c_p^l(T_l)$) for different BMG forming alloys. A higher increase of $c_p(T)$ upon cooling is linked to higher structural differences in G(r).

TABLE 6.1: Thermo-physical properties of a variety of BMG forming systems. $c_p^l(T_g)$-$c_p^l(T_l)$ correspond to the excess molar heat capacity at the glass transition temperature T_g and the increase of c_p^l upon cooling with respect to the value at the liquidus temperature T_l, respectively. ΔH_f and ΔS_f are the enthalpy and entropy of fusion. $\Delta G^{l-x}(T_g)$ represents the driving force for crystallization, D^* the fragility parameter and γ^{x-l} the interfacial energy between the liquid and the crystalline phase.

Alloy Composition [*at*%]	$c_p^l(T_g)$-$c_p^l(T_l)$ [J g-$atom^{-1}$ K^{-1}]	ΔH_f [kJ g-$atom^{-1}$]	ΔS_f [kJ g-$atom^{-1}$ K^{-1}]	$\Delta G^{l-x}(T_g)$ [kJ g-$atom^{-1}$]	D^*	γ^{x-l} [J m^{-2}]	Ref.
$Zr_{52.5}Ti_5Cu_{17.9}Ni_{14.6}Al_{10}$	4.05	8.20	7.5	4.05	18.6	0.01[a]	[53, 233, 271]
$Pd_{43}Cu_{27}Ni_{10}P_{20}$	4.61	5.02	6.1	0.99	14.0	0.079 0.068	[45, 216, 268, 269, 283]
$Pd_{31}Ni_{42}S_{27}$	37.76	11.1	14.7	2.9	8.3	0.11	this work
$Pt_{42.5}Cu_{27}Ni_{9.5}P_{21}$	10.22	10.5	12.0	3.19	15.3	0.11	[39]
$Pt_{57.3}Cu_{14.6}Ni_{5.3}P_{22.8}$	12.79	11.4	13.7	3.55	13.6	0.86	[39, 270]
$Pt_{60}Cu_{16}Co_2P_{22}$	14.36	10.7	12.1	3.38	11.8	—	[39]
$Ni_{69}Cr_{8.5}Nb_3P_{16}B_3$	6.31	10.3	8.9	3.16	14.9	—	[39]
$Au_{49}Cu_{26.9}Si_{16.3}Ag_{5.5}Pd_{2.3}$	5.28	5.3	8.2	1.99	21.7 (8.9)	0.039	[329, 330]

[a] The value refers to that of the $Zr_{59}Ti_3Cu_{20}Ni_8Al_{10}$ bulk glass forming alloy.

Chapter 7

Summarizing Remarks

In the first part of this work, a new family of metallic glass forming alloys, comprising Cu-, Ni-, Pd-, Zr- and Ti-alloys, have been developed, containing sulfur as a key element. The alloys cover a wide range of S-contents, whereby the main focus of this work lies on alloys on the basis of Ti, Zr and Pd, having moderate to high contents of S. It is shown, that S is indispensable for the process of glass formation and inter alia Be-free Ti-based alloys with high Ti- contents of up to 75 at% in combination with an unprecedented critical casting thicknesses have been developed.

The second part deals with a characterization of the novel alloys regarding their thermophysical properties in order to reveal the role of sulfur for the process of glass formation. It has been shown that sulfur has not an universal role for glass formation in the different alloying systems. In case of the kinetically very fragile bulk glass forming alloy $Pd_{31}Ni_{42}S_{27}$ ($D^* = 8.3$), a high interfacial energy between the liquid and the crystalline phase of 0.107 Jm^{-2} is calculated, which is assumed to stabilize the liquid phase and enable glass formation, whereas in case of the kinetically strong Ti-based bulk glass forming alloys $Ti_{60}Zr_{15}Cu_{17}S_8$ ($D^* = 19.6$) the sluggish kinetics above and below the liquidus temperature are responsible for the frustration of the crystallization process. The S-additions cause a drastic drop of the surface tension of $Ti_{60}Zr_{15}Cu_{17}S_8$ in comparison to pure Ti and other Ti-alloys. The reduced surface tension is suggested to improve the molding accuracy and the achievable surface quality in casting processes.

Regarding their properties especially the Ti-based alloys are of great interest for industrial applications. It is possible to produce synchrotron X-ray amorphous 3 mm rods of $Ti_{40}Zr_{35}Cu_{17}S_8$ from industrial grade raw materials, drastically decreasing the material costs. These alloys posses excellent mechanical properties like an outstanding strength-to-density ratio, a high hardness in the as-cast state in combination with an unexpected ductility. The low content of late transition metals (Cu, Ni) together with the high amounts of Ti result in an excellent corrosion behavior in chloride solutions, which has so far not been achieved with any other Ti- or Zr-based bulk metallic glasses. Therefore, parts produced from this alloy are able to outperform crystalline Ti-alloys such as Ti6Al4V. Additionally, a new customized die-casting machine has been designed, which is able to produce parts from highly reactive alloys such as Ti- and Zr-based alloys with cycle times below one minute. This technique enables for the first time an economic processing of complex parts from bulk metallic glasses without any quality cutbacks.

Structural investigation using high energy synchrotron X-ray diffraction reveals that the total structure factor S(Q) and the reduced pair distribution function G(r) of $Pd_{31}Ni_{42}S_{27}$ are similar to Pt-P-based alloys, which also exhibit a high interfacial energy, a high entropy of fusion and a rapidly ascending molar heat capacity, being decisive for the process of glass formation. The novel Ti-based alloys show structural similarities to S-free Zr-based alloys, which are known to have a low interfacial energy and low entropies of fusion. Finally, a comprehensive study of G(r) of several bulk glass forming alloys suggests that the high values of the entropy of fusion and fast rise of the excess molar heat capacity in the different alloying systems is also reflected in the structural difference between the equilibrium liquid and the crystalline phase. Furthermore it is observed that the liquids structure changes towards the structure of the corresponding crystal and signatures of the crystalline structure can also be found in the structure of the glass.

Appendix A

Additional Figures

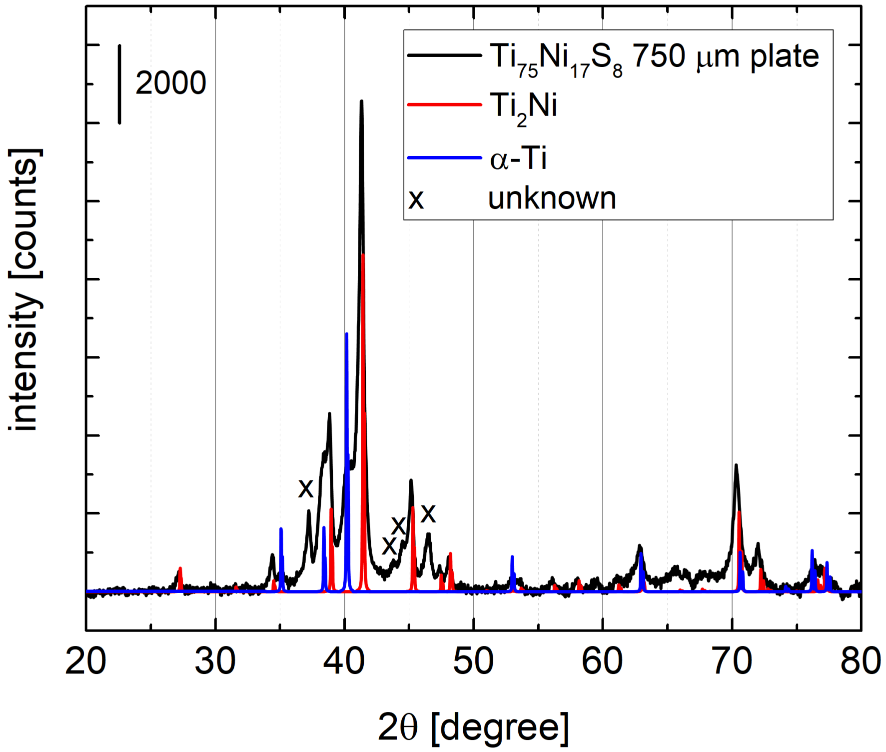

FIGURE A.1: Diffraction pattern of a 750 μm plate of $Ti_{75}Ni_{17}S_8$ together with the theoretical pattern of the fcc Ti_2Ni phase [332, 333] and hcp α-Ti [334], which have been simulated using Powder Cell [159]. Unidentified Bragg peaks are marked with a "x".

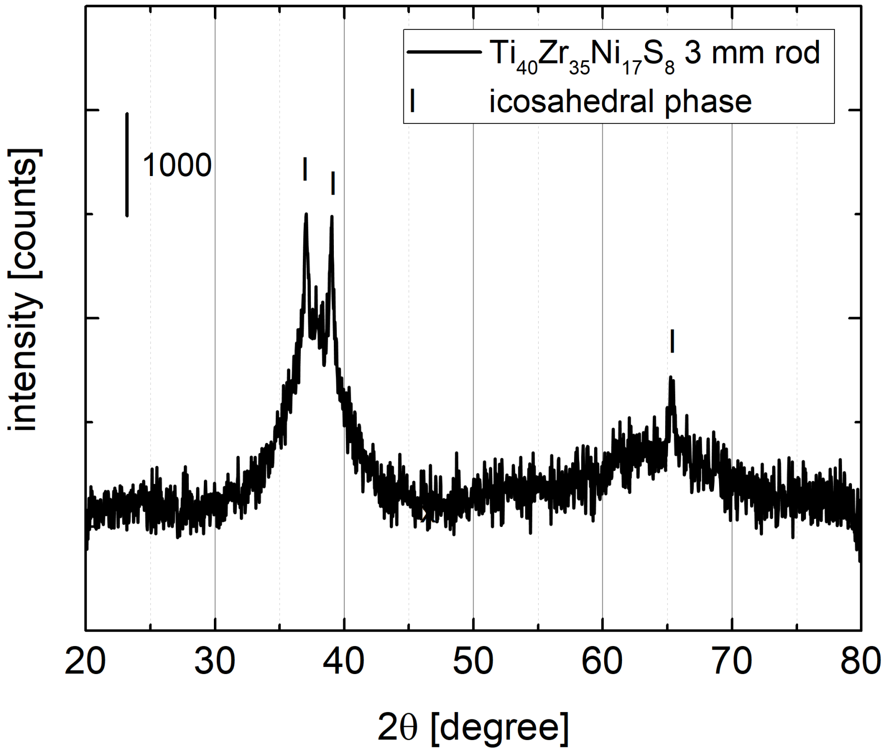

Figure A.2: Diffraction pattern of a 3 mm rod of $Ti_{40}Zr_{35}Ni_{17}S_8$. The Bragg peaks are allocated to an icosahedral phase and are marked with an "I".

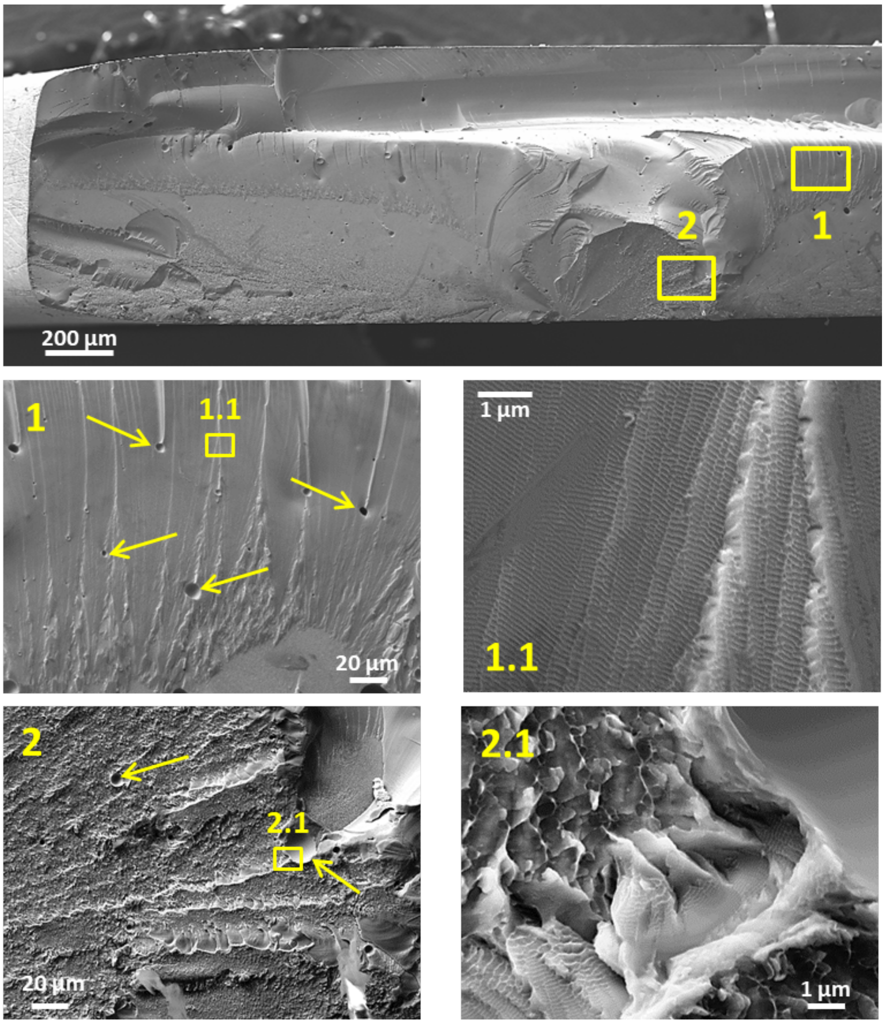

Figure A.3: SE images of the fracture surface of $pd_{31}Ni_{42}S_{27}$ revealing the brittle nature due to the observation of vein or rather dimple patterns on the nanometer scale. Figure and figure description taken from Ref. [8]. Some micrometer-sized pores are visible in the fracture surface and are highlighted with yellow arrows.

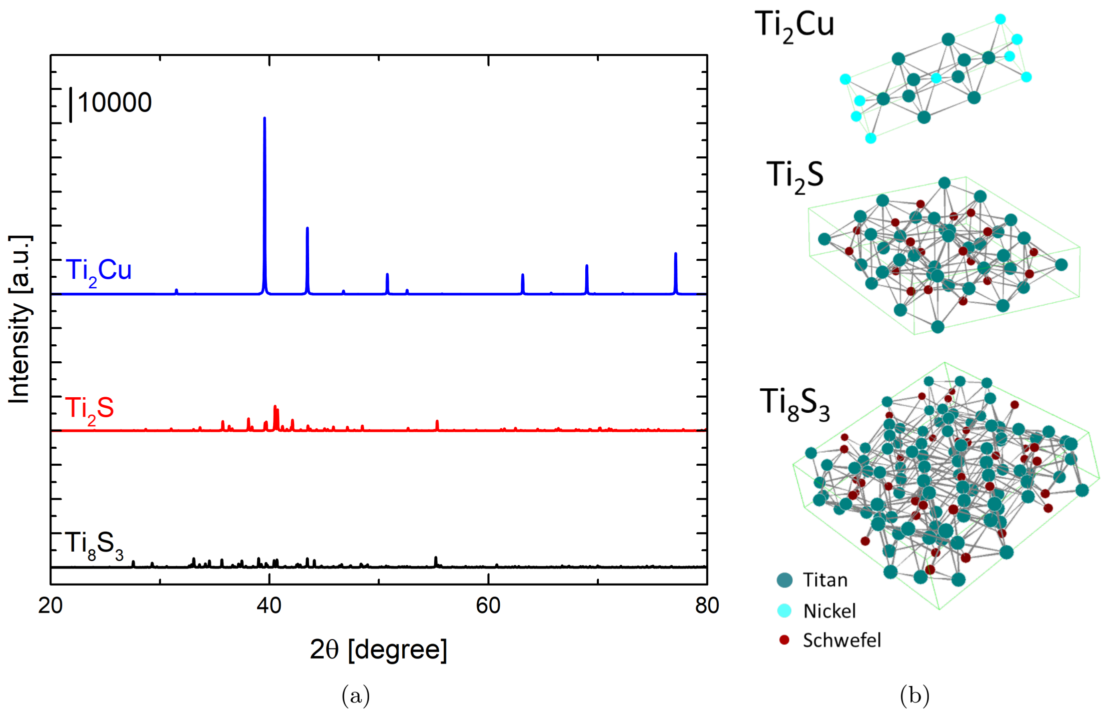

(a) (b)

FIGURE A.4: Simulated X-ray diffraction pattern and crystal structures of tetragonal Ti_2Cu, orthorhombic Ti_2S and monoclinic Ti_8S_3 using the Powder Cell software [159]. The information about the crystal structure are taken from Ref. [245, 317, 318].

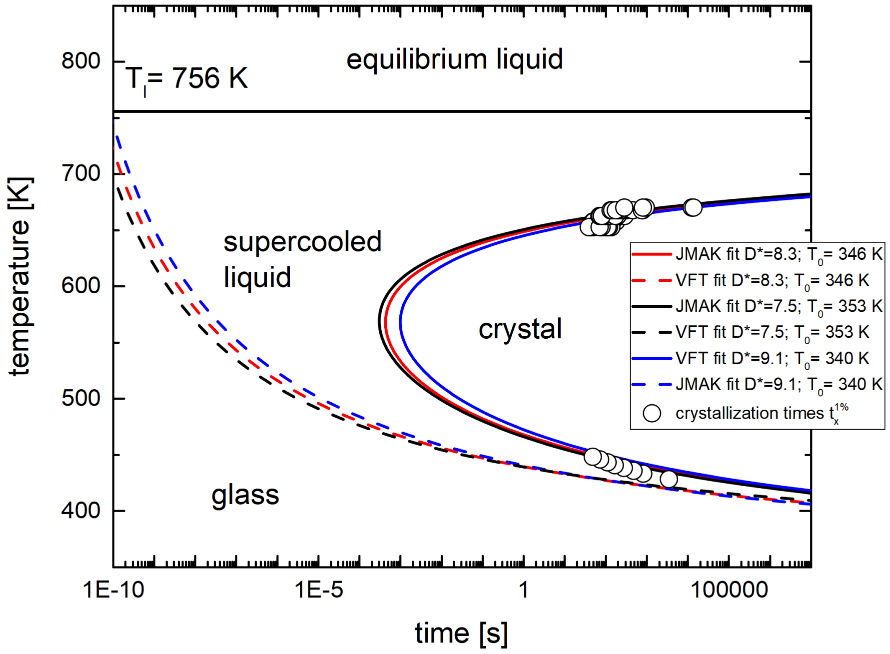

FIGURE A.5: Influence of the independent change of T_0 and D^* on the JMAK fit of the crystallization times $t_x^{\%}$ of $Pd_{31}Ni_{42}S_{27}$.

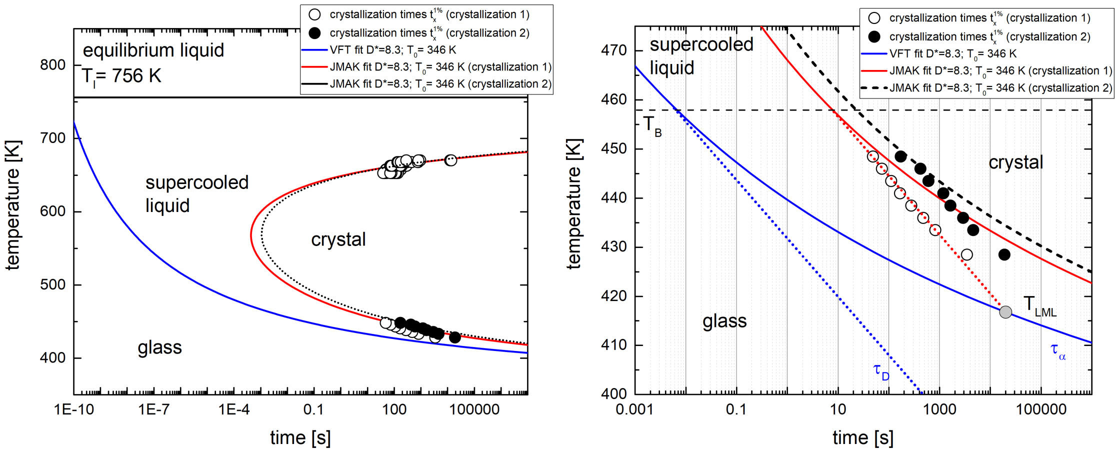

(a) (b)

Figure A.6: a) Comparison of the JMAK fit of the crystallization times $t_x^{1\%}$ of the 1^{st} and 2^{nd} crystallization event in the low temperature regime of $Pd_{31}Ni_{42}S_{27}$. b) Detailed illustration of the low temperature regime shown in a).

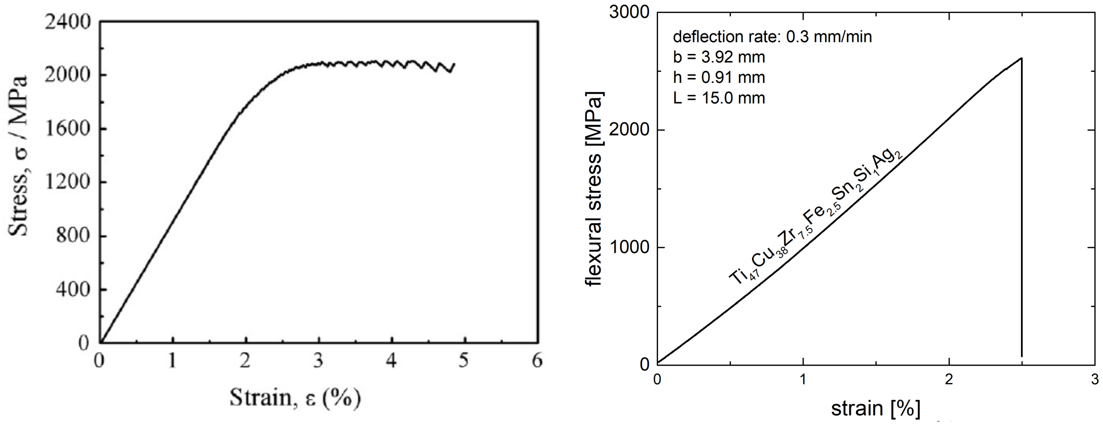

(a) (b)

Figure A.7: a) Compressive engineering stress strain curve of $Ti_{47}Cu_{38}Zr_{7.5}Fe_{2.5}Sn_2Si_1Ag_2$. Taken from Ref. [305]. b) Flexural engineering stress strain curve of $Ti_{47}Cu_{38}Zr_{7.5}Fe_{2.5}Sn_2Si_1Ag_2$ measured in this work.

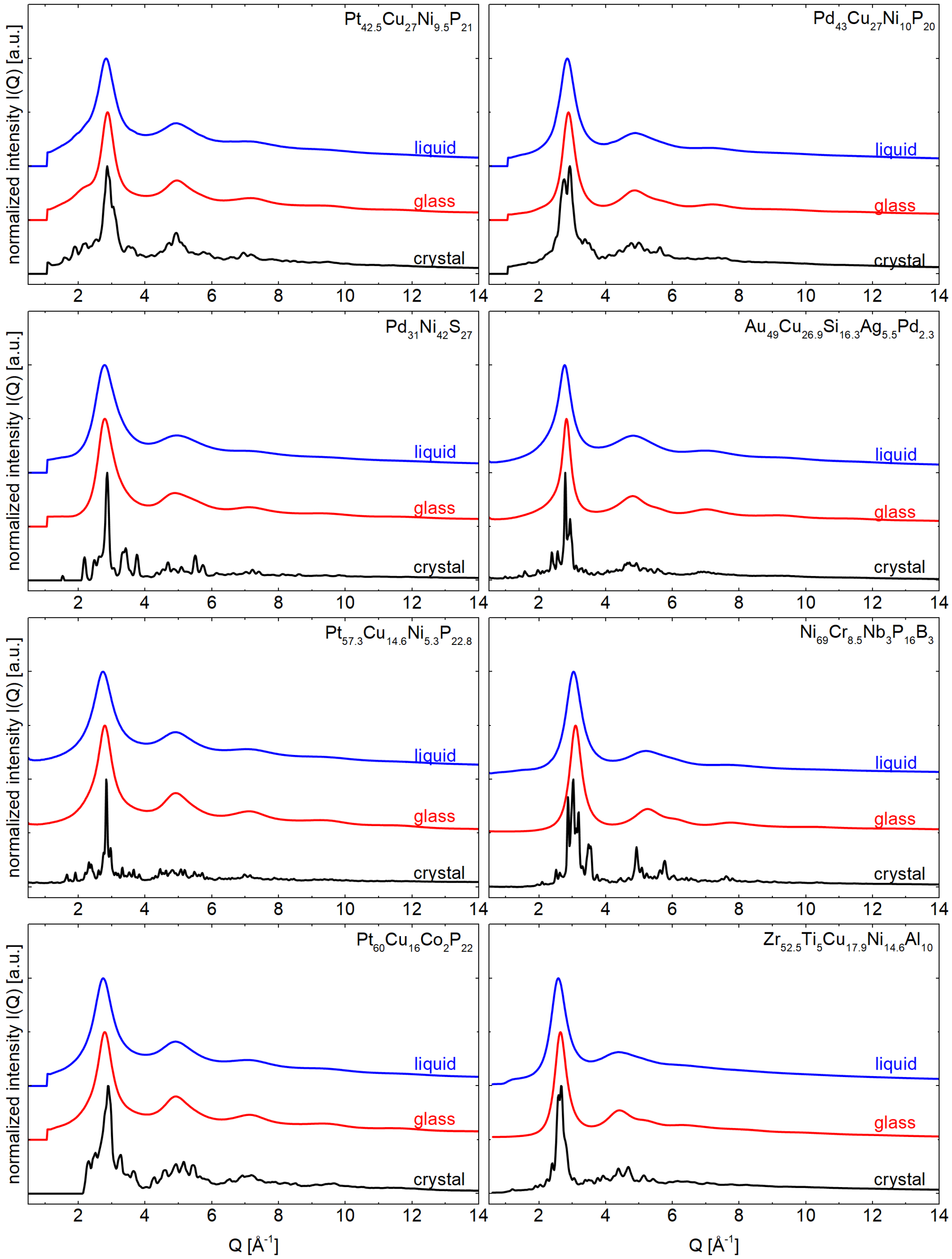

FIGURE A.8: Corrected raw intensities of the liquid, glassy and crystalline state used for the determination of the reduced distribution function shown in Fig. 6.21.

Appendix B

Copyright Permissions

Some figures of this work are reused from literature with perimssions of the respective publisher:

Table B.1

Figure	Reference	License
2.1	[10]	free of charge for a thesis
2.4b, 2.14b	[40]	RNP/19/JUL/017201
2.8	[67]	RNP/19/JUL/017199
2.10	[85]	4638820918806
2.11a	[74]	4638821446162
2.11b	[86]	free of charge for a thesis
2.12	[101]	free of charge for a thesis
2.13	[104]	4638830456822
2.14a	[50]	4638830636506
2.15	[3]	4638791391357
2.16a	[113]	4638830853402
2.16b	[114]	4638831307958
2.18b	[136]	4638840101750
2.19	[138]	4638840535466
3.6	[162]	RNP/19/JUL/017210
4.2a	[181]	4640750441607
4.2b	[176]	4638861029698
4.6a	[185]	4638870142911
4.6b	[186]	4639401374761
4.11	[199]	4638870505389
4.20	[209]	4638870683660
6.20a	[100]	RNP/19/JUL/017211
6.20b	[102]	4638871037343
A.7a	[305]	4638871212092

Bibliography

[1] W. Klement, R. H. Willens, and Pol Duwez. Non-crystalline Structure in Solidified Gold–Silicon Alloys. *Nature*, 187(4740):869–870, sep 1960. doi: 10.1038/187869b0.

[2] William L Johnson. Bulk metallic glasses — a new engineering material. *Current Opinion in Solid State and Materials Science*, 1(3):383–386, jun 1996. doi: 10.1016/S1359-0286(96)80029-5.

[3] Mark Telford. The case for bulk metallic glass. *Materials Today*, 7(3):36–43, 2004. doi: http://dx.doi.org/10.1016/S1369-7021(04)00124-5.

[4] M. F. Ashby and A. L. Greer. Metallic glasses as structural materials. *Scripta Materialia*, 54(3):321–326, 2006. doi: 10.1016/j.scriptamat.2005.09.051.

[5] A L Greer and E. Ma. Bulk Metallic Glasses: At the Cutting Edge of Metals Research. *MRS Bulletin*, 32(8):611–619, aug 2007. doi: 10.1557/mrs2007.121.

[6] Jan Schroers and Neil Paton. Amorphous metal alloys form like plastics. *Advanced Materials and Processes*, 164(1):61–63, 2006. doi: 10.1002/adma.200902776.

[7] Alexander Kuball, Oliver Gross, Benedikt Bochtler, and Ralf Busch. Sulfur-bearing metallic glasses: A new family of bulk glass-forming alloys. *Scripta Materialia*, 146:73–76, mar 2018. doi: 10.1016/j.scriptamat.2017.11.011.

[8] Alexander Kuball, Benedikt Bochtler, Oliver Gross, Victor Pacheco, Moritz Stolpe, Simon Hechler, and Ralf Busch. On the Bulk Glass Formation in the Ternary Pd-Ni-S System. *Acta Materialia*, 158:13–22, 2018. doi: 10.1016/J.ACTAMAT.2018.07.039.

[9] Alexander Kuball, Oliver Gross, Benedikt Bochtler, Bastian Adam, Lucas Ruschel, Mohammad Zamanzade, and Ralf Busch. Development and characterization of titanium-based bulk metallic glasses. *Journal of Alloys and Compounds*, 790:337–346, 2019. doi: 10.1016/j.jallcom.2019.03.001.

[10] Yanglin Li, Shaofan Zhao, Yanhui Liu, Pan Gong, and Jan Schroers. How Many Bulk Metallic Glasses Are There? *ACS Combinatorial Science*, 19(11):687–693, nov 2017. doi: 10.1021/acscombsci.7b00048.

[11] Rodrigo Miguel Ojeda Mota, T. E. Graedel, Evgenia Pekarskaya, and Jan Schroers. Criticality in Bulk Metallic Glass Constituent Elements. *Jom*, 69(11):2156–2163, 2017. doi: 10.1007/s11837-017-2415-6.

[12] H. S. Chen. Thermodynamic considerations on the formation and stability of metallic glasses. *Acta Metallurgica*, 22(12):1505–1511, 1974. doi: 10.1016/0001-6160(74)90112-6.

[13] X. H. Lin and W. L. Johnson. Formation of Ti-Zr-Cu-Ni bulk metallic glasses. *Journal of Applied Physics*, 78(11):6514–6519, 1995. doi: 10.1063/1.360537.

[14] A Peker and W L Johnson. A Highly Processable Metallic-Glass - Zr41.2Ti13.8Cu12.5Ni10.0Be22.5. *Applied Physics Letters*, 63(17):2342–2344, 1993. doi: Doi10.1063/1.110520.

[15] Nobuyuki Nishiyama, Kana Takenaka, Haruko Miura, Noriko Saidoh, Yuqiao Zeng, and Akihisa Inoue. The world's biggest glassy alloy ever made. *Intermetallics*, 30:19–24, 2012. doi: 10.1016/j.intermet.2012.03.020.

[16] Jong Hyun Na, Michael Floyd, Glenn Garrett, Marios D. Demetriou, and William L. Johnson. Bulk glass steel with high glass forming ability, 2015.

[17] J. H. Na, M. D. Demetriou, M. Floyd, A. Hoff, G. R. Garrett, and W. L. Johnson. Compositional landscape for glass formation in metal alloys. *Proceedings of the National Academy of Sciences*, 111(25):9031–9036, jun 2014. doi: 10.1073/pnas.1407780111.

[18] S. L. Zhu, X. M. Wang, and A. Inoue. Glass-forming ability and mechanical properties of Ti-based bulk glassy alloys with large diameters of up to 1 cm. *Intermetallics*, 16(8):1031–1035, 2008. doi: 10.1016/j.intermet.2008.05.006.

[19] Shiyan Ding, Yanhui Liu, Yanglin Li, Ze Liu, Sungwoo Sohn, Fred J. Walker, and Jan Schroers. Combinatorial development of bulk metallic glasses. *Nature Materials*, 13(5):494–500, 2014. doi: 10.1038/nmat3939.

[20] R. B. Schwarz, P. Nash, and D. Turnbull. The use of thermodynamic models in the prediction of the glass-forming range of binary alloys. *Journal of Materials Research*, 2(4):456–460, aug 1987. doi: 10.1557/JMR.1987.0456.

[21] R Bormann, F. Gärtner, and F Haider. Determination of the free energy of equilibrium and metastable phases in the Cu-Zr system. *Materials Science and Engineering*, 97:79–81, jan 1988. doi: 10.1016/0025-5416(88)90015-8.

[22] A. L. Greer. Metallic Glasses. In *Physical Metallurgy: Fifth Edition*, volume 1, pages 305–385. jan 2014. ISBN 9780444537713. doi: 10.1016/B978-0-444-53770-6.00004-6.

[23] A. Lindsay Greer. Confusion by design. *Nature*, 366(6453):303–304, dec 1993. doi: 10.1038/366303a0.

[24] David Turnbull. Under what conditions can a glass be formed? *Contemporary Physics*, 10(5):473–488, 1969. doi: 10.1080/00107516908204405.

[25] Z.P. Lu, H Tan, S.C. Ng, and Y Li. The correlation between reduced glass transition temperature and glass forming ability of bulk metallic glasses. *Scripta Materialia*, 42(7):667–673, mar 2000. doi: 10.1016/S1359-6462(99)00417-0.

[26] Akihisa Inoue. Stabilization of Metallic Supercooled Liquid. *Acta Mater.*, 48: 279–306, 2000. doi: 10.1016/S1359-6454(99)00300-6.

[27] K. Kelton and A. L. Greer. *Nucleation in Condensed Matter: Applications in Materials and Biology.* Elsevier, 2010. ISBN 9780080912646.

[28] H.S. Chen and D. Turnbull. The specific heat of tin and gallium in their stable and undercooled pure liquid states. *Acta Metallurgica*, 16(3):369–373, mar 1968. doi: 10.1016/0001-6160(68)90023-0.

[29] R. Busch, Y. J. Kim, and W. L. Johnson. Thermodynamics and kinetics of the undercooled liquid and the glass transition of the Zr41.2Ti13.8Cu12.5Ni10.0Be22.5alloy. *Journal of Applied Physics*, 77(8): 4039–4043, 1995. doi: 10.1063/1.359485.

[30] C. Austen Angell. Formation of glasses from liquids and biopolymers. *Science (New York, N.Y.)*, 267(5206):1924–1935, 1995. doi: 10.1126/science.267.5206.1924.

[31] D. Turnbull. Formation of crystal nuclei in liquid metals. *Journal of Applied Physics*, 21(10):1022–1028, 1950. doi: 10.1063/1.1699435.

[32] Alexander Bartsch, Klaus Rätzke, Andreas Meyer, and Franz Faupel. Dynamic Arrest in Multicomponent Glass-Forming Alloys. *Physical Review Letters*, 104 (19):195901, may 2010. doi: 10.1103/PhysRevLett.104.195901.

[33] U Geyer, W L Johnson, S Schneider, Y Qiu, T A Tombrello, and M P Macht. Small atom diffusion and breakdown of the Stokes–Einstein relation in the supercooled liquid state of the Zr46.7Ti8.3Cu7.5Ni10Be27.5 alloy. 2492(1996):25–28, 1996. doi: 10.1063/1.117716.

[34] M D Ediger, Peter Harrowell, and Lian Yu. Crystal growth kinetics exhibit a fragility-dependent decoupling from viscosity. *Journal of Chemical Physics*, 128 (3):034709, jan 2008. doi: 10.1063/1.2815325.

[35] Gilles Tarjus, Daniel Kivelson, Gilles Tarjus, and Daniel Kivelson. Breakdown of the Stokes-Einstein relation in supercooled liquids. 3071(1995), 2015. doi: 10.1063/1.470495.

[36] Li-min Wang, V Velikov, and C A Angell. Direct determination of kinetic fragility indices of glassforming liquids by differential scanning calorimetry: Kinetic versus thermodynamic fragilities. *The Journal of Chemical Physics*, 117(22):10184–10192, dec 2002. doi: 10.1063/1.1517607.

[37] Henry Eyring. Viscosity, plasticity, and diffusion as examples of absolute reaction rates. *The Journal of Chemical Physics*, 4(4):283–291, 1936. doi: 10.1063/1.1749836.

[38] L.-M. Martinez and C. A. Angell. A thermodynamic connection to the fragility of glass-forming liquids. *Nature*, 410(6829):663–667, apr 2001. doi: 10.1038/35070517.

[39] Oliver Gross, Benedikt Bochtler, Moritz Stolpe, Simon Hechler, William Hembree, Ralf Busch, and Isabella Gallino. The kinetic fragility of Pt-P- and Ni-P-based bulk glass-forming liquids and its thermodynamic and structural signature. *Acta Materialia*, 132:118–127, 2017. doi: 10.1016/j.actamat.2017.04.030.

[40] Moritz Stolpe, Isabell Jonas, Shuai Wei, Zach Evenson, William Hembree, Fan Yang, Andreas Meyer, and Ralf Busch. Structural changes during a liquid-liquid transition in the deeply undercooled Zr58.5Cu15.6Ni12.8Al10.3Nb2.8 bulk metallic glass forming melt. *Physical Review B - Condensed Matter and Materials Physics*, 93(1):1–7, 2016. doi: 10.1103/PhysRevB.93.014201.

[41] Shuai Wei, Zach Evenson, Isabella Gallino, and Ralf Busch. The impact of fragility on the calorimetric glass transition in bulk metallic glasses. *Intermetallics*, 55:138–144, dec 2014. doi: 10.1016/j.intermet.2014.07.018.

[42] C A Angell and S Borick. Specific heats Cp , C , Cconf and energy landscapes of glassforming liquids. 310:393–406, 2002. doi: https://doi.org/10.1016/S0022-3093(02)01500-4.

[43] R. Busch, J. Schroers, and W. H. Wang. Thermodynamics and Kinetics of Bulk Metallic Glass. *MRS Bulletin*, 32(8):620–623, aug 2007. doi: 10.1557/mrs2007.122.

[44] Gerold Adam and Julian H. Gibbs. On the Temperature Dependence of Cooperative Relaxation Properties in Glass-Forming Liquids. *The Journal of Chemical Physics*, 43(1):139–146, jul 1965. doi: 10.1063/1.1696442.

[45] Isabella Gallino, Jan Schroers, and Ralf Busch. Kinetic and thermodynamic studies of the fragility of bulk metallic glass forming liquids. *Journal of Applied Physics*, 108(6):063501, sep 2010. doi: 10.1063/1.3480805.

[46] Hajime Tanaka. Relationship among glass-forming ability, fragility, and short-range bond ordering of liquids. *Journal of Non-Crystalline Solids*, 351(8-9):678–690, 2005. doi: 10.1016/j.jnoncrysol.2005.01.070.

[47] Li-min Min Wang, C. Austen Angell, and Ranko Richert. Fragility and thermodynamics in nonpolymeric glass-forming liquids. *Journal of Chemical Physics*, 125 (7):1–8, 2006. doi: 10.1063/1.2244551.

[48] Jun Ding, Yong-Qiang Cheng, Hongwei Sheng, and Evan Ma. Short-range structural signature of excess specific heat and fragility of metallic-glass-forming supercooled liquids. *Physical Review B*, 85(6):060201, feb 2012. doi: 10.1103/PhysRevB.85.060201.

[49] Christopher Way, Prashant Wadhwa, and Ralf Busch. The influence of shear rate and temperature on the viscosity and fragility of the Zr41.2Ti13.8Cu12.5Ni10.0Be22.5 metallic-glass-forming liquid. *Acta Materialia*, 55(9):2977–2983, may 2007. doi: 10.1016/j.actamat.2006.12.032.

[50] Shuai Wei, Fan Yang, Jozef Bednarcik, Ivan Kaban, Olga Shuleshova, Andreas Meyer, and Ralf Busch. Liquid–liquid transition in a strong bulk metallic glass-forming liquid. *Nature Communications*, 4(1):2083, oct 2013. doi: 10.1038/ncomms3083.

[51] Shuai Wei, Moritz Stolpe, Oliver Gross, William Hembree, Simon Hechler, Jozef Bednarcik, Ralf Busch, and Pierre Lucas. Structural evolution on medium-range-order during the fragile-strong transition in Ge 15 Te 85. *Acta Materialia*, 129: 259–267, 2017. doi: 10.1016/j.actamat.2017.02.055.

[52] S. Lan, Y. Ren, X. Y. Wei, B. Wang, E. P. Gilbert, T. Shibayama, S. Watanabe, M. Ohnuma, and X. L. Wang. Hidden amorphous phase and reentrant supercooled liquid in Pd-Ni-P metallic glasses. *Nature Communications*, 8:1–8, 2017. doi: 10.1038/ncomms14679.

[53] Zach Evenson, Tobias Schmitt, Mathias Nicola, Isabella Gallino, and Ralf Busch. High temperature melt viscosity and fragile to strong transition in Zr – Cu – Ni – Al – Nb (Ti) and Cu 47 Ti 34 Zr 11 Ni 8 bulk metallic glasses. *Acta Materialia*, 60(12):4712–4719, 2012. doi: 10.1016/j.actamat.2012.05.019.

[54] Benedikt Bochtler, Oliver Gross, Isabella Gallino, and Ralf Busch. Thermophysical characterization of the Fe67Mo6Ni3.5Cr3.5P12C5.5B2.5 bulk metallic glass forming alloy. *Acta Materialia*, 118:129–139, 2016. doi: 10.1016/j.actamat.2016.07.031.

[55] Benedikt Bochtler, Oliver Gross, and Ralf Busch. Indications for a fragile-to-strong transition in the high- and low-temperature viscosity of the Fe 43 Cr 16 Mo 16 C 15 B 10 bulk metallic glass-forming alloy. *Applied Physics Letters*, 111(26):261902, 2017. doi: 10.1063/1.5013108.

[56] S. Hechler, B. Ruta, M. Stolpe, E. Pineda, Z. Evenson, O. Gross, A. Bernasconi, R. Busch, and I. Gallino. Microscopic evidence of the connection between liquid-liquid transition and dynamical crossover in an ultraviscous metallic glass former. *Physical Review Materials*, 2(8):085603, 2018. doi: 10.1103/PhysRevMaterials.2.085603.

[57] Wei Xu, Magdalena T. Sandor, Yao Yu, Hai Bo Ke, Hua Ping Zhang, Mao Zhi Li, Wei Hua Wang, Lin Liu, and Yue Wu. Evidence of liquid-liquid transition in glass-forming La50Al35Ni15melt above liquidus temperature. *Nature Communications*, 6:1–9, 2015. doi: 10.1038/ncomms8696.

[58] Hajime Tanaka, Rei Kurita, and Hiroshi Mataki. Liquid-Liquid Transition in the Molecular Liquid Triphenyl Phosphite. *Physical Review Letters*, 92(2):4, 2004. doi: 10.1103/PhysRevLett.92.025701.

[59] S. Aasland and P.F. McMillan. Density-driven liquid-liquid phase separation in the system Al2O3-Y2O3. *Nature*, 368:561 – 563, 1994. doi: 10.1038/368561a0.

[60] G. N. Greaves, M. C. Wilding, S. Fearn, D. Langstaff, F. Kargl, S. Cox, Q. Vu Van, O. Majérus, C. J. Benmore, R. Weber, C. M. Martin, and L. Hennet. Detection of first-order liquid/liquid phase transitions in yttrium oxide-aluminum oxide melts. *Science*, 322(5901):566–570, 2008. doi: 10.1126/science.1160766.

[61] Vishwas V. Vasisht, Shibu Saw, and Srikanth Sastry. Liquid-liquid critical point in supercooled silicon. *Nature Physics*, 7(7):549–553, 2011. doi: 10.1038/nphys1993.

[62] W L Johnson, J H Na, and M D Demetriou. Quantifying the origin of metallic glass formation. *Nature Communications*, 7:10313, jan 2016. doi: 10.1038/ncomms10313.

[63] Oliver Gross, Sascha S. Riegler, Moritz Stolpe, Benedikt Bochtler, Alexander Kuball, Simon Hechler, Ralf Busch, and Isabella Gallino. On the high glass-forming ability of Pt-Cu-Ni/Co-P-based liquids. *Acta Materialia*, 141:109–119, 2017. doi: 10.1016/j.actamat.2017.09.013.

[64] Jan Schroers and William L. Johnson. Highly processable bulk metallic glass-forming alloys in the Pt-Co-Ni-Cu-P system. *Applied Physics Letters*, 84(18): 3666–3668, 2004. doi: 10.1063/1.1738945.

[65] Walter. Kauzmann. The Nature of the Glassy State and the Behavior of Liquids at Low Temperatures. *Chemical Reviews*, 43(2):219–256, oct 1948. doi: 10.1021/cr60135a002.

[66] Gregg Jaeger. The ehrenfest classification of phase transitions: Introduction and evolution. *Archive for History of Exact Sciences*, 53(1):51–81, 1998. doi: 10.1007/s004070050021.

[67] Hajime Tanaka. Possible resolution of the Kauzmann paradox in supercooled liquids. (July):1–8, 2003. doi: 10.1103/PhysRevE.68.011505.

[68] Julian H. Gibbs and Edmund A. DiMarzio. Nature of the Glass Transition and the Glassy State. *The Journal of Chemical Physics*, 28(3):373–383, mar 1958. doi: 10.1063/1.1744141.

[69] G. P. Johari. An equilibrium supercooled liquid's entropy and enthalpy in the Kauzmann and the third law extrapolations, and a proposed experimental resolution. *The Journal of Chemical Physics*, 113(2):751–761, jul 2000. doi: 10.1063/1.481850.

[70] R Busch, A Masuhr, and W L Johnson. Themodynamics and kinetics of Zr-Ti-Cu-Ni-Be bulk metallic glass forming liquids. *Materials Science and Engineering A*, 304-306(1-2):97–102, 2001. doi: 10.1016/S0921-5093(00)01458-1.

[71] R. Busch, W. Liu, and W. L. Johnson. Thermodynamics and kinetics of the Mg 65 Cu 25 Y 10 bulk metallic glass forming liquid. *Journal of Applied Physics*, 83 (8):4134, 1998. doi: 10.1063/1.367167.

[72] Isabella Gallino, Minalben B. Shah, and Ralf Busch. Enthalpy relaxation and its relation to the thermodynamics and crystallization of the Zr58.5Cu15.6Ni12.8Al10.3Nb2.8bulk metallic glass-forming alloy. *Acta Materialia*, 55(4):1367–1376, 2007. doi: 10.1016/j.actamat.2006.09.040.

[73] CORNELIUS T. MOYNIHAN, ALLAN J. EASTEAL, MARY ANN De BOLT, and JOSEPH TUCKER. Dependence of the Fictive Temperature of Glass on

Cooling Rate. *Journal of the American Ceramic Society*, 59(1-2):12–16, 1976. doi: 10.1111/j.1151-2916.1976.tb09376.x.

[74] H W Sheng, W K Luo, F M Alamgir, J M Bai, and E Ma. Atomic packing and short-to-medium-range order in metallic glasses. *Nature*, 439(7075):419–425, jan 2006. doi: 10.1038/nature04421.

[75] J.A. Prins and H. Petersen. Theoretical diffraction patterns corresponding to some simple types of molecular arrangement in liquids. *Physica*, 3(1-4):147–153, jan 1936. doi: 10.1016/S0031-8914(36)80218-3.

[76] J. D. Bernal. An attempt at a molecular theory of liquid structure. *Transactions of the Faraday Society*, 33:27, 1937. doi: 10.1039/tf9373300027.

[77] J.D. Bernal. A Geometrical Approach to the Structure Of Liquids. *Nature*, 183 (4655):141–147, jan 1959. doi: 10.1038/183141a0.

[78] J. D. Bernal and J. Mason. Packing of Spheres: Co-ordination of Randomly Packed Spheres. *Nature*, 188(4754):910–911, dec 1960. doi: 10.1038/188910a0.

[79] J.D. Bernal. Geometry of the Structure of Monatomic Liquids. *Nature*, 185(4706): 68–70, jan 1960. doi: 10.1038/185068a0.

[80] C.F. Frank and N. F. Mott. Supercooling of liquids. *Proceedings of the Rocal Society A*, 215(1120):43–46, 1952. doi: https://doi.org/10.1098/rspa.1952.0194.

[81] P. H. GASKELL. A new structural model for transition metal–metalloid glasses. *Nature*, 276(5687):484–485, nov 1978. doi: 10.1038/276484a0.

[82] P H Gaskell. On the structure of simple inorganic amorphous solids. *Journal of Physics C: Solid State Physics*, 12(21):4337–4368, nov 1979. doi: 10.1088/0022-3719/12/21/004.

[83] G S Cargill. Structure of Metallic Alloy Glasses. *Solid State Physics*, 30:227–320, 1975. doi: https://doi.org/10.1016/S0081-1947(08)60337-9.

[84] J. L. Finney. Modelling the structures of amorphous metals and alloys. *Nature*, 266(5600):309–314, mar 1977. doi: 10.1038/266309a0.

[85] A. Hirata, L. J. Kang, T. Fujita, B. Klumov, K. Matsue, M. Kotani, A. R. Yavari, and M. W. Chen. Geometric Frustration of Icosahedron in Metallic Glasses. *Science*, 341(6144):376–379, jul 2013. doi: 10.1126/science.1232450.

[86] D B Miracle, D V Louzguine-Luzgin, L V Louzguina-Luzgina, and a Inoue. An assessment of binary metallic glasses: correlations between structure, glass forming

ability and stability. *International Materials Reviews*, 55(4):218–256, 2010. doi: 10.1179/095066010X12646898728200.

[87] Journal O F Non-crystalline Solids and Takeshi Egami. Atomic size effect on the formability of metallic glasses. (APRIL), 1984. doi: 10.1016/0022-3093(84) 90210-2.

[88] T Egami. Universal criterion for metallic glass formation. *Materials Science and Engineering: A*, 226-228:261–267, jun 1997. doi: 10.1016/S0921-5093(97)80041-X.

[89] Daniel B Miracle. A structural model for metallic glasses. *Nature Materials*, 3 (10):697–702, oct 2004. doi: 10.1038/nmat1219.

[90] D. B. Miracle. The efficient cluster packing model - An atomic structural model for metallic glasses. *Acta Materialia*, 54(16):4317–4336, 2006. doi: 10.1016/j.actamat.2006.06.002.

[91] D. B. Miracle and O. N. Senkov. A geometric model for atomic configurations in amorphous Al alloys. *Journal of Non-Crystalline Solids*, 319(1-2):174–191, 2003. doi: 10.1016/S0022-3093(02)01917-8.

[92] K. J. Laws, D. B. Miracle, and M. Ferry. A predictive structural model for bulk metallic glasses. *Nature Communications*, 6:1–10, 2015. doi: 10.1038/ncomms9123.

[93] Subir Sachdev and David R. Nelson. Theory of the structure factor of metallic glasses. *Physical Review Letters*, 53(20):1947–1950, 1984. doi: 10.1103/PhysRevLett.53.1947.

[94] Li Wang, Yu Qing Wang, Chuanxiao Peng, and Yanning Zhang. Medium-range structural order in liquid Ni20Al80 alloy: Experimental and molecular dynamics studies. *Physics Letters, Section A: General, Atomic and Solid State Physics*, 350 (5-6):405–409, 2006. doi: 10.1016/j.physleta.2005.10.041.

[95] Y. Q. Cheng and E. Ma. Atomic-level structure and structure-property relationship in metallic glasses. *Progress in Materials Science*, 56(4):379–473, 2011. doi: 10.1016/j.pmatsci.2010.12.002.

[96] V. P. Voloshin and Yu I. Naberukhin. On the origin of the splitting of the second maximum in the radial distribution function of amorphous solids. *Journal of Structural Chemistry*, 38(1):62–70, 1997. doi: 10.1007/BF02768808.

[97] C. H. Bennett. Serially deposited amorphous aggregates of hard spheres. *Journal of Applied Physics*, 43(6):2727–2734, 1972. doi: 10.1063/1.1661585.

[98] X. J. Liu, Y. Xu, X. Hui, Z. P. Lu, F. Li, G. L. Chen, J. Lu, and C. T. Liu. Metallic liquids and glasses: Atomic order and global packing. *Physical Review Letters*, 105(15):1–4, 2010. doi: 10.1103/PhysRevLett.105.155501.

[99] X. J. Liu, Y. Xu, Z. P. Lu, X. Hui, G. L. Chen, G. P. Zheng, and C. T. Liu. Atomic packing symmetry in the metallic liquid and glass states. *Acta Materialia*, 59(16): 6480–6488, 2011. doi: 10.1016/j.actamat.2011.07.012.

[100] S. P. Pan, J. Y. Qin, W. M. Wang, and T. K. Gu. Origin of splitting of the second peak in the pair-distribution function for metallic glasses. *Physical Review B*, 84 (9):092201, sep 2011. doi: 10.1103/PhysRevB.84.092201.

[101] Jun Ding, Evan Ma, Mark Asta, and Robert O. Ritchie. Second-nearest-neighbor correlations from connection of atomic packing motifs in metallic glasses and liquids. *Scientific Reports*, 5(July):1–9, 2015. doi: 10.1038/srep17429.

[102] Z. W. Wu, M. Z. Li, W. H. Wang, and K. X. Liu. Hidden topological order and its correlation with glass-forming ability in metallic glasses. *Nature Communications*, 6:1–7, 2015. doi: 10.1038/ncomms7035.

[103] Alain Reza Yavari, Alain Le Moulec, Akihisa Inoue, Nobuyuki Nishiyama, Nicoleta Lupu, Eiichiro Matsubara, Walter José Botta, Gavin Vaughan, Marco Di Michiel, and Åke Kvick. Excess free volume in metallic glasses measured by X-ray diffraction. *Acta Materialia*, 53(6):1611–1619, 2005. doi: 10.1016/j.actamat.2004.12.011.

[104] Shuai Wei, Moritz Stolpe, Oliver Gross, Zach Evenson, Isabella Gallino, William Hembree, Jozef Bednarcik, Jamie J Kruzic, and Ralf Busch. Linking structure to fragility in bulk metallic glass-forming liquids. *Applied Physics Letters*, 106(18): 181901, may 2015. doi: 10.1063/1.4919590.

[105] N. A. Mauro, M. Blodgett, M. L. Johnson, A. J. Vogt, and K. F. Kelton. A structural signature of liquid fragility. *Nature Communications*, 5:1–7, 2014. doi: 10.1038/ncomms5616.

[106] Sergey V. Sukhomlinov and Martin H. Müser. Anomalous system-size dependence of properties at the fragile-to-strong transition in a bulk-metallic-glass forming melt. *Computational Materials Science*, 156(August 2018):129–134, 2019. doi: 10.1016/j.commatsci.2018.09.047.

[107] A. L. Greer, Y. Q. Cheng, and E. Ma. Shear bands in metallic glasses. *Materials Science and Engineering R: Reports*, 74(4):71–132, 2013. doi: 10.1016/j.mser.2013.04.001.

[108] W. L. Johnson and K. Samwer. A Universal Criterion for Plastic Yielding of Metallic Glasses with a (T/Tg)ˆ2/3 Temperature Dependence. *Physical Review Letters*, 95(19):195501, nov 2005. doi: 10.1103/PhysRevLett.95.195501.

[109] David Turnbull and Morrel H. Cohen. Free-volume model of the amorphous phase: Glass transition. *The Journal of Chemical Physics*, 34(1):120–125, 1961. doi: 10.1063/1.1731549.

[110] A.S. Argon and H.Y. Kuo. Plastic flow in a disordered bubble raft (an analog of a metallic glass). *Materials Science and Engineering*, 39(1):101–109, jul 1979. doi: 10.1016/0025-5416(79)90174-5.

[111] A.S Argon. Plastic deformation in metallic glasses. *Acta Metallurgica*, 27(1):47–58, jan 1979. doi: 10.1016/0001-6160(79)90055-5.

[112] Frans Spaepen. A microscopic mechanism for steady state inhomogeneous flow in metallic glasses. *Acta Metallurgica*, 25(4):407–415, apr 1977. doi: 10.1016/0001-6160(77)90232-2.

[113] Christopher A. Schuh, Todd C. Hufnagel, and Upadrasta Ramamurty. Mechanical behavior of amorphous alloys. *Acta Materialia*, 55(12):4067–4109, 2007. doi: 10.1016/j.actamat.2007.01.052.

[114] H J Leamy, H S Chen, and T T Wang. Plastic flow and fracture of glass. *Proceedings of the Royal Society of London. Series A. Mathematical and Physical Sciences*, 282(1388):33–43, 1964. doi: 10.1098/rspa.1964.0210.

[115] J. J. Lewandowski and A. L. Greer. Temperature rise at shear bands in metallic glasses. *Nature Materials*, 5(1):15–18, 2006. doi: 10.1038/nmat1536.

[116] By Jamie J Kruzic. Bulk Metallic Glasses as Structural Materials : A Review. *Advanced Engineering Materials*, pages 1–24, 2016. doi: 10.1002/adem.201600066.

[117] Golden Kumar, Pascal Neibecker, Yan Hui Liu, and Jan Schroers. Critical fictive temperature for plasticity in metallic glasses. *Nature Communications*, 4, 2013. doi: 10.1038/ncomms2546.

[118] Y Yokoyama, K Yamano, K Fukaura, H Sunada, and A Inoue. Ductility improvement of Zr 55 Cu 30 Al 10 Ni 5 bulk amorphous alloy. *Scripta Materialia*, 44(8-9): 1529–1533, may 2001. doi: 10.1016/S1359-6462(01)00723-0.

[119] A. V. Sergueeva, N. A. Mara, J. D. Kuntz, E. J. Lavernia, and A. K. Mukherjee. Shear band formation and ductility in bulk metallic glass. *Philosophical Magazine*, 85(23):2671–2687, 2005. doi: 10.1080/14786430500154059.

[120] Y. Zhang, W. H. Wang, and A. L. Greer. Making metallic glasses plastic by control of residual stress. *Nature Materials*, 5(11):857–860, 2006. doi: 10.1038/nmat1758.

[121] S. V. Ketov, Y. H. Sun, S. Nachum, Z. Lu, A. Checchi, A. R. Beraldin, H. Y. Bai, W. H. Wang, D. V. Louzguine-Luzgin, M. A. Carpenter, and A. L. Greer. Rejuvenation of metallic glasses by non-affine thermal strain. *Nature*, 524(7564): 200–203, 2015. doi: 10.1038/nature14674.

[122] John R. Scully, A. Gebert, and Joe H. Payer. Corrosion and related mechanical properties of bulk metallic glasses. *Journal of Materials Research*, 22(2):302–313, 2007. doi: 10.1557/jmr.2007.0051.

[123] M. A. Streicher. Pitting Corrosion of 18Cr-8Ni Stainless Steel. *Journal of The Electrochemical Society*, 103(7):375, 1956. doi: 10.1149/1.2430359.

[124] I. Gurrappa. Characterization of titanium alloy Ti-6Al-4V for chemical, marine and industrial applications. *Materials Characterization*, 51(2-3):131–139, 2003. doi: 10.1016/j.matchar.2003.10.006.

[125] H. B. Lu, L. C. Zhang, A. Gebert, and L. Schultz. Pitting corrosion of Cu-Zr metallic glasses in hydrochloric acid solutions. *Journal of Alloys and Compounds*, 462(1-2):60–67, 2008. doi: 10.1016/j.jallcom.2007.08.023.

[126] MASAAKI NAKA, KOJI HASHIMOTO, and TSUYOSHI MASUMOTO. High Corrosion Resistance of Chromium-Bearing Amorphous Iron Alloys in Neutral and Acidic Solutions Containing Chloride. *CORROSION*, 32(4):146–152, apr 1976. doi: 10.5006/0010-9312-32.4.146.

[127] Mariana Calin, Annett Gebert, Andreea Cosmina Ghinea, Petre Flaviu Gostin, Somayeh Abdi, Christine Mickel, and Jürgen Eckert. Designing biocompatible Ti-based metallic glasses for implant applications. *Materials Science and Engineering: C*, 33(2):875–883, mar 2013. doi: 10.1016/j.msec.2012.11.015.

[128] Fengxiang Qin, Masahiro Yoshimura, Xinming Wang, Shengli Zhu, Asahi Kawashima, Katsuhiko Asami, and Akihisa Inoue. Corrosion Behavior of a Ti-Based Bulk Metallic Glass and Its Crystalline Alloys. *Materials Transactions*, 48 (7):1855–1858, 2007. doi: 10.2320/matertrans.MJ200713.

[129] L.H. Liu, J. Ma, C.Y. Yu, X.S. Huang, L.J. He, L.C. Zhang, P.J. Li, and Z.Y. Liu. Determination of forming ability of high pressure die casting for Zr-based metallic glass. *Journal of Materials Processing Technology*, 244:87–96, 2017. doi: 10.1016/j.jmatprotec.2017.01.015.

[130] Parthiban Ramasamy, Attila Szabo, Stefan Borzel, Jürgen Eckert, Mihai Stoica, and András Bárdos. High pressure die casting of Fe-based metallic glass. *Scientific Reports*, 6(September):1–11, 2016. doi: 10.1038/srep35258.

[131] ENGEL Austria. Mass production with amorphous metals. https://www.engelglobal.com/en/at/news-press/news-press-releases/detail/news/detail/News (date accessed: 2019-05-29), 2019.

[132] Panerai. Luminor Submersible 1950 BMG-TECH$^{\mathrm{TM}}$, http://www.paneraibmgtech.com/de/ (date accessed: 2019-09-18), 2019.

[133] Jan Schroers. The superplastic forming of bulk metallic glasses. *JOM*, 57(5):35–39, may 2005. doi: 10.1007/s11837-005-0093-2.

[134] G. Kumar, D. Rector, R. D. Conner, and J. Schroers. Embrittlement of Zr-based bulk metallic glasses. *Acta Materialia*, 57(12):3572–3583, 2009. doi: 10.1016/j.actamat.2009.04.016.

[135] Theodore A. Waniuk, Jan Schroers, and William L. Johnson. Critical cooling rate and thermal stability of Zr-Ti-Cu-Ni-Be alloys. *Applied Physics Letters*, 78(9): 1213–1215, 2001. doi: 10.1063/1.1350624.

[136] Golden Kumar, Hong X Tang, and Jan Schroers. Nanomoulding with amorphous metals. *Nature*, 457(7231):868–872, 2009. doi: 10.1038/nature07718.

[137] Hyo Yun Jung, Su Ji Choi, Konda G. Prashanth, Mihai Stoica, Sergio Scudino, Seonghoon Yi, Uta Kühn, Do Hyang Kim, Ki Buem Kim, and Jürgen Eckert. Fabrication of Fe-based bulk metallic glass by selective laser melting: A parameter study. *Materials and Design*, 86:703–708, 2015. doi: 10.1016/j.matdes.2015.07.145.

[138] Yiyu Shen, Yingqi Li, Chen Chen, and Hai Lung Tsai. 3D printing of large, complex metallic glass structures. *Materials and Design*, 117:213–222, 2017. doi: 10.1016/j.matdes.2016.12.087.

[139] Xiaopeng Li. Additive Manufacturing of Advanced Multi-Component Alloys: Bulk Metallic Glasses and High Entropy Alloys. *Advanced Engineering Materials*, (December), 2017. doi: 10.1002/adem.201700874.

[140] Punnathat Bordeenithikasem, Moritz Stolpe, Alexander Elsen, and Douglas C Hofmann. Glass forming ability, flexural strength, and wear properties of additively manufactured Zr-based bulk metallic glasses produced through laser powder bed fusion. *Additive Manufacturing*, 21(2010):312–317, may 2018. doi: 10.1016/j.addma.2018.03.023.

[141] Punnathat Bordeenithikasem, Yiyu Shen, Hai-Lung Tsai, and Douglas C. Hofmann. Enhanced mechanical properties of additively manufactured bulk metallic glasses produced through laser foil printing from continuous sheetmetal feedstock. *Additive Manufacturing*, 19:95–103, jan 2018. doi: 10.1016/j.addma.2017.11.010.

[142] G.W.H. Höhne, W.F. Hemminger, and H.-J. Flammersheim. *Differential Scanning Calorimetry.* Springer-Verlag Berlin Heidelberg, second edition, 2003.

[143] O. (Oswald) Kubaschewski, C. B. Alcock, P. J. Spencer, and O. (Oswald) Kubaschewski. Materials thermochemistry. page 363, 1993.

[144] S. Inaba, S. Oda, and K. Morinaga. Heat capacity of oxide glasses at high temperature region. *Journal of Non-Crystalline Solids*, 325(1-3):258–266, 2003. doi: 10.1016/S0022-3093(03)00315-6.

[145] Zach Evenson, Isabella Gallino, and Ralf Busch. The effect of cooling rates on the apparent fragility of Zr-based bulk metallic glasses. *Journal of Applied Physics*, 107(12), 2010. doi: 10.1063/1.3452381.

[146] R Busch, E Bakke, and W.L. Johnson. Viscosity of the supercooled liquid and relaxation at the glass transition of the Zr46.75Ti8.25Cu7.5Ni10Be27.5 bulk metallic glass forming alloy. *Acta Materialia*, 46(13):4725–4732, aug 1998. doi: 10.1016/S1359-6454(98)00122-0.

[147] Ralf Busch. The thermophysical properties of bulk metallic glass-forming liquids. *JOM*, 52(7):39–42, jul 2000. doi: 10.1007/s11837-000-0160-7.

[148] Ralf Busch, Eric Bakke, and William L. Johnson. On the Glass Forming Ability of Bulk Metallic Glasses. *Materials Science Forum*, 235-238:327–336, 1997. doi: 10.4028/www.scientific.net/MSF.235-238.327.

[149] H. E. HAGY. Experimental Evaluation of Beam-Bending Method of Determining Glass Viscosities in the Range 10E8 to 10E15 Poises. *Journal of the American Ceramic Society*, 46(2):93–97, feb 1963. doi: 10.1111/j.1151-2916.1963.tb11684.x.

[150] Graham Williams and David C Watts. Non-symmetrical dielectric relaxation behaviour arising from a simple empirical decay function. *Transactions of the Faraday Society*, 66(1):80, 1970. doi: 10.1039/tf9706600080.

[151] German Aerospace Center (DLR). Electromagnetic Levitator, 2014.

[152] G. Lohoefer and J. Piller. The new ISS Electromagnetic Levitation Facility - 'MSL-EML'. In *40th AIAA Aerospace Sciences Meeting & Exhibit*, number January, Reston, Virigina, jan 2002. American Institute of Aeronautics and Astronautics. doi: 10.2514/6.2002-764.

[153] German Aerospace Center (DLR). TEMPUS - Tiegelfreies Elektromagnetisches Prozessieren Unter Schwerelosigkeit.

[154] D M Herlach, R F Cochrane, I Egry, H. J. Fecht, and A L Greer. Containerless processing in the study of metallic melts and their solidification. *International Materials Reviews*, 38(6):273–347, jan 1993. doi: 10.1179/095066093790326267.

[155] I Egry, G. Lohöfer, I Seyhan, S Schneider, and B Feuerbacher. Viscosity and surface tension measurements in microgravity. *International Journal of Thermophysics*, 20(4):1005–1015, 1999. doi: https://doi.org/10.1023/A:1022686316437.

[156] I Egry, A Diefenbach, W Dreier, and J Piller. Containerless processing in space - Thermophysical property measurements using electromagnetic levitation. *International Journal of Thermophysics*, 22(2):569–578, 2001. doi: 10.1023/A:1010753805462.

[157] I Egry, H Giffard, and S Schneider. The oscillating drop technique revisited. *Measurement Science and Technology*, 16(2):426–431, feb 2005. doi: 10.1088/0957-0233/16/2/013.

[158] Lothar Spieß, Gerd Teichert, Robert Schwarzer, Herfried Behnken, and Christoph Genzel. Methoden der Röntgenbeugung. In *Moderne Röntgenbeugung*, pages 155–216. Vieweg+Teubner, Wiesbaden, 2009. doi: 10.1007/978-3-8349-9434-9_5.

[159] W. Kraus and G. Nolze. POWDER CELL - a program for the representation and manipulation of crystal structures and calculation of the resulting X-ray powder patterns. *Journal of Applied Crystallography*, 29:301–303, 1996. doi: 10.1107/S0021889895014920.

[160] T. Egami and Simon J.L. Billinge. *Underneath the Bragg Peaks.* Elsevier Ltd, 2nd editio edition, 2012. ISBN 9780080971414.

[161] Won-Kyu Rhim, Sang K. Chung, Daniel Barber, Kin F. Man, Gary Gutt, Aaron Rulison, and R. Erik Spjut. An electrostatic levitator for high-temperature containerless materials processing in 1-g. *Review of Scientific Instruments*, 64(10):2961–2970, oct 1993. doi: 10.1063/1.1144475.

[162] T Kordel, D. Holland-Moritz, F Yang, J Peters, T Unruh, T Hansen, and A Meyer. Neutron scattering experiments on liquid droplets using electrostatic levitation. *Physical Review B*, 83(10):104205, mar 2011. doi: 10.1103/PhysRevB.83.104205.

[163] AP Hammersley. FIT2D: an introduction and overview. *European Synchrotron Radiation Facility Internal Report*, (ESRF97HA02T), 1997.

[164] Giannis Ashiotis, Aurore Deschildre, Zubair Nawaz, Jonathan P. Wright, Dimitrios Karkoulis, Frédéric Emmanuel Picca, and Jérôme Kieffer. The fast azimuthal integration Python library: pyFAI. *Journal of Applied Crystallography*, 48(2): 510–519, apr 2015. doi: 10.1107/S1600576715004306.

[165] Mark Basham, Jacob Filik, Michael T. Wharmby, Peter C.Y. Chang, Baha El Kassaby, Matthew Gerring, Jun Aishima, Karl Levik, Bill C.A. Pulford, Irakli Sikharulidze, Duncan Sneddon, Matthew Webber, Sarnjeet S. Dhesi, Francesco Maccherozzi, Olof Svensson, Sandor Brockhauser, Gabor Náray, and Alun W. Ashton. Data Analysis WorkbeNch (DAWN). *Journal of Synchrotron Radiation*, 22:853–858, 2015. doi: 10.1107/S1600577515002283.

[166] J. Filik, A. W. Ashton, P. C.Y. Chang, P. A. Chater, S. J. Day, M. Drakopoulos, M. W. Gerring, M. L. Hart, O. V. Magdysyuk, S. Michalik, A. Smith, C. C. Tang, N. J. Terrill, M. T. Wharmby, and H. Wilhelm. Processing two-dimensional X-ray diffraction and small-angle scattering data in DAWN 2. *Journal of Applied Crystallography*, 50(3):959–966, 2017. doi: 10.1107/S1600576717004708.

[167] Xiangyun Qiu, Jeroen W. Thompson, and Simon J.L. Billinge. PDFgetX2: A GUI-driven program to obtain the pair distribution function from X-ray powder diffraction data. *Journal of Applied Crystallography*, 37(4):678, 2004. doi: 10.1107/S0021889804011744.

[168] L. Reimer. *Scanning Electron Microscopy: Physics of Image Formation and Microanalysis*. Springer-Verlag Berlin Heidelberg New York, second edition, 1998.

[169] Gunnar Kullerud. SULFIDE PHASE RELATIONS. *Mineral. Soc. Amer. Spec. Pap*, 3:199–210, 1970.

[170] H. W. Kui, A. L. Greer, and D. Turnbull. Formation of bulk metallic glass by fluxing. *Applied Physics Letters*, 45(6):615–616, 1984. doi: 10.1063/1.95330.

[171] Y He, R B Schwarz, and J I Archuleta. Bulk glass formation in the Pd-Ni-P system. *Applied Physics Letters*, 69(13):1861–1863, 1996. doi: 10.1063/1.117458.

[172] R.B. Schwarz and Ying He. Formation and Properties of Bulk Amorphous Pd-Ni-P Alloys. *Materials Science Forum*, 235-238:231–240, oct 1996. doi: 10.4028/www.scientific.net/MSF.235-238.231.

[173] R. Willnecker, K. Wittmann, and G. P. Görler. Undercooling investigations and heat capacity measurements on PdNiP melts. *Journal of Non-Crystalline Solids*, 156-158(PART 1):450–454, 1993. doi: 10.1016/0022-3093(93)90217-L.

[174] H. Okamoto. Ni-S (Nickel-Sulfur). *Journal of Phase Equilibria and Diffusion*, 30 (1):123–123, feb 2009. doi: 10.1007/s11669-008-9430-9.

[175] H Okamoto. Pd-s (palladium-sulfur). *Journal of Phase Equilibria*, 13(1):106–107, feb 1992. doi: 10.1007/BF02645396.

[176] Rongxiang Hu, Michael C Gao, Ömer N Doğan, Paul King, and Michael Widom. CALPHAD : Computer Coupling of Phase Diagrams and Thermochemistry Thermodynamic modeling of the Pd – S system supported by first-principles calculations. *CALPHAD: Computer Coupling of Phase Diagrams and Thermochemistry*, 34(3):324–331, 2010. doi: 10.1016/j.calphad.2010.07.002.

[177] P. Franke and D. Neuschütz. Ni-Pd. In *Binary Systems. Part 4: Binary Systems from Mn-Mo to Y-Zr*, pages 1–4. Springer-Verlag, Berlin/Heidelberg. doi: 10.1007/10757285_33.

[178] B. Predel. P-Pd (Phosphorus-Palladium). In Madelung O., editor, *Ni-Np – Pt-Zr*, chapter P-Pd (Phos, pages 1–3. Springer-Verlag, Berlin/Heidelberg, . doi: 10.1007/10542753_2368.

[179] H Okamoto. Ni-P (Nickel-Phosphorus). *Journal of Phase Equilibria and Diffusion*, 31(2):200–201, apr 2010. doi: 10.1007/s11669-010-9664-1.

[180] William L. Johnson. Bulk Glass-Forming Metallic Alloys: Science and Technology. *MRS Bulletin*, 24(10):42–56, oct 1999. doi: 10.1557/S0883769400053252.

[181] H. Okamoto. Ni-S (Nickel-Sulfur). *Journal of Phase Equilibria and Diffusion*, 30 (1):123–123, 2009. doi: 10.1007/s11669-008-9430-9.

[182] E. Makovicky and S. Karup-Moller. The system Pd-Fe-S at 900 degrees , 725 degrees , 550 degrees , and 400 degrees C. *Economic Geology*, 88(5):1269–1278, aug 1993. doi: 10.2113/gsecongeo.88.5.1269.

[183] Y. C. Kim, W. T. Kim, and D. H. Kim. A development of Ti-based bulk metallic glass. *Materials Science and Engineering A*, 375-377(1-2 SPEC. ISS.):127–135, 2004. doi: 10.1016/j.msea.2003.10.115.

[184] Akira Takeuchi and Akihisa Inoue. Classification of Bulk Metallic Glasses by Atomic Size Difference, Heat of Mixing and Period of Constituent Elements and Its Application to Characterization of the Main Alloying Element. *MATERIALS TRANSACTIONS*, 46(12):2817–2829, 2005. doi: 10.2320/matertrans.46.2817.

[185] J.L. Murray. The S-Ti (Sulfur-Titanium) System. *Bulletin of Alloy Phase Diagrams*, 7(2):156–163, 1986. doi: 10.1007/BF02881555.

[186] Jozefien De Keyzer, Gabriele Cacciamani, Nathalie Dupin, and Patrick Wollants. Thermodynamic modeling and optimization of the Fe-Ni-Ti system. *Calphad: Computer Coupling of Phase Diagrams and Thermochemistry*, 33(1):109–123, 2009. doi: 10.1016/j.calphad.2008.10.003.

[187] B. Predel. Ni-Ti (Nickel-Titanium). In *Ni-Np – Pt-Zr*, pages 1–5. Springer-Verlag, Berlin/Heidelberg, . doi: 10.1007/10542753_2272.

[188] K H J Buschow. Stability and electrical transport properties of amorphous Ti 1-x Ni x alloys. *Journal of Physics F: Metal Physics*, 13(3):563–571, mar 1983. doi: 10.1088/0305-4608/13/3/006.

[189] A Lindsay Greer. Metallic Glasses. *Science*, 267(5206):1947–1953, 1995. doi: 10.1126/science.267.5206.1947.

[190] Bao Chen Lu, Yan Ling Wang, and Jian Xu. Revisiting the glass-forming ability of Ti-Ni-Si ternary alloys. *Journal of Alloys and Compounds*, 475(1-2):157–164, 2009. doi: 10.1016/j.jallcom.2008.07.055.

[191] Bao chen Lu, Yi Li, and Jian Xu. Optimal glass-forming composition and its correlation with eutectic reaction in the Ti-Ni-Al ternary system. *Journal of Alloys and Compounds*, 467(1-2):261–267, 2009. doi: 10.1016/j.jallcom.2007.12.050.

[192] Bao chen Lu and Jian Xu. Glass formation of Ti-Ni-Sn ternary alloys correlated with TiNi-Ti3Sn pseudo binary eutectics. *Journal of Non-Crystalline Solids*, 354 (52-54):5425–5431, 2008. doi: 10.1016/j.jnoncrysol.2008.09.016.

[193] X F Wu, Z Y Suo, Y Si, L K Meng, and K Q Qiu. Bulk metallic glass formation in a ternary Ti – Cu – Ni alloy system. 452:268–272, 2008. doi: 10.1016/j.jallcom.2006.11.010.

[194] Y Guo, I Bataev, K Georgarakis, A M Jorge Jr, R P Nogueira, M Pons, and A R Yavari. Ni- and Cu-free Ti-based metallic glasses with potential biomedical application. *Intermetallics*, 63:86–96, 2015. doi: 10.1016/j.intermet.2015.04.004.

[195] Z. Zhang, H. Q. Ye, and K. H. Kuo. A new icosahedral phase with m35 symmetry. *Philosophical Magazine A: Physics of Condensed Matter, Structure, Defects and Mechanical Properties*, 52(6):1517–L52, 1985. doi: 10.1080/01418618508242135.

[196] Q. B. Yang. Structures of ti2(Ni,v) in crystalline and quasicrystalline phases. *Philosophical Magazine Letters*, 57(3):171–176, 1988. doi: 10.1080/09500838808203767.

[197] K F Kelton, W J Kim, and R M Stroud. A stable Ti-based quasicrystal. *Applied Physics Letters*, 70(24):3230–3232, jun 1997. doi: 10.1063/1.119133.

[198] Y C Kim, J M Park, J K Lee, D H Bae, W T Kim, and D H Kim. Amorphous and icosahedral phases in Ti – Zr – Cu – Ni – Be alloys. *Materials Science Engineering A*, 375-377:749–753, 2004. doi: 10.1016/j.msea.2003.10.116.

[199] D. J. Chakrabarti and D. E. Laughlin. The Cu-S (Copper-Sulfur) system. *Bulletin of Alloy Phase Diagrams*, 4(3):254–271, 1983. doi: 10.1007/BF02868665.

[200] A. P. Wang, J. Q. Wang, and E. Ma. Modified efficient cluster packing model for calculating alloy compositions with high glass forming ability. *Applied Physics Letters*, 90(12):88–91, 2007. doi: 10.1063/1.2715172.

[201] B. Predel. Ti-Zr (Titanium-Zirconium). In *Pu-Re – Zn-Zr*, pages 1–3. Springer-Verlag, Berlin/Heidelberg, . doi: 10.1007/10551312_2847.

[202] B. Predel. Cr-Zr (Chromium-Zirconium). In *Cr-Cs – Cu-Zr*, pages 1–3. Springer-Verlag, Berlin/Heidelberg, 1823. doi: 10.1007/10086090_1030.

[203] X. H. Lin, W. L. Johnson, and W. K. Rhim. Effect of Oxygen Impurity on Crystallization of an Undercooled Bulk Glass Forming Zr-Ti-Cu-Ni-All Alloy. *Materials Transactions, JIM*, 38(5):473–477, 1997. doi: 10.2320/matertrans1989.38.473.

[204] A. Gebert, J. Eckert, and L. Schultz. Effect of oxygen on phase formation and thermal stability of slowly cooled Zr65Al7.5Cu17.5Ni10 metallic glass. *Acta Materialia*, 46(15):5475–5482, 1998. doi: 10.1016/S1359-6454(98)00187-6.

[205] C. T. Liu, M. F. Chisholm, and M. K. Miller. Oxygen impurity and microalloying effect in a Zr-based bulk metallic glass alloy. *Intermetallics*, 10(11-12):1105–1112, 2002. doi: 10.1016/S0966-9795(02)00131-0.

[206] Jochen Heinrich, Ralf Busch, and Bernd Nonnenmacher. Processing of a bulk metallic glass forming alloy based on industrial grade Zr. *Intermetallics*, 25:1–4, jun 2012. doi: 10.1016/j.intermet.2012.02.011.

[207] I. Jonas, W. Hembree, F. Yang, R. Busch, and A. Meyer. Industrial grade versus scientific pure: Influence on melt properties. *Applied Physics Letters*, 112(17):1–5, 2018. doi: 10.1063/1.5021764.

[208] S. Mukherjee, Z. Zhou, J. Schroers, W. L. Johnson, and W. K. Rhim. Overheating threshold and its effect on time-temperature-transformation diagrams of zirconium based bulk metallic glasses. *Applied Physics Letters*, 84(24):5010–5012, 2004. doi: 10.1063/1.1763219.

[209] A. Mühlbauer, F. Bernier, M. Blum, M. Vogt, B. Nacke, and E. Baake. Experimental and numerical investigations of the temperature field and melt flow in

the induction furnace with cold crucible. *COMPEL - The international journal for computation and mathematics in electrical and electronic engineering*, 22(1): 88–97, 2003. doi: 10.1108/03321640310452196.

[210] Jan Schroers. On the formability of bulk metallic glass in its supercooled liquid state. *Acta Materialia*, 56(3):471–478, 2008. doi: 10.1016/j.actamat.2007.10.008.

[211] Jan Schroers, Tranquoc Nguyen, Sean O Keeffe, and Amish Desai. Thermoplastic forming of bulk metallic glass — Applications for MEMS and microstructure fabrication. 451:898–902, 2007. doi: 10.1016/j.msea.2006.02.398.

[212] Benedikt Bochtler, Moritz Stolpe, Benedikt Reiplinger, and Ralf Busch. Consolidation of amorphous powder by thermoplastic forming and subsequent mechanical testing. *Materials and Design*, 140:188–195, 2018. doi: 10.1016/j.matdes.2017.11.058.

[213] B. Bochtler. *Thermophysical and Structural Investigations of a CuTi- and a Zr-based Bulk Metallic Glass, the Influence of Minor Additions, and the Relation to Thermoplastic Forming - to be published.* Phd thesis, Saarland University, 2019.

[214] A J Drehman, A L Greer, and D Turnbull. Bulk Formation of a Metallic Glass: Pd40Ni40P20. *Applied Physics Letters*, 41(8):716–717, 1982. doi: doi:http://dx.doi.org/10.1063/1.93645.

[215] G. Wilde, G. P. Görler, R. Willnecker, and G. Dietz. Thermodynamic properties of Pd40Ni40P20 in the glassy, liquid, and crystalline states. *Applied Physics Letters*, 65(4):397–399, 1994. doi: 10.1063/1.112313.

[216] I.-R Lu, G Wilde, G.P Görler, and R. Willnecker. Thermodynamic properties of Pd-based glass-forming alloys. *Journal of Non-Crystalline Solids*, 250-252:577–581, aug 1999. doi: 10.1016/S0022-3093(99)00135-0.

[217] T.A. Waniuk, R. Busch, A. Masuhr, and W.L. Johnson. Equilibrium viscosity of the Zr41.2Ti13.8Cu12.5Ni10Be22.5 bulk metallic glass-forming liquid and viscous flow during relaxation, phase separation, and primary crystallization. *Acta Materialia*, 46(15):5229–5236, sep 1998. doi: 10.1016/S1359-6454(98)00242-0.

[218] Zach Evenson, Sven Raedersdorf, Isabella Gallino, and Ralf Busch. Equilibrium viscosity of Zr–Cu–Ni–Al–Nb bulk metallic glasses. *Scripta Materialia*, 63(6):573–576, 2010. doi: 10.1016/j.scriptamat.2010.06.008.

[219] R Busch, S Schneider, A Peker, and W L Johnson. Decomposition and primary crystallization in undercooled Zr 41.2 Ti 13.8 Cu 12.5 Ni 10.0 Be 22.5 melts. *Applied Physics Letters*, 67(11):1544–1546, sep 1995. doi: 10.1063/1.114487.

[220] Cornelius T. Moynihan, Allan J. Easteal, James Wilder, and Joseph Tucker. Dependence of the glass transition temperature on heating and cooling rate. *The Journal of Physical Chemistry*, 78(26):2673–2677, dec 1974. doi: 10.1021/j100619a008.

[221] A Masuhr, T A Waniuk, R Busch, and W L Johnson. Time Scales for Viscous Flow, Atomic Transport, and Crystallization in the Liquid and Supercooled Liquid States of Zr41.2Ti13.8Cu12.5Ni10.0Be22.5. *Physical Review Letters*, 82(11):2290–2293, mar 1999. doi: 10.1103/PhysRevLett.82.2290.

[222] Jan Schroers, Boonrat Lohwongwatana, William L. Johnson, and Atakan Peker. Precious bulk metallic glasses for jewelry applications. *Materials Science and Engineering A*, 448-451:235–238, 2007. doi: 10.1016/j.msea.2006.02.301.

[223] F. Grønvold and E. Røst. The crystal structures of Pd4Se and Pd4S. *Acta Crystallographica*, 15(1):11–13, 1962. doi: 10.1107/S0365110X62000031.

[224] John B Parise. Structure of hazelwoodite (Ni3S2). *Acta Crystallographica Section B: Structural Crystallography and Crystal Chemistry*, 36(5):1179–1180, 1980. doi: 10.1107/S0567740880005523.

[225] Christopher A. Schuh, Todd C. Hufnagel, and Upadrasta Ramamurty. Mechanical behavior of amorphous alloys. *Acta Materialia*, 55(12):4067–4109, 2007. doi: 10.1016/j.actamat.2007.01.052.

[226] G. Wang, Y. T. Wang, Y. H. Liu, M. X. Pan, D. Q. Zhao, and W. H. Wang. Evolution of nanoscale morphology on fracture surface of brittle metallic glass. *Applied Physics Letters*, 89(12):23–25, 2006. doi: 10.1063/1.2354011.

[227] G. Wang, D. Q. Zhao, H. Y. Bai, M. X. Pan, A. L. Xia, B. S. Han, X. K. Xi, Y. Wu, and W. H. Wang. Nanoscale periodic morphologies on the fracture surface of brittle metallic glasses. *Physical Review Letters*, 98(23):1–4, 2007. doi: 10.1103/PhysRevLett.98.235501.

[228] X. K. Xi, D. Q. Zhao, M. X. Pan, W. H. Wang, Y. Wu, and J. J. Lewandowski. Fracture of brittle metallic glasses: Brittleness or plasticity. *Physical Review Letters*, 94(12):25–28, 2005. doi: 10.1103/PhysRevLett.94.125510.

[229] A. Shamimi Nouri, X. J. Gu, S. J. Poon, G. J. Shiflet, and J. J. Lewandowski. Chemistry (intrinsic) and inclusion (extrinsic) effects on the toughness and Weibull modulus of Fe-based bulk metallic glasses. *Philosophical Magazine Letters*, 88(11):853–861, 2008. doi: 10.1080/09500830802438131.

[230] Z. Han, L. C. Tang, J. Xu, and Y. Li. A three-parameter Weibull statistical analysis of the strength variation of bulk metallic glasses. *Scripta Materialia*, 61 (9):923–926, 2009. doi: 10.1016/j.scriptamat.2009.07.038.

[231] C. J. Lee, Y. H. Lai, J. C. Huang, X. H. Du, L. Wang, and T. G. Nieh. Strength variation and cast defect distribution in metallic glasses. *Scripta Materialia*, 63 (1):105–108, 2010. doi: 10.1016/j.scriptamat.2010.03.028.

[232] Jijun Zhang, Diana Estévez, Yuan Yun Zhao, Lishan Huo, Chuntao Chang, Xinmin Wang, and Run Wei Li. Flexural Strength and Weibull Analysis of Bulk Metallic Glasses. *Journal of Materials Science and Technology*, 32(2):129–133, 2016. doi: 10.1016/j.jmst.2015.12.016.

[233] S C Glade, R Busch, D S Lee, W L Johnson, R K Wunderlich, and H J Fecht. Thermodynamics of Cu47Ti34Zr11Ni8, Zr52.5Cu17.9Ni14.6Al10Ti5 and Zr57Cu15.4Ni12.6Al10Nb5 bulk metallic glass forming alloys. *Journal of Applied Physics*, 87(10):7242–7248, may 2000. doi: 10.1063/1.372975.

[234] Zach Evenson and Ralf Busch. Equilibrium viscosity, enthalpy recovery and free volume relaxation in a Zr44Ti11Ni10Cu10Be25bulk metallic glass. *Acta Materialia*, 59(11):4404–4415, 2011. doi: 10.1016/j.actamat.2011.03.064.

[235] J. Tille and J. C. Kelly. The surface tension of liquid titanium. *British Journal of Applied Physics*, 14(10):717–719, 1963. doi: 10.1088/0508-3443/14/10/332.

[236] S. Schneider, I. Egry, and I. Seyhan. Measurement of the Surface Tension of Undercooled Liquid Ti 90Al6V4 by the Oscillating Drop Technique. *International Journal of Thermophysics*, 23(5):1241–1248, 2002. doi: 10.1023/A:1019896321431.

[237] Markus Mohr, Rainer K. Wunderlich, Kai Zweiacker, Silke Prades-Rödel, Romuald Sauget, Andreas Blatter, Roland Logé, Alex Dommann, Antonia Neels, William L. Johnson, and Hans-Jörg Fecht. Surface tension and viscosity of liquid Pd43Cu27Ni10P20 measured in a levitation device under microgravity. *npj Microgravity*, 5(1):4, dec 2019. doi: 10.1038/s41526-019-0065-4.

[238] William Hembree. *High temperature rheology of Zr-based bulk metallic glass forming liquids.* Phd thesis, Saarland University, 2015.

[239] William Hembree, Benedikt Bochtler, and Ralf Busch. High-temperature rotating cylinder rheometer for studying metallic glass forming liquids. *Review of Scientific Instruments*, 89(11), 2018. doi: 10.1063/1.5039318.

[240] J Schroers, R Busch, A Masuhr, W L Johnson, J Schroers, R Busch, A Masuhr, and W L Johnson. Continuous refinement of the microstructure during crystallization

of supercooled Zr41Ti14Cu12Ni10Be23 melts. 2806(1999):41–44, 1999. doi: 10.1063/1.124020.

[241] K. F. Kelton, G. W. Lee, A. K. Gangopadhyay, R. W. Hyers, T. J. Rathz, J. R. Rogers, M. B. Robinson, and D. S. Robinson. First X-Ray Scattering Studies on Electrostatically Levitated Metallic Liquids: Demonstrated Influence of Local Icosahedral Order on the Nucleation Barrier. *Physical Review Letters*, 90(19):4, 2003. doi: 10.1103/PhysRevLett.90.195504.

[242] Limin Wang, Liqun Ma, Chaoli Ma, and Akihisa Inoue. Formations of amorphous and quasicrystal phases in Ti-Zr-Ni-Cu alloys. *Journal of Alloys and Compounds*, 361(1-2):234–240, 2003. doi: 10.1016/S0925-8388(03)00430-4.

[243] L Q Xing, J Eckert, W Loser, and L Schultz. High-strength materials produced by precipitation of icosahedral quasicrystals in bulk Zr-Ti-Cu-Ni-Al amorphous alloys. *Applied Physics Letters*, 74(5):664–666, 1999. doi: 10.1063/1.122980.

[244] V.N. Chebotnikov and V.V. Molokanov. Structure and properties of alloys of Ti2Cu-Zr2Cu cross-section of Ti-Zr-Cu system in amorphous and crystalline states. *Neorganicheskie Materialy*, 26:960–964, 1990.

[245] Ti2Cu (CuTi2 rt) Crystal Structure: Datasheet from ”PAULING FILE Multinaries Edition – 2012” in SpringerMaterials (https://materials.springer.com/isp/crystallographic/docs/sd_0260616), 2012.

[246] Zr2Cu (CuZr2 ht) Crystal Structure: Datasheet from ”PAULING FILE Multinaries Edition – 2012” in SpringerMaterials (https://materials.springer.com/isp/crystallographic/docs/sd_1220325), .

[247] β-Ti (Ti ht, T = 1173 K) Crystal Structure: Datasheet from ”PAULING FILE Multinaries Edition – 2012” in SpringerMaterials (https://materials.springer.com/isp/crystallographic/docs/sd_0534323), .

[248] V. Keryvin, C. Bernard, J. C. Sangleboœuf, Y. Yokoyama, and T. Rouxel. Toughness of Zr55Cu30Al10Ni5 bulk metallic glass for two oxygen levels. *Journal of Non-Crystalline Solids*, 352(26-27):2863–2868, 2006. doi: 10.1016/j.jnoncrysol.2006.02.102.

[249] Yoshihiko Yokoyama, Atsushi Kobayashi, Kenzo Fukaura, and Akihisa Inoue. Oxygen Embrittlement and Effect of the Addition of Ni Element in a Bulk Amorphous Zr-Cu-Al Alloy. *Materials Transactions*, 43(3):571–574, 2002. doi: 10.2320/matertrans.43.571.

[250] Wen Chen, Haofei Zhou, Ze Liu, Jittisa Ketkaew, Ning Li, James Yurko, Nicholas Hutchinson, Huajian Gao, and Jan Schroers. Processing effects on fracture toughness of metallic glasses. *Scripta Materialia*, 130:152–156, 2017. doi: 10.1016/j.scriptamat.2016.11.011.

[251] J. J. Lewandowski, W. H. Wang, and A. L. Greer. Intrinsic plasticity or brittleness of metallic glasses. *Philosophical Magazine Letters*, 85(2):77–87, 2005. doi: 10.1080/09500830500080474.

[252] G. N. Greaves, A. L. Greer, R. S. Lakes, and T. Rouxel. Poisson's ratio and modern materials. *Nature Materials*, 10(11):823–837, nov 2011. doi: 10.1038/nmat3134.

[253] H Bala and S. Szymura. Acid corrosion of amorphous and crystalline Cu-Zr alloys. *Applied Surface Science*, 35(1):41–51, oct 1988. doi: 10.1016/0169-4332(88)90036-0.

[254] Chunling Qin, Katsuhiko Asami, Tao Zhang, Wei Zhang, and Akihisa Inoue. Corrosion Behavior of Cu-Zr-Ti-Nb Bulk Glassy Alloys. *MATERIALS TRANSACTIONS*, 44(4):749–753, 2003. doi: 10.2320/matertrans.44.749.

[255] Fengxiang Qin, Xinmin Wang, Shengli Zhu, Asahi Kawashima, Katsuhiko Asami, and Akihisa Inoue. Fabrication and Corrosion Property of Novel Ti-Based Bulk Glassy Alloys without Ni. *Materials Transactions*, 48(3):515–518, 2007. doi: 10.2320/matertrans.48.515.

[256] Daniela Zander, Beate Heisterkamp, and Isabella Gallino. Corrosion resistance of Cu-Zr-Al-Y and Zr-Cu-Ni-Al-Nb bulk metallic glasses. *Journal of Alloys and Compounds*, 434-435(SPEC. ISS.):234–236, 2007. doi: 10.1016/j.jallcom.2006.08.112.

[257] C. H. Huang, Y. S. Huang, Y. S. Lin, C. H. Lin, J. C. Huang, C. H. Chen, J. B. Li, Y. H. Chen, and J. S.C. Jang. Electrochemical and biocompatibility response of newly developed TiZr-based metallic glasses. *Materials Science and Engineering C*, 43:343–349, 2014. doi: 10.1016/j.msec.2014.06.040.

[258] Annett Gebert, Flaviu Gostin, Uta Kuehn, and Ludwig Schultz. Corrosion of a Zr-based Bulk Metallic Glass with Different Surface Finishing States. In *ECS Transactions*, volume 16, pages 1–7. ECS, 2009. doi: 10.1149/1.3091901.

[259] Y. Li, S.C. Ng, C.K. Ong, H.H. Hng, and T.T. Goh. Glass forming ability of bulk glass forming alloys. *Scripta Materialia*, 36(7):783–787, apr 1997. doi: 10.1016/S1359-6462(96)00448-4.

[260] Z.P. Lu and C.T. Liu. A new glass-forming ability criterion for bulk metallic glasses. *Acta Materialia*, 50(13):3501–3512, aug 2002. doi: 10.1016/S1359-6454(02)00166-0.

[261] Shiyan Ding, John Gregoire, Joost J. Vlassak, and Jan Schroers. Solidification of Au-Cu-Si alloys investigated by a combinatorial approach. *Journal of Applied Physics*, 111(11), 2012. doi: 10.1063/1.4722996.

[262] G Wilde, G. P. Görler, R Willnecker, and H J Fecht. Calorimetric, thermomechanical, and rheological characterizations of bulk glass-forming Pd40Ni40P20. *Journal of Applied Physics*, 87(3):1141–1152, feb 2000. doi: 10.1063/1.371991.

[263] Nobuyuki Nishiyama and Akihisa Inoue. Glass Transition Behavior and Viscous Flow Working of Pd40Cu30Ni10P20 Amorphous Alloy. *Materials Transactions, JIM*, 40(1):64–71, 1999. doi: 10.2320/matertrans1989.40.64.

[264] AJ Drehman and AL Greer. Kinetics of crystal nucleation and growth in Pd40Ni40P20 glass. *Acta Metallurgica*, 32(3):323–332, mar 1984. doi: 10.1016/0001-6160(84)90105-6.

[265] D. Granata, E. Fischer, V. Wessels, and J. F. Löffler. Fluxing of Pd-Si-Cu bulk metallic glass and the role of cooling rate and purification. *Acta Materialia*, 71: 145–152, 2014. doi: 10.1016/j.actamat.2014.03.008.

[266] Ji-jun Zhang, Ya-qiang Dong, Lu-yang Bie, Qiang Li, Jia-wei Li, and Xin-min Wang. Influences of preparation techniques on glass-forming ability of Fe–P–B–Si–C amorphous alloys. *Journal of Iron and Steel Research International*, 25(6):674–679, jun 2018. doi: 10.1007/s42243-018-0089-0.

[267] M. Volmer and . Weber. Keimbildung in uebersaettigten Gebilden. *Zeitschrift fuer Physikalische Chemie*, 119U(1):277–301, 1926. doi: 10.1515/zpch-1926-11927.

[268] Jörg F. Löffler, Jan Schroers, and William L. Johnson. Time-temperature-transformation diagram and microstructures of bulk glass forming Pd40Cu30Ni10P20. *Applied Physics Letters*, 77(5):681–683, 2000. doi: 10.1063/1.127084.

[269] J Schroers, Y Wu, R Busch, and W.L. Johnson. Transition from nucleation controlled to growth controlled crystallization in Pd43Ni10Cu27P20 melts. *Acta Materialia*, 49(14):2773–2781, aug 2001. doi: 10.1016/S1359-6454(01)00159-8.

[270] Benjamin A. Legg, Jan Schroers, and Ralf Busch. Thermodynamics, kinetics, and crystallization of Pt57.3Cu14.6Ni5.3P22.8 bulk metallic glass. *Acta Materialia*, 55 (3):1109–1116, 2007. doi: 10.1016/j.actamat.2006.09.024.

[271] Y. T. Shen, T. H. Kim, A. K. Gangopadhyay, and K. F. Kelton. Icosahedral order, frustration, and the glass transition: Evidence from time-dependent nucleation and supercooled liquid structure studies. *Physical Review Letters*, 102(5):6–9, 2009. doi: 10.1103/PhysRevLett.102.057801.

[272] Z. Wang, S. V. Ketov, C. L. Chen, Y. Shen, Y. Ikuhara, A. A. Tsarkov, D. V. Louzguine-Luzgin, and J. H. Perepezko. Nucleation and thermal stability of an icosahedral nanophase during the early crystallization stage in Zr-Co-Cu-Al metallic glasses. *Acta Materialia*, 132:298–306, 2017. doi: 10.1016/j.actamat.2017.04.044.

[273] K. F. Kelton, A. L. Greer, and C. V. Thompson. Transient nucleation in condensed systems. *The Journal of Chemical Physics*, 79(12):6261–6276, dec 1983. doi: 10.1063/1.445731.

[274] K.F. Kelton and A.L. Greer. Transient nucleation effects in glass formation. *Journal of Non-Crystalline Solids*, 79(3):295 – 309, 1986. doi: https://doi.org/10.1016/0022-3093(86)90229-2.

[275] S R Elliott. the Origin of the 1St Sharp Diffraction Peak in the Structure Factor of Covalent Glasses and Liquids. *Journal of Physics-Condensed Matter*, 4(38): 7661–7678, 1992. doi: 10.1088/0953-8984/4/38/003.

[276] D. Ma, A. D. Stoica, and X. L. Wang. Power-law scaling and fractal nature of medium-range order in metallic glasses. *Nature Materials*, 8(1):30–34, 2009. doi: 10.1038/nmat2340.

[277] I. I. Salamatov. Upgrading the manufacture of chemical process equipment to modern engineering levels. *Chemical and Petroleum Engineering*, 1(5):341–343, 1965. doi: 10.1007/s11661-007-9335-y.

[278] Takahiro Nakamura, Eiichiro Matsubara, Masaki Sakurai, Masayuki Kasai, Akihisa Inoue, and Yoshio Waseda. Structural study in amorphous Zr-noble metal (Pd, Pt and Au) alloys. *Journal of Non-Crystalline Solids*, 312-314:517–521, 2002. doi: 10.1016/S0022-3093(02)01738-6.

[279] Salman Ali Khan, X. D. Wang, Q. P. Cao, D. X. Zhang, and J. Z. Jiang. Structural signature in Au-based amorphous alloys. *Acta Materialia*, 140:31–38, 2017. doi: 10.1016/j.actamat.2017.08.020.

[280] W Hoyer and R. Jödicke. Short-range and medium-range order in liquid Au-Ge alloys. *Journal of Non-Crystalline Solids*, 192-193:102–105, dec 1995. doi: 10.1016/0022-3093(95)00335-5.

[281] K. S. Bondi, A. K. Gangopadhyay, Z. Marine, T. H. Kim, Anindita Mukhopadhyay, A. I. Goldman, William E. Buhro, and K. F. Kelton. Effects of microalloying with 3d transition metals on glass formation in AlYFe alloys. *Journal of Non-Crystalline Solids*, 353(52-54):4723–4731, 2007. doi: 10.1016/j.jnoncrysol.2007.06.063.

[282] Y. W. Bai, X. F. Bian, X. Q. Lv, S. P. Pan, J. Y. Qin, X. B. Qin, and L. N. Hu. Heredity of medium-range order structure from melts to amorphous solids. *Journal of Applied Physics*, 112(8), 2012. doi: 10.1063/1.4759143.

[283] Oliver Gross, Nico Neuber, Alexander Kuball, Benedikt Bochtler, Simon Hechler, Maximilian Frey, and Ralf Busch. Signatures of structural differences in Pt–P- and Pd–P-based bulk glass-forming liquids. *Communications Physics*, 2(1):83, dec 2019. doi: 10.1038/s42005-019-0180-2.

[284] Qiaoshi Zeng, Yu Lin, Yijin Liu, Zhidan Zeng, Crystal Y. Shi, Bo Zhang, Hongbo Lou, Stanislav V. Sinogeikin, Yoshio Kono, Curtis Kenney-Benson, Changyong Park, Wenge Yang, Weihua Wang, Hongwei Sheng, Ho-kwang Mao, and Wendy L. Mao. General 2.5 power law of metallic glasses. *Proceedings of the National Academy of Sciences*, 113(7):1714–1718, 2016. doi: 10.1073/pnas.1525390113.

[285] Z. Evenson, S. E. Naleway, S. Wei, O. Gross, J. J. Kruzic, I. Gallino, W. Possart, M. Stommel, and R. Busch. Beta-relaxation and low-temperature aging in a Au-based bulk metallic glass: From elastic properties to atomic-scale structure. *Physical Review B*, 89(17):174204, may 2014. doi: 10.1103/PhysRevB.89.174204.

[286] Raymond F Bacon and Rocco Fanelli. The Viscosity of Sulfur 1. *Journal of the American Chemical Society*, 65(4):639–648, apr 1943. doi: 10.1021/ja01244a043.

[287] Gabriel O. Sofekun, Erin Evoy, Kevin L. Lesage, Nancy Chou, and Robert A. Marriott. The rheology of liquid elemental sulfur across the λ-transition. *Journal of Rheology*, 62(2):469–476, 2018. doi: 10.1122/1.5001523.

[288] H. Lou, X. Wang, Q. Cao, D. Zhang, J. Zhang, T. Hu, H.-k. Mao, and J.-Z. Jiang. Negative expansions of interatomic distances in metallic melts. *Proceedings of the National Academy of Sciences*, 110(25):10068–10072, 2013. doi: 10.1073/pnas.1307967110.

[289] A. K. Gangopadhyay, M. E. Blodgett, M. L. Johnson, J. McKnight, V. Wessels, A. J. Vogt, N. A. Mauro, J. C. Bendert, R. Soklaski, L. Yang, and K. F. Kelton. Anomalous thermal contraction of the first coordination shell in metallic alloy liquids. *Journal of Chemical Physics*, 140(4), 2014. doi: 10.1063/1.4861666.

[290] J. Ding, M. Xu, P. F. Guan, S. W. Deng, Y. Q. Cheng, and E. Ma. Temperature effects on atomic pair distribution functions of melts. *Journal of Chemical Physics*, 140(6), 2014. doi: 10.1063/1.4864106.

[291] V N Novikov and A P Sokolov. Correlation of fragility and Poisson's ratio: Difference between metallic and nonmetallic glass formers. pages 1–7, 2006. doi: 10.1103/PhysRevB.74.064203.

[292] E S Park, J H Na, and D H Kim. Correlation between fragility and glass-forming ability/plasticity in metallic glass-forming alloys. *Applied Physics Letters*, 91(3): 031907, jul 2007. doi: 10.1063/1.2759266.

[293] Jan Schroers and William L. Johnson. Ductile bulk metallic glass. *Physical Review Letters*, 93(25):20–23, 2004. doi: 10.1103/PhysRevLett.93.255506.

[294] Golden Kumar, Silke Prades-Rodel, Andreas Blatter, and Jan Schroers. Unusual brittle behavior of Pd-based bulk metallic glass. *Scripta Materialia*, 65(7):585–587, 2011. doi: 10.1016/j.scriptamat.2011.06.029.

[295] J Shen, Y.J. Huang, and J.F. Sun. Plasticity of a TiCu-based bulk metallic glass: Effect of cooling rate. *Journal of Materials Research*, 22(11):3067–3074, nov 2007. doi: 10.1557/JMR.2007.0410.

[296] H. X. Li, Z. C. Lu, S. L. Wang, Y. Wu, and Z. P. Lu. Fe-based bulk metallic glasses: Glass formation, fabrication, properties and applications. *Progress in Materials Science*, 103(December 2018):235–318, 2019. doi: 10.1016/j.pmatsci.2019.01.003.

[297] M. Q. Tang, H. F. Zhang, Z. W. Zhu, H. M. Fu, A. M. Wang, H. Li, and Z. Q. Hu. TiZr-base Bulk Metallic Glass with over 50 mm in Diameter. *Journal of Materials Science and Technology*, 26(6):481–486, 2010. doi: 10.1016/S1005-0302(10) 60077-1.

[298] S. F. Zhao, N. Chen, P. Gong, and K. F. Yao. New centimeter-sized quaternary Ti-Zr-Be-Cu bulk metallic glasses with large glass forming ability. *Journal of Alloys and Compounds*, 647:533–538, 2015. doi: 10.1016/j.jallcom.2015.05.214.

[299] P Gong, X Wang, Y Shao, N Chen, X Liu, and K F Yao. A Ti-Zr-Be-Fe-Cu bulk metallic glass with superior glass-forming ability and high specific strength. *Intermetallics*, 43:177–181, 2013. doi: 10.1016/j.intermet.2013.08.003.

[300] Jin Man Park, Yu Chan Kim, Won Tae Kim, and Do Hyang Kim. Ti-Based Bulk Metallic Glasses with High Specific Strength. *MATERIALS TRANSACTIONS*, 45(2):595–598, 2004. doi: 10.2320/matertrans.45.595.

[301] Shaofan Zhao, Na Chen, Pan Gong, and Kefu Yao. Centimeter-Sized Quaternary Ti-Based Bulk Metallic Glasses with High Ti Content of 50 at%. *Advanced Engineering Materials*, 18(2):231–235, feb 2016. doi: 10.1002/adem.201500165.

[302] Chaoli Ma, Satoru Ishihara, Hideki Soejima, Nobuyuki Nishiyama, and Akihisa Inoue. Formation of New Ti-based Metallic Glassy Alloys. *Materials Transactions*, 45(5):1802–1806, 2004. doi: 10.2320/matertrans.45.1802.

[303] Tao Zhang and Akihisa Inoue. Thermal and Mechanical Properties of Ti–Ni–Cu–Sn Amorphous Alloys with a Wide Supercooled Liquid Region before Crystallization. *Materials Transactions, JIM*, 39(10):1001–1006, 1998. doi: 10.2320/matertrans1989.39.1001.

[304] Yan-Ling Wang and Jian Xu. Ti (Zr)-Cu-Ni Bulk Metallic Glasses with Optimal Glass-Forming Ability and Their Compressive Properties. *Metallurgical and Materials Transactions A*, 39(12):2990–2997, dec 2008. doi: 10.1007/s11661-008-9647-6.

[305] Shujie Pang, Ying Liu, Haifei Li, Lulu Sun, Yan Li, and Tao Zhang. New Ti-based Ti-Cu-Zr-Fe-Sn-Si-Ag bulk metallic glass for biomedical applications. *Journal of Alloys and Compounds*, 625:323–327, 2015. doi: 10.1016/j.jallcom.2014.07.021.

[306] S.L. Zhu, X.M. Wang, F.X. Qin., and A Inoue. A new Ti-based bulk glassy alloy with potential for biomedical application. *Materials Science and Engineering: A*, 459(1-2):233–237, jun 2007. doi: 10.1016/j.msea.2007.01.044.

[307] Shengli Zhu, Guoqiang Xie, Fengxiang Qin, Xinmin Wang, and Akihisa Inoue. Effect of Minor Sn Additions on the Formation and Properties of TiCuZrPd Bulk Glassy Alloy. *Materials Transactions*, 53(3):500–503, 2012. doi: 10.2320/matertrans.M2011281.

[308] Alethea Liens, Aurélien Etiemble, Pascaline Rivory, Sandra Balvay, Jean-Marc Pelletier, Sandrine Cardinal, Damien Fabrègue, Hidemi Kato, Philippe Steyer, Tais Munhoz, Jerome Adrien, Nicolas Courtois, Daniel Hartmann, and Jérôme Chevalier. On the Potential of Bulk Metallic Glasses for Dental Implantology: Case Study on Ti40Zr10Cu36Pd14. *Materials*, 11(2):249, feb 2018. doi: 10.3390/ma11020249.

[309] Baran Sarac, Supriya Bera, Sascha Balakin, Mihai Stoica, Mariana Calin, and Jürgen Eckert. Hierarchical surface patterning of Ni- and Be-free Ti- and Zr-based bulk metallic glasses by thermoplastic net-shaping. *Materials Science and Engineering C*, 73:398–405, 2017. doi: 10.1016/j.msec.2016.12.059.

[310] Alexander Kuball, Moritz Stolpe, and Ralf Busch. Crystallization behavior of the Al 86 Ni 8 Y 6 metallic glass forming alloy upon rapid cooling. *Journal of Alloys and Compounds*, 737:398–404, mar 2018. doi: 10.1016/j.jallcom.2017.12.044.

[311] C.A. Angell. Glass-Formers and Viscous Liquid Slowdown since David Turnbull: Enduring Puzzles and New Twists. *MRS Bulletin*, 33(5):544–555, 2008. doi: 10.1557/mrs2008.108.

[312] R. W. Hyers, R. C. Bradshaw, J. R. Rogers, T. J. Rathz, G. W. Lee, A. K. Gangopadhyay, and K. F. Kelton. Surface tension and viscosity of quasicrystal-forming Ti-Zr-Ni alloys. *International Journal of Thermophysics*, 25(4):1155–1162, 2004. doi: 10.1023/B:IJOT.0000038507.99417.5b.

[313] R. C. Bradshaw, A. D. Arsenault, R. W. Hyers, J. R. Rogers, T. J. Rathz, G. W. Lee, A. K. Gangopadhyay, and K. F. Kelton. Nonlinearities in the undercooled properties of Ti39.5 Zr 39.5 Ni21. *Philosophical Magazine*, 86(3-5):341–347, 2006. doi: 10.1080/14786430500253968.

[314] C C Hays, C P Kim, and W L Johnson. Large supercooled liquid region and phase separation in the Zr-Ti-Ni-Cu-Be bulk metallic glasses. *Applied Physics Letters*, 75(8):1089–1091, 1999. doi: doi:http://dx.doi.org/10.1063/1.124606.

[315] Sergio Scudino, Jürgen Eckert, Hergen Breitzke, Klaus Lüders, and Ludwig Schultz. Effect of Zr on the crystallization behavior of multi-component Zr-based metallic glasses. *Journal of Alloys and Compounds*, 434-435(SPEC. ISS.):217–220, 2007. doi: 10.1016/j.jallcom.2006.08.162.

[316] Supriya Bera, Baran Sarac, Sascha Balakin, Parthiban Ramasamy, Mihai Stoica, Mariana Calin, and Jürgen Eckert. Micro-patterning by thermoplastic forming of Ni-free Ti-based bulk metallic glasses. *Materials and Design*, 120:204–211, 2017. doi: 10.1016/j.matdes.2017.01.080.

[317] J. P. Owens, B. R. Conrad, and N. F. Franzen. The crystal structure of Ti 2 S. *Acta Crystallographica*, 23(1):77–82, jul 1967. doi: 10.1107/S0365110X67002154.

[318] J. P. Owens and H. F. Franzen. Preparation and structure determination of Ti 8 S 3. *Acta Crystallographica Section B Structural Crystallography and Crystal Chemistry*, 30(2):427–430, feb 1974. doi: 10.1107/S0567740874002949.

[319] B. Adam. *Entwicklung und Herstellung titanreicher Metallischer Massivgläser im System Ti-Ni-S*. Bachelor thesis, Saarland University, 2018.

[320] N. Zheng, R. T. Qu, S. Pauly, M. Calin, T. Gemming, Z. F. Zhang, and J. Eckert. Design of ductile bulk metallic glasses by adding "soft" atoms. *Applied Physics Letters*, 100(14):1–5, 2012. doi: 10.1063/1.3700721.

[321] J M Park, G Wang, S Pauly, N Mattern, D H Kim, and J Eckert. Ductile Ti-Based Bulk Metallic Glasses with High Specific Strength. 2010. doi: 10.1007/s11661-010-0416-y.

[322] V N Novikov and A P Sokolov. Poisson's ratio and the fragility of glass-forming liquids. *Nature*, 431(7011):961–963, oct 2004. doi: 10.1038/nature02947.

[323] Livio Battezzati. Is There a Link between Melt Fragility and Elastic Properties of Metallic Glasses? *MATERIALS TRANSACTIONS*, 46(12):2915–2919, 2005. doi: 10.2320/matertrans.46.2915.

[324] C.H. Lin, C.H. Huang, J.F. Chuang, J.C. Huang, J.S.C. Jang, and C.H. Chen. Rapid screening of potential metallic glasses for biomedical applications. *Materials Science and Engineering: C*, 33(8):4520–4526, dec 2013. doi: 10.1016/j.msec.2013.07.006.

[325] F. A. Halden and W D Kingery. Surface Tension at Elevated Temperatures. II. Effect of C, N, O and S on Liquid Iron Surface Tension and Interfacial Energy with Al 2 O 3. *The Journal of Physical Chemistry*, 59(6):557–559, jun 1955. doi: 10.1021/j150528a018.

[326] S. Klan. *Beitrag zur Evolution von Aluminium-Gusslegierungen für warmfeste Anwendungen.* PhD thesis, TU Bergakademie Freiberg, 2004.

[327] Hillary L. Smith, Chen W. Li, Andrew Hoff, Glenn R. Garrett, Dennis S. Kim, Fred C. Yang, Matthew S. Lucas, Tabitha Swan-Wood, J. Y. Y. Lin, M. B. Stone, D. L. Abernathy, Marios D. Demetriou, and B. Fultz. Separating the configurational and vibrational entropy contributions in metallic glasses. *Nature Physics*, 13(9):900–905, sep 2017. doi: 10.1038/nphys4142.

[328] Ralf Busch and Isabella Gallino. Kinetics, Thermodynamics, and Structure of Bulk Metallic Glass Forming Liquids. *JOM*, 69(11):2178–2186, nov 2017. doi: 10.1007/s11837-017-2574-5.

[329] Zachary J Evenson. *On the thermodynamic and kinetic properties of bulk glass forming metallic systems.* Phd thesis, Saarland University, 2012.

[330] Isabella Gallino, Daniele Cangialosi, Zach Evenson, Lisa Schmitt, Simon Hechler, Moritz Stolpe, and Beatrice Ruta. Hierarchical aging pathways and reversible

fragile-to-strong transition upon annealing of a metallic glass former. *Acta Materialia*, 144:400–410, feb 2018. doi: 10.1016/j.actamat.2017.10.060.

[331] O. Gross. *Precious metal based bulk glass-forming liquids: Development, thermodynamics, kinetics and structure.* Phd thesis, Saarland University, 2018.

[332] Ti2Ni Crystal Structure: Datasheet from "PAULING FILE Multinaries Edition – 2012" in SpringerMaterials (https://materials.springer.com/isp/crystallographic/docs/sd_0252202), .

[333] G. A. Yurko, J. W. Barton, and J. G. Parr. The crystal structure of Ti2Ni. *Acta Crystallographica*, 12(11):909–911, nov 1959. doi: 10.1107/S0365110X59002559.

[334] α-Ti (Ti rt) Crystal Structure: Datasheet from "PAULING FILE Multinaries Edition – 2012" in SpringerMaterials (https://materials.springer.com/isp/crystallographic/docs/sd_0308501), .